Thermochemical energy storage and transport system of unused heat from sugar mill utilizing zeolite ad/desorption cycle

ゼオライトの吸脱着サイクルを用いた製糖工場の未利用熱蓄熱輸送システム

February 2020

Shoma FUJII

藤井　祥万

Thermochemical energy storage and transport system of unused heat from sugar mill utilizing zeolite ad/desorption cycle

ゼオライトの吸脱着サイクルを用いた
製糖工場の未利用熱蓄熱輸送システム

February 2020

Waseda University
Graduate School of Creative Science and Engineering
Department of Modern Mechanical Engineering
Research on Exergy Engineering

Shoma FUJII
藤井　祥万

Table of contents

Chapter 1 Introduction

1.1 Effective use of local natural energy for sustainable society

Climate change has become a fundamental global problem following the industrial revolution, with the Intergovernmental Panel on Climate Change warning that the Earth is now approaching a number of tipping points of irreversible change. The concept of "Planetary Boundaries" (i.e., climate change, land system change, freshwater use, biogeochemical flows, ocean acidification, stratospheric ozone depletion, biosphere integrity, novel entities, and atmospheric aerosol loading, see **Fig. 1.1**) [1,2] was first proposed by Rockström et al., in 2009. The Planetary Boundaries represent the limits of safety and stability of the Earth system. Exceeding any one of these boundaries means the planet may undergo irreversible change. The concept of Planetary Boundaries was promoted by the Stockholm Resilience Centre [3] and helped lead to the 17 Sustainable Development Goals (SDGs) [4] as adopted by the United Nations in 2015.

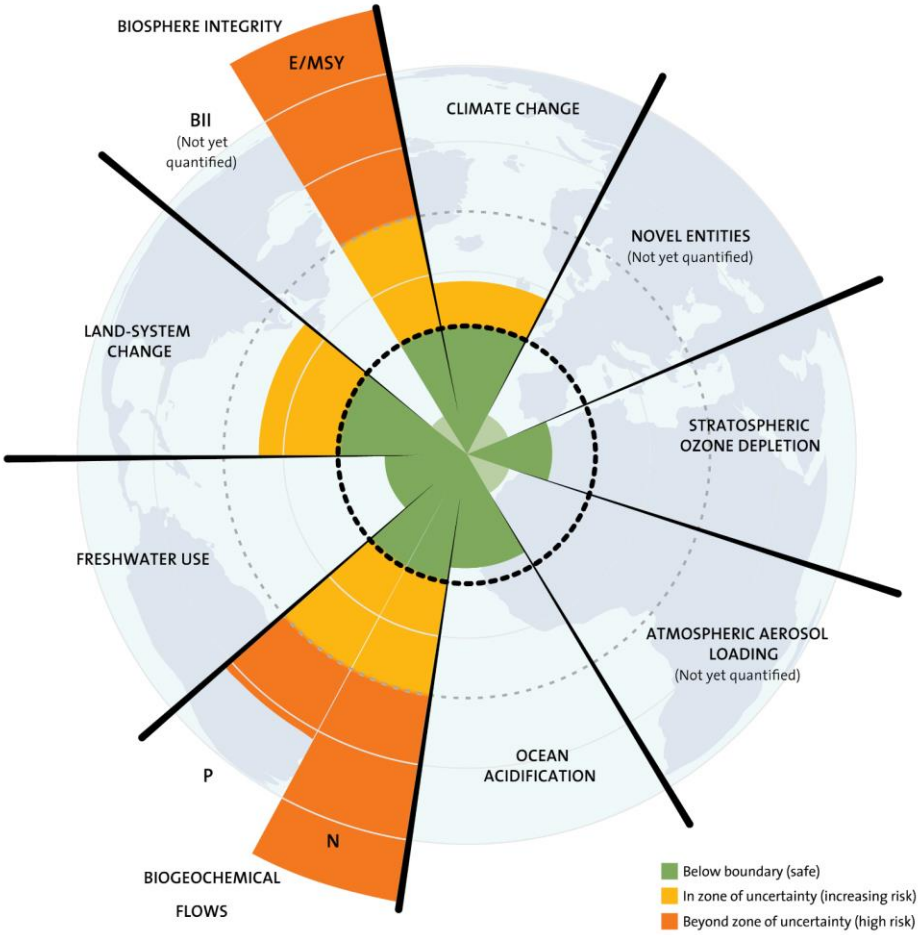

Fig. 1.1. Planetary Boundaries [3].

The nine Planetary Boundaries and 17 SDGs are not independent but share strong commonalities. In particular, energy production strongly effect the other areas such as the local economy, agricultural productivity, water availability, and the like. For instance, to realize a green economy which reconciles economic growth and sustainability via establishing a low carbon society, efficient use of local natural resources (e.g., untapped renewable energy) has a vital role [5].

This dissertation focuses on the unused energy of sugarcane as a local natural resource. An advanced, independently-operable method to utilize unused heat from sugar mill operations is established through the design of heat discharging and charging devices. Demonstration and techno-economic analysis of the designed thermochemical energy storage and transport system is provided.

1.2 Unused heat utilization

1.2.1 Spatiotemporal mismatch between unused heat source and heat demand

If unused, low temperature, renewable waste heat could be applied to heat demands, reduction of fossil fuel use and increase of local sustainability could be achieved. The distribution of waste and renewable heat depends on existing assets (e.g., factories, farms, etc.), their location, and the season. Thermal energy is difficult to directly transport via pipeline unless the waste heat sources and demands are very close spatially and temporally. Thermal energy storage technology has the potential to overcome this spatiotemporal mismatch.

1.2.2 Waste heat

Roughly half of global energy use is in the form of heat, almost exclusively derived from fossil fuel combustion. The industrial sector exhausts up to 50% of generated energy as waste heat, with 80% of this heat being below 300 °C [6] as shown in **Fig. 1.2**. On the other hand, industrial processes consume a substantial amount of low temperature heat. For example, roughly a quarter of the total final energy demand in the EU is heat below 100 °C. The breakdown of heat demand temperature is industry-dependent; the majority of heat used in the food industry is below 500 °C [7]. In Japan, most industries, excluding steel making and petroleum refining, require heat below 180 °C for concentration, drying, and other processes [8]. If such low temperature heat demands can be compensated using the unused heat, significant improvement in total energy efficiency are expected.

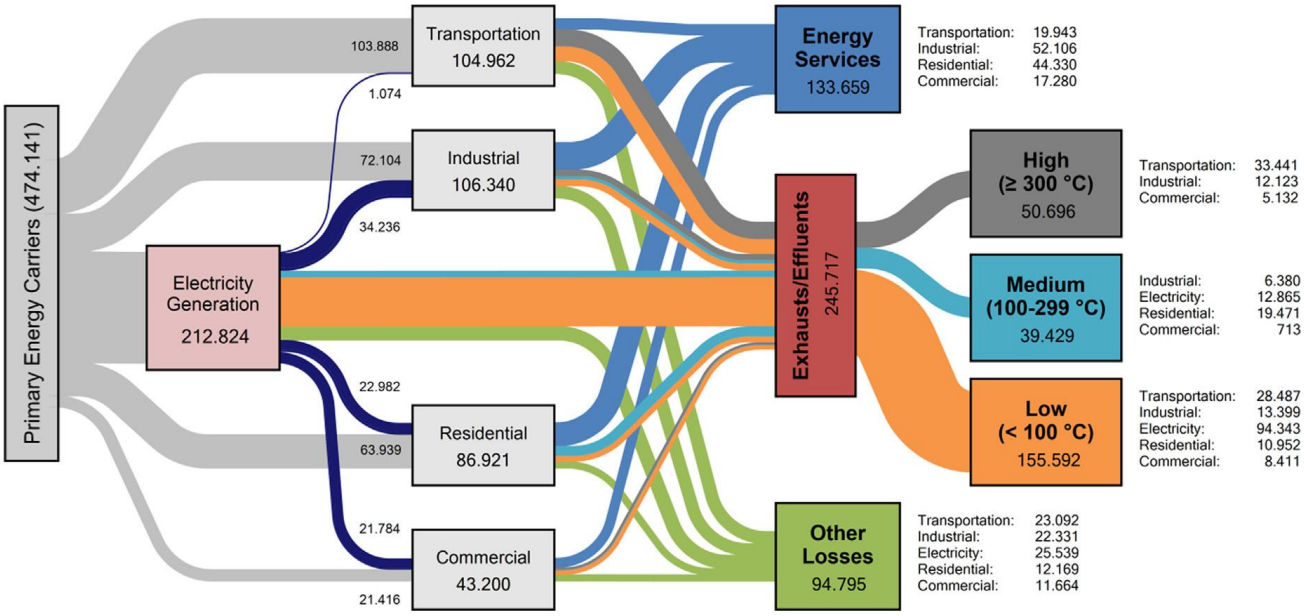

Fig. 1.2. Estimated global waste heat in 2012 in PJ [6].

Fig. 1.3. IEA Tracking Clean Energy Progress 2017 [9].

1.2.3 Renewable heat

A summary of the status of various technologies needed to meet the 2 °C scenario targets is shown in **Fig. 1.3** [9]. Renewable heat utilization must increase by 32% by 2025. However, the growth of renewable heat is much slower than that of renewable electricity. There are both economic (e.g., high capital cost) and non-economic (e.g., suitability issues) barriers. In 2014, direct utilization of renewable heat was 14.2 EJ, an 8% increase from 2010. Biomass utilization accounts for 90% of renewable heat, which is mainly used in Europe. The main problem of biomass energy is the logistics of operation [10], which has economic implications. Sugarcane, the focus of this doctoral dissertation, has the benefit of the operational logistics (collection system) already being established in the sugarcane industry.

1.3 Sugarcane industry overview

1.3.1 Features of sugarcane industry

Sugarcane is one of the most productive biomasses from the standpoint of conversion of solar energy into material [11]. Recently, sugar mills which produce raw sugar from sugarcane have been regarded as an energy hub in local areas. For example, Cuba is planning to increase renewable power, with sugarcane-based biomass playing a vital role [12]. In Brazil, one of the major sugar producers in the world [13], around 18% of primary energy supply came from sugarcane in 2009 [14].

In some sugarcane producing areas, crop rotation (e.g., potato, tobacco, soybeans) is used to maintain soil health. The post-harvest processing of crops often occurs close to farms in factories consuming fossil fuels. Utilizing the biomass from sugarcane as a local energy supply can help these relevant agricultural industries to sustain lower cost and greater independence.

1.3.2 Process of typical sugar mill

A schematic of a typical sugar mill is shown in **Fig. 1.4**. Almost all sugar mills employ a cogeneration system of heat and power. After the cultivation and harvesting processes, sugarcane is transported to a sugar mill where raw sugar is produced via milling, evaporation, and crystallization processes. Transported sugarcane is firstly milled in a series of milling rolls. Hot water is poured onto the final milling roll to enhance the extraction of sugar (so-called “maceration water”). The exhausted water is introduced to previous milling roll as its maceration water. This process continues until reaching the initial milling roll or a desired sugar concentration, thus producing “sugar juice” which is further processed downstream. The residue of sugarcane after the milling process (termed “bagasse”) is transported to a specialized boiler (“bagasse boiler”) to generate biomass energy. Impurities are eliminated via precipitation from the sugar juice by the addition of flocculants. The clarified sugar juice is sent to the evaporation process. Multiple effect evaporation processes are commonly

employed in sugar mills. Steam generated by the bagasse boiler is introduced to the primary evaporation vessel. Evaporated steam from the primary evaporation vessel is fed to the secondary negative-pressure vessel as a heat source with a large latent heat. By repeating this process, steam from the bagasse boiler can be efficiently utilized. After sufficient evaporation, the clarified sugar juice has been concentrated into so-called “syrup”. The syrup is crystallized by adding solid sugar seeds resulting in sugar crystals and a remnant liquid phase known as “molasses”. The mixture of molasses and sugar crystals is sent to a centrifuge which separates the sugar crystals from molasses. The molasses is sometimes used as a feed for livestock. The sugar crystals are stored in hermetic vessels and transported to a centralized sugar refinery.

As noted above, bagasse is fed into the bagasse boiler to provide energy and process heat. The bagasse boiler generates steam which is sent to the mill turbine and steam turbine for power generation. The exhaust steam from the mill and steam turbine is utilized in the evaporation and crystallization processes as a heat source. This means, the sugar mill is self-sufficiently operated in terms of their heat and power supply. However, bagasse cannot be stored long-term due to its high perishability and bulky nature. Excess bagasse could be stored and utilized in the off-season to drive the steam turbine to generate the electricity to sell to the power grid. However, typical sugar mills are designed as stand-alone plants without connection to the local power grid. These sugar mills utilize almost all of the bagasse during the sugar milling season because there is no heat demand in the sugar mill during the off-season. Currently, these sugar mills burn more bagasse than is needed internally, and exhaust the unused heat as a high temperature flue gas. Recently, to better utilize the potential of sugarcane, polygeneration in the sugarcane industry has been considered.

1.3.3 Polygeneration in the sugarcane industry

Recently, polygeneration in the sugarcane industry has been implemented through the sale of excess electricity to the power grid and production of ethanol [15]. The simplest way to increase power generation for sale to the power grid is by reduction of steam consumption in sugar mills. Reducing steam consumption can be achieved by increasing the efficiency of auxiliary power draws (e.g., lighting) and installing an electrically-driven mill turbine instead of steam turbine. Additionally, power generation can be increased by the same manner in electricity business, for example installing an efficient high-pressure bagasse boiler, installing a condensing steam turbine, and extracting for evaporation processes. The biomass integrated gasification combined cycle (BIG-CC), the biomass integrated gasification with gas turbine (BIG-GT), and the biomass integrated gasification with steam injected gas turbine (BIG-STIG) have the potential to utilize bagasse efficiently, but they are still under development [16].

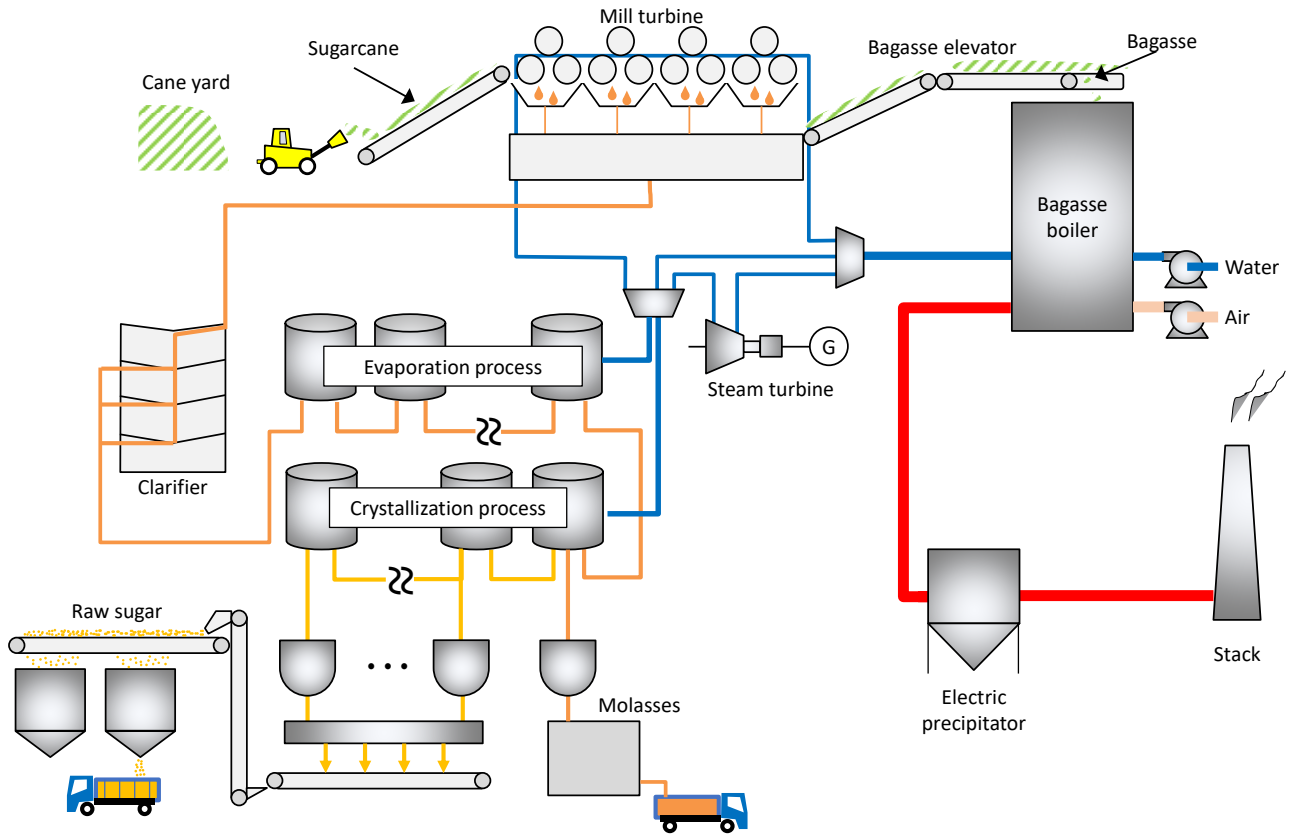

Fig. 1.4. Schematic design of a typical sugar mill.

Many sugar mills in Brazil produce not only raw sugar, but also ethanol [17]. Ethanol production from sugarcane has greatly reduces greenhouse gas emission but has some social issues (e.g., competition with food production, land use change impacts, etc.). Recent research has worked to resolve these issues with alternative polygeneration methods utilizing a high yield sugarcane to generate sugar, ethanol, and electricity [18].

This doctoral dissertation focuses on recovering and effectively utilizing the unused heat from sugar mills via thermal energy storage technology as a polygeneration method for the sugarcane industry (see **Fig. 1.5**). Benefits of applying the thermal energy storage technology to sugar mills are summarized as follows:

- resolves spatial and seasonal heat supply-demand mismatch
- no impact on the sugar producing process as only final unused heat is recovered
- easily retrofitted to extant sugar mills
- improves flexibility in sugar mill design

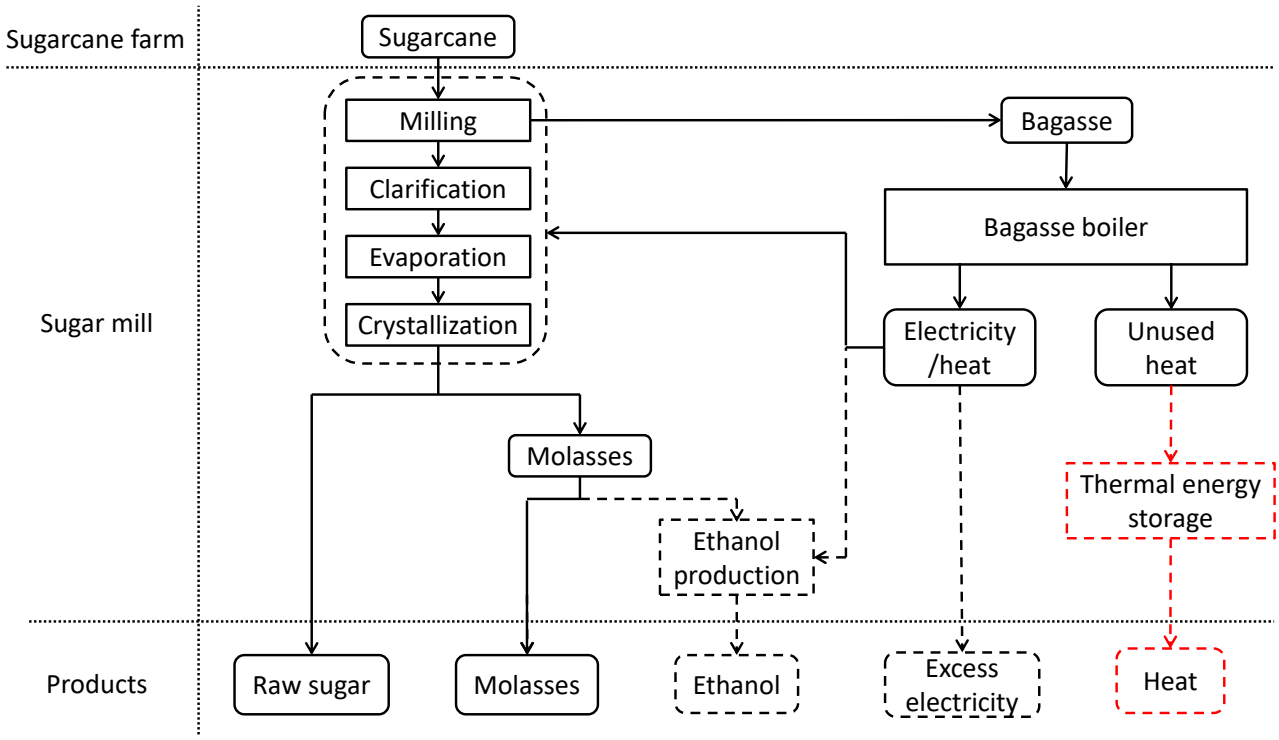

Fig. 1.5. Polygeneration in sugarcane industry.

1.4 Sustainability of island and isolated areas in Japan

Japan is now facing multiple enormous social issues including a decreasing birthrate, an aging society, a high reliance on imported energy source, gender inequality, and the like, which are strongly related to the problems that the SDGs aim to resolve. In Japan, the Fifth Basic Environment Plan, adopted by the Japanese cabinet in 2018 [19], includes the concept of “Circulating and Ecological Economy”. In short, each region aims to build a self-reliant and decentralized society referring the concept of SDGs. This model is especially relevant in the numerous island and isolated areas in Japan which currently depend strongly on imported energy, food, material and like that sources. Realization of the “Circulating and Ecological Economy” for island and isolated areas would not only greatly increase Japan’s sustainability but would also provide know-how for realizing global sustainability.

Energy issues are strongly related to climate change in the Planetary Boundaries and Goals 7 and 13 of the SDGs (Goal 7: Ensure access to affordable, reliable, sustainable and modern energy for all; Goal 13: Take urgent action to combat climate change and its impact). Though the electricity price on Japanese islands is almost the same as that on mainland Japan, there are additional transportation costs that increase the levelized cost of electricity. In Japan, those living on the mainland bear this additional cost based on the concept of “Universal Service”[20]. From the perspective of economic, environmental, energy security and national defense, a low-carbon, self-reliant, and distributed energy system is required for island and isolated areas.

This doctoral dissertation aims to realize a low-carbon society and distributed energy system for the island of Tanegashima in Japan by building the thermochemical energy storage and transport system needed to utilize local, renewable, unused heat derived from the sugarcane industry.

1.5 Current situation of Tanegashima

1.5.1 Overview

This dissertation focuses on Tanegashima, an isolated island located southern part of Japan (~115 km south of the southernmost tip of Kyushu, the southernmost island in 'mainland' Japan, see **Fig. 1.6**). Tanegashima covers an area of ~445 m^2 with a population of roughly 30,000 [21]. The island is a plateau, the tallest point being 282 m above sea level [21]. In comparison, the neighboring island, Yakushima, is mountainous with a peak elevation of 1936 meters [22]. Due to its geography, Yakushima is able to provide the majority of its electricity demand through hydro power plants. However, as Tanegashima lacks such fortunate topography, it relies on diesel power plants (two power plants with 40,500 kW [23]). The diesel oil is imported from outside the island, which leads to an increase in the levelized cost of electricity. Hopefully, the island ought to independent in imported energy source via utilizing island's local source.

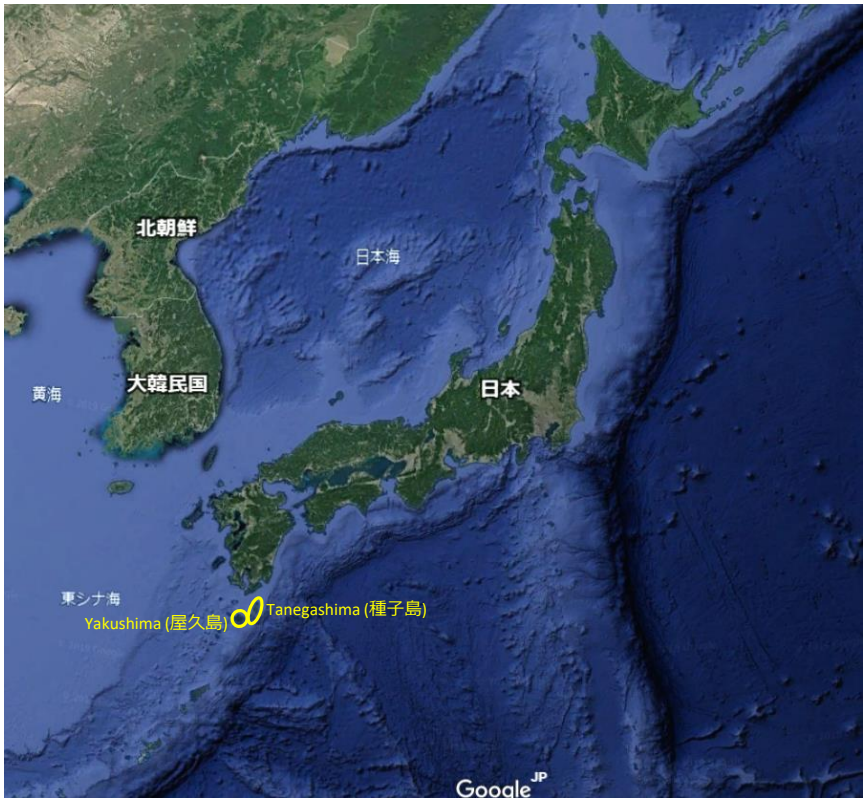

Fig. 1.6. Location of Tanegashima (Google earth).

1.5.2 Sugarcane industry

Agriculture, predominantly sugarcane and sweet potato, is the main industry on Tanegashima. Due to the extensive processing of sugarcane that also takes place on the island, the economy of Tanegashima centers around the sugarcane industry. Thus, new technology implementation such as effective exploitation of unused energy derived from the sugarcane industry will induce a strong socio-economic benefit to the island [24].

A single sugar mill, located in the middle of Tanegashima, processes all the sugarcane harvested on the island. This mill processes 1600 t per day (TPD) of sugarcane, which is the largest scale in Kagoshima prefecture. During sugarcane harvesting season, which usually lasts from December to middle of April, sugarcane is systematically harvested, bundled, transported to the stock yard of mill, and milled. The bagasse supplied to the bagasse boiler often exceeds the temporal heat and power demands. Because bagasse cannot be readily stored due to its perishability, excess bagasse is burned in the bagasse boiler, and a large quantity of ~200 °C heat is exhausted as flue gas.

A decrease in the number of farmers has become a serious problem in recent decades across Japan, but in particular on remote islands. Population decline in the city of Nishinoomote in Tanegashima began in 1960 [25], while Japan as a whole did not see a population decline until 2011. Those over 65 years old accounted for 33.6% of the population in 2014 in the city of Nishinoomote, with their numbers continuing to increase. The labor shortage for agricultural work due to the population decline has supplanted by mechanical harvesters. However, 90% of sugarcane is harvested by mechanical harvesters in Kagoshima prefecture [26], which means further labor shortages will be difficult to offset with mechanical harvesters. Thus, a decrease in the quantity of sugar harvested may be expected in the near future. To improve sugarcane yield, some new types of sugarcane have been developed (e.g., “KY10-1380”, “KY01-2043”). These engineered sugarcanes are taller than conventional breeds and should produce a larger sugar yield. However, some strains of engineered sugarcane have a higher share of bagasse. Thus, the production of bagasse is also expected to increase, meaning the efficient utilization of energy derived from bagasse will become more and more important in the near future.

1.5.3 Heat demand in Tanegashima

In Tanegashima, food processing factories (i.e., liquor factories, starch factories), cleaning factories, and other industrial processes consume process steam at a pressure up to 0.2 MPa year-round. Some food processing factories operate from the beginning of December to the middle of February, and other industries operate year-round. They generally have installed small once-thorough boilers (package boiler) which generate about 0.6 MPa steam. Steam generated by package boilers is

depressurized to the demand pressure. The main fuel source for package boilers is imported heavy oil and liquefied petroleum gas (LPG).

Tanegashima has a spatial and seasonal heat supply-demand mismatch between the unused heat from the sugar mill (December-April, centrally-located) and the heat demand of other industrial processes (year-round, dispersed) as shown in **Fig. 1.7**. Utilization of the unused heat from the sugar mill to these heat demand sites enhances the circulation of local resources, and thus decreases the amount of imported energy.

1.5.4 Applying thermochemical energy storage and transport system

As described above, Tanegashima has a spatial and seasonal heat mismatch between the unused heat from the sugar mill and heat demands from other industrial processes. Bagasse can be dried and pelletized to be transformed into a storable fuel for use in boilers. However, existing boilers must be completely replaced with a bagasse boiler in order to utilize such dried bagasse pellets. The burden of additional equipment costs is not reasonable for most industries. This doctoral dissertation focuses on “heat transportation” utilizing a thermal energy storage technology. The system charges the unused heat derived from sugarcane bagasse in a heat storage media. The heat storage media is then transported to adjacent factories where the stored heat is released as shown in **Fig. 1.8**.

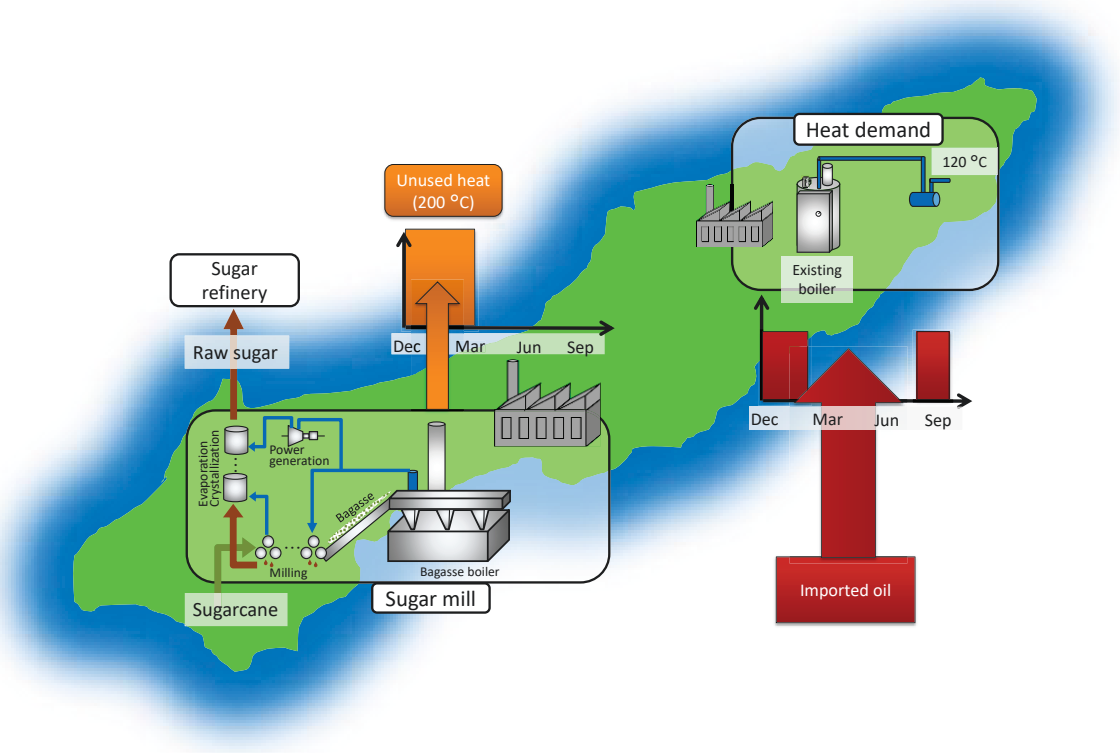

Fig. 1.7. Spatial and seasonal heat supply-demand mismatch in Tanegashima.

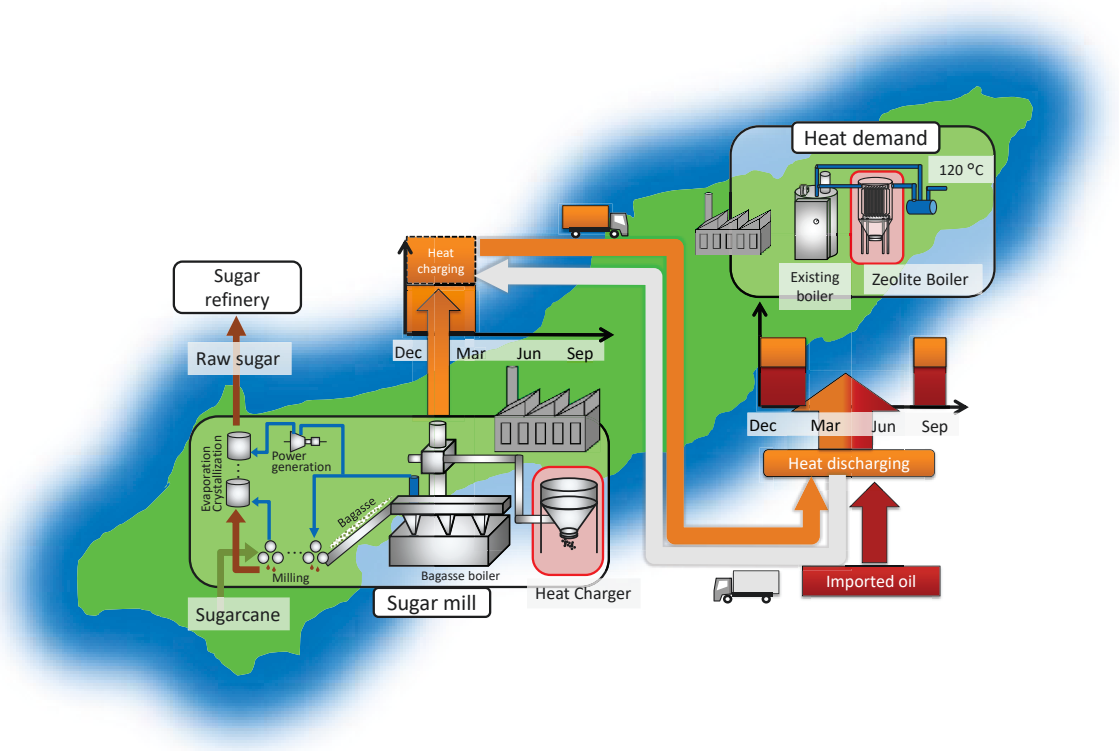

Fig. 1.8. Concept of the thermal energy storage (TES) and transport system of unused heat from sugar mill.

1.6 Objectives and structure of this dissertation

The objectives of this dissertation are to design the heat charging and discharging devices from both experimental and numerical approaches, and to clarify the condition of the thermochemical energy storage and transport system that is financially viable through techno-economic analysis.

The structure of this dissertation is shown in **Fig. 1.9 (a)**. Relevant main publications are shown in **Fig. 1.9 (b)**. The dissertation consists of three categories from the point of view scale: system level, component level, and material level. After the introduction in this chapter and the state of the art of thermochemical energy storage technology in Chapter 2, the technical contents consist of 4 chapters.

Chapter 3 focuses on system level analysis. A process model of the Tanegashima sugar mill was conducted to quantify its heat charging potential. Some modified processes to improve both the heat charging potential and power generation were considered.

Chapter 4 focuses on component and material level analysis and design of a heat discharging device termed the “Zeolite Boiler”. Adsorption and heat transfer characteristics were quantified experimentally and numerically. A bench-scale Zeolite Boiler was constructed and demonstration tests of continuous pressurized steam generation were performed. The design of a full-scale Zeolite

Boilers for use at the Tanegashima was evaluated by performance prediction using a numerical simulation.

Chapter 5 focuses on the component and material level design and analysis of a heat charging device called the “Heat Charger”. Desorption characteristics were quantified experimentally and numerically. A bench-scale Heat Charger was manufactured, and continuous heat charging was demonstrated. Alternative gas flow designs for a full-scale Heat Charger at the sugar mill in Tanegashima were numerically investigated. A design method minimizing power consumption was used to establish system configurations and operation conditions. The design policy was used in the techno-economic analysis of Chapter 6.

Chapter 6 returns to a system level analysis, this time in terms of techno-economic and environmental analyses combining results and design methods from Chapters 3-5. Through the techno-economic and environmental analyses, and a sensitivity analysis, the conditions leading to financially viability of the thermochemical energy storage and transport system were determined.

Chapter 7 summarizes the main achievements, academic contributions to the scientific community, and future research direction from this dissertation.

1.7 Novel contributions of this dissertation

The novel contributions to the scientific community of this dissertation are as follows:

- The effect of altering the sugar mill process on heat charging quantity and economic viability was clarified
- Continuous generation of pressurized steam via zeolite steam adsorption was demonstrated
- Fuel savings for existing boilers cooperating with the Zeolite Boiler were shown numerically
- Financially viable conditions for the thermochemical energy storage and transport system utilizing unused heat from a sugar mill were determined through techno-economic analysis

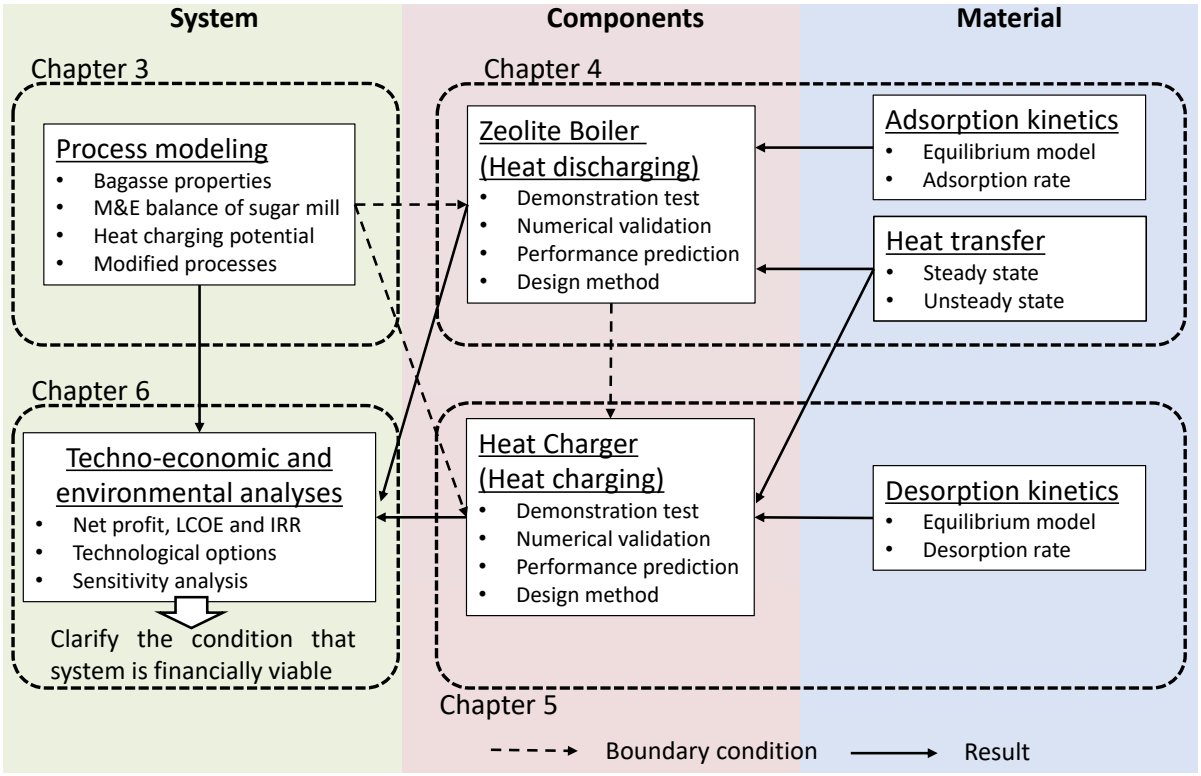

(a) Structure of this dissertation.

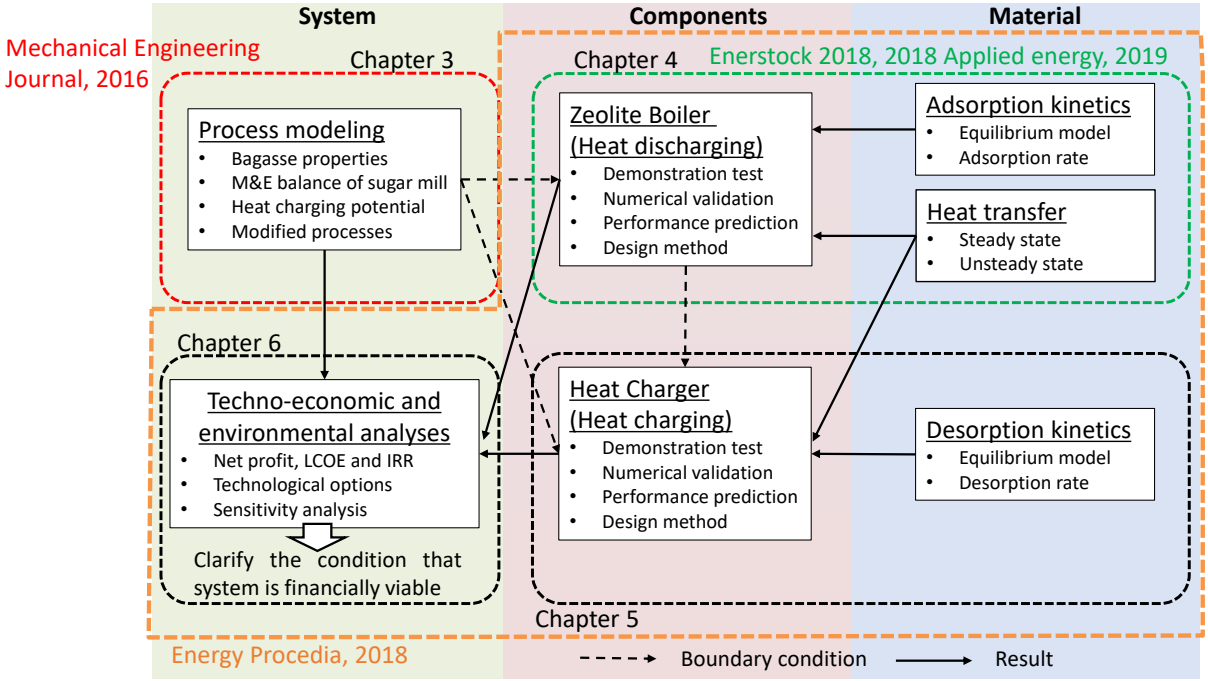

(b) Relevant main publications.

Fig. 1.9. Structure of this dissertation with relevant main publications.

References

[1] Rockström J, Steffen W, Noone K, Persson Å, Chapin FS, Lambin EF, et al. A safe operating space for humanity. Nature 2009;461:472–5.

[2] Rockström J, Steffen W, Noone K, Persson Å, Chapin FS, Lambin EF, et al. Planetary Boundaries : Exploring the Safe Operating Space for Humanity. Ecol Soc 2009;14.

[3] https://www.stockholmresilience.org/research/planetary-boundaries.html (accessed on Oct, 2019) n.d.

[4] United Nations,Transforming our world: the 2030 agenda for Sustainable Development. 2015. https://doi.org/10.5040/9781782257790.part-008.

[5] https://www.unenvironment.org/regions/asia-and-pacific/regional-initiatives/supporting-resource-efficiency/green-economy (accessed on Dec, 2019) n.d.

[6] Forman C, Muritala IK, Pardemann R, Meyer B. Estimating the global waste heat potential. Renew Sustain Energy Rev 2016;57:1568–79. https://doi.org/10.1016/J.RSER.2015.12.192.

[7] Naegler T, Simon S, Klein M, Gils HC. Quantification of the European industrial heat demand by branch and temperature level. Int J Energy Res 2015;39:2019–30. https://doi.org/doi:10.1002/er.3436.

[8] Agency, Center for Research and Development Strategy Japan Science and Technology,Technology Survey on Advance Utilization of Medium to Low Temperature Heat (in Japanese). 2013.

[9] https://www.iea.org/tracking/tcep2018/energyintegration/renewableheat/ (accessed on Oct, 2019) n.d.

[10] Rentizelas AA, Tolis AJ, Tatsiopoulos IP. Logistics issues of biomass: The storage problem and the multi-biomass supply chain. Renew Sustain Energy Rev 2009;13:887–94. https://doi.org/10.1016/J.RSER.2008.01.003.

[11] Ramjeawon T. Life cycle assessment of electricity generation from bagasse in Mauritius. J Clean Prod 2008;16:1727–34. https://doi.org/10.1016/J.JCLEPRO.2007.11.001.

[12] Sagastume Gutiérrez A, Cabello Eras JJ, Huisingh D, Vandecasteele C, Hens L. The current potential of low-carbon economy and biomass-based electricity in Cuba. The case of sugarcane, energy cane and marabu (Dichrostachys cinerea) as biomass sources. J Clean Prod 2018;172:2108–22. https://doi.org/10.1016/j.jclepro.2017.11.209.

[13] Du C, Dias LC, Freire F. Robust multi-criteria weighting in comparative LCA and S-LCA: A case study of sugarcane production in Brazil. J Clean Prod 2019;218:708–17. https://doi.org/10.1016/j.jclepro.2019.02.035.

[14] Seabra JEA, Macedo IC, Chum HL, Faroni CE, Sarto CA. Life cycle assessment of Brazilian sugarcane products: GHG emissions and energy use. Biofuels, Bioprod Biorefining 2011;5:519–32. https://doi.org/10.1002/bbb.289.

[15] Palacio JCE, Renó MLG, Martínez Reyes AM, de Souza GF, Batlle EAO, del Olmo OAA, et al. Exergy and Environmental Analysis of a Polygeneration System of Alcohol Industry. Waste and Biomass Valorization 2018;0:0. https://doi.org/10.1007/s12649-018-0509-1.

[16] Deshmukh R, Jacobson A, Chamberlin C, Kammen D. Thermal gasification or direct combustion? Comparison of advanced cogeneration systems inthe sugarcane industry. Biomass and Bioenergy 2013;55:163–74. https://doi.org/10.1016/j.biombioe.2013.01.033.

[17] Goldemberg J, Coelho ST, Guardabassi P, Nastari PM. Bioethanol from Sugar: The Brazilian Experience. Energy from Org Mater 2019:925–54. https://doi.org/10.1007/978-1-4939-7813-7_312.

[18] Ohara S, Terajima Y, Kikuchi Y, Fukushima Y, Yasuhara T, Sugimoto A. Pilot Scale Demonstration of Technologies for Enhancing Production of Sugar and Ethanol from Sugarcane (in Japanese). KAGAKU KOGAKU RONBUNSHU 2018;44:260–70. https://doi.org/10.1252/kakoronbunshu.44.260.

[19] Ministry of the Environment Japan, The fifth Basic Environment Plan. 2018.

[20] http://www.kyuden.co.jp/wheeling_stipulation_universal.html (in Japanese accessed on Oct, 2019) n.d.

[21] http://www.pref.kagoshima.jp/ac07/pr/shima/gaiyo/tanegashima/tanegashima_top.html(in Japanese, accesed on Sep. 2019) 2018.

[22] http://www.pref.kagoshima.jp/ac07/pr/shima/gaiyo/yakushima/yakushima.html(in Japanese, accesed on Sep. 2019) 2018.

[23] https://www.emsc.meti.go.jp/activity/emsc_electricity/pdf/006_06_06.pdf (in Japanese, accessed on Oct, 2019) 2015.

[24] Oshita Y, Heiho A, Ouchida K, Kanematsu Y, Fukushima Y, Kikuchi Y. Analyzing Socio-economic Effect Induced by Technology Implementation on Available Renewables: A Case Study of Tanegashima, Japan (in Japanese). J Life Cycle Assessment, Japan 2019;15:360–76.

[25] http://www.city.nishinoomote.lg.jp/material/files/group/9/73680808.pdf (in Japanese accessed on Oct, 2019) 2015.

[26] https://www.alic.go.jp/joho-s/joho07_001516.html (in Japanese accessed on Oct, 2019) 2017.

This page intentionally left blank.

Chapter 2 Specifying limitation of thermal energy storage

2.1 Objectives of this chapter

In this chapter, the state of the art of thermal energy storage is conducted to specify the limitation of thermal energy storage and the originality of this doctoral dissertation. In Tanegasihma, some industrial processes such as food processing factories and cleaning factories consume process steam at a pressure up to 0.2 MPa and a temperature of 120 °C; this quality of steam forms the target of the heat discharging device in the thermochemical energy storage and transport system herein. The minimum requirements of the system are to resolve the spatial and seasonal heat supply-demand mismatch and to continuously provide pressurized steam at 0.2 MPa. In addition, cheaper equipment and operating expenses are preferred. The conventional reactor for desorption process can be employed as a conceptual design of heat charging device because the purpose of the heat charging device is simply to desorb the water adsorbed on the zeolite. Thermochemical energy storages that utilize adsorption, that can store heat over seasonal time scales, that can provide high temperature heat, and relevant reactor designs are reviewed. Since industrial processes in Tanegashima require steam of 120 °C, the review is undertaken from the point of view of the discharging temperature. The novel conceptual design of heat charging and discharging reactors developed in this doctoral dissertation are built upon the literature review.

2.2 Classification of thermal energy storage

The classification of thermal energy storage is shown in **Fig. 2.1**. Thermal energy storage can be classified in mainly three types: sensible energy storage, latent energy storage, and thermochemical energy storage.

2.2.1 Sensible energy storage

The most popular thermal energy storage systems are based on sensible energy storage. In sensible energy storage, the heat capacity of the material is the storage media. Sensible energy storage can be separated into solid and liquid processes. The main heat storage materials of solid processes are rocks and metals [1]. For instance, Concentrating Solar Power (CSP) can be used to heat a fixed bed of rocks, from which heat can be recovered at a later time using a fluid medium such as air [2]. The main heat storage materials of liquid process are hot water, thermal oil, and molten salt [1]. For instance, the hot water system was connected to a district heating system and used to buffer heat [3].

In spite of its low-cost, sensible energy storage is not applicable to Tanegashima. The primary reason is that sensible energy storages are unable to store heat over seasonal timespans due to a

decrease in storage capacity via heat leakage from the system (i.e., natural cooling). An additional inadequacy of sensible energy storage systems is their comparatively low thermal energy storage density. The system in Tanegashima requires the transportation of the energy storage material, so lower energy density leads to an increase in transportation cost.

2.2.2 Latent energy storage

Latent energy storage utilizing Phase Change Material (PCM) has been well studied for application in thermal energy storage and transport systems. As the name implies, PCMs store and release heat through the solid-liquid phase change. In general, PCMs can be categorized as inorganic vs. organic, granules vs. powders, and eutectics. Many PCMs are commercially available, covering a wide range of melting temperatures [4], allowing for a flexibility in equipment and system design. As an example, Sanki Engineering Co., LTD. operates a thermal energy storage and transport system utilizing PCMs in Japan. In their system, Sodium Acetate Trihydrate and erythritol are used as the heat storage and transport material for lower temperature applications (58 °C) and a higher temperature applications (118 °C), respectively [5]. Sanki's heat transportation system utilizing PCMs is shown in **Fig. 2.2**; the larger system has a thermal storage capacity of 1.4 MWh/trailer when using erythritol as the heat storage material.

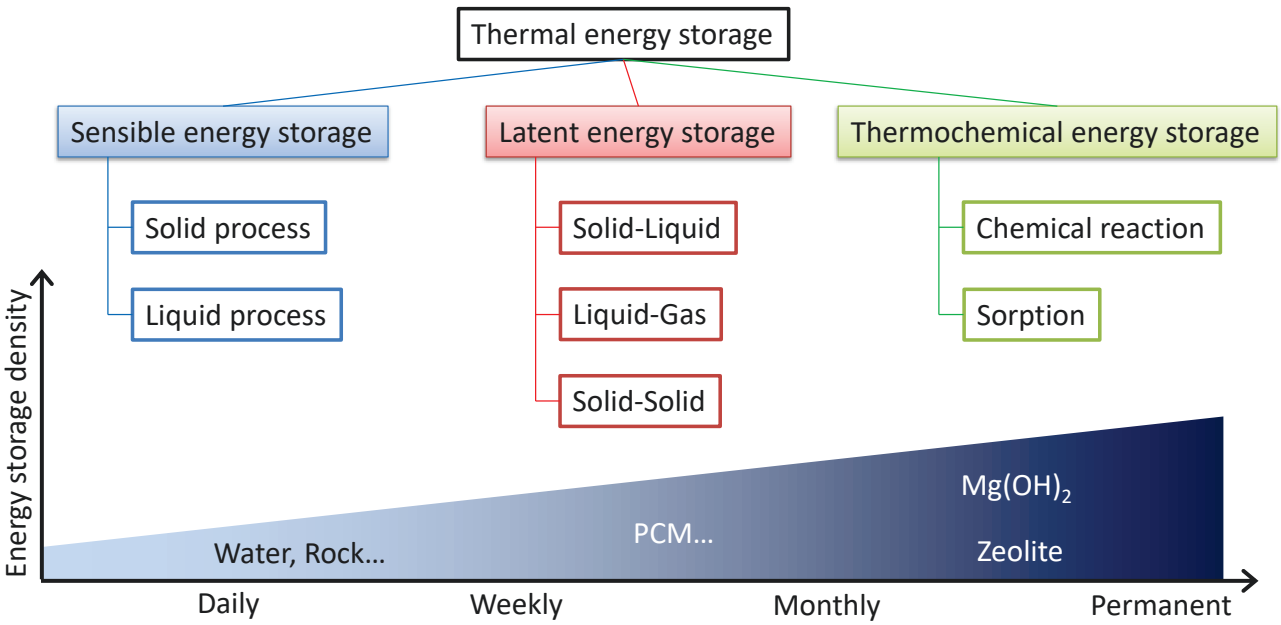

Fig. 2.1. Classification of thermal energy storage.

(a) 1.4 MWh/trailer (Erythritol), 1.1 MWh/trailer (Sodium Acetate Trihydrate)

(b) 0.50 MWh/trailer (Erythritol), 0.35 MWh/trailer (Sodium Acetate Trihydrate)

Fig. 2.2. "Heat Trans Container" provided by Sanki Engineering [6].

Other institute demonstrated a thermal energy storage and transport system utilizing erythritol. The erythritol was charged with industrial waste heat below 200 °C, erythritol was then transported to a heat demand where it successfully generated >90 °C water from the heat discharging station [7].

The concept of "Mobile Thermal Energy Storage (M-TES)" utilizing erythritol was considered in Sweden to resolve a spatial heat mismatch between an industrial waste heat source and a local district heating system [8]. The test unit, which contained 40 L of erythritol and 20 L of heat transfer fluid in a shell and tube heat exchanger, was able to discharge the stored heat at a temperature around 110 °C [9].

Latent energy storage is clearly viable for thermal energy storage and transport systems. However, the temperature level of supplied heat is limited by the melting temperature of the PCM. This limitation makes latent energy storage insufficient to produce pressurized steam. In addition, heat leakage from the system reduces the heat storage capacity over time, similar to the case of sensible energy storage. As such, latent energy storage is unable to resolve the seasonal heat supply-demand mismatch in Tanegashima.

2.2.3 Thermochemical energy storage

Thermochemical energy storage utilizes reversible processes (e.g., chemical reactions, adsorption/desorption) with high temperature operation. Thermochemical reactions are the only viable method to provide seasonal heat storage and to generate pressurized steam in the heat discharging process. Thermochemical materials, summarized in terms of charging temperature and volumetric storage capacity, are shown in **Fig. 2.3** [4].

Thermochemical energy storage materials utilizing chemical reactions have a few shortcomings. While they generally have larger energy storage density and higher-temperature operation than adsorption process, degradation of material due to irreversible reactions with contaminants is a major problem. Another difficulty is control of the reaction rate. Heat discharging (i.e., exothermic) reactions such as hydration induce a positive feedback following the Arrhenius laws. This doctoral dissertation utilizes the physical adsorption process because adsorbents undergo essentially no degradation, are cheap, and are safe. As an adsorbate, water was selected due to its ubiquity and safety. Zeolite and water were paired for thermal energy storage because they can provide sufficient temperature to generate pressurized steam up to 0.2 MPa (saturation temperature at this pressure is 120 °C) and have a relatively high energy storage density. Conventional “Zeolite 13X” was selected because of its high water uptake capacity which results in a high energy storage density.

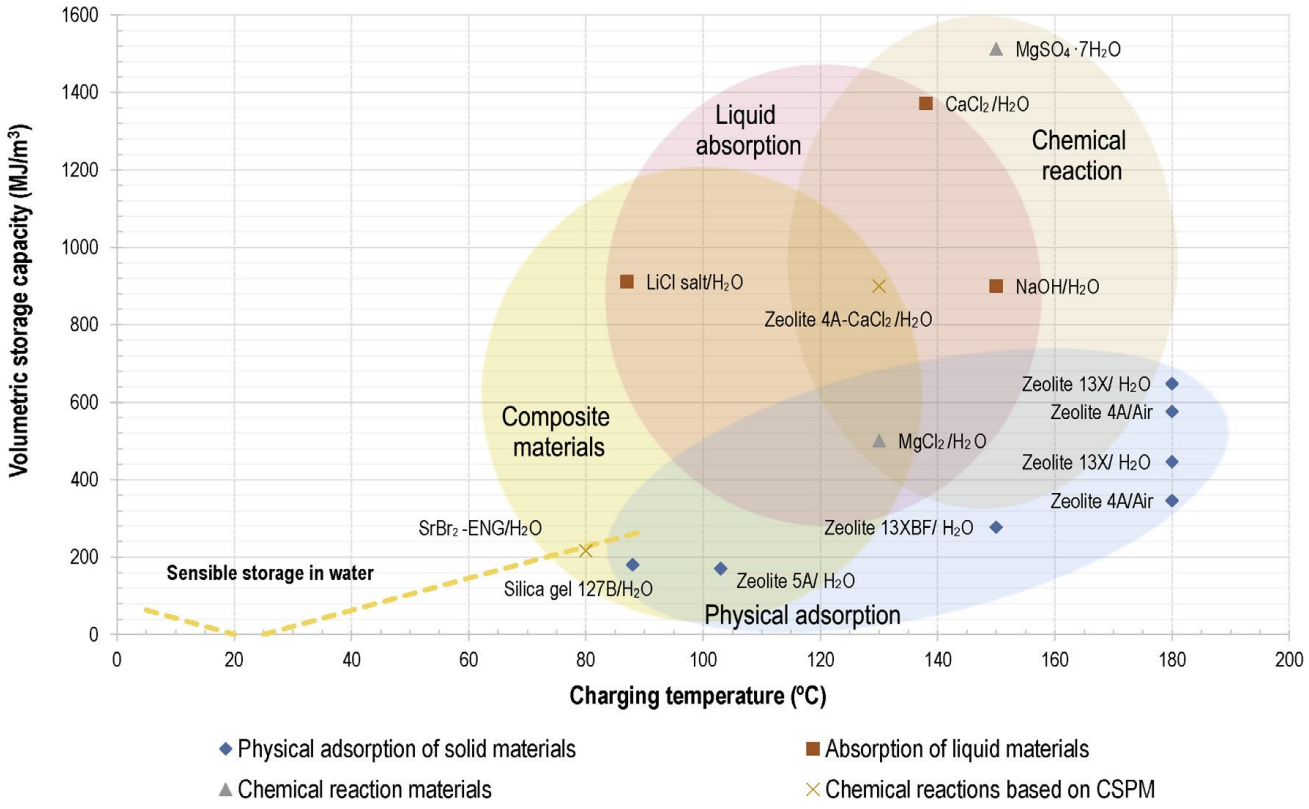

Fig. 2.3. Thermochemical energy storage material summarized in charging temperature and volumetric storage capacity [4].

2.3 State of the art of systems and components for thermochemical energy storage

2.3.1 Outline of reactor types

As shown in **Fig. 2.4**, reactor types in adsorption/desorption processes can be categorized as open vs. closed and indirect vs. direct heat exchange. Closed systems consist of a vacuum chamber, heat exchanger, and an evaporator/condenser. In the adsorption process, low quality heat is provided to the evaporator causing evaporation at the operating pressure; this water vapor is adsorbed onto the adsorbent. Adsorption heat is transferred to the heat transfer fluid via the heat exchanger. In the desorption process, unused heat is provided to the heat exchanger, causing water to desorb from the adsorbent. The desorbed water is condensed and stored in the water reservoir in liquid state to reduce the required storage volume.

Open systems can employ both indirect and direct heat exchanging types. In the adsorption process, ambient air with humidity or steam is fed into the adsorbent bed. In the indirect heat exchanging type, the heat exchanger is placed into the bed, and adsorption heat is transferred to the heat transfer fluid which is circulated in the heat exchanger. The main problem of this type of reactor is the low overall heat transfer which decreases the total heat yield from the material and the accompanying performance. To customize to heat discharging applications, a heat exchanger is sometimes placed after the reactor and the hot heat transfer fluid provides sensible heat to the heat exchanger. In the desorption process, a heat source is introduced to the heat exchanger and provides heat to the material for desorption.

Direct heat exchanging types have a larger specific heat transfer area between the heat transfer fluid and particle, leading to higher overall heat transfer coefficient. In the adsorption process, the outlet air of the reactor heated by adsorption heat is directly used in the heat demand. In the desorption process, hot air is blown into the bed to desorb the material.

In the following sections, a comprehensive review of adsorption based thermal energy storage systems is conducted with particular focus on the operating temperature required to continuously generate pressurized steam.

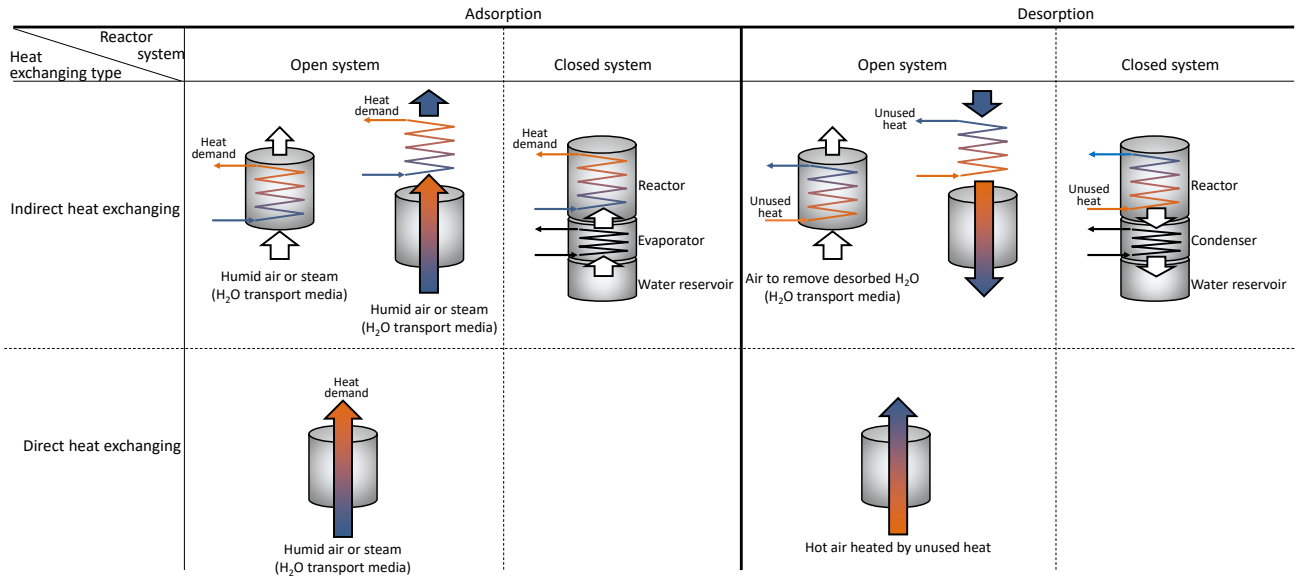

Fig. 2.4. Classification of reactors and processes in ad/desorption.

2.3.2 Closed systems

E-hub (Energy-Hub)

The E-hub system aimed to use solar energy to charge the system and discharge the heat for space heating and domestic hot water applications [10]. Zeolite 5A was coupled with water for the process, where Zeolite was packed into 8-finned heat exchangers which were placed into a cylindrical chamber as shown in **Fig. 2.5**. A test module with a capacity of 3 kWh was designed and manufactured. Before the discharging test, zeolite was dried at 103 °C. During the discharging process, a maximum temperature increase (calculated as the temperature difference between the outlet and inlet water) of 31.2 K was achieved. This temperature increase was suitable for the space heating needs of the target project. However, this temperature lift is not sufficient to provide 0.2 MPa steam as required by Tanegashima's industrial processes.

Fig. 2.5. Picture of a packed bed and heat exhcanger (left) and the evaporator/condensor from the front (middle), and back (right) [10].

*MODESTORE (*Modular high energy density sorption heat storage) *and COMTES (*Compact thermal storage technologies)

The Austrian research institute AEE-INTEC developed a thermochemical energy storage concept for solar heating systems with the closed system reactor as shown in **Fig. 2.6** [11,12] as part of the MODESTORE project. The working pair was silica-gel and water. The reactor consisted of a fixed bed packed with silica-gel, a spiral heat exchanger, and a water reservoir with a heat exchanger used as an evaporator/condenser. During the desorption process, heat was provided to the material through the heat exchanger and the desorbed water was condensed and stored in the water reservoir. The process was run in reverse to achieve adsorption. A prototype with 200 kg of silica-gel was tested successfully. AEE-INTEC suggested new working pair combinations could be employed to improve the temperature increase. The COMTES project followed MODESTORE, employing a binderless Zeolite 13X and water vapor as the working pair [13], but maintaining the reactor concept from the MODESTORE project. A prototype test with 164 kg of zeolite was performed successfully and a zeolite bed temperature of 75 °C was observed during adsorption. The maximum temperature of adsorber in this project was higher than that in the E-hub project, but remains insufficient to produce 0.2 MPa steam.

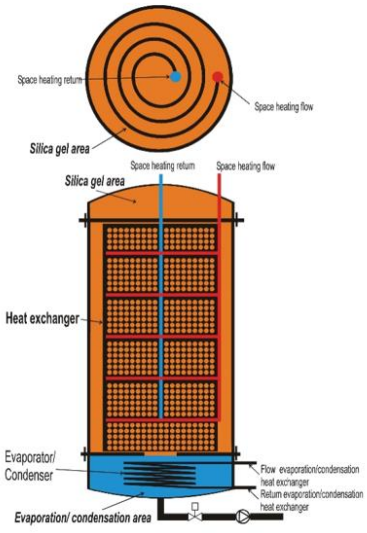

Fig. 2.6. Conceptual design of the closed system reactor of the MODESTORE project [12].

2.3.3 Open systems

CWS-NT (Chemical heat storage-low temperature), EnErChem (Development and testing of a long term sorption heat store for domestic heating)

A conceptual design of a moving bed reactor was considered in Germany for long-term heat storage [14]. The thermochemical energy storage system was combined with a solar heating system to provide for space heating. The reactor was a cross-flow type with two separate compartments for

adsorption/desorption separated by an air/water (or oil) heat exchanger as shown in **Fig. 2.7**. For both heat charging and discharging the material was removed at a regular interval with new material input from the top. In the charging process, the adsorbed material was fully packed, dry air was heated by the air/water heat exchanger and the hot air regenerated the zeolite. In the discharging process, the regenerated material was packed into the other side of the reactor. Humid air was blown into the bed and was heated by the adsorption heat released from the zeolite. Heated air was cooled down via the air/water heat exchanger providing its sensible heat to the heat demand. In the discharging test without zeolite exchange, a temperature increase of 30 K was measured [15]. The heat of the air was transferred to the oil via the heat exchanger and the outlet oil temperature reached around 30 - 35 °C.

A similar reactor design with material discharged by a rotary valve mounted under the reactor was developed. The prototype is shown in **Fig. 2.8** [16]. Continuous heat charging and discharging were achieved. In the discharging process, the outlet fluid temperature reached 54 °C. The large volumetric flow of humidified air diluted the adsorption heat by zeolite to 54 °C. While this temperature level is suitable for the space heating, it is not sufficient to generate pressurized steam.

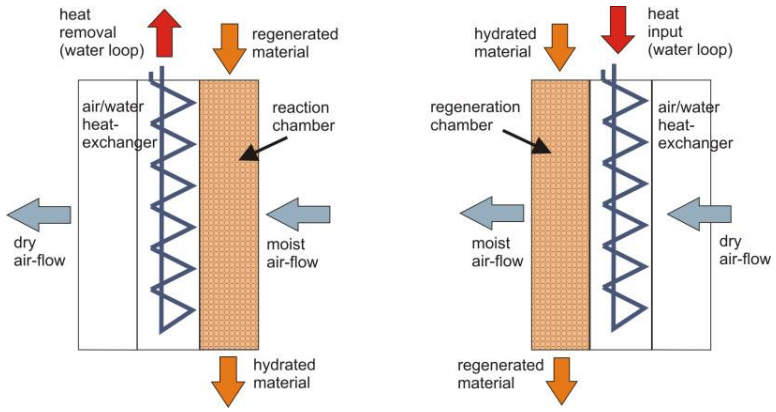

Fig. 2.7. Conceptual design of cross-flow type reactor [15].

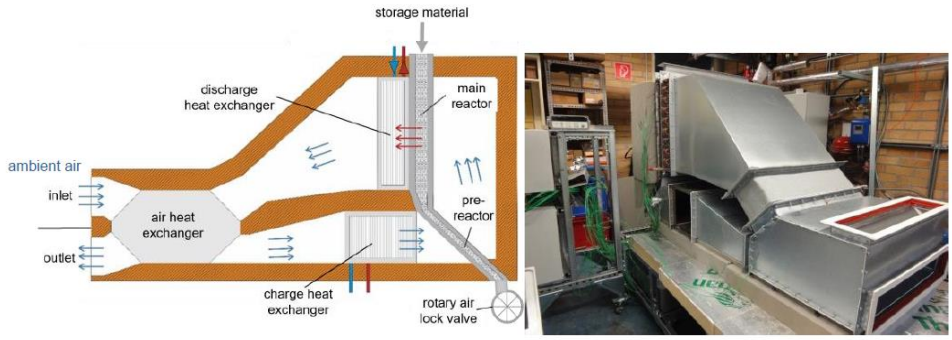

Fig. 2.8. Prototype of HIL (hard ware in loop) [16].

STAID (Seasonal Thermochemical heAt storage In builDings) Project

Another open adsorption system employing Zeolite 13X was developed in France. The system design and the overview of a prototype reactor are shown in **Fig. 2.9** [17]. This system was charged with solar heat and discharged the heat for space heating systems in single-family houses. A conceptual design of the reactor had two separated cylinders with fixed beds packed with a total 80 kg zeolite as shown in **Fig. 2.10** [17]. In the charging process, air heated by a solar collector to 120 to 180 °C was blown into the zeolite bed to desorb water. In the discharging process, humid air exhausted from the building was provided to the zeolite bed and adsorption heat was transferred to the gas. During the discharging test, the outlet temperature reached up to 57 °C [18]. The large volumetric flow of vapor-laden air causes the adsorption heat generated by zeolite to fall below 60 °C. This temperature level is insufficient to generate pressurized steam, but is suitable for the space heating.

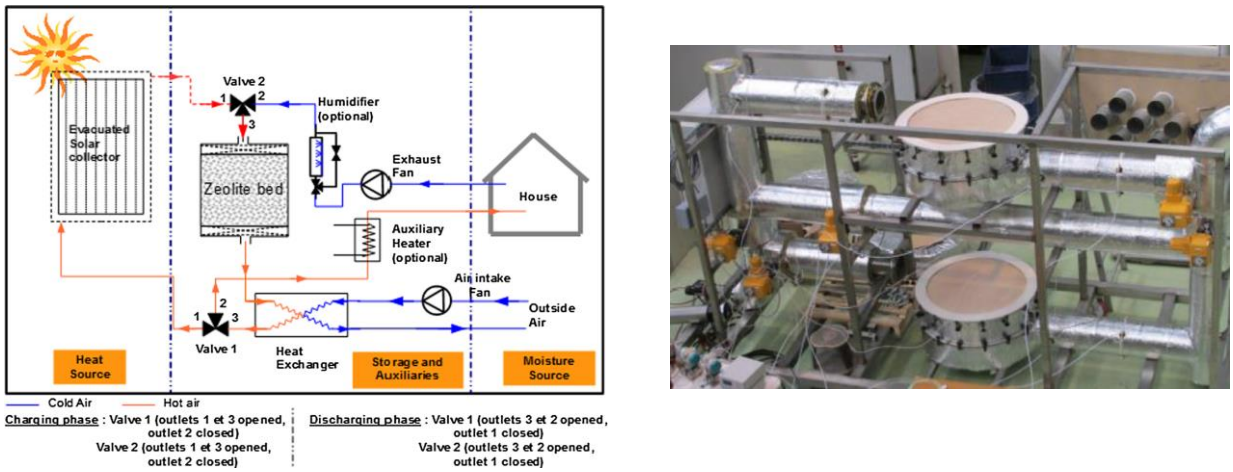

Fig. 2.9. System design and overview of test rig of STAID Project [17].

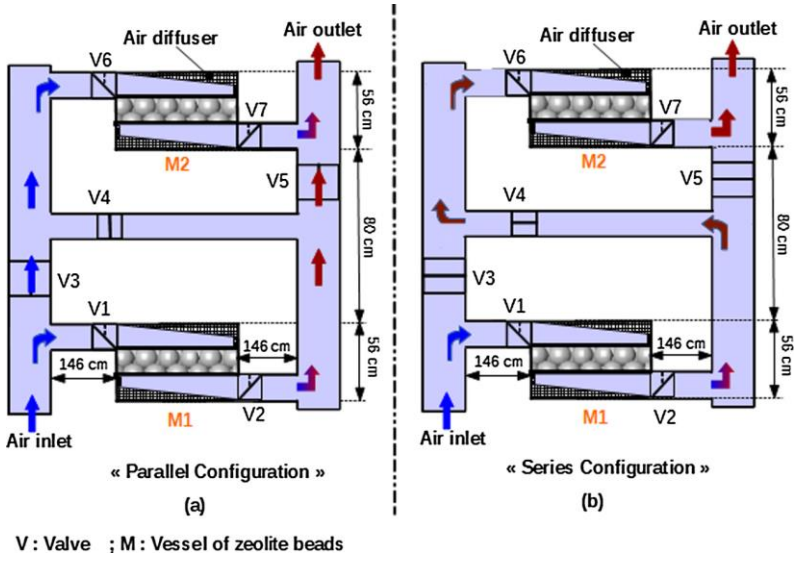

Fig. 2.10. Schematic design of test section in STAID project [17].

E-hub (Energy-Hub)

An open adsorption system combined with an air-to-air heat exchanger to provide heat to buildings through the solar-based heat charging was developed in the E-hub project [19]. A schematic of the prototype is depicted in **Fig. 2.11**. In the discharging process, ambient air was blown into the system from the bottom and the humidity was controlled by a humidification system. Next, the intake air was preheated by an air-to-air heat exchanger. The pre-heated gas passed through two zeolite beds with total 150 kg of Zeolite 13X. The gas heated by adsorption heat provided sensible heat to thermal oil via an oil-to-air heat exchanger. In the experiment, the bed temperature reached 70 °C, notably higher than previously described projects. This higher temperature was due primarily to heat recovery via the air-to-air heat exchanger and the humidified process. Nevertheless, this temperature level remains insufficient to generate 0.2 MPa steam.

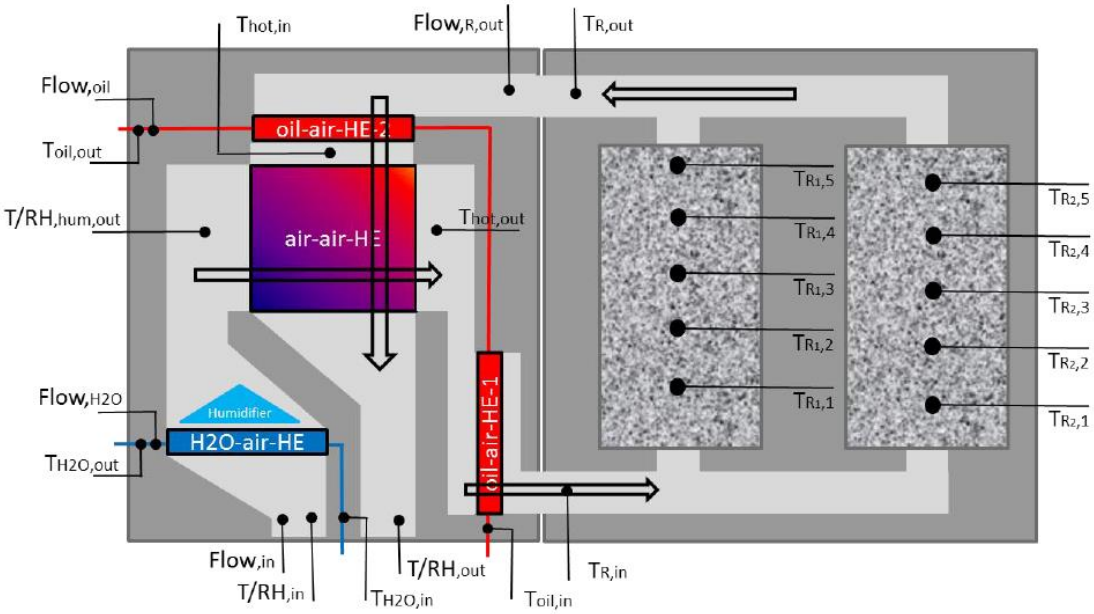

Fig. 2.11. Schematic design of reactor in E-hub project [19].

Flow TCS

A conceptual design of a rotated reactor for charging solar energy in the summer and discharging it in winter was built in Austria as shown in **Fig. 2.12** [20]. The rotating equipment design prevents inactive materials from reducing system performance. Air conditioning systems and domestic hot water systems were considered as the applications for this system [21]. The slowly rotating chamber was packed with 53 kg of Zeolite 4A. In the adsorption process, inlet gas was blown downwards into the reactor. As the gas exit was above the gas inlet, the gas flow changes direction inside the chamber. The zeolite adsorbed water vapor in the inlet gas and gave its adsorption heat to the gas. After the adsorption process, the gas was exhausted from the center. During the experiment, up to around 60

K temperature increase of material was confirmed. The maximum temperature was 84 °C, substantially higher than other projects designed for space heating application. This higher temperature was due mainly to lack of dilution by inactive material.

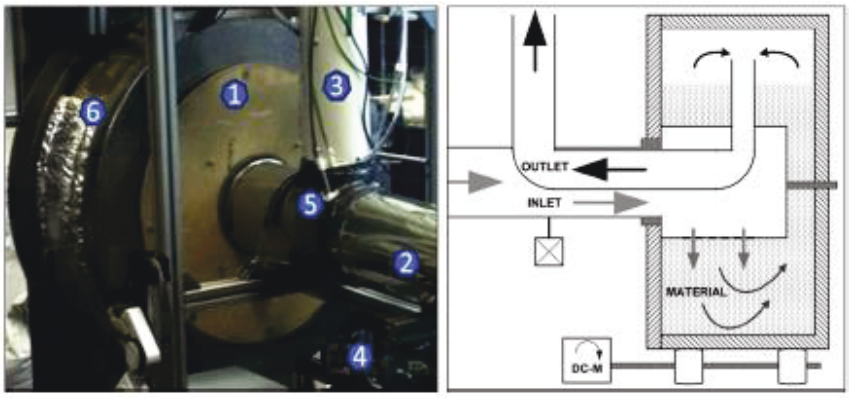

Fig. 2.12. Picture of rotating reactor in Flow TCS project [20].

ZAE Bayern

ZAE Bayern in Germany developed and demonstrated an open adsorption thermochemical energy storage system for space heating application as shown in **Fig. 2.13** [22]. A tank consisting of three connected cylinders was packed with 7000 kg of zeolite. The system was connected to the local district heating system and the space heating system of a school. In the charging phase, hot air heated by the waste heat from the district heating system to 130 °C was blown into the zeolite bed, and the water content of the zeolite was reduced to 9%. Once the temperature of gas exhausted from the first tank began to increase, heat charging in the next tank began. In the discharging phase, the inlet air was humidified to the dew point of 25~30 °C (25~30 °Cdp) and blown into the zeolite bed. The outlet temperature of gas exceeded 100 °C and the system was able to provide heat at 50 °C for space heating. The higher dew point (=vapor pressure) in vapor-laden air contributed increasing the maximum bed temperature over 100 °C because of less cooling effect by vapor-laden air than above projects.

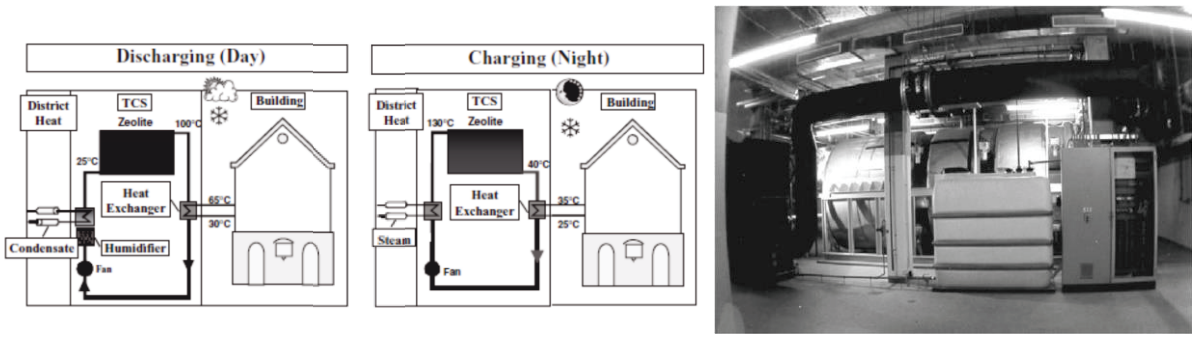

Fig. 2.13. Design of an open adsorption heat charging and discharging system connected to the local district heating system [22].

Mobile sorption system by ZAE Bayern

A thermochemical energy storage and transport system was demonstrated in Germany. The sorption storage module was built as shown in **Fig. 2.14** [23]. During charging, dry air heated by the excess heat derived from a waste incineration plant to 130 °C was used to desorb water from 14 t of zeolite. The regenerated zeolite was transported 7 km away to serve as a heat supply to an industrial drying process. The exhausted humid air from the industrial drying process was introduced to the zeolite bed and dried air at 160 °C was obtained by the adsorption of water vapor by the zeolite. This system generated much higher temperatures than other projects because of adsorption of humid air with a higher dew point exhausted from the industrial drying process. This result implies the sorption system is preferable for the industrial drying process because no additional energy is needed to generate adsorbed water vapor. However, this process can only produce dry, high temperature air whereas Tanegashima requires 0.2 MPa saturated steam.

Fig. 2.14. Picture of mobile sorption reactor [23].

Nakaso et al.

Nakaso et al. proposed a fixed bed reactor packed with zeolite generating high-pressure steam [24]. The steam generation process of this study is shown in **Fig. 2.15**. Liquid water was selected as the adsorbate. First, a vacuum was drawn on the chamber. Next, low-pressure steam was introduced from the bottom for the pre-heating. Liquid water was introduced from the bottom of chamber, and some steam was generated by the adsorption heat in the bottom of chamber. The zeolite packed in the upper side of chamber adsorbed steam generated by the lower section, and its adsorption heat increased the temperature of super-heated steam. After the adsorption process, water in the chamber was drained and dry gas was blown through the bed to regenerate the zeolite.

A bench scale test rig with 169 kg of zeolite was demonstrated [25]. During the heat discharging process, the bed temperature exceeded 200 °C (i.e., sufficient to generate pressurized steam) due to adsorption of high concentration steam. However, multiple pressurized chambers are required to provide pressurized steam continuously, making this method expensive.

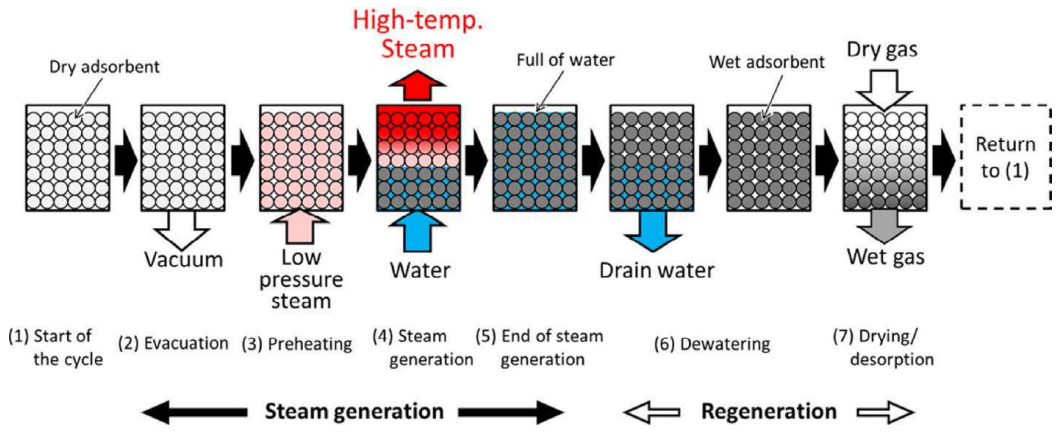

Fig. 2.15. Steam generation process [24].

2.4 Summary of literature review and target of this dissertation

2.4.1 Heat discharging

Table 2.1 summarizes the projects reported above in terms of the reactor process (open vs. closed), the charging temperature, the maximum bed temperature, and the Heat Transfer Fluid (HTF) temperature. In some projects, the HTF temperature was treated as the same as the maximum bed temperature, termed as “potentially providable temperature”. The thermal energy storage projects utilizing ad/desorption and the mobile thermal energy storage projects utilizing PCM are summarized in terms of temperature level and specific enthalpy of heat demand in **Fig. 2.16**.

Closed system reactors basically consist of two chambers with a heat exchanger for the adsorber/desorber and the evaporator/condenser. In these closed systems, the material is sealed in the vessel and thus cannot be replaced easily. As such, they are not applicable to offsite systems with material transportation. Transporting the material along with the reactor is not reasonable because the additional components (evaporator/condenser, water reservoir, etc.) decrease the transportable thermal energy storage material and accompanying energy storage density on the trailer.

Open systems can be realized using various reactor types (e.g., fixed bed, moving bed, rotating reactor). In the open adsorption systems, the maximum temperature of the zeolite bed represents the potential providable temperature level for customers; this temperature can be determined by the discharging temperature and humidity of the inlet gas. For applications to space heating, domestic hot water systems, and to air conditioning systems, a low temperature level below 100 °C is required. Adsorption of water vapor in the ambient air by zeolite is a reasonable as it provides the low

temperature heat level required without the need for an additional heat source. However, such systems cannot provide the temperature level requirement of industrial processes in Tanegashima because the large volumetric flow of air moderates the adsorption heat to lower temperatures.

ZAE's demonstration project can provide higher temperature dried air for industrial processes, but not superheated steam. Using liquid water as the adsorbate, such as Nakaso's proposal, can provide high-pressure steam at the temperature needs of industries in Tanegashima. However, to realize continuous generation of pressurized steam, multiple expensive pressurized chambers would need to be operated in a parallel batch process.

From the above review of the state of the art, the concept of adsorbate and reactor of heat discharging device is summarized below to match Tanegashima's industrial requirement.

1. High-concentration steam adsorption to keep higher bed temperature for steam generation.
2. Moving bed to operate continuously.
3. Indirect heat exchanging process to avoid the chamber being pressurized.

The conceptual design of the heat discharging device named "Zeolite Boiler" proposed in this study is shown in **Fig. 2.17**. It meets the design requirements as follows.

1. High-concentration steam adsorption to keep higher bed temperature for steam generation.
   - The Zeolite Boiler operates concurrently with an existing boiler installed to meet heat demand. Pure steam adsorption increases the bed temperature, which means the zeolite can provide pressurized steam.
2. Moving bed to operate continuously.
   - The Zeolite Boiler employs a moving bed reactor in which zeolite is passing through the chamber driven by gravity. The mass flow rate of zeolite is controlled by a control valve mounted under the chamber. Steady state operation can be realized by using the moving bed reactor.
3. Indirect heat exchanging process to avoid the chamber being pressurized.
   - Steam from the existing boiler is assumed to be depressurized to the ambient pressure and injected into the zeolite bed. Adsorption heat of zeolite is transferred to the water via an internal heat exchanger. Thus, pressurized steam is generated without a pressurized chamber by using non-pressurized steam injection and indirect heat exchange.

Table 2.1. Summary of reported project employing ad/desorption cycle of zeolite.

		Temperature (°C)			
		Charging	Discharging		
Source	Type		Maximum	HTF	(Fluid type)
E-hub	Closed	103	-	51.2	(water)
COMTES	Closed	150	-	45	(oil)
CWS-NT	Open	180	58	30-35	(oil)
EnErChem	Open	180	54	35	(oil)
STAID	Open	120-180	57	57*	(air)
E-hub	Open	185	70	70*	(oil)
Flow-TCS	Open	180	84	84*	(air, water)
ZAE Bayern	Open	130	>100	50	(air)
ZAE Bayern	Open	130	160	160	(air)
Nakaso et al.	Open	125	240-260	240-260	(steam)
**Potential*					

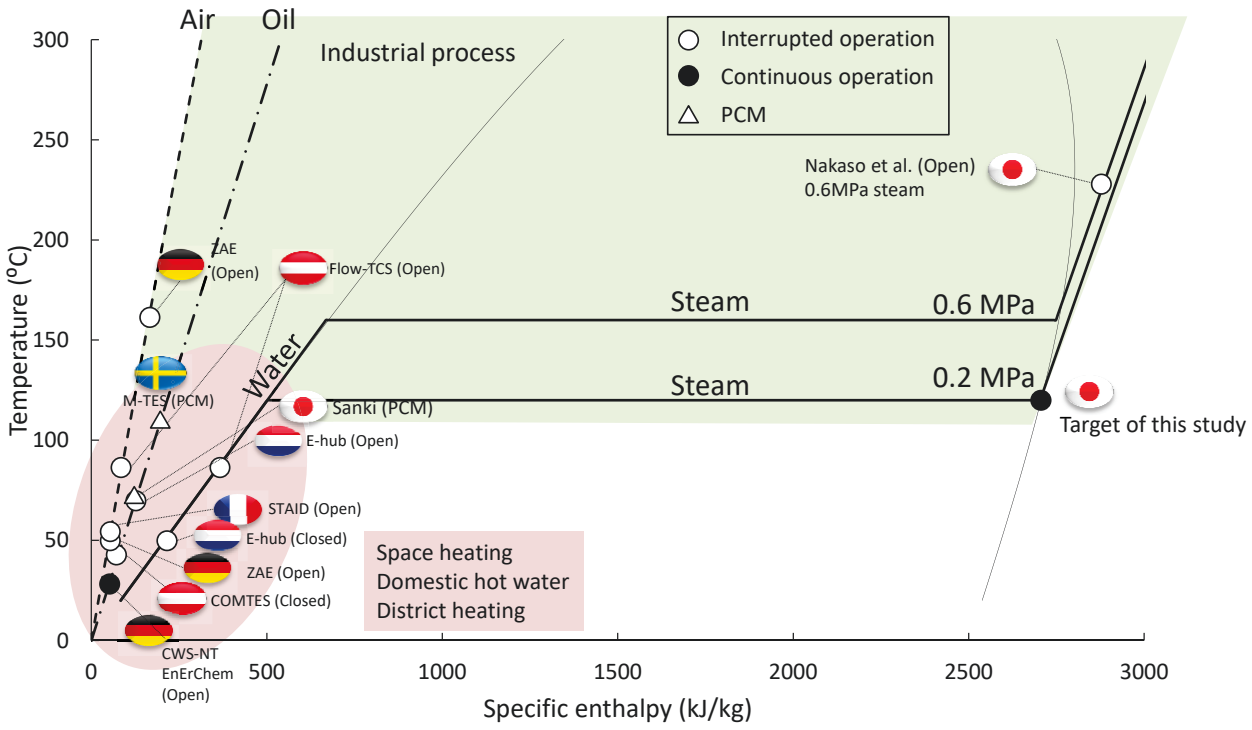

Fig. 2.16. Thermal energy storage projects utilizing ad/desorption and mobile thermal energy storage utilizing PCM summarized in temperature level and specific enthalpy of heat demand.

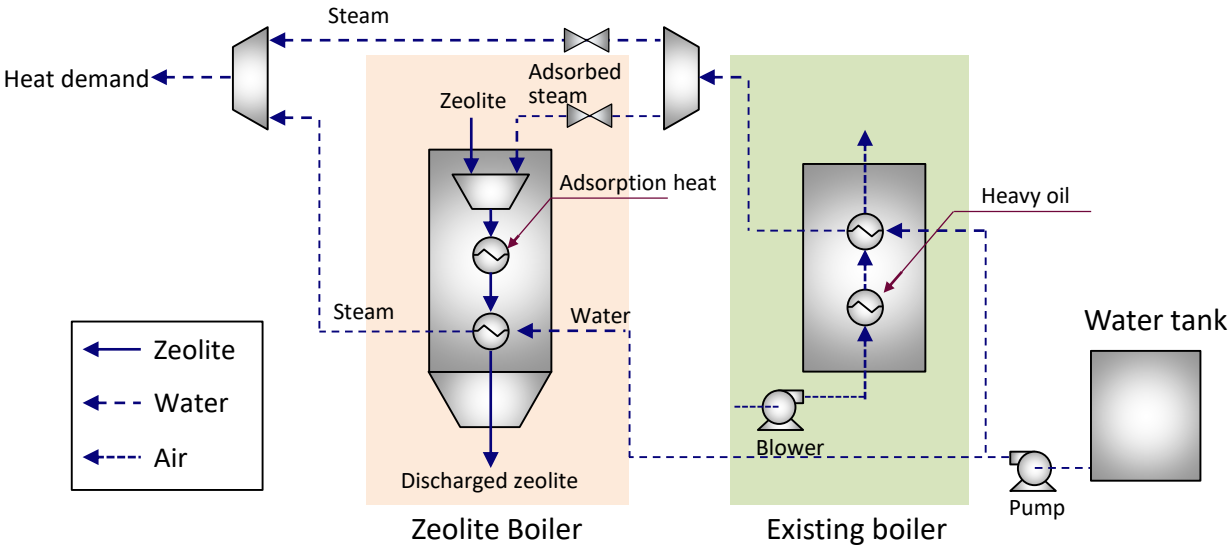

Fig. 2.17. Process outline of heat discharging device namely “Zeolite Boiler”.

2.4.2 Heat charging

As described in Chapter 1, the temperature level of unused heat from the Tanegashima sugar mill is around 200 °C. As shown in **Table 2.1**, the temperature levels of charging temperature in previous projects are of a similar temperature. Almost all reported open system reactors have employed the direct heat exchanging process because of the massive heat transfer area between gas and solid particles. This doctoral dissertation also employs direct heat exchange for the charging process, while indirect heat exchange is employed as the conceptual design for the heat discharging device. The moving bed reactor was employed to charge the heat continuously.

References

[1] Lefebvre D, Tezel FH. A review of energy storage technologies with a focus on adsorption thermal energy storage processes for heating applications. Renew Sustain Energy Rev 2017;67:116–25. https://doi.org/10.1016/J.RSER.2016.08.019.

[2] Trevisan S, Guédez R, Bouzekri H, Laumert B. Initial design of a radial-flow high temperature thermal energy storage concept for air-driven CSP systems. AIP Conf Proc 2019;2126:200031. https://doi.org/10.1063/1.5117746.

[3] Stanford University, http://sustainable.stanford.edu/sites/default/files/documents/Stanford_SESI_General_Information_Brochure.pdf (accessed on Sep, 2019) n.d.

[4] Lizana J, Chacartegui R, Barrios-Padura A, Valverde JM. Advances in thermal energy storage materials and their applications towards zero energy buildings: A critical review. Appl Energy 2017;203:219–39. https://doi.org/10.1016/J.APENERGY.2017.06.008.

[5] https://www.sanki.co.jp/product/thc/outline/ (in Japanese, accessed on Sep, 2018) n.d.

[6] https://www.sanki.co.jp/product/thc/mechanism/ (in Japanese, accessed on Sep, 2018) n.d.

[7] https://www.kobelco-eco.co.jp/topics/news/2006/20070326.html (in Japanese, accessed on April, 2019) 2007.

[8] Chiu JNW, Flores JC, Martin V, Lacarrière B. Industrial surplus heat transportation for use in district heating. Energy 2016;110:139–47. https://doi.org/http://dx.doi.org/10.1016/j.energy.2016.05.003.

[9] Chiu JNW, Jaconelli L, Pettersson A, Maurel M. Numerical and experimental validation of latent heat based mobile thermal energy storage. In: EnerSTOCK2018, 14th internaional conference on thermal energy storage, Adana(Turkey): 2018.

[10] Finck C, Henquet E, van Soest C, Oversloot H, de Jong A-J, Cuypers R, et al. Experimental Results of a 3 kWh Thermochemical Heat Storage Module for Space Heating Application. Energy Procedia 2014;48:320–6. https://doi.org/10.1016/J.EGYPRO.2014.02.037.

[11] Gartler G, Jähnig D, Purkarthofer G, Wagner W. Development of a high energy density sorption storage system. In: EuroSun Conference, Freiburg (Germany): 2004.

[12] Jaehnig D, Hausner R, Wagner W, Isaksson C. Thermo-chemical storage for solar space heating in a single-family house. In: Ecostock, 10th internaional conference on thermal energy storage, New Jersey (USA): 2006.

[13] Helden W Van, Wagner W, Schubert V, Krampe-Zadler C, Kerskes H, Bertsch F, et al. Experimental tests on a solid sorption prototype for seasonal solar thermal storage. In:Eurotherm Seminar#99 Advences in Thermal Energy Storage, Lleida (Spain): 2014.

[14] Mette B, Kerskes H, Drück H. Process and reactor design for thermo- chemical energy stores. In: ISES Solar World Congress 2011, Kassel (Germany): 2011.

[15] Kerskes H, Mette B, Bertsch F, Asenbeck S, Drück H. Chemical energy storage using reversible solid/gas-reactions (CWS) – results of the research project. Energy Procedia 2012;30:294–304. https://doi.org/10.1016/J.EGYPRO.2012.11.035.

[16] Bonk S, Kerskes H, Drück H. Development and testing of a thermo-chemical energy store - results of a five year research project -. In: ISES Solar World Congress 2017, Abu Dhabi (UAE): 2017.

[17] Tatsidjodoung P, Le Pierres N, Heintz J, Lagre D, Luo L, Durier F. Experimental and numerical investigations of a zeolite 13X / water reactor for solar heat storage in buildings. Energy Convers Manag 2016;108:488–500. https://doi.org/http://dx.doi.org/10.1016/j.enconman.2015.11.011.

[18] Johannes K, Kuznik F, Hubert J-L, Durier F, Obrecht C. Design and characterisation of a high powered energy dense zeolite thermal energy storage system for buildings. Appl Energy 2015;159:80–6. https://doi.org/http://dx.doi.org/10.1016/j.apenergy.2015.08.109.

[19] de Boer R, Smeding S, Zondag H, Krol G. Development of a prototype system for seasonal solar heat storage using an open sorption process. In:Eurotherm Seminar#99 Advences in Thermal Energy Storage, Lleida (Spain): 2014.

[20] Zettl B, Englmair G, Steinmaurer G. Development of a revolving drum reactor for open-sorption heat storage processes. Appl Therm Eng 2014;70:42–9. https://doi.org/http://dx.doi.org/10.1016/j.applthermaleng.2014.04.069.

[21] Englmair G, Zettl B, Lager D. Characterisation of a rotating adsorber designed for thermochemical heat storage processes In: EuroSun 2014, Aix-Les-Bains (France): 2014. https://doi.org/10.18086/eurosun.2014.10.12.

[22] Hauer A. Adsorption systems for TES—design and demonstration projects. In: Thermal energy storage for sustainable energy consumption, Springer; 2007, p. 409–27.

[23] Krönauer A, Lävemann E, Brückner S, Hauer A. Mobile sorption heat storage in industrial waste heat recovery. Energy Procedia 2015;73:272–80. https://doi.org/http://dx.doi.org/10.1016/j.egypro.2015.07.688.

[24] Nakaso K, Tanaka Y, Eshima S, Kobayashi S, Fukai J. Performance of a novel steam generation system using a water-zeolite pair for effective use of waste heat from the iron and steel making process. ISIJ Int 2015;55:448–56. https://doi.org/10.2355/isijinternational.55.448.

[25] Nakaso K, Fukai J, Nakagawa T, Ito K, Abe Y, Kawakami Y, et al. Performance test for scale-up characteristics of adsorption steam generators (in Japanese). Kagaku Kogaku Ronbunshu 2018:71–7. https://doi.org/https://doi.org/10.1252/kakoronbunshu.44.71.

Chapter 3 Material and heat flow analysis of sugar mill

3.1 Objectives of this chapter

Figure 3.1 shows the structure of dissertation and position of this chapter. This chapter focuses on the sugar mill as a heat charging station in the thermochemical energy storage and transport system and the material and heat flow of the sugar mill is quantified by the process simulation. To design both the heat discharging device namely “Zeolite Boiler” in Chapter 4 and the heat charging device namely “Heat Charger” in Chapter 5, necessary boundary conditions such as temperature, flow rate, power supply from the sugar mill and so on must be quantified. The objectives of this chapter are quantifying

- the material and heat flow of current process of the sugar mill
- the temperature, flow rate and power supply from the sugar mill for heat charging process
- the effect of modified process on heat charging potential and additional power supply

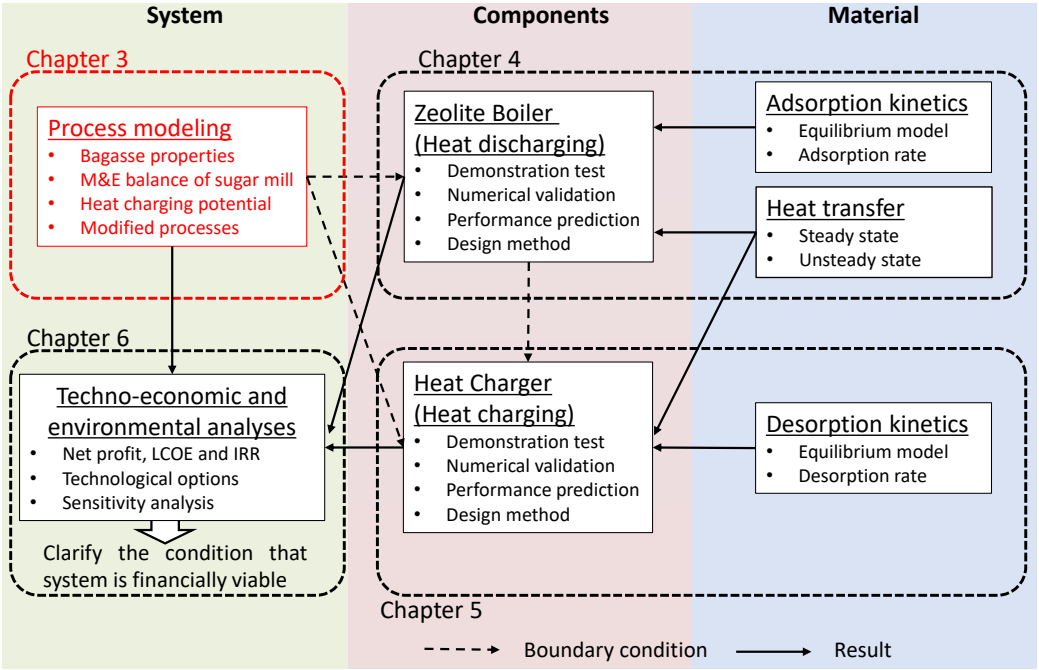

Fig. 3.1. Structure of dissertation and position of this chapter.

3.2 Specification of sugarcane bagasse as fuel

As mentioned in Chapter 1, sugar mills burn sugarcane bagasse in the bagasse boiler to generate process steam for their own sugar milling and refining process. To clarify the material and heat flow around bagasse boiler by process simulation, properties of bagasse as fuel must be quantified. The CHN (Carbon, Hydrogen and Nitrogen) elemental analysis can detect carbon and hydrogen contents of bagasse which determine the heating value of bagasse. In addition, the bagasse contains high

moisture content (Approximately 45%) which affects the effective heating value of bagasse. To quantify the moisture content of bagasse which is milled by the sugar mill in Tanegashima, the bagasse drying test must be done.

In this section, bagasse drying test was described firstly, following CHN elemental analysis of fully dried bagasse.

3.2.1 Moisture content of bagasse

The wet bagasse generally contains approximately 40 to 50 % of moisture which is ultimately exhausted from the stack with heat loss of vaporization and affects effective heating value of bagasse, so moisture content was measured by bagasse drying test as following procedure. Aluminum cups were put in the electric furnace and heated up till approximately 100 °C to ensure its dry condition. Then aluminum cups were put out from the electric furnace and cooled down for 30 minutes in the desiccator. Bagasse was packed into the aluminum cup and dried in the electric furnace for 30 minutes at 110 °C. After drying the bagasse for 30 minutes, the aluminum cups were put out from the electric furnace and measured the weight of cups after cooling down in the desiccator for 30 minutes. This procedure was repeated until no weight change of bagasse in the cups was observed.

Table 3.1 and **Fig. 3.2** show the result of weight change summarized in elapsed time. It took about 3 hours to dry the bagasse completely. Wet-based moisture content which can be calculated by the following equation is shown in the same table. The moisture content was calculated by weighted mean of all 5 samples, which results in 44.4%.

$$w_{\mathrm{wet}} = \frac{(m_{\mathrm{wet}} - m_{\mathrm{dry}})}{m_{\mathrm{wet}}} \tag{3.1}$$

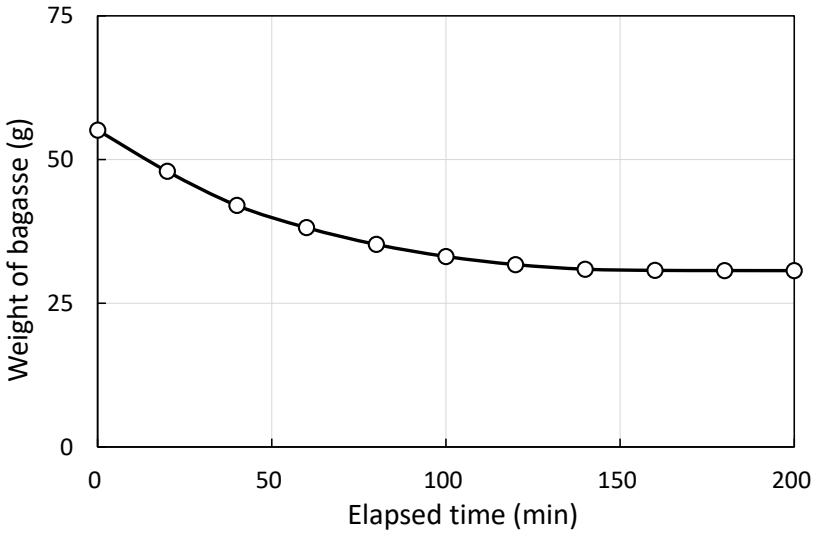

Fig. 3.2. Change in total bagasse weight during drying.

Table 3.1. Result of bagasse drying test.

Time (min)	Sample weight (g)				
	No.1	No.2	No.3	No.4	No.5
0	12.05	9.60	10.87	11.36	11.26
20	10.77	7.93	9.08	10.12	10.04
40	9.28	7.01	7.85	9.12	8.76
60	8.56	6.19	7.10	8.31	7.99
80	7.98	5.68	6.61	7.55	7.41
100	7.51	5.43	6.22	7.07	6.91
120	7.03	5.43	6.10	6.59	6.58
140	6.84	5.40	6.05	6.35	6.27
160	6.79	5.39	6.03	6.30	6.20
180	6.78	5.39	6.03	6.28	6.21
200	6.76	5.39	6.03	6.28	6.20
Moisture content	43.9%	43.9%	44.5%	44.7%	44.9%

3.2.2 Composition of bagasse

The elemental analysis of bagasse was done to detect the higher heating value of bagasse. Fully dried bagasse obtained from the bagasse drying test in the previous section was pulverized into the powder by a mixer. Dried and pulverized bagasse of 2.0 to 2.5 mg was packed into the vial and CHN elemental analysis was done utilizing elemental analyzer (Perkin elmer Japan, 2400Ⅱ). **Table 3.2** shows the result of elemental analysis of 4 samples and mean weighted. Oxygen content was calculated by subtracting C, H and N from 100%, while the bagasse contains a small amount of Ca, Na, K, S, Cl and so on. **Table 3.3** shows some reference data of elemental analysis of bagasse by some literatures. The sugarcane bagasse milled in Tanegashima has roughly the same composition as other bagasse cultivated and milled in other area.

Table 3.2. Result of CHN elemental analysis.

	C (wt%)	H (wt%)	N (wt%)	O (wt%)	Weight (mg)
Sample.01	46.19	5.54	0.16	48.11	2.024
Sample.02	46.11	5.65	0.14	48.1	1.967
Sample.03	46.12	5.79	0.19	47.9	2.409
Sample.04	46.07	5.74	0.18	48.01	2.292
Ave.	46.12	5.69	0.17	48.02	

Table 3.3. References of elemental analysis and Higher Heating Value (HHV) of bagasse (including ash).

	Elemental analysis (wt%)						Ash (wt%)	HHV (MJ/kg-dry)
Reference	C	H	O	N	S	Cl		
[1]	48.64	5.87	42.82	0.16	0.04	0.03	2.44	18.99
[2]	48.19	5.65	42.35	0.14	0.08	-	3.61	18.5
[3]	42.9	5.9	49.0	0.2	-	-	2.0	18.7
[4]	41.36	5.75	49.41	0.61	0.12	0.10	2.93	17.20
[5]	44.69	6.01	48.23	0.30	0.01	0.50	0.69	15.98
[6]	45.48	5.96	45.21	0.15	-	-	3.20	18.73
[6]	43.79	5.96	43.36	1.69	-	-	5.20	17.70
This work	46.12	5.69	48.02	0.17	-	-	-	-

3.2.3 Heating value of bagasse

There are some approximations to predict higher heating value of solid fuel by elemental analysis (Klass's [7], Dulong's [8] etc.) or proximate analysis (Parikh's [9], etc.). This study employed Klass's approximation as described as follows, which predicts heating value by simply carbon content in the fuel. **Table 3.4** shows predicted higher heating value of bagasse of some literatures using Klass's approximation. According to **Table 3.4**, Klass's approximation can simulate the higher heating value of bagasse with around 10% of error. The higher heating value of bagasse which is milled by the sugar mill in Tanegashima was predicted by Klass's approximation (**Eq.(3.2)**) reflecting the carbon content of this bagasse (see **Table 3.3**). It was 18.38 MJ/kg, which is shown in **Table 3.4** as well.

$$HHV = 45.71C - 2.70 \qquad (3.2)$$

Table 3.4. Result of heating value of bagasse.

Reference	HHV (MJ/kg-dry)	Klass's approximation (MJ/kg-dry)	error (%)
[1]	18.99	19.53	2.9%
[2]	18.5	19.33	4.5%
[3]	18.7	16.91	-9.6%
[4]	17.20	16.78	-2.5%
[5]	15.98	17.87	11.8%
[6]	18.73	18.09	-3.4%
[6]	17.70	17.32	-2.2%
This work	-	18.38	-

The lower heating value of bagasse and effective lower heating value considering moisture content of bagasse can be calculated as following equations. Lower heating value and effective lower heating value of bagasse are calculated by **Eqs. (3.3)** and **(3.4)** and resulted in 17.2 MJ/kg and 8.1 MJ/kg, respectively.

$$LHV = HHV - 20.18H \tag{3.3}$$

$$LHV_{\text{eff}} = HHV(1-w) - 2.257(8.94H + w) \tag{3.4}$$

3.3 Process modeling of sugar mill

In previous sections, the heating value of bagasse was obtained. In this section, material and heat balance of sugar mill around bagasse boiler was quantified by the conventional process simulator Aspen HYSYS® utilizing the heating value of bagasse. During the sugar milling operation, the total steady operation time of bagasse boiler is 2638 hours from one operation data. It can be divided in three terms, which are from the middle to end of December (372 hours) as the first term, at the beginning of the year to the middle of February (1186 hours) as the second term, and the end of February to the middle of April (1080 hours) as the third term. While sugar mill operation stopped, the maintenance and washing the vessels are conducted. Daily averaged vapor pressure and temperature from 2012 to 2018 are shown in **Figs. 3.3** and **3.4**, respectively [10].

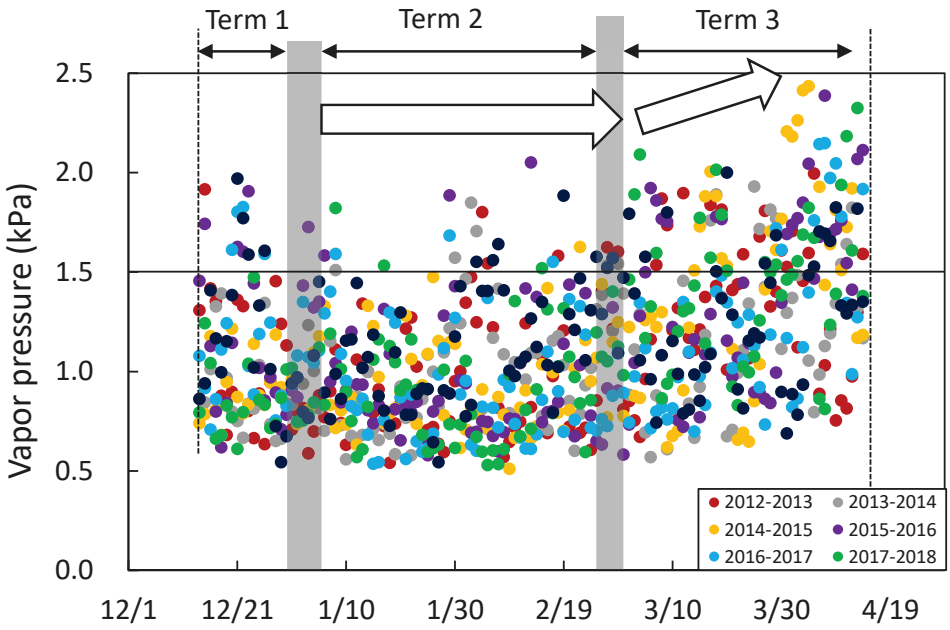

Fig. 3.3. Ambient vapor pressure of Tanegashima during sugar milling period.

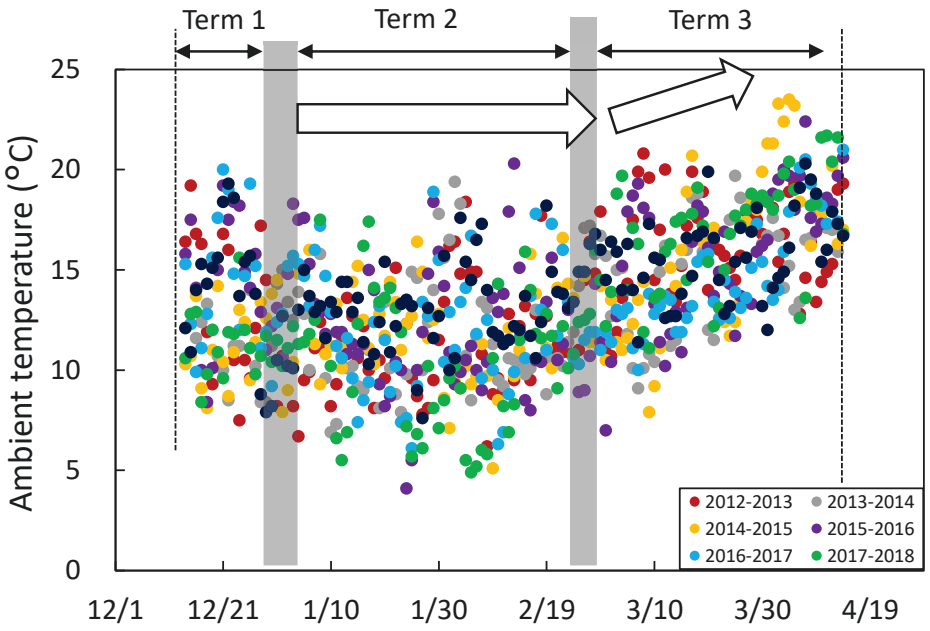

Fig. 3.4. Ambient temperature of Tanegashima during sugar milling operation.

The ambient temperature and vapor pressure in the first and second term are relatively lower than those in the third term. In the first and second term, the averaged vapor pressure of around 90% of days were below than 1.5 kPa. In the third term, temperature and vapor pressure were gradually increased, and then the averaged vapor pressure of over 30% were above 1.5 kPa. **Table 3.5** shows the average temperature of flue gas, where heat storage unit would be attached, and intake air temperature with the standard deviation in each operation term calculated by one sugar mill operation data. Also, average ambient temperature and vapor pressure for 6 years are shown in **Table 3.5**. From the **Table 3.5**, the sugar mill operated the same condition in the first and second term. However, the temperature of flue gas and intake air temperature in the third term were increased due to ambient temperature increase. As a vicinal factory as a heat demand in the thermochemical energy storage and transport system operates from the beginning of December to the middle of February as mentioned in the Chapter 1, the material and heat balance of the sugar mill should be simulated utilizing operation data of the first and second term.

Figure 3.5 shows the schematic of streams and units around bagasse boiler. As **Fig. 3.5** shows, the main steam generated in the bagasse boiler is splitted at the high-pressure header to each process. The half of the main steam flow goes to the power turbine, and expanded steam is recovered in the low-pressure mixer. A part of the main steam is blown to control the mass flow rate of steam and the rest of the main steam directly goes to the low-pressure steam mixer. The low-pressure steam is supplied to a vessel to concentrate and crystalize sugar. The system boundary in the analysis of material and heat balance by Aspen HYSYS® was set from the bagasse boiler to before the low-pressure header, as shown in **Fig. 3.5**.

Table 3.6 shows the temporally-averaged operation data of sugar mill during the first and second term with the standard deviation including steam data (mass flow rate, temperature and pressure) and flue gas data (temperature and pressure).

Table 3.5. Environmental data around bagasse boiler (temporally-averaged data).

		Term 1	Term 2	Term 3
Temperature of flue gas at stack	(°C)	182.0	182.2	186.3
(Standard deviation)		(5.5)	(5.6)	(5.0)
Intake air temperature	(°C)	26.7	26.0	29.5
(Standard deviation)		(2.8)	(2.5)	(2.4)
Ambient temperature	(°C)	12.9	11.7	15.8
(Standard deviation)		(3.1)	(2.9)	(3.0)
Ambient vapor pressure	(kPa)	1.05	0.96	1.32
(Standard deviation)		(0.34)	(0.30)	(0.42)

Table 3.6. Operation data of sugar mill (temporally-averaged data of Term 1 and 2).

	Stream name	Mass flow (t/h)	Temperature (°C)	Pressure (kPaG)
Steam	Main steam (Standard deviation)	28.75 (2.5)	343.8 (1.8)	1856.8 (8.2)
	Supplied water (Standard deviation)		86.3 (3.5)	
	Turbine inlet (Standard deviation)	16.02 (0.63)	342.7 (1.6)	1800.4 (11.0)
	Turbine outlet (Standard deviation)		160.2 (2.3)	81.8 (6.1)
	Mill turbine (Standard deviation)	8.48 (0.58)	*	
	Others (Standard deviation)	3.07 (2.37)		
	Blow steam (Standard deviation)	1.18 (0.56)		
Exhaust gas	Boiler outlet (Standard deviation)	Unknown	304.0 (8.1)	-0.392 (0.03)
	Air pre-heater (Standard deviation)		205.2 (5.4)	-0.379 (0.04)
	Precipitator (Standard deviation)		182.2 (5.6)	0.000
Bagasse		Unknown	35.0**	-

*Assume the same as “Turbine inlet”

** Maceration temperature

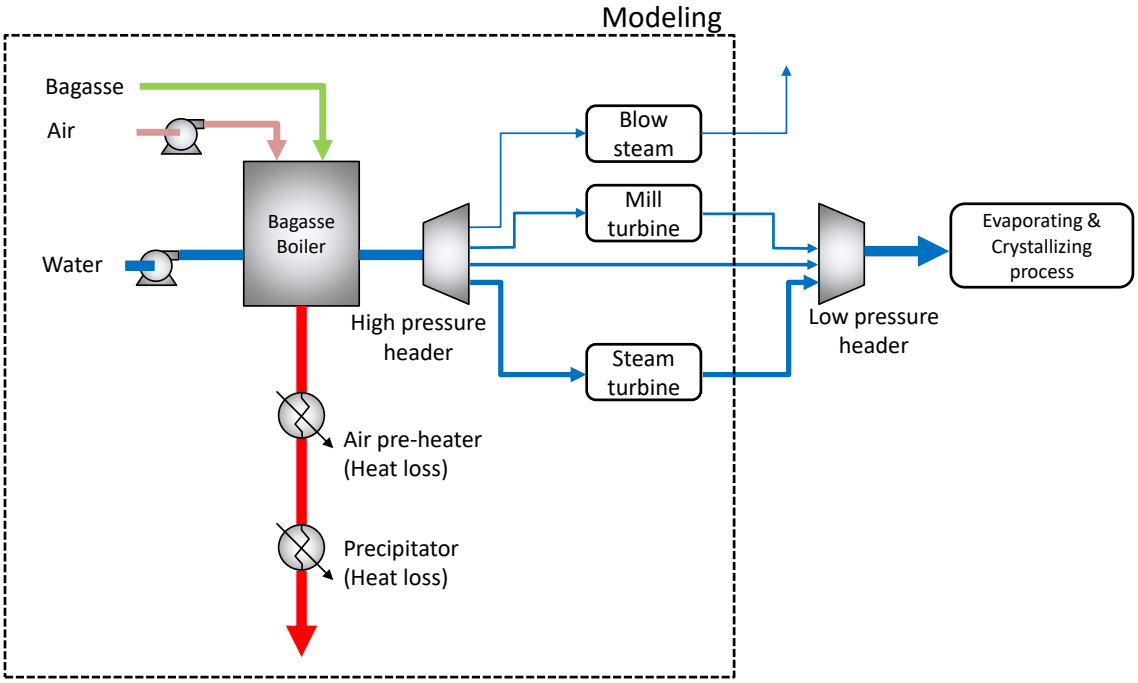

Fig. 3.5. Schematic of process flow of sugar mill.

Unknown parameters of the system are mass flow rate of bagasse and volumetric flow of intake air. The mass flow rate of bagasse relies on sugarcane milling condition, and an operator controlled the mass flow rate of bagasse with looking the combustion condition in the bagasse boiler. Excess bagasse is transported to the bagasse yard and some of them are returned to the boiler. The rated throughput of sugarcane mill in this factory is 1600 TPD (t per day). Assuming that 25% of sugarcane is bagasse and load factor of the sugar mill is 70 ~ 80%, 280 ~ 320 t of bagasse were produced in one day. This means 11 to 13 t per hour bagasse was fed into the bagasse boiler.

Accurate flow rate of the intake air is unknown because the volumetric flow of intake air is controlled by a valve to maintain a constant oxygen concentration in the stack. From the literature, the excess air ratio of bagasse boiler is approximately from 1.3 to 1.8 [11].

The following stoichiometric combustion reaction of carbon, hydrogen and nitrogen of bagasse are considered, producing CO_2, H_2O and NO_2.

$$C+O_2 \rightarrow CO_2$$

$$2H+\frac{1}{2}O_2 \rightarrow H_2O$$

$$N+O_2 \rightarrow NO_2$$

The oxygen used for combustion of bagasse comes from the bagasse and ambient air. From the elemental analysis, 1 kg of bagasse contains 461.2 g of carbon, 56.87 g of hydrogen, 1.69 g of nitrogen, and 480.2 g of oxygen. After the stoichiometric combustion of 1 kg of bagasse by the above reactions,

1690 g of CO_2, 508.4 g of H_2O and 5.5 g of NO_2 are generated. The total weight of these compositions is 2.20 kg, of which 1.20 kg oxygen derives from the ambient air.

The components of ambient air are N_2, O_2, Ar, H_2O, and CO_2, of which concentration are employed higher molar percentage of JIS's (Japan Industrial Standard) standard atmosphere [12]. The vapor pressure of ambient air during the first and second term of sugar milling operation was set to 1.5 kPa. Mass fraction of each composition was summarized in **Table 3.7**.

In the calculation of Aspen HYSYS®, chemical reaction of combustion was ignored because detailed combustion models were not essential to simulate the bagasse boiler system, while only specific heat capacity may affect. In order to calculate heat duties of heat exchangers properly, combustion gas stream adapted its composition to the realistic value measured at the site. The composition of the combustion gas is calculated by the result of the mixer, so the component mass flow of oxygen in intake air was adjusted. Resultant compositions of intake air and bagasse for the software are shown in **Table 3.7**.

Table 3.7. Mass fraction of composition.

	H_2O	CO_2	N_2	O_2	Ar	NO_2
Air	0.93%	0.05%	74.82%	22.93%	1.28%	-
Air (Aspen)	1.07%	0.05%	86.18%	11.23%	1.47%	-
Bagasse (Aspen)	23.07%	76.68%	-	-	-	0.25%

Figure 3.6 shows the process flow diagram of sugar mill around the bagasse boiler on the process simulator. The inlet mass flow rate of bagasse, which was one of the unknown parameters, were adjusted until the outlet temperature of bagasse boiler was equal to the operation data (see **Table 3.6**). The volumetric flow of intake air was also adjusted as the other unknown parameter until the oxygen concentration in the stack was equal to the operation data (9.71%). As a result, the mass flow rate of bagasse was 11.0 t/h, and excess air ratio resulted in 1.67. These values were adequate in comparison with the range of the bagasse production rate equivalent to the rated condition of this sugar mill (11 to 13 t/h) and literature data of excess air ratio (1.3 to 1.8).

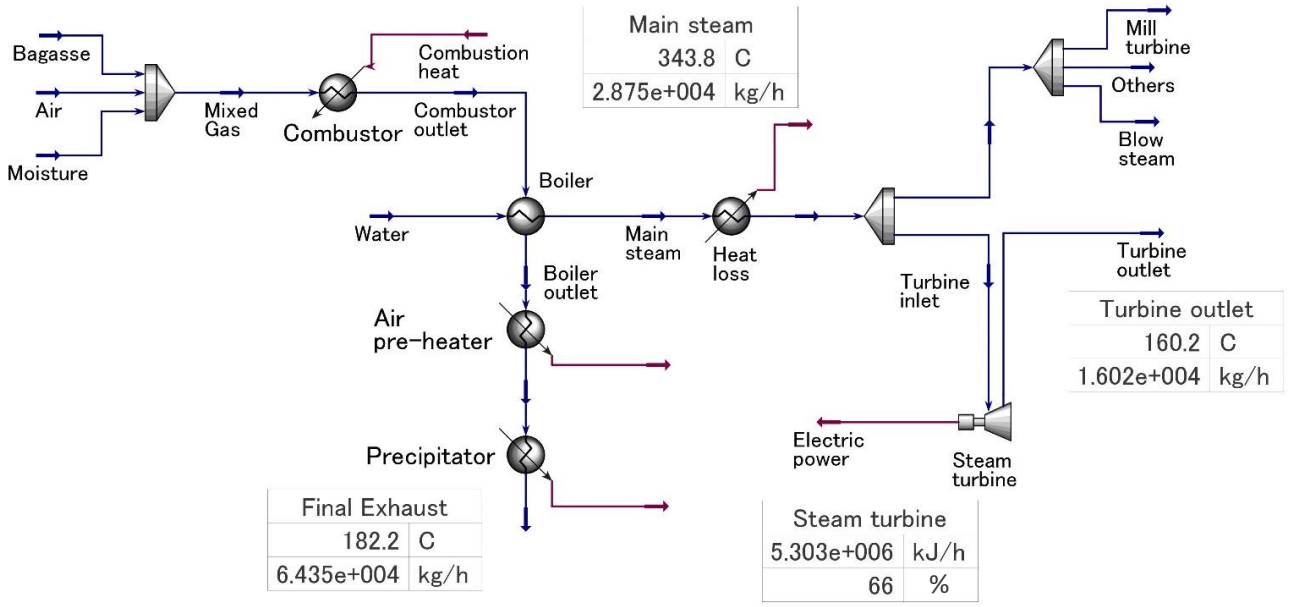

Fig. 3.6. Process flow diagram of sugar mill around bagasse boiler on Aspen HYSYS®.

3.4 Current process of sugar mill

Until the previous section, property of bagasse in terms of boiler fuel was fixed, and next material and heat balance of sugar mill was simulated. In this section, the heat charging potential was estimated by using the process flow diagram shown in **Fig. 3.6**. One of possible unused heat flows for thermal energy storage in the sugar mill is the blow steam that is 342 °C of superheated steam and the highest temperature among them. However, this blow steam is mainly used to stabilize the mass flow rate of main steam, which means the charging heat is not available continuously. Exhaust steam and hot water from the multi evaporators and crystallizer (not shown in the process flow diagram) have enormous potential of heat. However, temperature of these unused heat media is below 80 °C. Some of previous studies assume to utilize heat sources below 80 °C for thermochemical energy storage [13]. This study aims to generate pressurized steam and to do so, an initial water uptake of zeolite lower than 0.1 kg/kg is necessary, which requires desorption heat sources higher than 150 °C. From the viewpoint of temperature level, exhaust steam and hot water in the sugar mill are not suitable for this purpose. The ultimate flue gas has 182 °C and a sufficient enthalpy for the thermochemical energy storage and transport system. Therefore, it was chosen as the heat source. As the flue gas contains a lot of water vapor and some ash derived from bagasse, directly introducing flue gas to the zeolite bed is not inconvenient because of their disturbance for desorption of zeolite. To avoid the inconvenience, indirect heat transfer with drying air is necessary, and a heat exchanger should be installed in the flue gas duct. A heat exchanger unit was added on the process flow diagram shown in **Fig. 3.7**. The minimum temperature approach between the flue gas and hot air for thermal energy storage (TES) was set to 10 °C and resulting temperature of hot air for TES is 172 °C. Bagasse

contains traces of sulfur (around 0.1 wt% [14]) and thereby the flue gas of bagasse boiler contains some sulfur oxides. The sulfur oxides may affect corrosion of flue gas duct, if the temperature of flue gas is cooled down below the acid dew point. According to the operator's experience, the corrosion was occurred when the ultimate flue gas temperature was below approximately 135 °C, so the ultimate flue gas temperature in this analysis was set to 150 °C. Average ambient temperature is about 12.0 °C (see **Table 3.5**), but dew point of air containing 1.5 kPa vapor is 13.0 °C, which means the moisture in ambient air condenses at the average temperature. Therefore, the relative humidity and temperature were set to 90% and 15 °C, respectively, in this analysis. The heat charging potential for TES is 663 kW given by the enthalpy of 172 °C hot drying air based on 15 °C. Within this potential, the heat charging device ("Heat Charger" described in Chapter 5) was assumed to use the heat from 172 °C to 100 °C of the air for TES, which is 307 kW equivalent to 46.3% of the potential. If the Heat Charger is operated during whole of the first and second term of sugar mill operation, cumulative operation time is 1558 hours, and thereby heat charging potential and actual use of it resulted in 1032 MWh and 478 MWh, respectively.

In the following sections, some processes to increase heat charging potential or power generation were considered. Since the dominant factor of the operating cost of the thermochemical energy storage and transport system is power consumption of the blower to inject the hot air to the heat charging device, which will be discussed in Chapter 6, increase in heat charging potential was considered primary, and then increase in power generation to compensate for the blower power was also investigated.

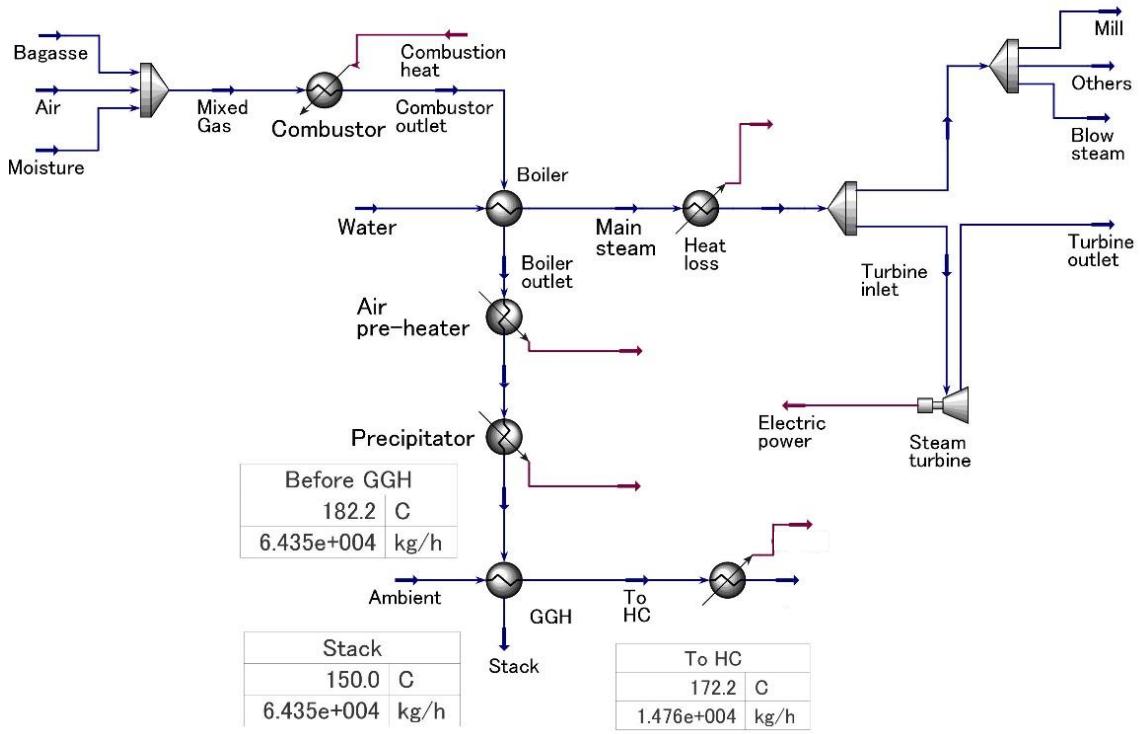

Fig. 3.7. Process flow diagram applying thermal energy storage unit.

3.5 Blow steam reduction

3.5.1 Effect of blow steam reduction on heat charging potential

Steam blowing stabilizes the mass flow rate of main steam, but the flow rate of steam blow varies with the yield of sugarcane. The reduction of steam can rise flue gas temperature or power generation under the same mass flow rate of bagasse. The steam in the range of 0.4 ~ 10 t/h (average: 1.2 t/h, standard deviation: 0.6 t/h) might be blown which was aggregated from operation data in a given year. In this study, 0.4 t/h of steam was assumed to be reduced and increase in flue gas temperature and power generation were predicted. In the process flow diagram, the mass flow rate of bagasse was not changed and only the mass flow rate of blow steam was reduced by 0.4 t/h. The volumetric flow of intake air was adjusted to keep the temperature of main steam at 344 °C.

The heat leakage from the electric precipitator Q_{EP} is determined by temperature difference between flue gas T_{flue} and ambient air T_{amb}. Overall heat transfer coefficient K_0 was calculated dividing the heat loss flux of current process Q_{EP} by temperature difference between flue gas T_{flue} and ambient air T_{amb} as described in **Eq. (3.5)**. Then updated heat loss flux Q_{EP}' was given by **Eq. (3.6)** assuming that overall heat transfer coefficient does not change under any condition.

$$K_0 = \frac{Q_{\mathrm{EP}}}{T_{\mathrm{flue}} - T_{\mathrm{amb}}} \tag{3.5}$$

$$Q_{\mathrm{EP}}{}' = K_0 (T_{\mathrm{flue}}{}' - T_{\mathrm{amb}}) \tag{3.6}$$

The heat exchange amount in the air-preheater and the amount of heat leakage from the electric precipitator were updated. Temperature increase of intake air by the air-pre heater of the current process ΔT_0 was calculated by dividing the heat exchange amount between flue gas and intake air of the current process Q_{pre} by the mass heat capacity of intake air $m_{\mathrm{air}}\, c_{p\mathrm{air}}$ as expressed in **Eq.(3.7)**, and updated heat exchange amount Q_{pre}' was calculated by **Eq. (3.8)** multiplying this temperature difference ΔT_0 and updated mass heat capacity of intake air m_{air}' $c_{p\mathrm{air}}$.

$$\Delta T_0 = \frac{Q_{\mathrm{pre}}}{m_{\mathrm{air}} c_{p\mathrm{air}}} \tag{3.7}$$

$$Q_{\mathrm{pre}}{}' = m_{\mathrm{air}}{}' c_{p\mathrm{air}} \Delta T_0 \tag{3.8}$$

Figure 3.8 shows the increase in temperature and heat charging potential as a function of reduction of mass flow rate of blow steam. The flue gas temperature increases up to 189 °C, and thereby temperature of hot air for TES rises to 179 °C, from 172 °C of the current process applying heat charging unit. The heat charging potential also increases to 850 kW.

3.5.2 Effect of blow steam reduction on power generation

Reduction of blow steam increases the turbine steam, and additional power could be generated. **Figure 3.9** shows the relationship between reduction of blow steam (= increase in turbine steam) and increase in power generation. Additional power generation lineally increases with increase in reduction of blow steam. By saving the blow steam, 37 kW of additional power is expected. **Figure 3.10** shows the increase in the temperature of flue gas and hot air for TES, the mass flow rate of hot air and heat charging potential as a function of additional power generation.

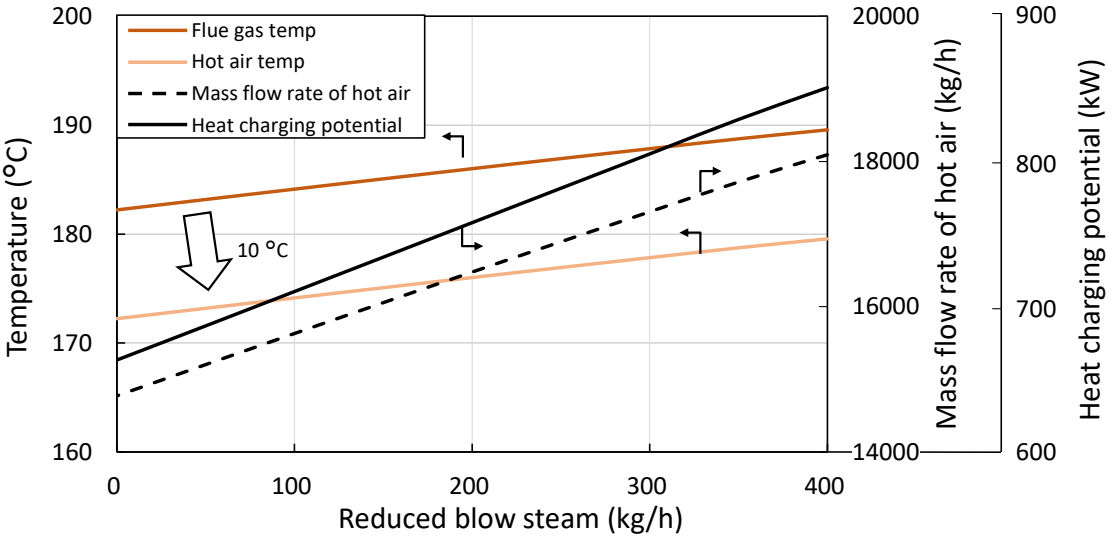

Fig. 3.8. Temperature of flue gas and heat charging potential in applying blow steam reduction.

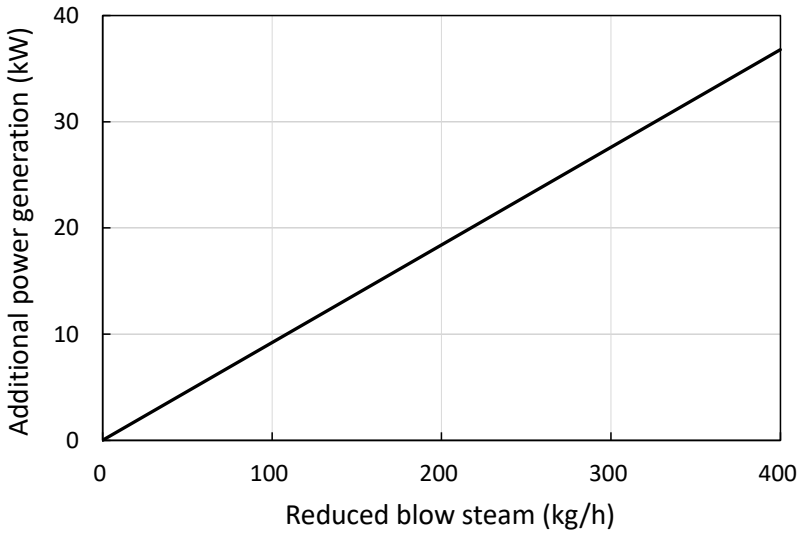

Fig. 3.9. Effect of blow steam reduction on increase in power generation.

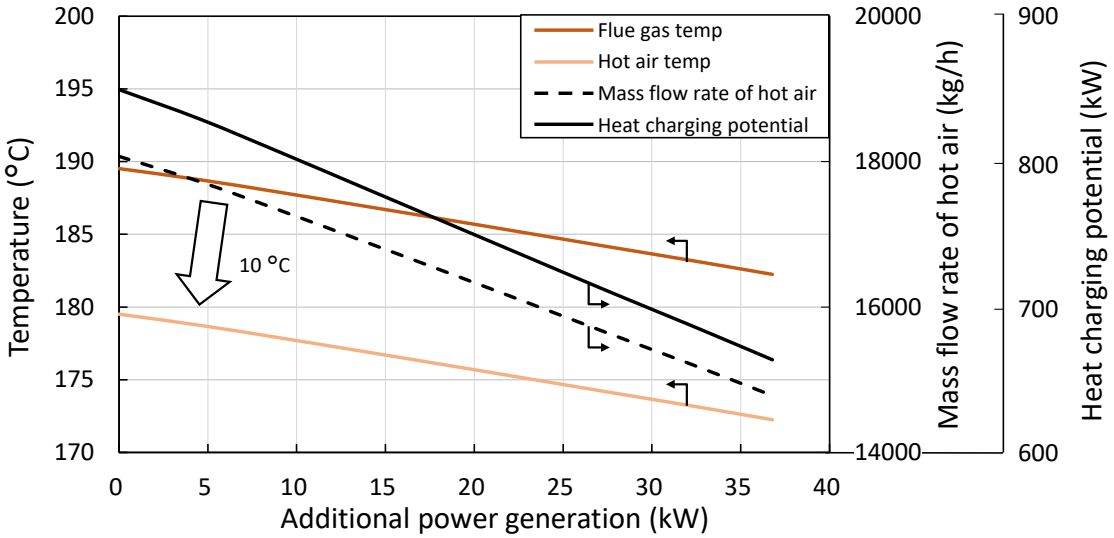

Fig. 3.10. Effect of blow steam reduction on temperature of flue gas and hot air for TES, mass flow rate of hot air and heat charging potential.

3.6 Bagasse drying

Bagasse contains about 44% moisture that spoils 45% of lower heating value of dried bagasse. Reduction of moisture content (= drying bagasse) would contribute the increase in heat charging potential and power generation due to increase in the heating value. **Figure 3.11** shows the effect of drying bagasse on effective heating value. By reducing 1% of moisture content of bagasse, 0.2 MJ/kg of heating value is expected to increase and the total heating value increase by approximately 350 kW.

If bagasse drying process is installed inside the bagasse elevator, the residence time for drying process is about 1 minute. In this case, moisture reduction is determined by drying rate of bagasse, of which phenomena are complex heat and mass transfer with indeterminate interface, so it should be obtained experimentally. In this section, bagasse drying test with forced convection utilizing the fixed bed of bagasse was conducted to quantify the drying rate of bagasse and then, bagasse drying process in sugar mill was simulated by using the bagasse drying rate.

3.6.1 Fixed bed test for quantification of drying rate

Figure 3.12 shows the schematic of experimental apparatus for the bagasse drying test. A cylindrical stainless container with φ = 300 mm (2 mm thickness) × L = 250 mm was packed with 1 kg wet bagasse in a length of 130 mm and a mesh sheet was laid on the bottom of container to keep the bagasse. Before the test, hot air heated by hot air generator (Suiden,Hot Dryer SHD-7.5J) was blown to the ambient until the temperature of hot air reached the target value. After that, the hot air was

blown into the bagasse bed by switching the valve. Inside the bagasse bed, three thermocouples were embedded at 0, 50, 100 mm from the bottom, and a thermocouple was fixed at the 150 mm from the bottom to measure the outlet temperature of gas. A humidity sensor (Testo, Robust digital humidity probe 06369753) and a pitot tube were placed in the ventilation duct to measure the change in the dew point and the flow velocity at the outlet of drying gas.

In the series of bagasse drying test, inlet temperature conditions are 120 °C as a higher temperature and 70 °C as a lower temperature, and volumetric flow of the drying gas varied in the range of 0.77 ~ 1.48 m^3/min by changing the frequency of inverter of the hot air generator from 30 Hz to 50 Hz. The conditions of all 6 tests are shown in **Table 3.8**.

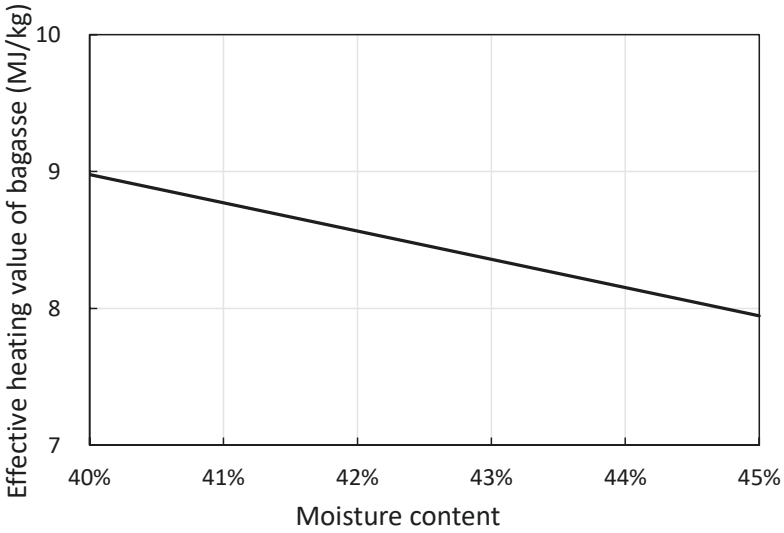

Fig. 3.11. Effect of moisture content of bagasse on effective heating value.

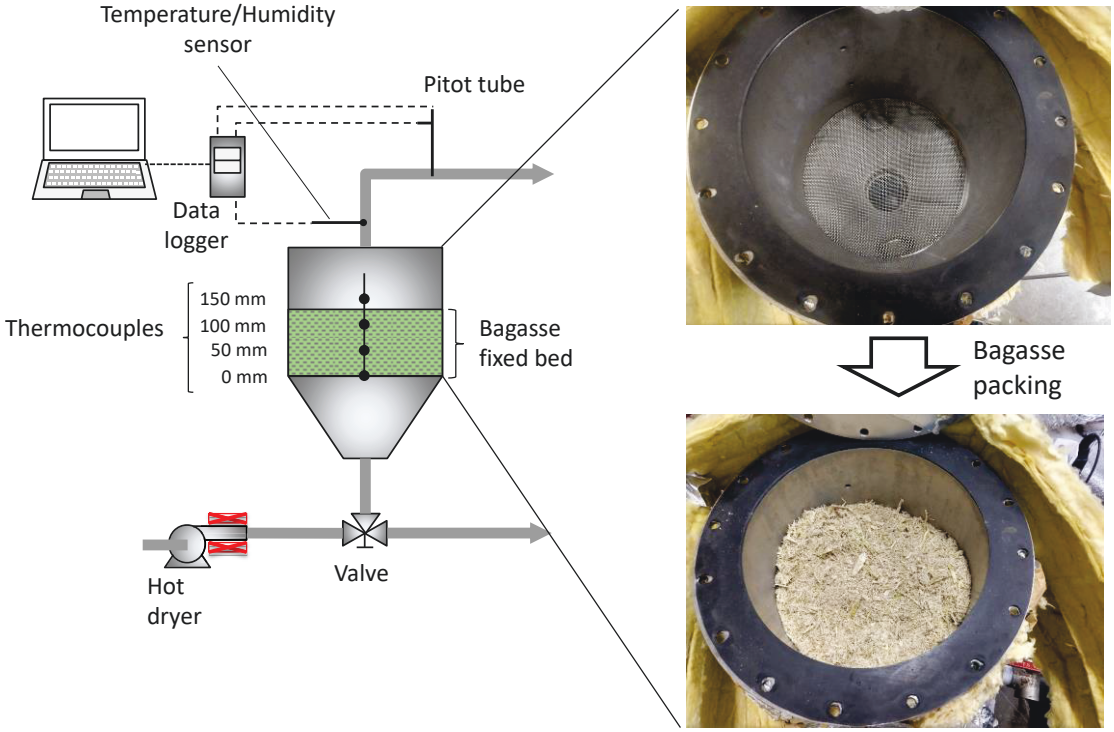

Fig. 3.12. Experimental apparatus of bagasse drying test.

Table 3.8. Experimental conditions of bagasse drying test.

		Test 1	Test 2	Test 3	Test 4	Test 5	Test 6
Weight (Wet)	(kg)	1.0					
Inlet gas temperature	(°C)	119.9	117.5	123.1	69.7	70.6	70.9
Frequency of inverter	(Hz)	50.0	40.0	30.0	50.0	40.0	30.0
Volumetric flow of gas	(m^3/min)	1.48	1.09	0.77	1.22	1.00	0.77
Ambient vapor pressure	(kPa)	1.11	1.02	1.02	0.67	0.71	0.71
Ambient temperature	(°C)	19.0	17.4	18.4	15.3	17.4	18.5
Ambient wet bulb temperature	(°C)	9.9	7.3	7.3	11.1	10.4	13.0

3.6.2 Numerical model

To simulate the bagasse drying test, a one-dimensional unsteady state numerical model was constructed with assumptions as follows;

- Bagasse is packed uniformly
- Gas is treated as ideal gas

Mass balance of bagasse and gas can be expressed by **Eqs. (3.9)** and **(3.10)**, respectively;

$$\frac{\partial \rho_b}{\partial t} = -r \tag{3.9}$$

$$\frac{\partial}{\partial t}\left(\varepsilon_{bed}\rho_g\right) + \frac{\partial}{\partial x}\left(\rho_g u_g\right) = r \tag{3.10}$$

where r is drying rate of bagasse. Drying process of solid material is generally divided in three periods, pre-heating phase, constant rate phase and falling rate phase. Three periods as a function of elapsed time and drying rate as a function of moisture content are summarized in **Figs. 3.13** and **3.14**, respectively. In the pre-heating phase, the solid material is heated up to equilibrium temperature ($\simeq$ the wet bulb temperature of gas) by heating gas. Shifting to the constant rate phase, vaporization mainly occurs from the surface of the material. Temperature of material is kept constant during this phase. Water evaporates at a rate corresponding to the heat transferred from the gas. Therefore, drying rate keep constant, and thereby moisture content decreases linearly.

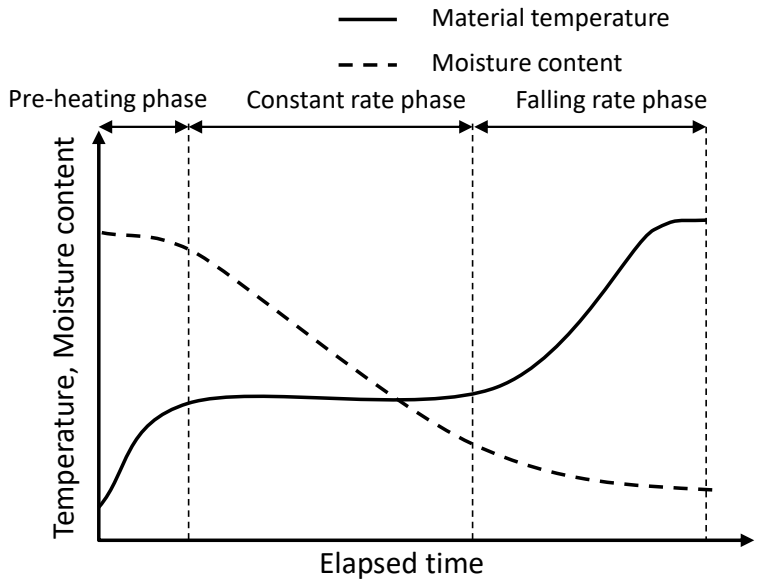

Fig. 3.13. Typical drying curve against elapsed time.

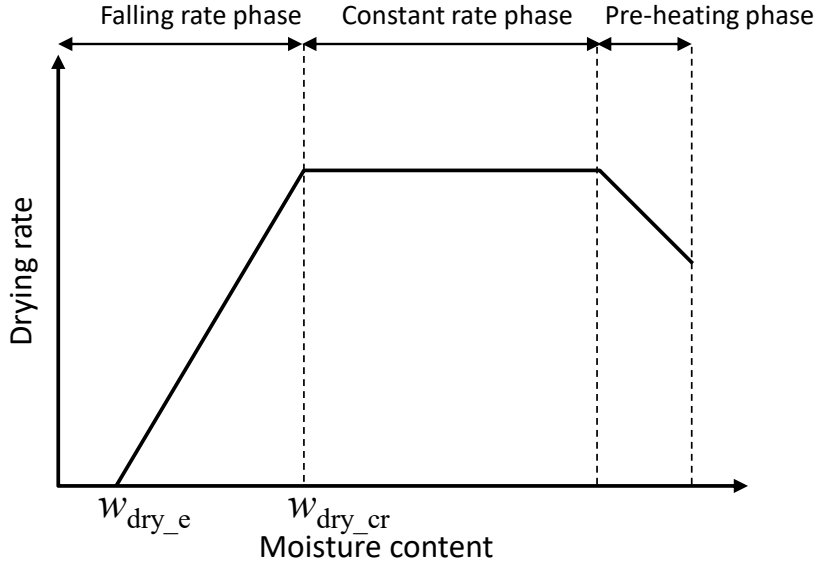

Fig. 3.14. Typical drying rate curve as a function of moisture content.

In the constant rate phase, temperature of bagasse is equal to the wet bulb temperature of gas. Drying rate during this period can be calculated by **Eq. (3.11)** obtained by the balance of the heat transfer and the heat of vaporization on the surface of bagasse.

$$r_{\mathrm{const}} = \frac{\alpha_{\mathrm{g\text{-}b}}\sigma_{\mathrm{g\text{-}b}}(T_{\mathrm{g}} - T_{\mathrm{bulb}})}{\Delta L} \tag{3.11}$$

In this model, bagasse was treated as a cylindrical pellet, and then heat transfer coefficient was calculated by **Eq. (3.12)** [15].

$$Nu_{\text{g-b}} = \frac{\alpha_{\text{g-b}} d_{\text{b}}}{\lambda_{\text{g}}} = 2.0 + 1.1 Re^{0.6} Pr^{1/3} \tag{3.12}$$

where d_{b} is the equivalent diameter of pellet. The specific surface area of bagasse can be calculated by **Eq. (3.13)**.

$$\sigma_{\text{g-b}} = \frac{6(1-\varepsilon_{\text{bed}})}{d_{\text{b}}} \tag{3.13}$$

The porosity of the bed was set to 0.66 [16]. The latent heat of water ΔL employed the constant value of 2500 kJ/kg. The wet bulb temperature of gas can be calculated by the Sprung's equation as expressed as the following equation;

$$p_{\text{s}} = p_{\text{sat}}(T_{\text{bulb}}) - Ap(T_{\text{g}} - T_{\text{bulb}}) \tag{3.14}$$

where A is psychrometer constant (0.000662 1/K).

The falling rate can be expressed by **Eq. (3.15)**.

$$r_{\text{fall}} = r_{\text{const}} \frac{w_{\text{dry}} - w_{\text{dry\_eq}}}{w_{\text{dry}} - w_{\text{dry\_cr}}} \tag{3.15}$$

The equilibrium moisture content $w_{\text{dry\_eq}}$ and the critical moisture content $w_{\text{dry\_cr}}$ were estimated by the experimental result.

Steam conservation equation can be expressed by **Eq. (3.16)**.

$$\frac{\partial}{\partial t}\left(\varepsilon_{\text{bed}}\rho_{\text{s}}\right) + \frac{\partial}{\partial x}\left(\rho_{\text{s}} u_{\text{g}}\right) = \frac{\partial}{\partial x}\left(D_{\text{ax}} \frac{\partial \rho_{\text{s}}}{\partial x}\right) + r \tag{3.16}$$

where D_{ax} is the axial effective diffusivity, which can be calculated by **Eq. (3.17)** [17].

$$D_{\text{ax}} = 0.7 D_{\text{m}} + \frac{0.5 u_{\text{g}} d_{\text{b}}}{\varepsilon_{\text{bed}}} \tag{3.17}$$

where D_{m} is molecular diffusivity which can be calculated by **Eq. (3.18)**.

$$D_{\mathrm{m}} = \frac{1.8583\times10^{-7}\times T_{\mathrm{g}}^{1.5}}{p{d_{\mathrm{co}}}^{2}\Omega}\left(\frac{1}{M_{\mathrm{s}}}+\frac{1}{M_{\mathrm{air}}}\right)^{0.5} \tag{3.18}$$

The collision diameter d_{co} was calculated as the averaged value of molecular diameter of air (3.7 Å) and water (2.6 Å). The order of the collision integral Ω is around 1.0 [18], and then 1.0 was applied to this value.

Energy conservation equations of both bagasse and gas can be expressed by **Eqs. (3.19)** and **(3.20)**, respectively.

$$\frac{\partial}{\partial t}\left(\rho_{\mathrm{b}}c_{p\mathrm{b}}T_{\mathrm{b}}\right) = \frac{\partial}{\partial x}\left(\lambda_{\mathrm{b\_eff}}\frac{\partial T_{\mathrm{b}}}{\partial x}\right) - \frac{6(1-\varepsilon_{\mathrm{bed}})\alpha_{\mathrm{g\text{-}b}}}{d_{\mathrm{b}}}(T_{\mathrm{b}}-T_{\mathrm{g}}) - r\Delta L \tag{3.19}$$

$$\begin{aligned}&\frac{\partial}{\partial t}\left(\varepsilon_{\mathrm{bed}}\rho_{\mathrm{g}}c_{p\mathrm{g}}T_{\mathrm{g}}\right)+\frac{\partial}{\partial x}\left(\rho_{\mathrm{g}}u_{\mathrm{g}}c_{p\mathrm{g}}T_{\mathrm{g}}\right)\\ &=\frac{\partial}{\partial x}\left(\lambda_{\mathrm{gax\_eff}}\frac{\partial T_{\mathrm{g}}}{\partial x}\right)+\frac{6(1-\varepsilon_{\mathrm{bed}})\alpha_{\mathrm{g\text{-}b}}}{d_{\mathrm{b}}}(T_{\mathrm{b}}-T_{\mathrm{g}})-\frac{4\alpha_{\mathrm{g\text{-}amb}}}{d_{\mathrm{c\_in}}}(T_{\mathrm{g}}-T_{\mathrm{amb}})\end{aligned} \tag{3.20}$$

Inherent thermal conductivity of bagasse (0.1 W/(m·K) [19]) was set to effective thermal conductivity of bagasse bed. The axial effective thermal conductivity of gas can be calculated by **Eq. (3.21)** [20].

$$\frac{1}{Pe} = \frac{1}{\dfrac{\rho_{\mathrm{g}}u_{\mathrm{g}}c_{p\mathrm{g}}d_{\mathrm{b}}}{\lambda_{\mathrm{gax\_eff}}}} = \frac{0.73\varepsilon_{\mathrm{bed}}}{RePr}+\frac{0.5}{1+\dfrac{9.7\varepsilon_{\mathrm{bed}}}{RePr}} \tag{3.21}$$

The specific heat capacity of dried bagasse was set to 0.46 kJ/(kg·K) [21] and treated as a function of moisture content expressed as the following equation.

$$c_{p\mathrm{b}} = \frac{c_{p\mathrm{b\_dry}}+c_{p\mathrm{w}}w_{\mathrm{dry}}}{1+w_{\mathrm{dry}}} \tag{3.22}$$

The heat leakage only through the gas phase was considered because the bagasse has a low contact area to the vessel wall due to fiber form. The heat loss was calculated utilizing overall heat transfer coefficient considering heat transfer between gas and wall, thermal conduction of container wall

(Stainless, 2 mm thickness, 16.7 W/(m·K)), thermal conduction of thermal insulation (glass wool, 50 mm thickness, 0.05 W/(m·K)) and natural convection from the outer wall of thermal insulation to the ambient air (10 W/(m^2·K)). The heat transfer coefficient between gas and wall can be calculated by **Eq. (3.23)** [20].

$$Nu_{\text{g-wall}} = \frac{\alpha_{\text{g-wall}} d_{\text{b}}}{\lambda_{\text{g}}} = 0.2 Re^{0.8} Pr^{1/3} \tag{3.23}$$

Other thermophysical properties are shown in **Table 3.9**. Viscosity and thermal conductivity of mixed gaseous were calculated by Wilke's estimation [22] and Mason and Saxena's estimation [23], respectively. The pressure drop of the bagasse bed is negligible due to higher porosity of the bed (0.66).

The boundary conditions of this analysis are shown in **Fig. 3.15**.

Table 3.9. Thermophysical properties.

Density of bagasse (kg/m^3)	
Dried bagasse (kg/m^3)	61.5
Wet bagasse (kg/m^3)	111.8
Heat capacity (J/(kg·K))	
$c_{ps} = 13604 - 90.4304 \times T_{\text{g}} + 0.2774 \times T_{\text{g}}^2 - 4.2126 \times 10^{-4} \times T_{\text{g}}^3 + 3.1837 \times 10^{-7} \times T_{\text{g}}^4 - 9.5615 \times 10^{-11} \times T_{\text{g}}^5$	
$c_{p\text{air}} = 1047 - 0.3726 \times T_{\text{g}} + 9.4530 \times 10^{-4} \times T_{\text{g}}^2 - 6.0241 \times 10^{-7} \times T_{\text{g}}^3 + 1.2859 \times 10^{-10} \times T_{\text{g}}^4$	
$c_{p\text{w}} = 12010 - 80.4073 \times T_{\text{b}} + 0.3099 \times T_{\text{b}}^2 - 5.3819 \times 10^{-4} \times T_{\text{b}}^3 + 3.6254 \times 10^{-7} \times T_{\text{b}}^4$	
Thermal conductivity (W/(m·K))	
$\lambda_{\text{s}} = 1.3173 \times 10^{-4} + 5.1497 \times 10^{-5} \times T_{\text{g}} + 3.8965 \times 10^{-8} \times T_{\text{g}}^2 - 1.3681 \times 10^{-11} \times T_{\text{g}}^3$	
$\lambda_{\text{air}} = -0.002276 + 1.1548 \times 10^{-4} \times T_{g} - 7.9025 \times 10^{-8} \times T_{\text{g}}^2 + 4.1170 \times 10^{-11} \times T_{\text{g}}^3 - 7.4386 \times 10^{-15} \times T_{\text{g}}^4$	
Viscosity (Pa·s)	
$\mu_{\text{s}} = -1.4202 \times 10^{-6} + 3.8346 \times 10^{-8} \times T_{\text{g}} - 3.8522 \times 10^{-12} \times T_{\text{g}}^2 + 2.1020 \times 10^{-15} \times T_{\text{g}}^3$	
$\mu_{\text{air}} = -8.3828 \times 10^{-7} + 8.3572 \times 10^{-8} \times T_{\text{g}} - 7.6943 \times 10^{-11} \times T_{\text{g}}^2 + 4.6437 \times 10^{-14} \times T_{\text{g}}^3 - 1.0659 \times 10^{-17} \times T_{\text{g}}^4$	

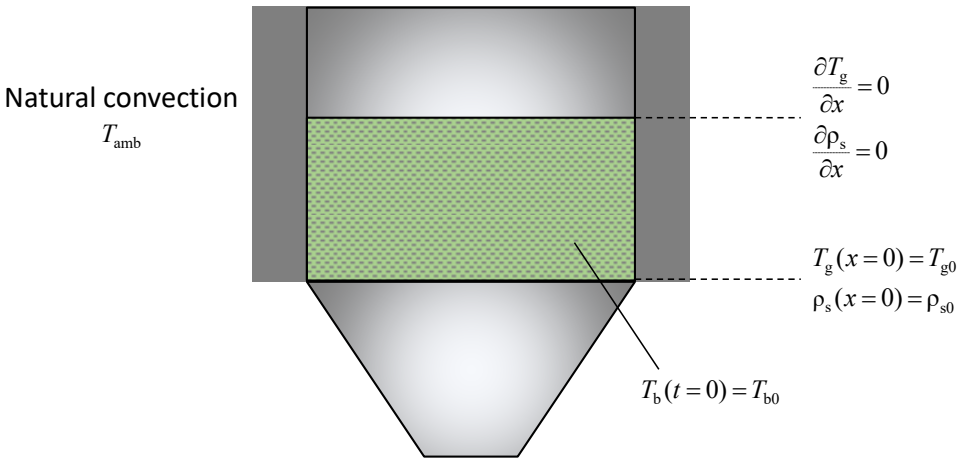

Fig. 3.15. Boundary conditions of bagasse drying test.

3.6.3 Experimental and numerical analysis result of bagasse drying test

History of axial temperature distribution in bagasse fixed bed, change in outlet vapor pressure and moisture content and change in drying rate during bagasse drying test of Test 5 as an example result are shown in **Figs. 3.16**, **3.17** and **3.18**, respectively.

From the **Fig. 3.16**, temperatures of bagasse bed rise from the bottom to the top of container. Looking at the position of x = 100 mm, temperature rose to 25 °C after 100 seconds, which was corresponding to the pre-heating phase. After the pre-heating phase, constant rate period started, and temperature was kept at 25 °C. After 750 seconds, the drying phase was moved to the falling rate phase and started to increase the temperature. At the bottom (x = 0), temperature immediately increased right after the pre-heating phase. The reason for lack of constant rate phase is that moisture content at the bottom of container decreased below the critical moisture content during the pre-heating phase and thereby falling rate phase started with no time lag. As can be seen from **Fig. 3.17** outlet vapor pressure rapidly increased due to strong drying during the pre-heating period. After 200 seconds from the start, whole bed was pre-heated and constant rate phase started except the bottom area. In the constant rate phase, the drying rate kept at a constant, which resulted in constant outlet vapor pressure of 3 kPa (See **Fig. 3.17**) and in linear decrease in moisture content. After 750 seconds from the start, drying rate started to decrease and outlet vapor pressure decrease, too.

As can be seen from **Fig. 3.18**, the critical moisture content, which is found at the time of phase transition from the constant to falling rate, is approximately 50%-dried condition (phase transition time = 750 s), and equilibrium moisture content is 10%. From this result, the critical moisture content w_{dry_cr} and the equilibrium moisture content w_{dry_eq} were determined as 50% (w_{wet_cr} = 20%) and 10% (w_{wet_eq} = 5%), respectively and used in the numerical simulation.

Bagasse consists of pith, fiber and rind and each mass fraction is 5%, 73% and 22%, respectively and these parts have different bulk density [16]. The configuration of bagasse packed in the container might be diverse, so numerical simulation was conducted utilizing various equivalent diameter (12, 18 and 24 mm).

All the experimental and numerical analysis results of temperature history are shown in **Fig. 3.19** and outlet vapor pressure are shown in **Fig. 3.20**. At x =50 mm in Test 4 and x = 100 mm in Test 6, unexpected behaviors were observed. As for one of reasons, evaporated water from the bagasse was condensed at the thermocouple, which leaded to delay of temperature increase. Other result shows the temperature increase in order from the bottom to top. The numerical analysis result can simulate the experimental result in the range of equivalent diameter from 12 to 24 mm. It implies that bagasse fibers with equivalent diameter from 12 to 24 mm were packed randomly in the vessel. To predict the performance of bagasse drying rate in the bagasse elevator, 24 mm of equivalent diameter was used to avoid overestimate in the following section.

Figure 3.21 shows the numerical analysis result of change in moisture content of bagasse at x =0, 50 and 100 mm. The moisture content of bagasse decreases from the bottom to the top and reaches equilibrium moisture content.

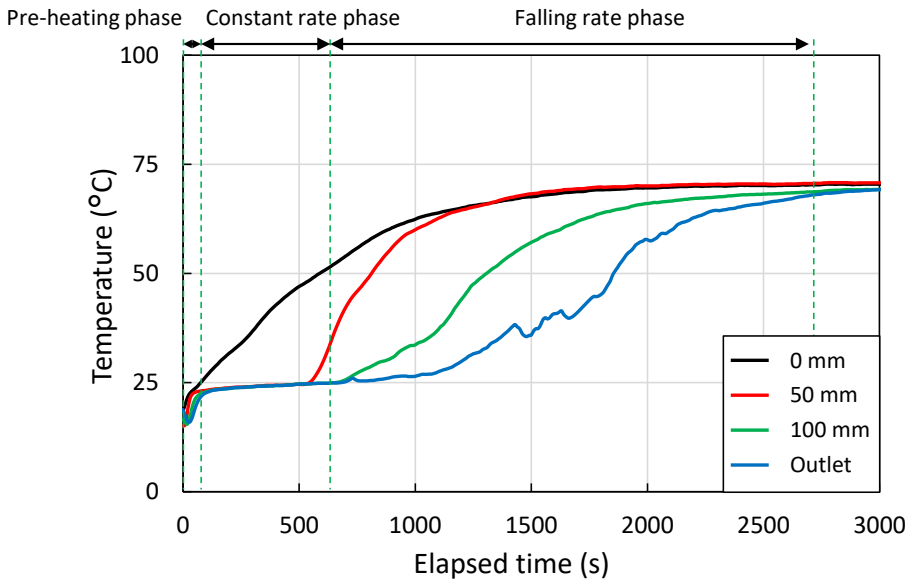

Fig. 3.16. History of axial temperature distribution in bagasse fixed bed during bagasse drying test.

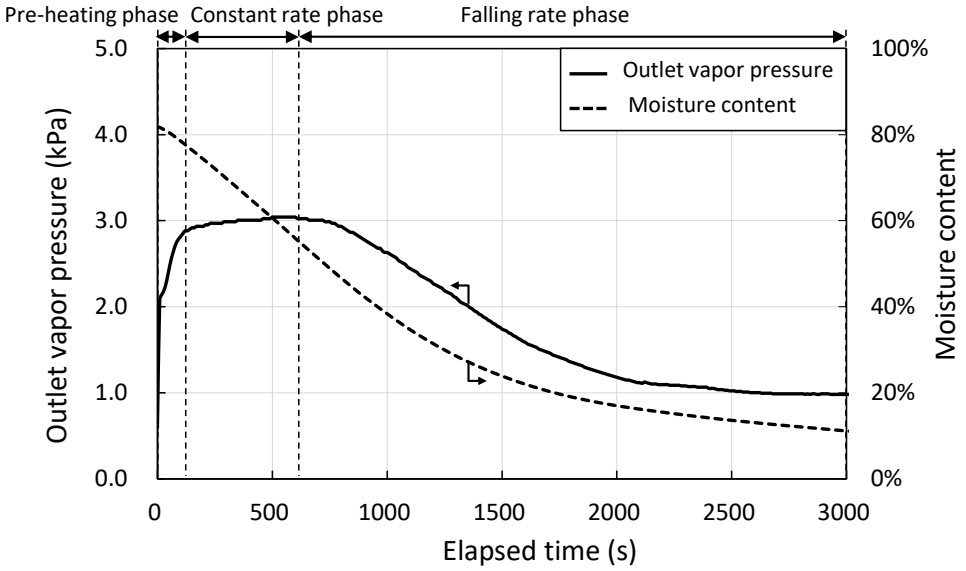

Fig. 3.17. Change in outlet vapor pressure and moisture content.

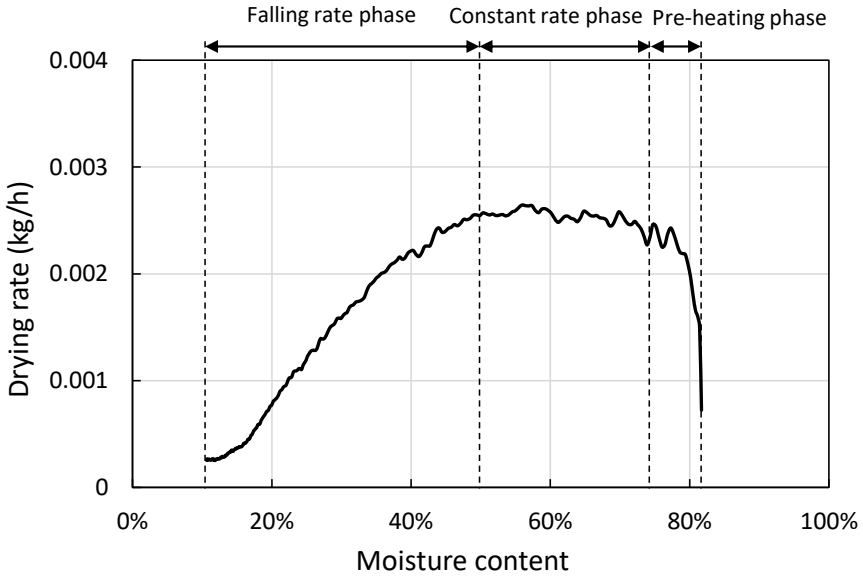

Fig. 3.18. Drying rate curve by experimental result.

3.6.4 Modeling and numerical prediction of bagasse drying process in bagasse elevator

Figure 3.22 shows the schematic of bagasse elevator. Sugarcane is milled by the mill turbine and thereafter, the bagasse is transported by bagasse elevator to feed into the bagasse boiler. At the top of bagasse elevator, bagasse is transferred from the bagasse elevator to the supply conveyor and fed into the bagasse boiler controlled by the rotary feeder. The excess bagasse is transported to the bagasse yard. The return elevator with a screw feeder in the bagasse yard returns back the bagasse to the bagasse boiler. The bagasse elevator and supply conveyor are covered with a hood, while return elevator is opened. In the bagasse drying process, the drying air is assumed to be introduced to the

covered bagasse elevator in the counter flow against the bagasse conveyor. **Table 3.10** shows the configuration and operating condition of bagasse elevator.

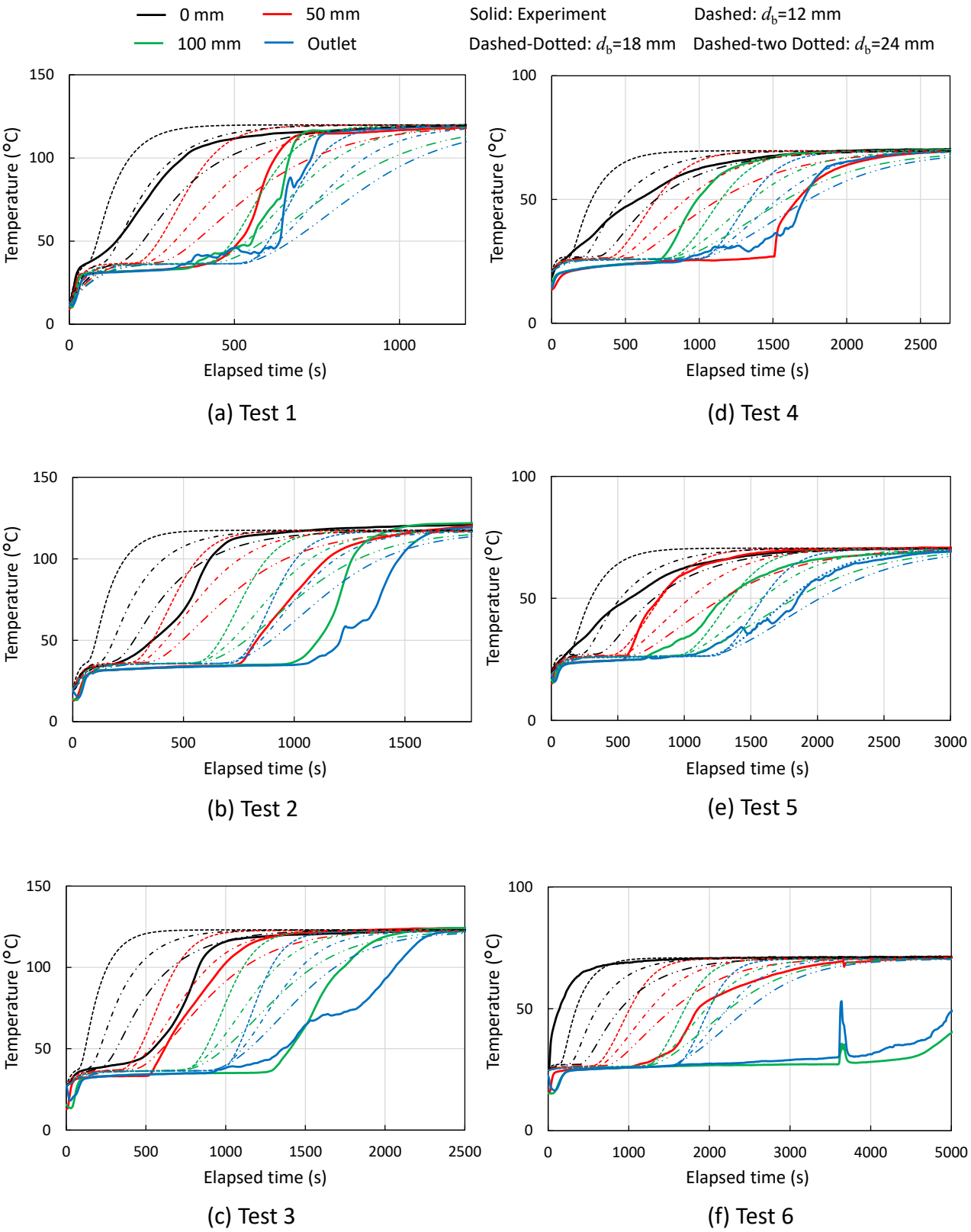

Fig. 3.19. Experimental and numerical analysis results of axial temperature distribution history.

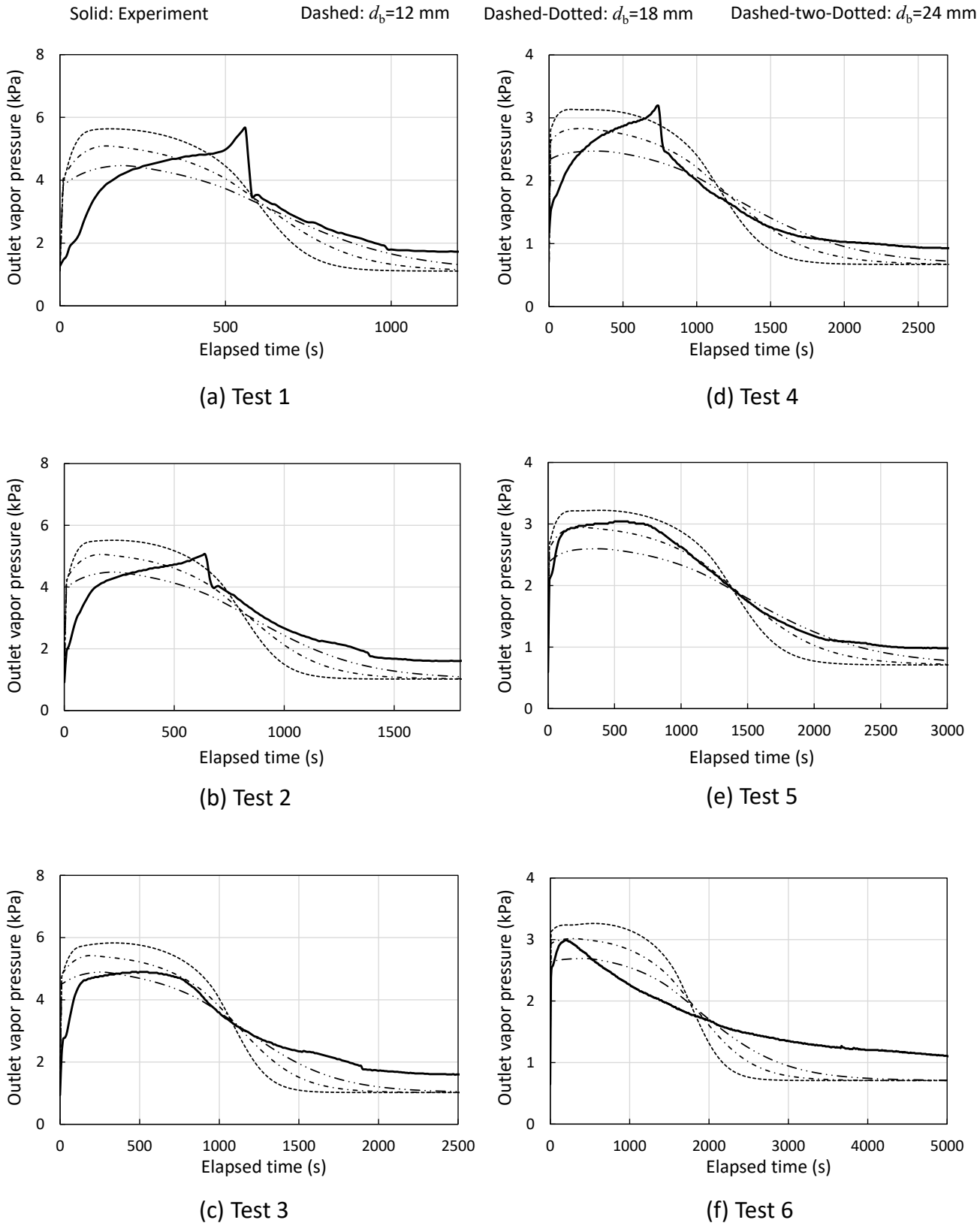

Fig. 3.20. Experimental and numerical analysis results of outlet vapor pressure change.

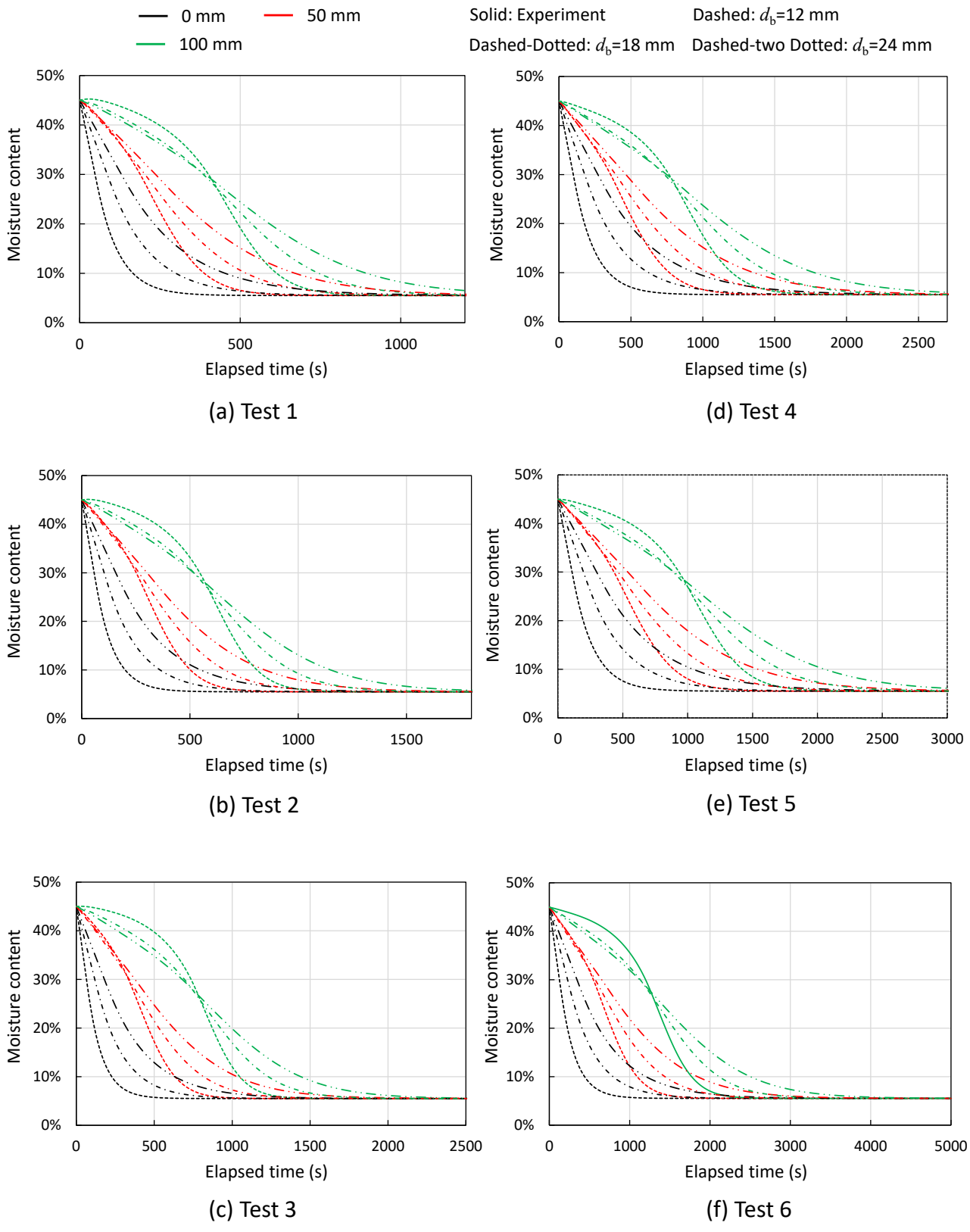

Fig. 3.21. Numerical analysis results of moisture content change.

Table 3.10. Configuration and operating condition of bagasse elevator.

Speed (m/min)	22
Inlet temperature (°C)	35
Length (mm) (Approximate)	20000
Cross section, Width (mm) x Hight (mm) (Approximate)	1200 x 900

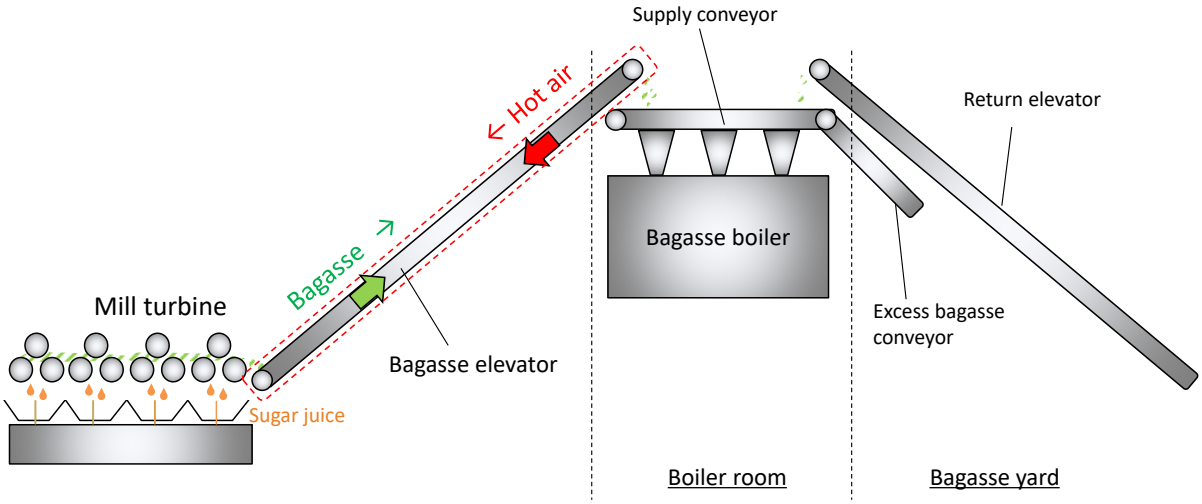

Fig. 3.22. Schematic of bagasse elevator, supply conveyor and return elevator.

The exhaust water from the multiple effect evaporator with 70 °C is considered as a heat source to dry the bagasse. The multiple effect evaporator consists of five vessels and steam generated by the bagasse boiler is introduced to the first vessel. The exhaust steam generated in the first vessel is fed into the second vessels and cascadic use for evaporation. From this multiple effective evaporators, 56 t/h hot water around 70 °C were exhausted. If the half of enthalpy of exhaust hot water from the temperature of 70 °C to 60 °C is recovered by exchanging heat with 15 °C air, the air heated at 60 °C, can be obtained with volumetric flow of 390 m^3/min.

Assuming that bagasse and hot air are inputted in a constant rate continuously into the bagasse elevator, the bagasse drying process could be simulated as a steady state condition. The mass balance equations of both bagasse and gas can be expressed by **Eqs. (3.24)** and **(3.25)**, respectively.

$$\frac{\partial}{\partial x}(\rho_b u_b) = -r \tag{3.24}$$

$$-\frac{\partial}{\partial x}(\rho_g u_g) = r \tag{3.25}$$

The bulk density of bagasse was determined by the mass weight of bagasse on the bagasse elevator and volume of the elevator (4.27 kg/m^3). The bulk porosity of the bagasse elevator was determined by the volume of bagasse and elevator as well (0.93).

The steam conservation equation can be expressed by **Eq. (3.26)**.

$$-\frac{\partial}{\partial x}\left(\rho_s u_g\right)=\frac{\partial}{\partial x}\left(D_{ax}\frac{\partial \rho_s}{\partial x}\right)+r \tag{3.26}$$

The energy conservation equations for bagasse and gas can be expressed by **Eqs. (3.27)** and **(3.28)**, respectively.

$$\frac{\partial}{\partial x}\left(\rho_b u_b c_{pb} T_b\right)=\frac{\partial}{\partial x}\left(\lambda_{b\_eff}\frac{\partial T_b}{\partial x}\right)-\frac{6(1-\varepsilon_{bed})\alpha_{g\text{-}b}}{d_b}(T_b-T_g)-r\Delta L \tag{3.27}$$

$$\begin{aligned}&-\frac{\partial}{\partial x}\left(\rho_g u_g c_{pg} T_g\right)\\&=\frac{\partial}{\partial x}\left(\lambda_{gax\_eff}\frac{\partial T_g}{\partial x}\right)+\frac{6(1-\varepsilon_{bed})\alpha_{g\text{-}b}}{d_b}(T_b-T_g)-\alpha_{g\text{-}amb}\sigma_{g\text{-}amb}(T_g-T_{amb})\end{aligned} \tag{3.28}$$

Heat leakage only through the gas phase was considered as the same reason of the bagasse drying test (see **3.6.2**). The heat transfer coefficient was determined by the equivalent diameter of rectangular cross section of the bagasse elevator. The overall heat transfer consists of the heat transfer between gas and inner wall, thermal conduction of stainless wall (50 mm of thickness) and heat transfer from the outer wall to the ambient air. The heat transfer from the outer wall of elevator to the ambient air was assumed to be the natural convection giving 10 W/(m^2·K) of heat transfer coefficient. The boundary conditions of the bagasse drying system are shown in **Fig. 3.23**.

Figure 3.24 shows the numerical calculation result of bagasse drying process when 390 m^3/min hot air at 60 °C was provided. The initial moisture content of bagasse was set to 44.4% based on the experimental data (See **3.2.1**). The introduced gas is cooled down by contacting bagasse, and thereby temperature of gas reaches the same temperature of bagasse at about x = 10 m. In this case, the moisture content of bagasse decreases by approximately 2%, from 44.4% to 42.5%. **Figure 3.25** shows the relationship between volumetric flow of gas and moisture content of bagasse. The moisture content of bagasse decreases linearly down to 42.5% with increase in the volumetric flow of gas up to 390 m^3/min.

From the experimental and numerical analysis approach for the bagasse drying process, the heat charging potential for the range of 42.4 to 44.4% of moisture content of bagasse was predicted by the process simulation, discussing in the next section.

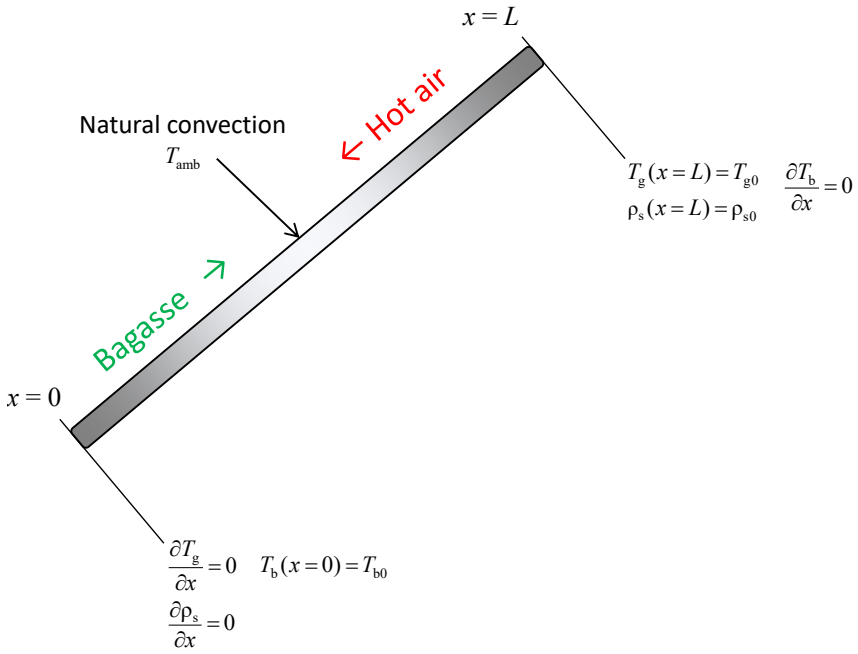

Fig. 3.23. Boundary conditions of bagasse drying system in bagasse elevator.

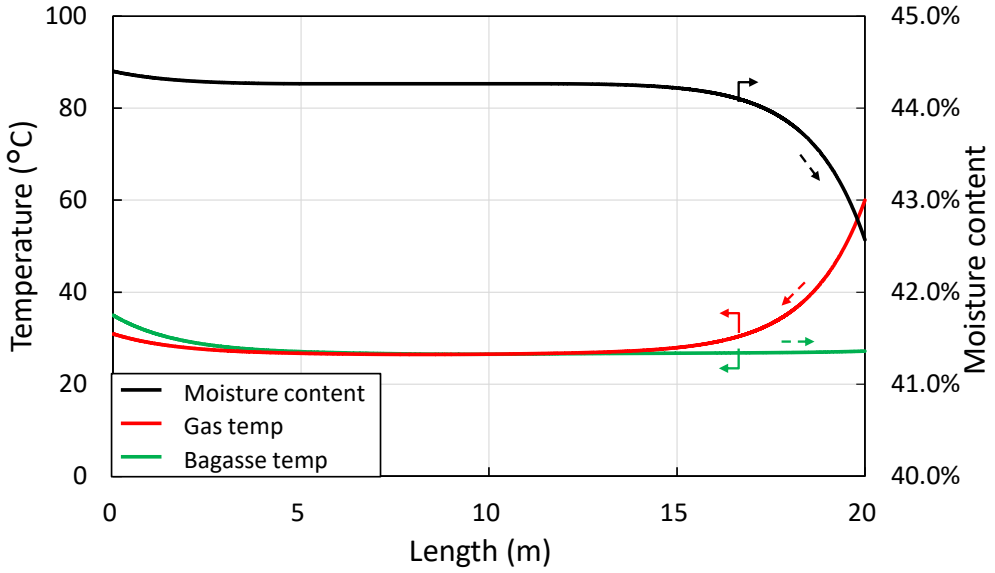

Fig. 3.24. Performance prediction of bagasse drying process in bagasse elevator.

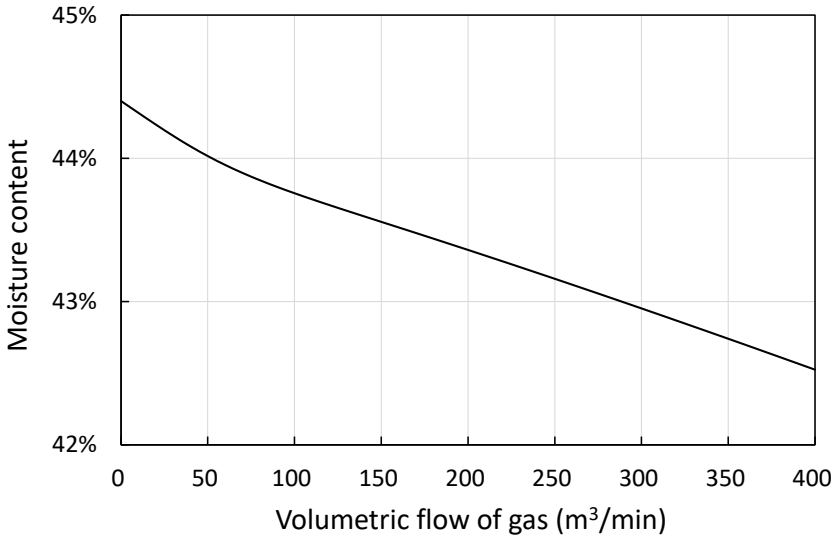

Fig. 3.25. Relationship between volumetric flow of gas and moisture content.

3.6.5 Effect of bagasse drying on bagasse saving

Firstly, effect of bagasse saving was considered independently detaching the TES. The overall heat transfer coefficient of bagasse boiler (UA value) was fixed to the same value as the current process. The mass flow rate of bagasse and volumetric flow of intake air were adjusted to keep the same flue gas temperature when the moisture content of bagasse was declined.

Figure 3.26 shows the effect of drying bagasse on bagasse saving. The heat charging potential was kept at 663 kW constant. Moisture content reduction of 2% is equivalent to bagasse saving of 0.9%.

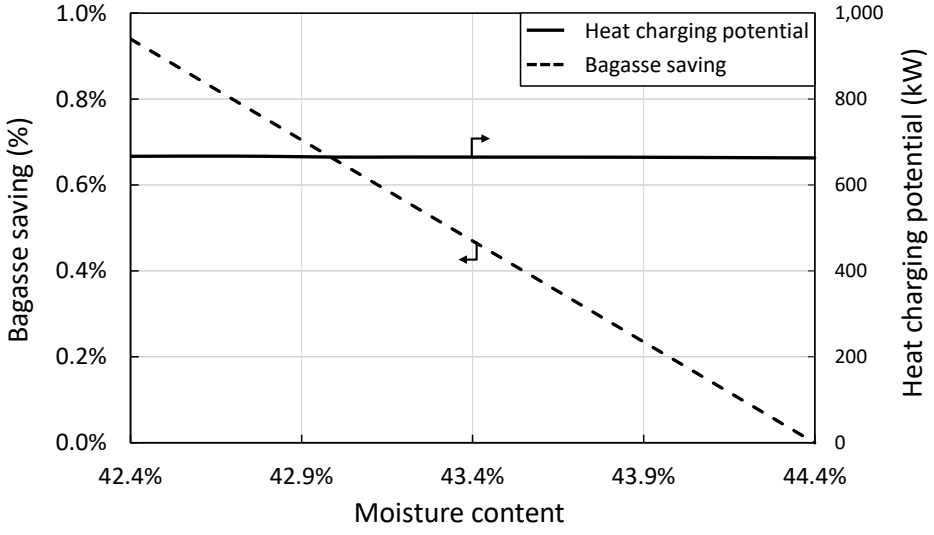

Fig. 3.26. Effect of bagasse drying on bagasse saving and heat charging potential.

3.6.6 Effect of bagasse drying on heat charging potential

If the mass flow rate of dried bagasse and main steam (= heat duty in the bagasse boiler) are kept at a constant, temperature of flue gas increase due to increase in the heating value of bagasse by

drying process. The same UA value was given to bagasse boiler, and the volumetric flow of intake air was adjusted to keep the temperature of main steam at 344 °C. **Figure 3.27** shows the change in temperature of flue gas and hot air used for TES, the mass flow rate of hot air and heat charging potential as a function of moisture content. By drying bagasse, the flue gas temperature and the heat charging potential increase up to 188 °C and 817 kW, respectively.

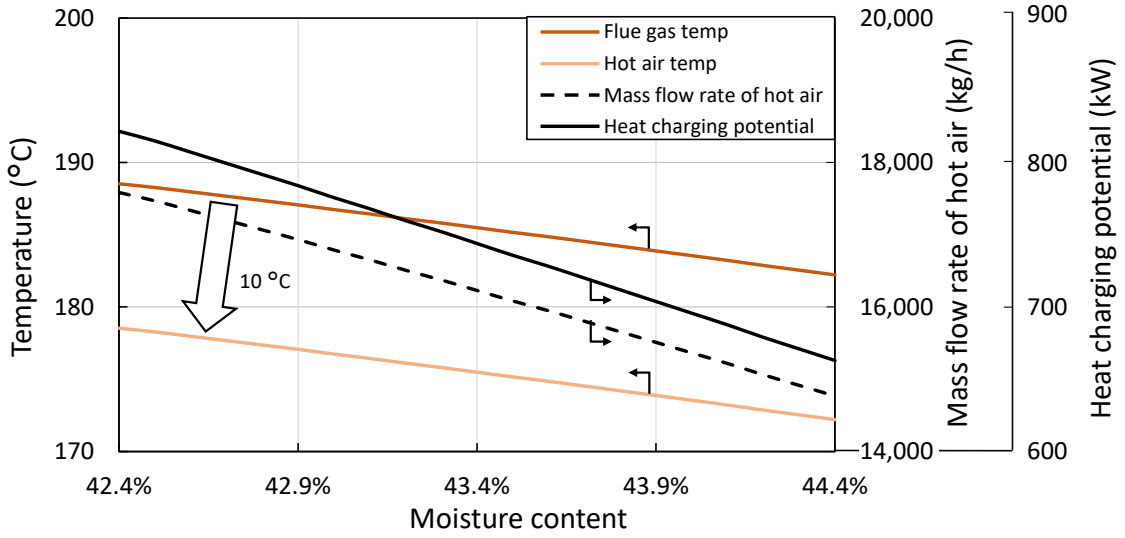

Fig. 3.27. Effect of bagasse drying on flue gas temperature increase and heat charging potential.

3.6.7 Effect of bagasse drying on power generation

Increase in the heating value of bagasse by drying process can be used not only for increase in flue gas temperature but increase in the mass flow rate of main steam. Increase in the mass flow rate of steam leads increase in power generation. The UA value of bagasse boiler was kept, and the volumetric flow of intake air was adjusted to keep the temperature of flue gas as the same as current process. The mass flow rate of main steam was adjusted to keep the temperature of main steam. **Figure 3.28** shows the increase in power generation as a function of moisture content of bagasse. The heat charging potential kept the same. By drying the bagasse, up to 32 kW of additional power is expected to be generated.

3.6.8 Effect of bagasse drying on power generation and heat charging potential

Figure 3.29 shows the effect of drying bagasse on temperature of flue gas and hot air for TES, the mass flow rate of hot air and the heat charging potential as a function of additional power generation when bagasse is assumed to be dried to 42.4%. The heat charging potential is roughly decreased lineally against the additional power generation increase.

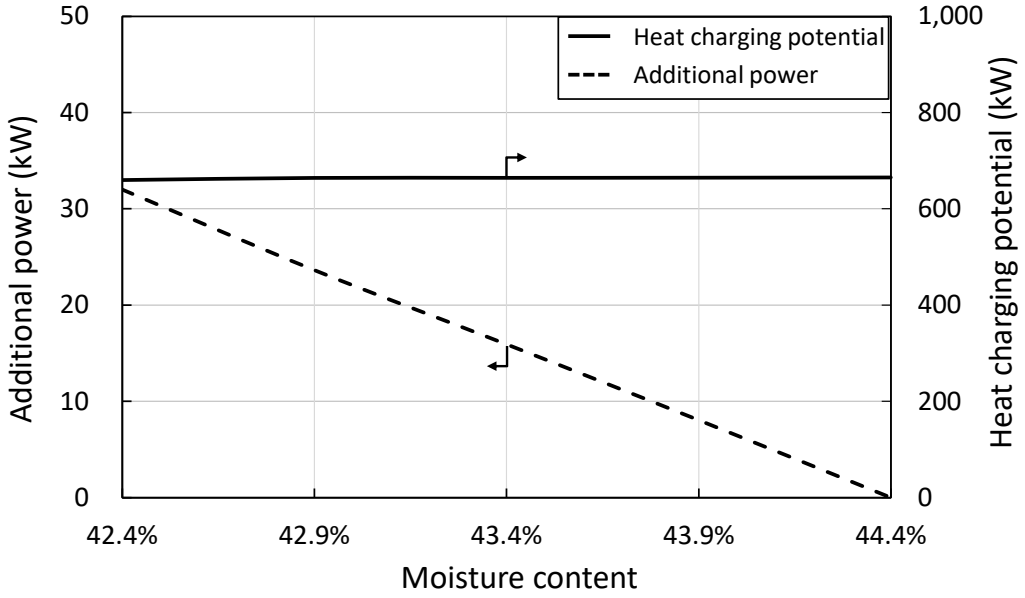

Fig. 3.28. Effect of bagasse drying on increase in power generation and heat charging potential.

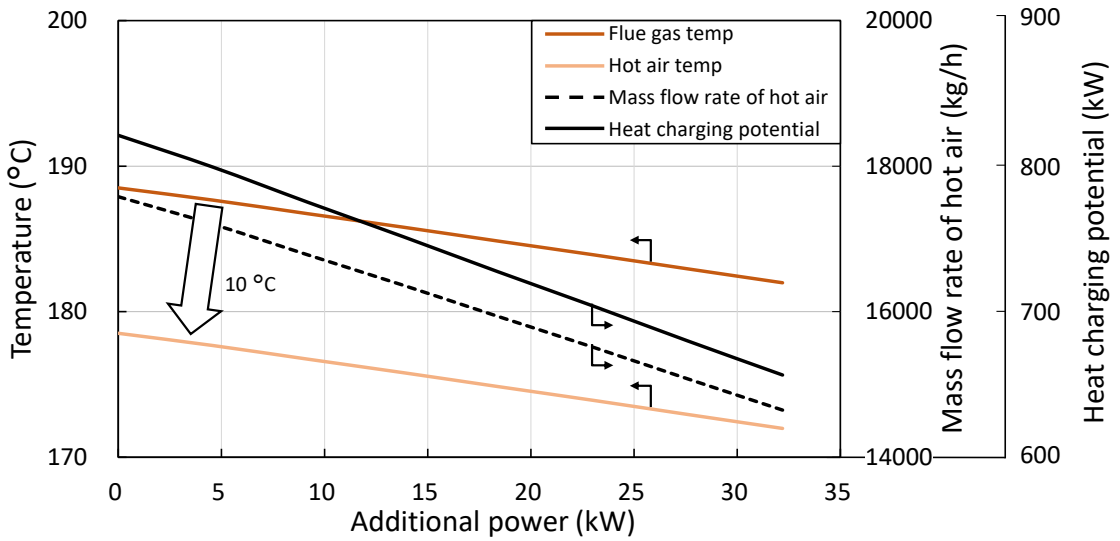

Fig. 3.29. Effect of bagasse drying on temperature of flue gas and hot air for TES, mass flow rate of hot air and heat charging potential.

3.7 Combination of blow steam reduction and bagasse drying

The combined process of blow steam reduction and bagasse drying was considered. Both increase in flue gas temperature and power generation was considered.

(1) Increase in flue gas temperature

The assumptions of process simulation are that the moisture content of bagasse was set to the minimum value (42.4%), the same UA value was given to the bagasse boiler and the mass flow rate

of blow steam and accompanying that of main steam were reduced by 0.4 t/h. As a result, the flue gas temperature and the heat charging potential increase up to 195 °C and 1009 kW, respectively. In this case, the flue gas temperature at the inlet of electric precipitator increases up to 218 °C, which is lower than 350 °C of maximum allowable temperature of the precipitator.

(2) Increase in power generation

The moisture content of bagasse was set to the minimum value (42.4%), the flue gas temperature was kept at 182 °C, and the mass flow rate of blow steam was reduced by 0.4 t/h. The mass flow rate of turbine steam was adjusted to keep the same flue gas temperature of current process (182 °C). In this case, the total power generation is 1542 kW, which increases by 69 kW in comparison with the current process.

(3) Performance diagram

Figure 3.30 shows the summary of the relationship between flue gas temperature, additional power generation and moisture content of bagasse as a performance diagram. In the case of prioritizing the flue gas temperature increase, temperature increases by 7 °C from 182 °C of current process by reducing the blow steam. In addition, by applying bagasse drying process, the flue gas temperature increases up to 195 °C. In the case of prioritizing increase in power generation, 37 kW of additional power is expected by reducing the blow steam. In addition, by applying bagasse drying process, additional power generation is expected to increase by up to 69 kW. In the actual operation, the TES system should be operated in the range of red color zone shown in **Fig. 3.30**. Implementation of bagasse drying process requires additional cost of the heat exchanger and blower. Therefore, reducing blow steam is an easy way to increase the flue gas temperature or power generation and then, bagasse drying process will be considered to increase more gain. (The gradation of red zone in **Fig. 3.30** means the priority of operation. Dark side indicate the effect of blow steam on temperature and power generation and light side indicate the effect of bagasse drying process).

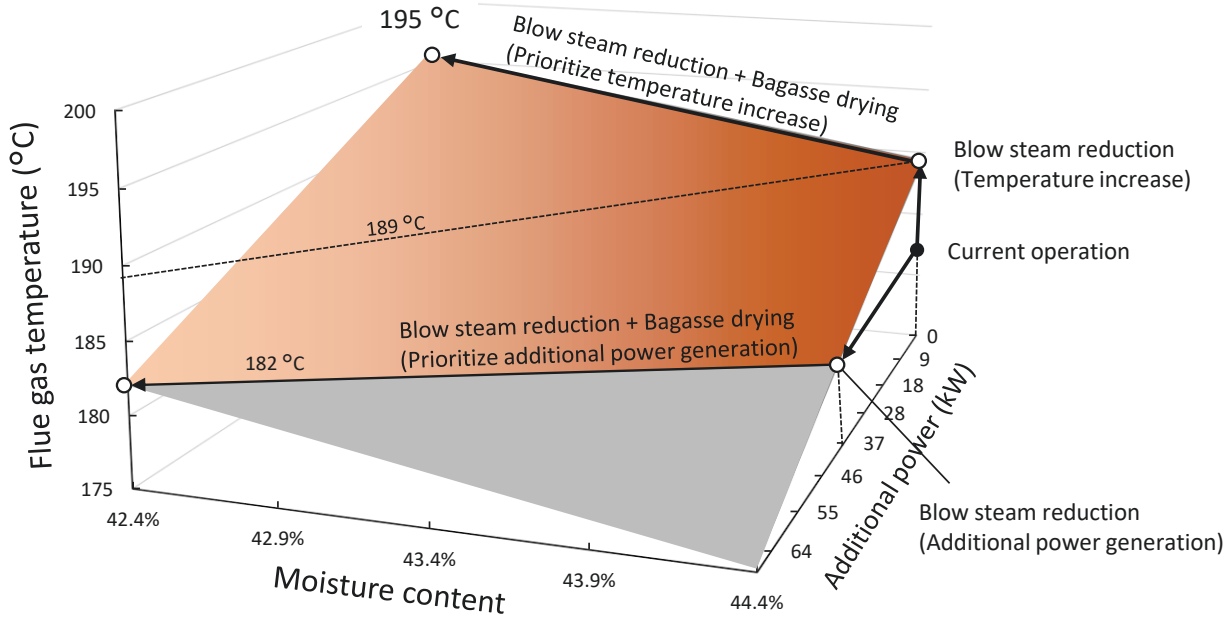

Fig. 3.30. Performance diagram: Effect of drying bagasse and blow steam reduction on flue gas temperature and increase in power generation.

3.8 Increase in power generation

Increase in power generation in the sugar mill was considered aiming to establish a self-sufficient system of TES under the current process without blow steam reduction and bagasse drying. To increase the power generation, steam mass flow to the power turbine should be increased, which decrease the temperature of flue gas unless more bagasse is fueled to the bagasse boiler. Increase in power generation and resulting decrease in heat charging potential due to temperature drop of the flue gas were calculated. The flow rate of air was adjusted to keep the main steam temperature at 344 °C.

Figure 3.31 shows the decrease in temperature of flue gas and hot air for TES with the assumption of 10 °C of minimum temperature approach, the mass flow rate of hot air and heat charging potential as a function of additional power generation. Increase in power generation leads increase in mass flow rates of steam for turbine inlet and accompanying main steam, temperature of flue gas linearly decreases and thereby, heat charging potential decreases lineally as well. When temperature of flue gas reached at the limitation of acid dew point (150 °C), power generation increases to 129 kW. On the contrary, the no heat charging potential is remaining.

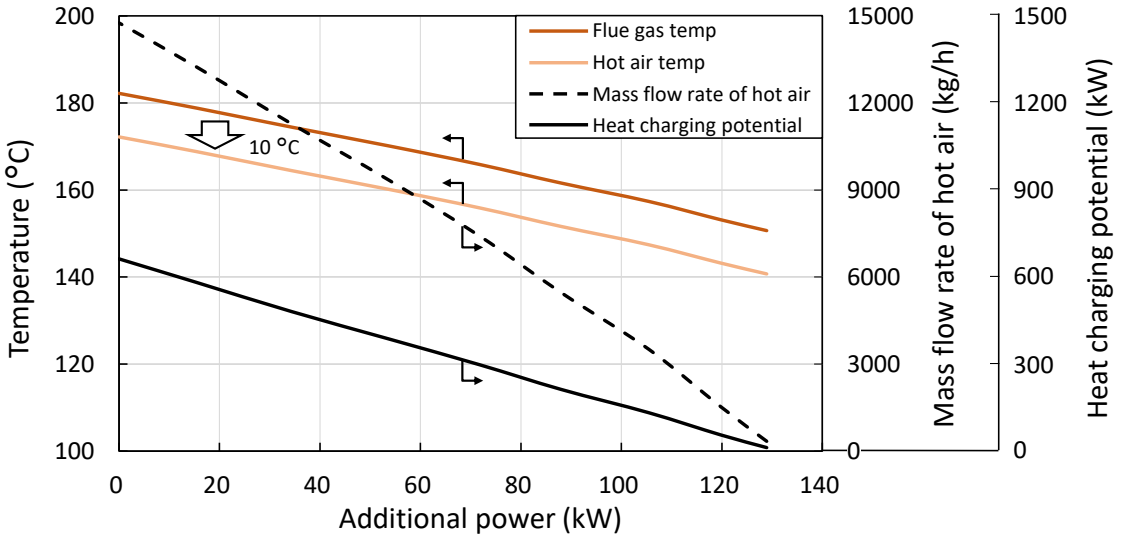

Fig. 3.31. Effect of increase in power generation on flue gas and hot air temperature, the mass flow rate of hot air and heat charging potential.

3.9 Summary of process modeling of sugar mill

For the heat charging process, the current process and 4 promising improved processes were discussed.

A) Current process (described in section **3.4**)

B) Blow steam reduction (described in **3.5**)

C) Bagasse drying (described in **3.6**)

D) Combined process with blow steam reduction and bagasse drying (described in **3.7**)

E) Increase in power generation (described in **3.8**)

The maximum and minimum temperature of flue gas and heat charging potential, the maximum additional power generation of each process is summarized in **Table 3.11**.

Table 3.11. Summary of process simulation result of sugar mill.

	Flue gas temperature (°C)		Heat charging potential (kW)		Increase in power generation (kW)
	Maximum	Minimum	Maximum	Minimum	Maximum
A)	182		663		-
B)	189	182	850	663	37
C)	188	182	817	663	32
D)	195	182	1009	663	69
E)	182	150	663	0	129

3.10 Chapter conclusion

In this chapter, the material and heat flow analysis of the sugar mill, which was assumed to be a heat charging station in the thermochemical energy storage and transport system, was quantified to predict the heat charging potential. In addition, increase in heat charging potential and additional power generation were clarified when promising improved processes were applied. Main achievements of this chapter were shown as follows;

- The elemental composition and moisture content of bagasse were investigated at first and then, the process flow diagram of sugar mill was built on the commercial process simulation software Aspen HYSYS®. The mass flow rate of bagasse and intake air for bagasse boiler, which were unknow parameters, were predicted in accordance with the operation data and the validity of calculated data was confirmed.
- The heat charging potential of the current sugar milling process resulted in 663 kW and promising improved processes (blow steam reduction, bagasse drying and increase in additional power generation) were applied to increase the heat charging potential and additional power generation.
- The feasibility of bagasse drying process was investigated. The rate of bagasse drying was quantified experimentally, and 2% reduction of moisture content was expected by numerical analysis.

The relationships between the additional power generation and the mass flow rate of hot air for TES, and temperature of flue gas and hot air were clarified, which are used for boundary conditions to design the heat discharging device namely “Zeolite Boiler” in Chapter 4, heat charging device namely “Heat Charger” in Chapter 5 and to conduct techno-economic and environmental analyses in Chapter 6.

Nomenclature

Symbols

A:	Psychrometer constant	1/K
c_p:	Specific heat capacity	J/(kg·K)
d:	Diameter	m
D:	Diffusivity	m^2/s
HHV:	Higher heating value	MJ/kg
K:	Overall heat transfer coefficient	W/K
L:	Length of chamber	m
LHV:	Lower heating value	MJ/kg
m:	Mass weight, mass flow rate	kg, kg/h
M:	Molecular weight	g/mol
p:	Pressure	kPa
Q:	Heat flux	W
r:	Drying rate	$kg/(m^3·s)$
t:	Time	s
T:	Temperature	K
u:	Velocity	m/s
w:	Moisture content	-
x:	Axial coordinate	m
α:	Heat transfer coefficient	$W/(m^2·K)$
ΔL:	Latent heat	kJ/kg
ε:	Porosity	-
λ:	Thermal conductivity	W/(m·K)
μ:	Viscosity	Pa·s
ρ:	Density	kg/m^3
σ:	Specific heat transfer area	m^2/m^3
Ω:	Collision integral	-

Dimensionless parameters

Nu:	Nusselt number
Pe:	Peclet number
Pr:	Prandtl number
Re:	Reynolds number

Subscript

air:	Air
amb:	Ambient
ax:	Axial

b: Bagasse
bed: Packed bed
bulb: Wet bulb
c: Chamber
co: Collision
const: Constant
cr: Critical
dry: Dry based
eff: Effective
EP: Electric precipitator
eq: Equilibrium
fall: Falling rate
flue: Flue gas
g: Gas
in: inner
m: Molecular
pre: Pre-heating
s: Steam
sat: Saturation
w: Water
wall: Wall
wet: Wet based
0: Original or Initial

References

[1] Jenkins B., Baxter L., Miles T., Miles T. Combustion properties of biomass. Fuel Process Technol 1998;54:17–46. doi:10.1016/S0378-3820(97)00059-3.

[2] Turn SQ, Kinoshita CM, Ishimura DM. Removal of inorganic constituents of biomass feedstocks by mechanical dewatering and leaching. Biomass and Bioenergy 1997;12:241–52. doi:10.1016/S0961-9534(97)00005-6.

[3] De Filippis P, Borgianni C, Paolucci M, Pochetti F. Gasification process of Cuban bagasse in a two-stage reactor. Biomass and Bioenergy 2004;27:247–52. doi:10.1016/J.BIOMBIOE.2003.11.009.

[4] Antonio Bizzo W, Lenço PC, Carvalho DJ, Veiga JPS. The generation of residual biomass during the production of bio-ethanol from sugarcane, its characterization and its use in energy production. Renew Sustain Energy Rev 2014;29:589–603. doi:10.1016/J.RSER.2013.08.056.

[5] Virmond E, De Sena RF, Albrecht W, Althoff CA, Moreira RFPM, José HJ. Characterisation of agroindustrial solid residues as biofuels and potential application in thermochemical processes. Waste Manag 2012;32:1952–61. doi:10.1016/J.WASMAN.2012.05.014.

[6] Yin C-Y. Prediction of higher heating values of biomass from proximate and ultimate analyses. Fuel 2011;90:1128–32. doi:10.1016/J.FUEL.2010.11.031.

[7] Klass DL. Biomass for renewable energy and fuels. Encycl Energy 2004;1:193–212. doi:https://doi.org/10.1016/B0-12-176480-X/00353-3.

[8] Nzihou JF, Hamidou S, Bouda M, Koulidiati J, Segda BG. Using dulong and vandralek formulas to estimate the calorific heating value of a household waste model. Int J Sci Eng Res 2014;5:1878–83.

[9] Parikh J, Channiwala SA, Ghosal GK. A correlation for calculating HHV from proximate analysis of solid fuels. Fuel 2005;84:487–94. doi:10.1016/J.FUEL.2004.10.010.

[10] http://www.jma.go.jp/jma/index.html(in Japanese, accessed on Jun, 2019) n.d.

[11] Teixeira FN, Lora ES. Experimental and analytical evaluation of NOX emissions in bagasse boilers. Biomass and Bioenergy 2004;26:571–7. doi:10.1016/J.BIOMBIOE.2003.08.013.

[12] Japanese Industrial Standards, JIS 0201 1990 Standard Atmosphere n.d.

[13] National Institute of Advanced Industrial Science and Technology, https://www.aist.go.jp/aist_j/press_release/pr2019/pr20190725/pr20190725.html (in Japanese, accessed on Sep, 2019) 2019.

[14] Titiloye JO, Abu Bakar MS, Odetoye TE. Thermochemical characterisation of agricultural wastes from West Africa. Ind Crops Prod 2013;47:199–203. doi:10.1016/J.INDCROP.2013.03.011.

[15] Wakao N, Kaguei S, Funazkri T. Effect of fluid dispersion coefficients on particle-to-fluid heat transfer coefficients in packed beds. Correlation of nusselt numbers. Chem Eng Sci 1979;34:325–36. doi:10.1016/0009-2509(79)85064-2.

[16] Shu L, Berndt CC, Hodzic A. Sugar Cane Bagasse Fibre for Sustainable Manufacturing : An Overview of Applications In: ACUN-5 “Developments in Composites: Advanced, Infrastructual, Natural, and Nano-Composites,” Sydney(Australia): 2006.

[17] Wakao N, Funazkri T. Effect of fluid dispersion coefficients on particle-to-fluid mass transfer coefficients in packed beds. Chem Eng Sci 1978;33:1375–84. doi:https://doi.org/10.1016/0009-2509(78)85120-3.

[18] He W, Lu W, Dickerson J. Gas transport in solid oxide fuel cells. Springer; 2014. doi:10.1007/978-3-319-09737-4.

[19] El-Sayed SA, Mostafa ME-S. Estimation of thermal and kinetic parameters of sugarcane bagasse and cotton stalks dust layers from hot surface ignition tests. Combust Sci Technol 2016;188:1655–73. doi:10.1080/00102202.2016.1193495.

[20] Dixon AG, Cresswell DL. Theoretical prediction of effective heat transfer parameters in packed beds. AIChE J 1979;25:663–76. doi:10.1002/aic.690250413.

[21] Shrivastav S, Hussain I. Design of bagasse dryer to recover energy of water tube boiler in a sugar factory. Int J Sci Res 2013;2:356–8.

[22] Wilke CR. A Viscosity equation for gas mixtures. J Chem Phys 1950;18:517–9. doi:10.1063/1.1747673.

[23] Mason EA, Saxena SC. Approximate formula for the thermal conductivity of gas mixtures. Phys Fluids 1958;1:361–9. doi:10.1063/1.1724352.

Chapter 4 Zeolite Boiler: Testing and design methodology

4.1 Objectives of this chapter

The structure of this dissertation and position of this chapter is shown in **Fig. 4.1**. This chapter focuses on the heat discharging process in the thermochemical energy storage and transport system and develops a heat discharging device namely “Zeolite Boiler”. This chapter aims to establish a designing method of the Zeolite Boiler via demonstrating continuous generation of pressurized steam utilizing steam adsorption of zeolite. The designing method is used in techno-economic analysis described in Chapter 6. To achieve the objective, the following research items are described in this chapter. The structure of this chapter which consists of “Preparation of one-dimensional (1D) numerical simulation of Zeolite Boiler”, “Bench-scale Zeolite Boiler” and “Full-scale Zeolite Boiler in Tanegashima” is shown in **Fig. 4.2**.

Preparation of 1D numerical simulation of Zeolite Boiler

- Investigating adsorption characteristics and formulation of equilibrium and kinetic model (described in **4.4**)
- Investigating heat transfer characteristics of packed bed of zeolite (described in **4.5**)

Bench-scale Zeolite Boiler

- Developing a numerical model to simulate the Zeolite Boiler by combining the above empirical adsorption and heat transfer characteristics of zeolite (described in **4.6.5**)
- A 1/200th scale (bench-scale) Zeolite Boiler was designed when a full-scale Zeolite Boiler in Tanegashima is assumed to supply 0.4 t/h of steam (described in **4.6.2**).
- Demonstrating continuous generation of pressurized steam using a bench-scale test rig of Zeolite Boiler (described in **4.6.6**).
- Validating the developed numerical model to predict the performance of a full-scale Zeolite Boiler (described in **4.6.6**).

Full-scale Zeolite Boiler in Tanegashima

- Clarifying relationship among design parameters of Zeolite Boiler via calculation of the performance characteristics (described in **4.7**).
- Proposal for improving the performance of Zeolite Boiler (described in **4.8**)

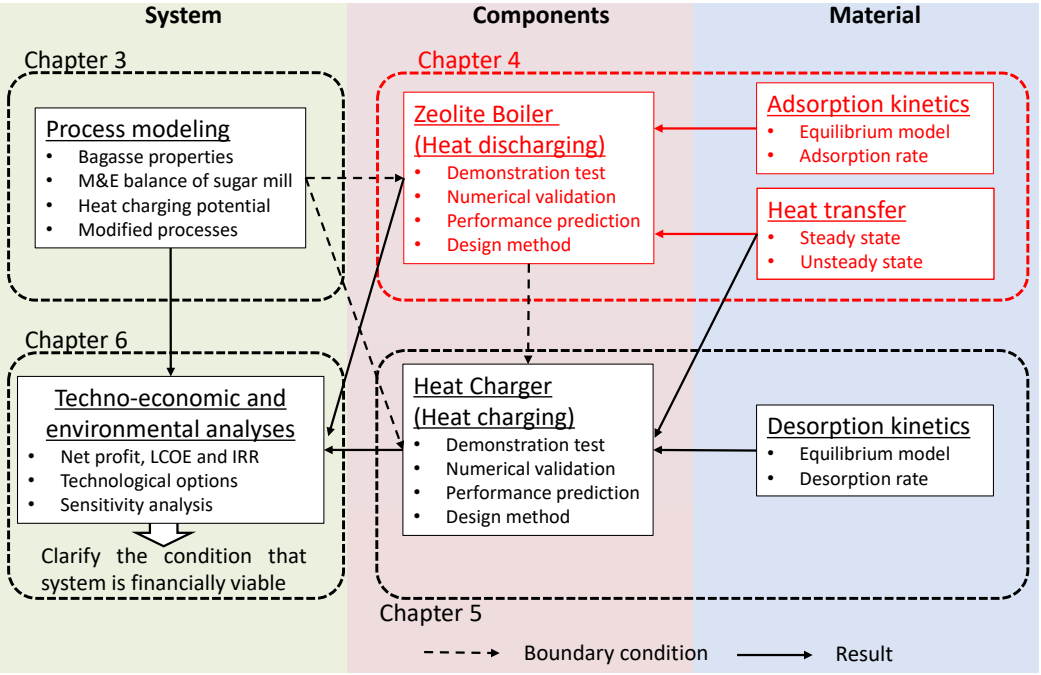

Fig. 4.1. Structure of dissertation and position of this chapter.

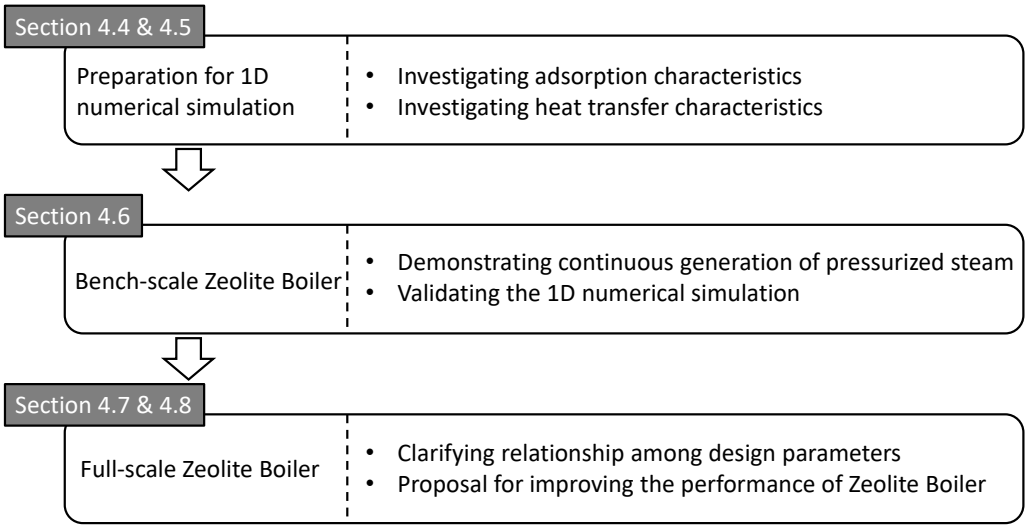

Fig. 4.2. Structure of this chapter.

4.2 Reactor types

The type of adsorption reactor should be carefully selected to meet the requirement of heat demand sites. Reactor types in the thermochemical energy storage system can be classified by employing open or closed chamber of zeolite, fixed or moving bed of zeolite, and direct or indirect heat exchanging types as shown in **Fig. 4.3.** In the closed system, adsorbate water vapor which is evaporated by changing temperature is adsorbed into zeolite packed in the reactor. Adsorption heat is provided to the heat consumers via heat exchanger. This closed system of which the material in the

sealed vessel cannot be replaced easily is not applicable to offsite systems with material transportation. On the other hand, in the open system, steam or humid air is introduced to the zeolite packed bed directly and adsorption heat is transferred to the heat exchanger inside/outside the bed indirectly or to the gas directly as shown in **Fig. 4.3**. This type can adopt both fixed and moving bed type reactor. The heat demands in Tanegashima requires continuous generation of pressurized steam up to 0.2 MPa for their industrial process (mainly for food process) which currently uses heavy-oil fired boilers. In order to generate steam continuously, the open system and moving bed reactor was employed as a conceptual design of heat discharging device.

Heat transfer process has two candidates. The indirect heat exchanging process transfers the adsorption heat through a heat exchanger and there are many practical usages in industry sector. The main problem of the indirect heat exchanging process is a relatively low UA (product of overall heat transfer coefficient and area between the bed and the heat exchanger). Recently, there are many research projects that employed the direct heat exchanging process in which the heat recovery fluid is directly introduced into the packed bed to enhance heat transfer. However, the multiple expensive pressurized chambers are required to provide the pressurized steam continuously in the direct heat exchanging process. While a large UA is sacrificed, the indirect heat exchanging process was employed as a conceptual design of the heat discharging device in this study to avoid the expensive pressurized chambers.

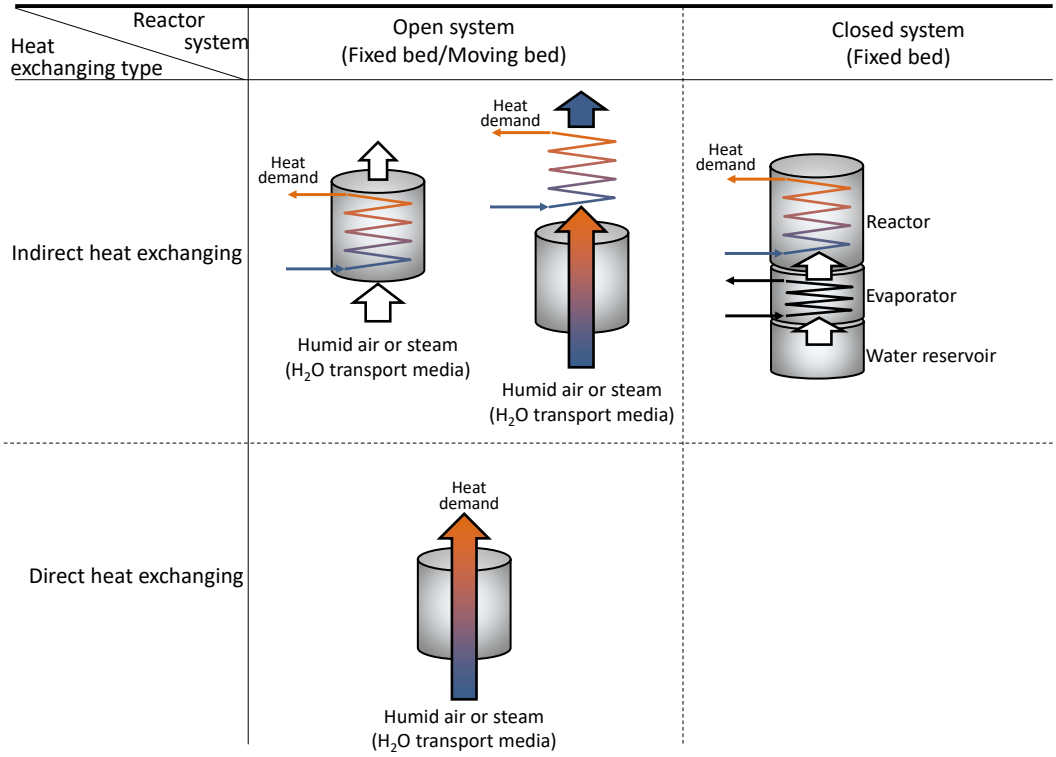

Fig. 4.3. Reactor types of adsorber.

4.3 Conceptual design of “Zeolite Boiler”

Figure 4.4 shows a conceptual design of heat discharging device namely “Zeolite Boiler” which employs moving bed and indirect heat exchanging process. The Zeolite Boiler consists of a non-pressurized cylindrical chamber and a multi-tubular heat exchanger. Steam is employed as an adsorbate of the system. Liquid water adsorption cannot generate > 100 °C steam at pressurized condition in indirect heat exchanging process because the zeolite bed temperature is stuck at evaporation temperature of surrounding water. As an alternative adsorbate, humid air has potential to recover the latent heat of adsorbed water when zeolite adsorbs the vapor in the humid air. However, the large heat capacity of air disperses adsorption heat and thereby bed temperature cannot reach the temperature required in the Zeolite Boiler to provide pressurized steam. Only pure steam adsorption can provide the function to generate > 100 °C steam at pressurized condition. To realize the pure steam adsorption, the Zeolite Boiler must be co-operated with an existing boiler that supplies steam for adsorption. Co-operation with an existing boiler has the other benefit. If the Zeolite Boiler stops due to an unexpected trouble, the existing boiler can continue to supply the process steam without interruption, which can ensure the reliability of the system.

The zeolite externally desorbed by unused heat of bagasse boiler in the sugar mill is supplied from the top of chamber and naturally moves downwards driven by gravity. The velocity of zeolite (mass flow rate of zeolite) is controlled by a particle discharger which is mounted under the bottom of chamber. Saturated steam generated by the existing oil-fired boiler is depressurized to the ambient pressure and injected into the zeolite bed from the top of chamber. Zeolite adsorbs injected steam and generates their adsorption heat which is transferred to the water through the heat exchanger. Water is supplied from the bottom of heat exchanger and flows upwards with evaporation. The Zeolite Boiler can save the fuel consumption of the existing boiler by generating more steam than injection steam.

Total heat output of zeolite and transferred heat to the water, which depends on adsorption kinetics and heat transfer characteristics, determine the fuel saving performance. The equilibrium water uptake and adsorption rate related to the adsorption kinetics, and the heat transfer characteristics were obtained experimentally. They are numerically modeled according to the empirical equations and validated in the following sections.

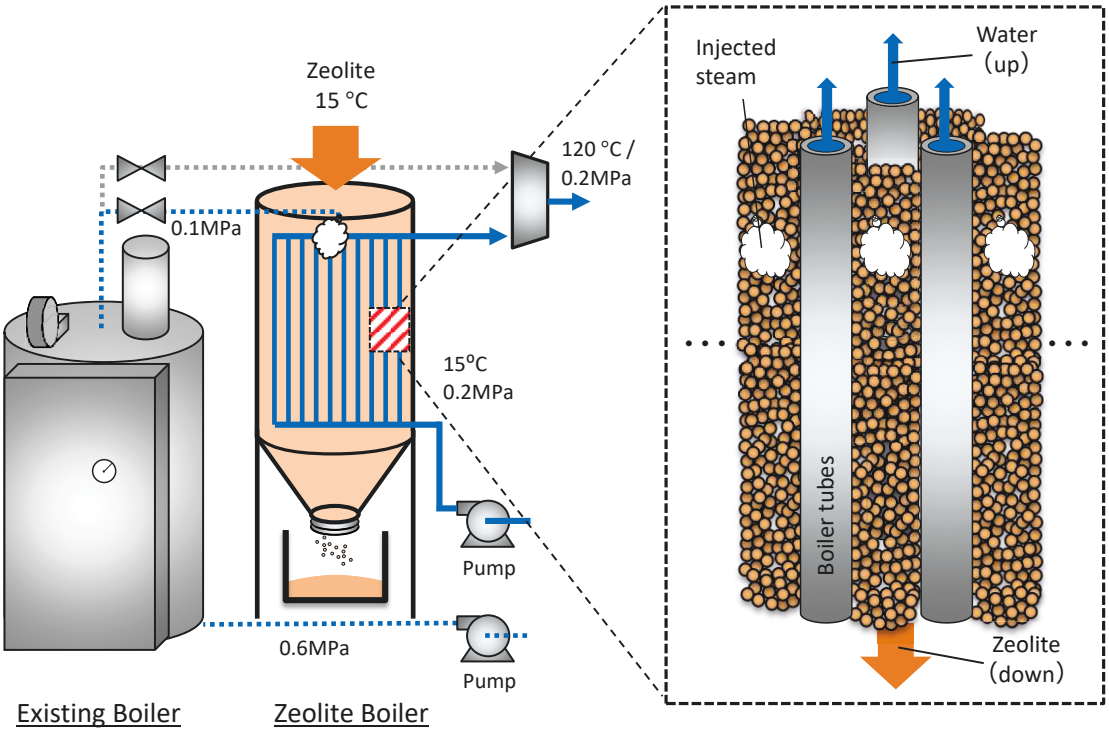

Fig. 4.4. Conceptual design of "Zeolite Boiler".

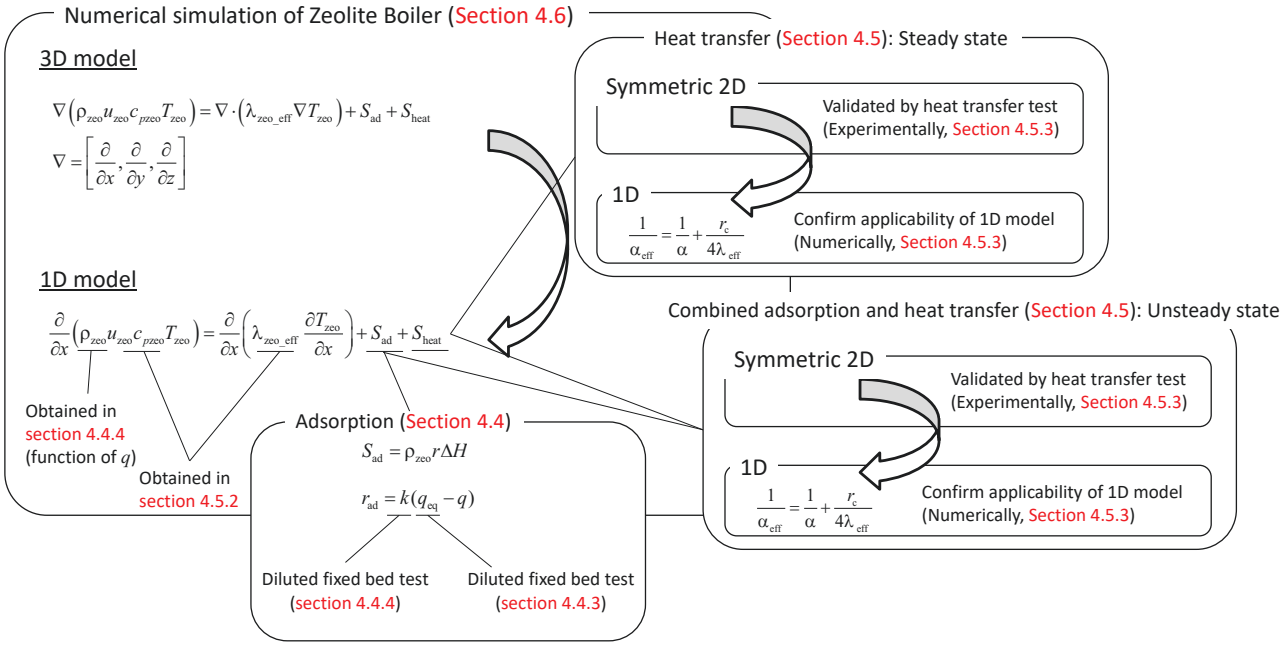

Fig. 4.5. Relationship between each section in preparation of 1D numerical simulation of Zeolite Boiler.

Three-dimensional (3D) models are preferable for a detail design of Zeolite Boiler because accurate results are expected by detailed expression of 3D models. Since the 3D models require more effort and time to compute partial differential equations, reduced dimension models are preferable to overcome the shortcoming as long as the deteriorated result is allowable. Since the heat exchanger tube was distributed symmetrically and uniformly across a large cross-section area of cylindrical chamber of the Zeolite Boiler assuming negligible boundary effect by the insulated chamber wall, a 1D numerical model is applicable to design and analyze behavior of the Zeolite Boiler. Relationship among each section in preparation of numerical simulation of Zeolite Boiler is shown in **Fig. 4.5**.

Two important source terms (adsorption and heat transfer characteristics) in energy conservation equations of Zeolite Boiler determine the performance. Adsorption characteristics was described in **4.4**. Equilibrium water uptake on zeolite was obtained by diluted fixed bed test experimentally and was formulated by the literature model. A kinetic model was included in a 1D numerical model and was evaluated by comparing to the experimental data. Heat transfer characteristics was described in **4.5**. Temperature distribution of cylindrical packed bed of zeolite under steady state was measured and modelled by a symmetric cylindrical two-dimensional (2D) model. Applicability of the 1D overall heat transfer model considering radial effective thermal conductivity was confirmed by comparing the 2D model with the 1D model of the fixed bed test. A combined 1D numerical model of adsorption and heat transfer characteristics was experimentally validated by unsteady heat transfer test.

The 1D model including empirical adsorption and heat transfer characteristics was used for the simulation of the bench-scale and the full-scale Zeolite Boiler in **4.6 ~ 4.8**.

4.4 Adsorption characteristics

4.4.1 Material selection

The commercial zeolite of 13X type (purchased from Tosoh cooperation, nominal water uptake: >0.25 kg/kg and nominal density: 790 ±30 kg/m^3) was selected as heat storage material because of a large water uptake capacity. The diameter of zeolite particle was selected carefully from the viewpoint of internal temperature distribution and pressure drop of the bed. Generally, larger diameter of zeolite reduces pressure drop of the bed, while concentric temperature distribution inside the particle disturbs overall heat transfer and vice versa. The maximum diameter of particle was selected in the range that Biot number is less than 1.0, which can neglect the temperature distribution inside particles. In the Zeolite Boiler, the heat transfer coefficient between injected steam and zeolite takes a value from roughly 30 to 100 W/(m^2·K) because of a small Reynolds number. In contrast in the heat charging device, relatively higher heat transfer coefficient up to roughly 250 W/(m^2·K) is expected because of a large Reynolds number caused by high flow rate of drying hot air. Inherent thermal conductivity of zeolite is about 0.2 ~ 0.4 W/(m·K). Mesh 9 ~ 14 of zeolite, which corresponds to φ_{zeo} =1.18 mm ~ 2.00 mm, was selected considering < 1.0 Biot number in the case of φ_{zeo} =2.0 mm and

250 W/(m^2·K) of the heat transfer coefficient. Assuming that particle diameter distribution follows gaussian distribution, the representative diameter of particle in this study was given as 1.6 mm.

4.4.2 Diluted fixed bed test

Adsorption kinetics relates to equilibrium water uptake and adsorption rate. To evaluate these values under isothermal condition, a diluted fixed bed test was conducted.

The schematic of experimental apparatus of diluted fixed bed test is shown in **Fig. 4.6**. The experimental apparatus consists of mainly adsorber unit and humidity control unit. The diameter and length of stainless tube of adsorber were 3/4-inch and 220 mm, respectively. From the top to 50 mm in length, only alumina ball (φ = 2.0 mm) was packed as the pre-heating zone of inlet gas. In the following section of pre-heating zone, 4.92 g of zeolite and 59.5 g of alumina ball were randomly packed together with 170 mm height. Packing the alumina ball which is inert to water vapor can dilute zeolite and disperse its adsorption heat, which enables to obtain the adsorption characteristics under isothermal condition. A K-type thermocouple was embedded in the middle of the adsorber and measured bed temperature. Dried air was supplied from a gas cylinder and the flow rate was controlled by the mass flow controller (KOFLOC, FLOW COMPO MODEL 3660). Vapor pressure was controlled by changing water temperature of the bubbler unit. Humidified air was heated in the pipeline by a ribbon heater at intended temperature. The heated humidified air was sent to the dew point sensor (Rotoronic Hygroflex model HF53) via the bypass line and the dew point was measured. After the dew point of humidified air stabilized within ±0.1 °Cdp and was converted to the inlet vapor pressure, the humidified air was introduced to the adsorber by switching the valve 3 and 4.

The change in the bed temperature and outlet vapor pressure through a typical experimental run are shown in **Fig. 4.7**. By switching the valve from bypass line to the adsorber, the dew point sensor measured the outlet vapor pressure of adsorber. The outlet vapor pressure sharply decreased due to temporal lack of vapor. After the zeolite reached equilibrium adsorption, the water vapor in the humidified air slipped without adsorption and thereby outlet vapor pressure resumed. The equilibrium water uptake under the intended relative humidity was given by integrating the change in outlet water vapor pressure during adsorption process. Once outlet vapor pressure resumed to the inlet value, temperature of the bed and inlet gas were simultaneously cooled down to the next intended temperature. The equilibrium water uptake increased corresponding to increase in the relative humidity at cooled temperature. The zeolite adsorbed additional water vapor according to the equilibrium adsorption line, therefore the outlet vapor pressure decreased again by additional adsorption. The result of equilibrium water uptake obtained from an experimental run is shown in **Fig. 4.8**. The equilibrium water uptake at 200 °C was calculated by adding the integral water uptake in the step 2 to that in the step 1. By repeating this procedure with cooling the bed temperature stepwise, the equilibrium water uptake at each relative humidity was obtained.

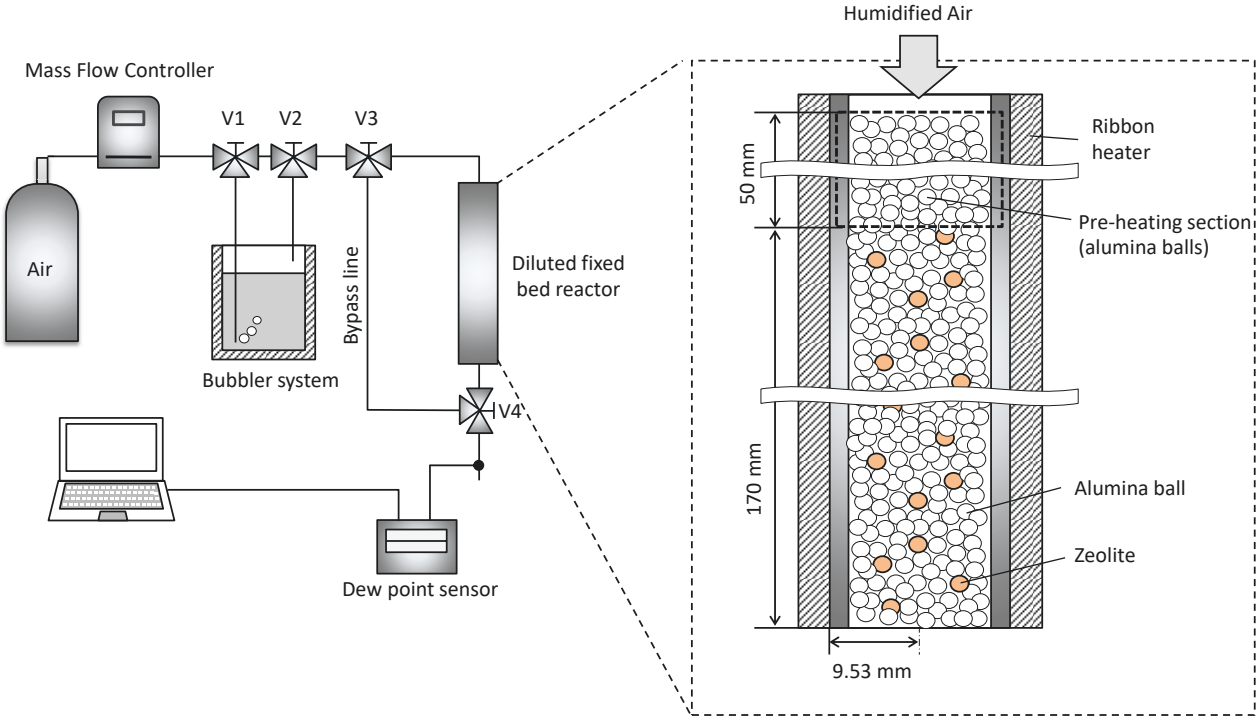

Fig. 4.6. Experimental apparatus of diluted fixed bed test.

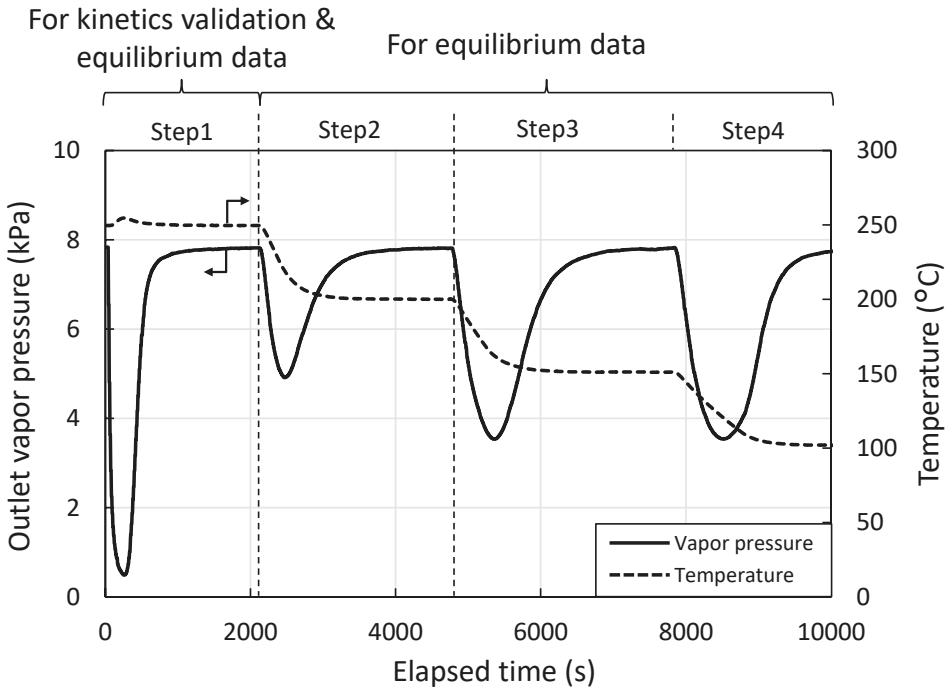

Fig. 4.7. Change in outlet vapor pressure and temperature change during adsorption.

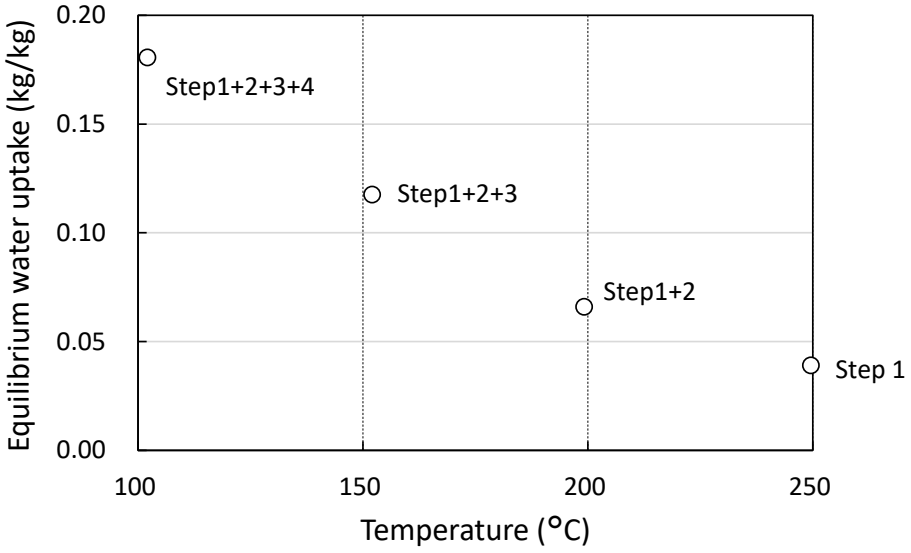

Fig. 4.8. Adsorption isobars obtained from Run 1.

All the experimental conditions and results of equilibrium water uptake are shown in **Table 4.1**. Since the bubbler system in this experimental setup was controlled stably under the 40 °Cdp of dew point, vapor pressures were set at 7.8, 5.9 and 4.3 kPa corresponding to the dew point of 40, 35, and 30 °Cdp, respectively. Experimental runs were categorized into higher temperature range (250 °C to 100 °C, relative humidity is 0.001 to 0.07) and lower temperature range (100 °C to 45 °C, relative humidity is 0.04 to 0.76) because equilibrium water uptakes of zeolite 13X are significantly different from each temperature range.

4.4.3 Equilibrium adsorption model

The experimental result of equilibrium water uptake and predicted data by the equilibrium model which is described as follows, are shown in **Fig. 4.9**. The experimental result was summarized in adsorption isobars because this experiment was conducted at a constant inlet vapor pressure with changing temperature. The equilibrium water uptake rapidly increased in the range of higher relative humidity because of condensation of water vapor (capillary effect). Dubinin-Astakhov model is widely used for the equilibrium water uptake on zeolite, which is based on the micropore filling theory [1]. However, the D-A model cannot simulate the capillary effect properly, the following model including Freundlich term into the Dubinin-Astakhov model was employed to predict the experimental result considering the capillary effect.

$$W_{\mathrm{eq}} = K\left(\frac{p_{\mathrm{s}}}{p_{\mathrm{sat}}}\right)^{n'} + W_{\max}\exp\left\{-\left(\frac{A_{\mathrm{ad}}}{E}\right)^{n}\right\} \tag{4.1}$$

where W_{eq} , A_{ad} and E are volumetric equilibrium water uptake on zeolite, adsorption potential and interaction energy, respectively. The A_{ad} is calculated by **Eq. (4.2)**;

$$A_{ad} = R_w T_{zeo} \ln\left(\frac{p_{sat}}{p_s}\right) \tag{4.2}$$

Table 4.1. Experimental conditions and results of diluted fixed bed test.

	Run	Step	Experimental conditions			Results
			Reactor temperature (°C)	Inlet vapor pressure (kPa)	Relative humidity (-)	Water uptake (kg/kg)
Higher temperature range	Run 1	S1	249.6	7.83	0.0020	0.040
		S2	200.1	7.82	0.0051	0.067
		S3	151.1	7.81	0.0155	0.121
		S4	101.9	7.83	0.0717	0.183
	Run 2	S1	250.1	5.88	0.0015	0.037
		S2	203.8	5.86	0.0035	0.059
		S3	154.0	5.88	0.0111	0.109
		S4	102.1	5.88	0.0538	0.181
	Run 3	S1	249.8	4.26	0.0010	0.031
		S2	199.3	4.23	0.0028	0.052
		S3	148.7	4.26	0.0093	0.100
		S4	104.7	4.23	0.0354	0.158
Lower temperature range	Run 4	S1	100.2	7.85	0.0768	0.181
		S2	71.6	7.83	0.2342	0.209
		S3	59.7	7.84	0.3986	0.222
		S4	46.3	7.80	0.7671	0.261
	Run 5	S1	99.3	5.90	0.0596	0.179
		S2	73.6	5.87	0.1614	0.205
		S3	60.9	5.83	0.2804	0.216
		S4	43.8	5.85	0.6489	0.243
	Run 6	S1	99.3	4.35	0.0440	0.181
		S2	74.2	4.33	0.1161	0.208
		S3	59.7	4.33	0.2201	0.223
		S4	43.1	4.34	0.4987	0.241

The unknown parameters (E, n, W_{max}, K, n') were fitted to the experimental data using non-linear square fitting, which were resulted in E = 1072 kJ/kg, n =1.73, W_{max} = 237.2 mL/kg, K =104.4 and n'=4.9, respectively. The mass specific equilibrium water uptake can be calculated by **Eq. (4.3)** using the volumetric equilibrium water uptake.

$$q_{eq} = \rho_{ad} W_{eq} \tag{4.3}$$

The density of adsorbed water was correlated by **Eq. (4.4)** [2];

$$\rho_{ad} = \rho_{w-10°C} \left\{1 - 3.781 \times 10^{-4} \times (T_{zeo} - 283.15)\right\} \tag{4.4}$$

As shown in **Fig. 4.9**, the Freundlich-Dubinin-Astakhov model can simulate experimental data in the all range of relative humidity.

The isosteric adsorption heat obtained by TG-DTA (Thermo Gravimetry - Differential Thermal Analysis) is shown in **Fig. 4.10**. The isosteric adsorption heat decreases corresponding to increase in the water uptake. This tendency was observed in the experimental data, while the range of experimental data is limited to the higher water uptake range. This study predicted the isosteric adsorption heat by the logarithmic approximation of literature data [3].

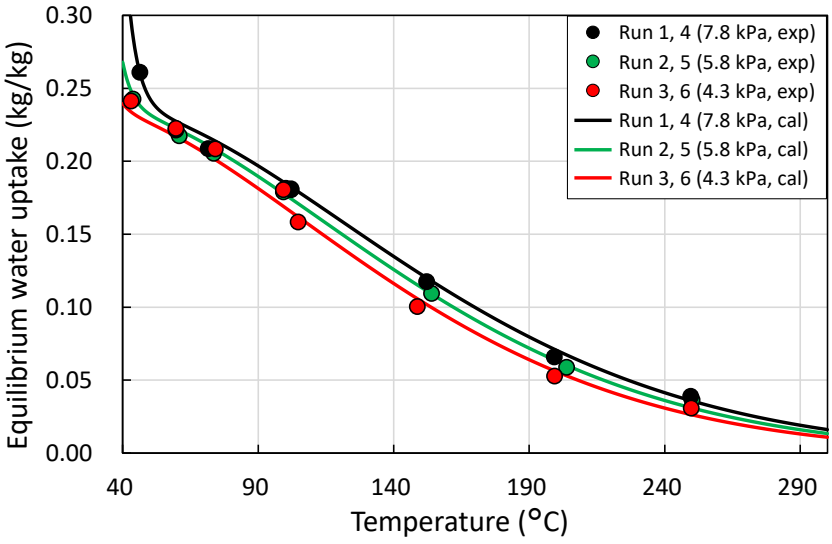

Fig. 4.9. Adsorption isobars.

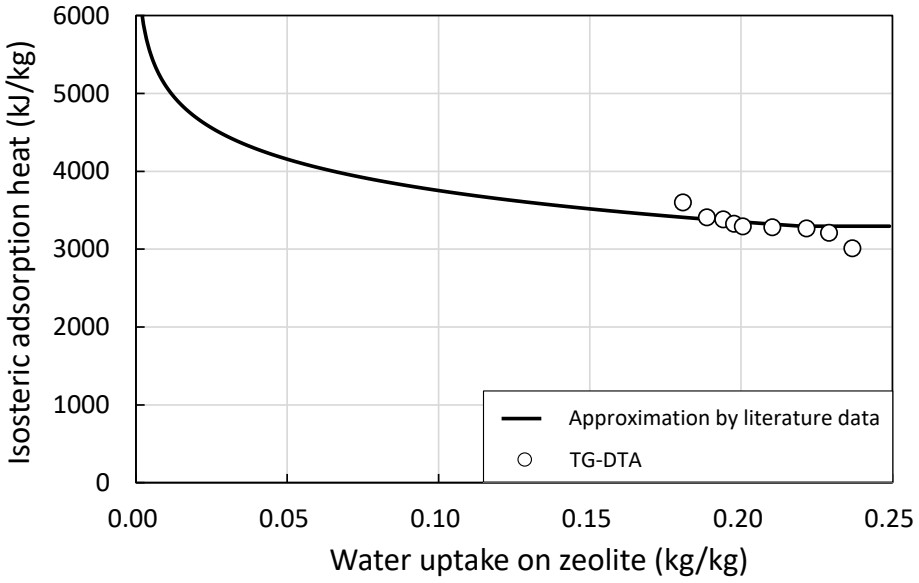

Fig. 4.10. Isosteric adsorption heat as a function of water uptake on zeolite.

4.4.4 Kinetic model

Adsorption rate data should be obtained under isothermal condition. To ensure the adsorption test at the intended constant temperature, the diluted fixed bed was employed to disperse adsorption heat of zeolite through the heat capacity of the surrounding alumina ball. Nevertheless, a certain degree of temperature increase was observed especially during the first adsorption step of each run though. **Table 4.2** shows the maximum bed temperature during adsorption. Temperature increase up to 11 °C was observed especially in the lower temperature condition giving a larger water uptake. **Table 4.2** also shows the equilibrium water uptake calculated by the F-D-A model described in **4.4.3** at both initial and maximum bed temperature during adsorption. The effect of temperature increase during adsorption is negligible because of less than 10% of error in water uptake. The adsorption kinetic model was evaluated using the experimental result of step 1 of each run under the isothermal condition.

To evaluate the adsorption rate of zeolite 13X, a 1D unsteady numerical model was built on a commercial software COMSOL Multiphysics 5.3a®. The mass conservation equations for zeolite and gas can be expressed by **Eqs. (4.5)** and **(4.6)**.

$$\frac{\partial \rho_{zeo}}{\partial t} = \rho_{zeo0} r_{ad} \tag{4.5}$$

$$\frac{\partial}{\partial t}\left(\varepsilon_b \rho_g\right) + \frac{\partial}{\partial x}\left(\rho_g u_g\right) = -\rho_{zeo0} r_{ad} \tag{4.6}$$

Table 4.2. Temperature increase and equilibrium water uptake during the 1st step adsorption in diluted fixed bed test.

Test	Initial Temperature T_0 (°C)	Equilibrium water uptake at T_0 (kg/kg)	Maximum temperature $T_{\max}$ (°C)	Equilibrium water uptake at $T_{\max}$ (kg/kg)	Error (%)
R1S1	249.6	0.0360	254.8	0.0333	7.4%
R2S1	250.1	0.0308	254.4	0.0289	6.5%
R3S1	249.8	0.0262	253.4	0.0247	5.8%
R4S1	100.2	0.1847	111.0	0.1714	7.3%
R5S1	99.3	0.1780	108.1	0.1668	6.4%
R6S1	99.3	0.1694	110.3	0.1557	8.2%

where r_{ad} can be discretized as the following equation based on LDF (Linear Driving Force) model [4].

$$r_{\mathrm{ad}} = k_{\mathrm{LDF}}(q_{\mathrm{eq}} - q) \tag{4.7}$$

Overall mass transfer coefficient k_{LDF} consists of three resistances which are mass transfer through the gas film on zeolite particles, diffusion resistances into macro pore and micro pore. Generally, the micro pore resistance is negligible because of immediate adsorption in the micro pore [5]. The first term and second term of the following equation express the mass transfer resistance in gas film and macro pore diffusion resistance, respectively.

$$\frac{1}{k_{\mathrm{LDF}}} = \frac{r_{\mathrm{p}}}{3k_{\mathrm{f}}(1-\varepsilon_{\mathrm{b}})} \cdot \frac{\rho_{\mathrm{zeo}} R T_{\mathrm{zeo}} q_{\mathrm{eq}}}{p_s} + \frac{r_{\mathrm{p}}^{\,2}}{15\varepsilon_{\mathrm{pore}}(1-\varepsilon_{\mathrm{b}})D_{\mathrm{eff}}} \cdot \frac{\rho_{\mathrm{zeo}} R T_{\mathrm{zeo}} q_{\mathrm{eq}}}{p_{\mathrm{s}}} \tag{4.8}$$

where the mass transfer coefficient k_{f} in gas film can be described by **Eq. (4.9)** analogous to heat transfer [6].

$$Sh = \frac{k_{\mathrm{f}} d_{\mathrm{p}}}{D_{\mathrm{m}}} = 2.0 + 1.1 Re_{\mathrm{p}}^{\,0.6} Sc^{1/3} \tag{4.9}$$

where D_{m} is the molecular diffusivity of gas which can be described by **Eq. (4.10)**.

$$D_{\mathrm{m}} = \frac{1.8583\times10^{-7}\times T_{\mathrm{g}}^{1.5}}{p d_{\mathrm{co}}{}^{2}\Omega}\left(\frac{1}{M_{\mathrm{s}}}+\frac{1}{M_{\mathrm{a}}}\right)^{0.5} \tag{4.10}$$

The effective diffusivity D_{eff} can be expressed by **Eq. (4.11)** using the molecular diffusivity D_{m} and Knudsen diffusivity D_{kn}.

$$D_{\mathrm{eff}} = \tau\left(\frac{1}{D_{\mathrm{m}}}+\frac{1}{D_{\mathrm{kn}}}\right) \tag{4.11}$$

The Knudsen diffusivity can be expressed by **Eq. (4.12)**.

$$D_{\mathrm{kn}} = \frac{d_{\mathrm{pore}}}{3}\left(\frac{8R_{\mathrm{g}}T_{\mathrm{g}}}{\pi M_{\mathrm{s}}}\right)^{0.5} \tag{4.12}$$

Pore diameter d_{pore} was obtained by the mercury porosimetry. The result of pore diameter distribution is shown in **Fig. 4.11**. The mode diameter of 181 nm was employed as the representative diameter. The pore volume was measured as 0.201 cc/g.

Particle density, particle porosity and bed porosity were given by experimental data. Sample of zeolite was heated up to 500 °C by 10 °C/min in the TG-DTA to completely desorb the adsorbed water in the zeolite. The particle density was calculated by the weight of dried zeolite and volume of particle, resulted in 1295 kg/m^3 ±100 kg/m^3 (7.7% of error, weighted average value by three times measurements). The particle porosity was calculated by the porous capacity, which resulted in 0.26.

The bed porosity in a cylindrical container inherently has a radial distribution and increases drastically around the wall, which can be given by **Eq. (4.13)** found in the literature [7].

$$\varepsilon_{\mathrm{b}}(r) = \varepsilon_{\mathrm{b}}\left\{1+1.36\exp\left(-5.0\frac{r_{\mathrm{c}}-r}{d_{\mathrm{p}}}\right)\right\} \tag{4.13}$$

The bed porosity was measured by packing the dried zeolite into stainless tubes with different inner diameter of 15.8 mm, 21.2 mm and 54.5 mm. **Table 4.3** shows the result of measured bed density and calculated bed porosity of each stainless tube. The smaller diameter tube has higher porosity due to the effect of the wall. The representative bed porosity ε_{b} was 0.4, which was determined as the volumetric average of experimental data and correspond to the bed density of 774 kg/m^3. These

representative bed porosity and density are used in the numerical simulation of Zeolite Boiler in this chapter and Heat Charger in Chapter 5.

The mass transfer resistance through the gas film and macro pore diffusion resistance were calculated using the obtained parameters which are mentioned above. The tortuosity which determines effective diffusivity was assumed to be 4.0. The mass transfer resistance through the gas film is 1/13 ~ 1/14 of macro pore diffusion resistance in the all conditions. Therefore, only the macro pore diffusion resistance was considered to simulate the adsorption rate neglecting other two terms.

Table 4.3. Bed density and porosity.

Chamber diameter	Bed density (kg/m^3) (Experimentally obtained)	Porosity (Experimentally obtained)	The bed porosity ε_b (Fitted data)
15.8 mm	722	0.442	0.400
21.2 mm	740	0.429	0.397
54.5 mm	752	0.419	0.406

The steam conservation equation in the diluted fixed bed test can be expressed by **Eq. (4.14)**.

$$\frac{\partial}{\partial t}\left(\varepsilon_b \rho_s\right)+\frac{\partial}{\partial x}\left(\rho_s u_g\right)=\frac{\partial}{\partial x}\left(D_{ax}\frac{\partial \rho_s}{\partial x}\right)-\rho_{zeo0} r_{ad} \tag{4.14}$$

The axial effective diffusivity of packed bed can be calculated by **Eq. (4.15)** [6].

$$D_{ax}=0.7D_m+\frac{0.5u_g d_p}{\varepsilon_b} \tag{4.15}$$

The boundary conditions for the simulation were shown as follows.

$$\rho_s=\rho_{s0}(x=0),\ \frac{\partial \rho_s}{\partial x}=0\ (x=L),\ \rho_s=\rho_{s0}\ (t=0),\ q=q_0\ (t=0) \tag{4.16}$$

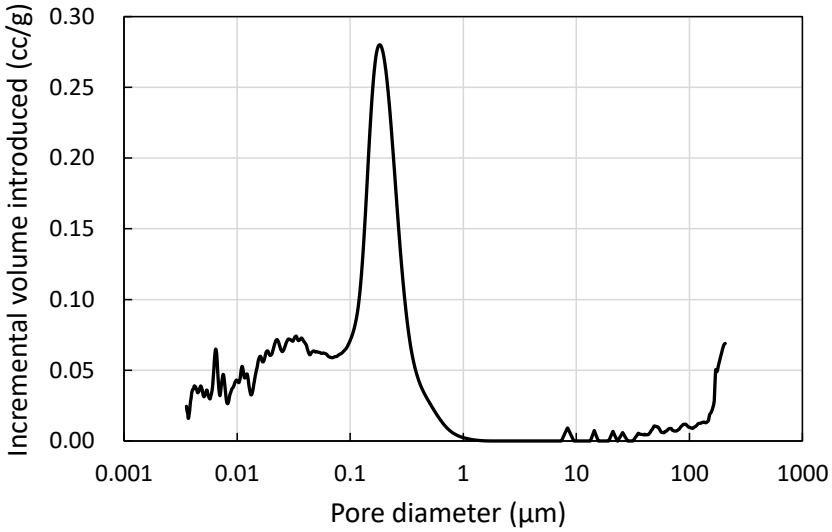

Fig. 4.11. Result of pore size distribution.

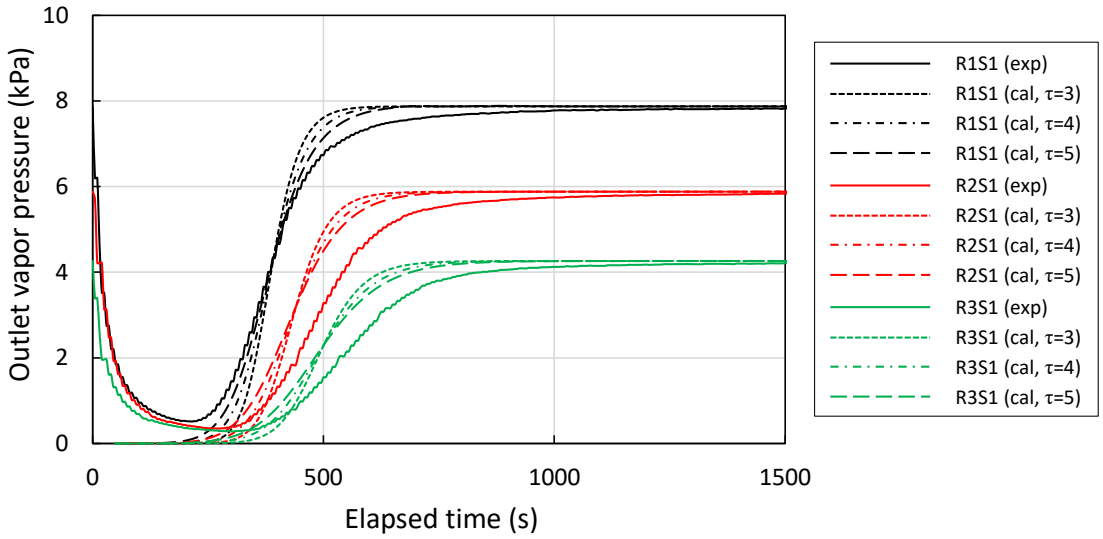

Fig. 4.12. Experimental and numerical analysis results of diluted fixed bed test under lower relative humidity.

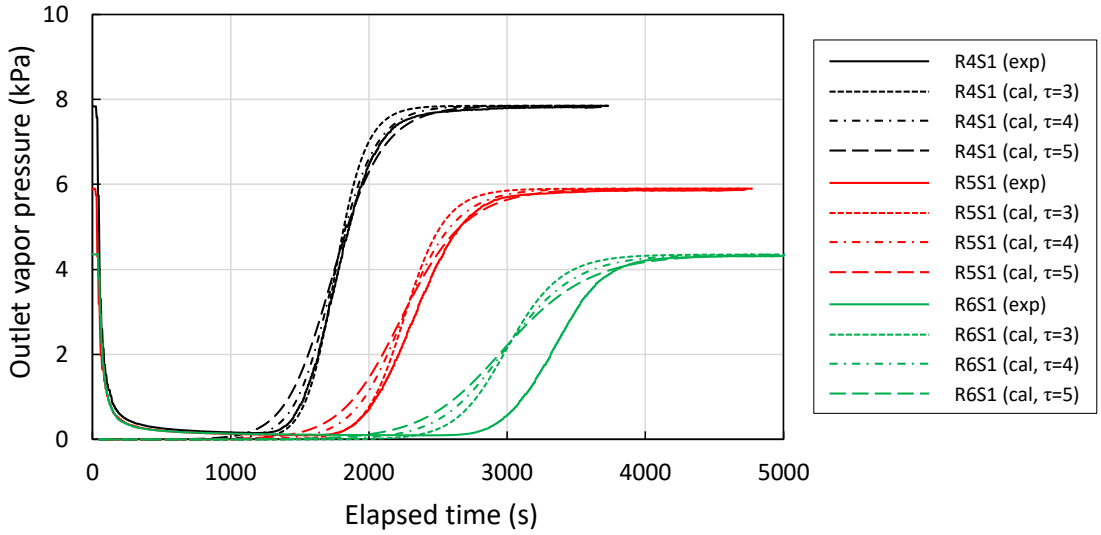

Fig. 4.13. Experimental and numerical analysis result of diluted fixed bed test under higher relative humidity.

The experimental and numerical analysis results of change in outlet vapor pressure of higher temperature conditions (R1S1, R2S1 and R3S1), and those of lower temperature conditions (R4S1, R5S1 and R6S1) with elapsed time are shown in **Figs. 4.12** and **4.13** respectively. The only unknown parameter in the model was the tortuosity of zeolite particle which was difficult to be measured experimentally. The range of tortuosity of silica-alumina was reported from 2.1 to 5.7 [8]. The simulation was conducted assuming different tortuosity of 3.0, 4.0 and 5.0. The tortuosity gives little impact on the numerical analysis result, and tortuosity of 4.0 was selected, which has the best agreement with the experimental result.

4.5 Heat transfer characteristics

4.5.1 Experimental setup

The heat transfer characteristics affect the performance of Zeolite Boiler as well as the adsorption kinetics. In this section, the heat transfer characteristics in the packed bed was measured experimentally under steady and unsteady condition. While the conceptual design of Zeolite Boiler employs moving bed as shown in **Fig. 4.4**, the fixed bed heat transfer model is applicable for the Zeolite Boiler because the velocity of zeolite was quite slow (< 50 mm/min). To obtain the heat transfer characteristics experimentally, an experimental apparatus of fixed bed adsorber was built.

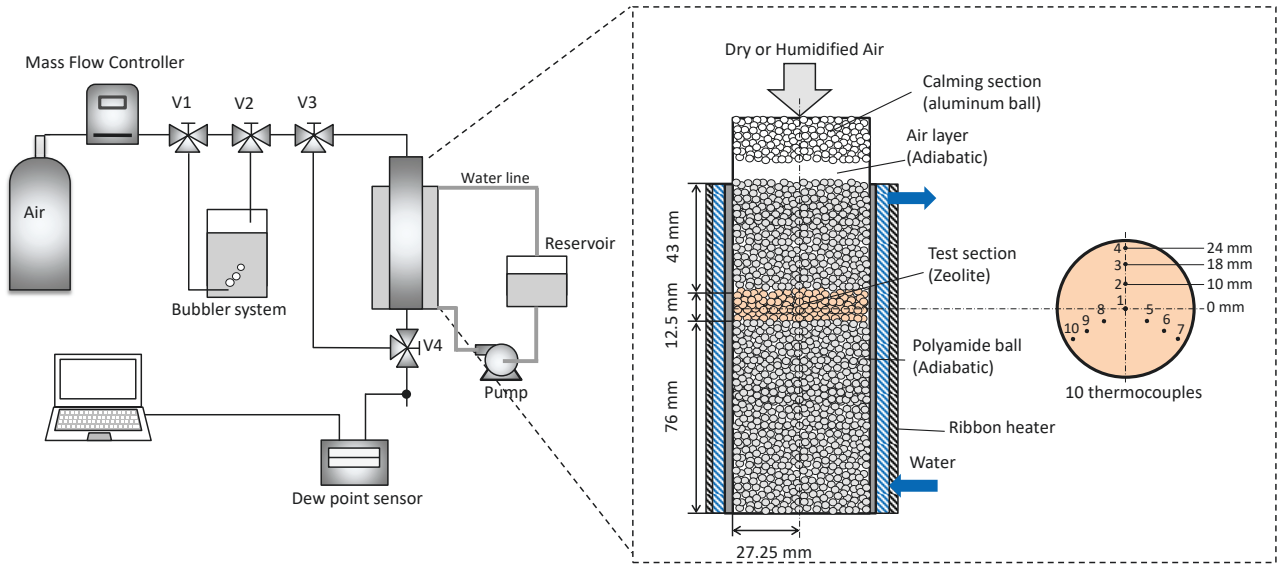

Fig. 4.14. Experimental apparatus of heat transfer test.

The schematic of experimental apparatus of the heat transfer test is shown in **Fig. 4.14**. The reactor had double tube configuration and water was circulated by a pump in the outer tube of the reactor to keep the wall at a constant temperature. The gas supplying system and the humidity control unit were the same as the diluted fixed bed test. The inner diameter and thickness of wall of stainless reactor are 54.5 mm and 3.0 mm, respectively. In the reactor, φ = 2 mm alumina ball was packed in the top section as a calming section which makes introduced gas plug flow. In the test section, 21.9 g of zeolite was packed in a height of 12.5 mm between polyamide ball (thermal conductivity is 0.25 W/(m·K)) bed which was intended to adiabatic condition. The heights of polyamide ball bed on and under the test section were 43 mm and 76 mm, respectively. Total 10 thermocouples were embedded concentrically as shown in **Fig. 4.14** and measured the radial temperature distribution of zeolite bed. One of the 10 thermocouples measured the center temperature of the bed and 3 thermocouples were embedded at 10, 18 and 24 mm from the center on azimuth of every 120 °. The dew point of outlet gas was measured by the same dew point sensor used in the diluted fixed bed test.

Before the testing for unsteady behavior with adsorption heat, the temperature distribution under steady state was measured by introducing dried gas to the reactor. The inlet gas temperature and circulated water temperature were set to 60 and 40 °C, respectively. After temperatures of all measuring points were stabilized within ± 0.5 °C, the temperature distribution was recorded for 30 minutes as a steady state data. In the Zeolite Boiler, Reynolds number around the particle is below 10, and the gas flow rate of the heat transfer test was controlled to realize that value shown in **Table 4.4**.

Table 4.4. Experimental conditions of steady state heat transfer test.

Test number		1	2	3
Volumetric flow of dried air	(ccm)	6395	8342	9676
Inlet temperature of gas	(°C)	57.5	58.5	59.0
Initial temperature of zeolite bed	(°C)	40.6	40.7	40.8
Reynolds number	(-)	3.79	4.92	5.69

Next, both temperatures of the introduced gas and the circulated water were set to 90 °C and the zeolite packed in the reactor was desorbed at 90 °C for over 8 hours. After the desorption treatment, both temperatures of adsorber and inlet gas were changed to 70 °C. Concurrently, the humidified air of which the dew point was controlled by the bubbler unit passed through the bypass line to be ready to supply to the reactor. After confirming that the dew point of humidified air was stabilized (the same procedure as diluted fixed bed test, see **4.4.2**), the humidified air was introduced to the reactor by quickly switching both the valve 3 and 4, and the temperature distribution in the bed and the dew point of outlet of reactor were logged simultaneously until the end of adsorption. The water uptake during the adsorption process was calculated by integration of change in outlet vapor pressure. Assuming equilibrium condition at the temperature and vapor pressure at the end of the test, the equilibrium water uptake was obtained employing the Freundlich-Dubinin-Astakhov model which was validated in **4.4.3**, and thereby the initial water uptake of zeolite before the test was calculated by subtracting the integrated water uptake from the equilibrium water uptake. **Table 4.5** summarizes the experimental conditions.

Table 4.5. Experimental conditions of unsteady state heat transfer test.

Volumetric flow of dried air	(ccm)	6396
Inlet temperature of gas	(°C)	71.3
Initial water uptake on zeolite before adsorption	(kg/kg)	0.032
Inlet vapor pressure of gas	(kPa)	7.433

4.5.2 Numerical model

To analyze the heat transfer characteristics obtained by the test, the cylindrical symmetric 2D simulation model was built on COMSOL Multiphysics 5.3a®. The mass conservation equation of zeolite can be expressed by **Eq. (4.17)**. The continuous equations of gas in zeolite bed and polyamide ball bed can be expressed by **Eqs. (4.18)** and **(4.19)**, respectively.

$$\frac{\partial \rho_{zeo}}{\partial t} = \rho_{zeo0} r_{ad} \tag{4.17}$$

$$\frac{\partial}{\partial t}\left(\varepsilon_{b\_zeo}\rho_g\right) + \frac{\partial}{\partial z}(\rho_g u_g) = -\rho_{zeo0} r_{ad} \tag{4.18}$$

$$\frac{\partial}{\partial t}\left(\varepsilon_{b\_po}\rho_g\right) + \frac{\partial}{\partial z}(\rho_g u_g) = 0 \tag{4.19}$$

The steam conservation equations for zeolite bed and polyamide ball bed can be expressed by **Eqs. (4.20)** and **(4.21)**.

$$\frac{\partial}{\partial t}\left(\varepsilon_{b\_zeo}\rho_s\right) + \frac{\partial}{\partial z}(\rho_s u_g) = \frac{1}{r}\frac{\partial}{\partial r}\left(D_{m\_zeo}\frac{\partial \rho_s}{\partial r}\right) + \frac{\partial}{\partial z}\left(D_{ax\_zeo}\frac{\partial \rho_s}{\partial z}\right) - \rho_{zeo0} r_{ad} \tag{4.20}$$

$$\frac{\partial}{\partial t}\left(\varepsilon_{b\_po}\rho_s\right) + \frac{\partial}{\partial z}(\rho_s u_g) = \frac{1}{r}\frac{\partial}{\partial r}\left(D_{m\_po}\frac{\partial \rho_s}{\partial r}\right) + \frac{\partial}{\partial z}\left(D_{ax\_po}\frac{\partial \rho_s}{\partial z}\right) \tag{4.21}$$

The energy conservation equations of both zeolite and polyamide ball bed can be expressed by **Eqs. (4.22)** and **(4.23)**, respectively.

$$\begin{aligned}&\frac{\partial}{\partial t}\left(\rho_{zeo} c_{pzeo} T_{zeo}\right)\\ &= \frac{1}{r}\frac{\partial}{\partial r}\left(\lambda_{zeo\_eff}\frac{\partial T_{zeo}}{\partial r}\right) + \frac{\partial}{\partial z}\left(\lambda_{zeo\_eff}\frac{\partial T_{zeo}}{\partial z}\right) - \frac{6(1-\varepsilon_{b\_zeo})\alpha_{g\text{-}zeo}}{d_{p\_zeo}}(T_{zeo} - T_g) + \rho_{zeo0} r_{ad}\Delta H\end{aligned} \tag{4.22}$$

$$\begin{aligned}&\frac{\partial}{\partial t}\left(\rho_{po} c_{ppo} T_{po}\right)\\ &= \frac{1}{r}\frac{\partial}{\partial r}\left(\lambda_{po\_eff}\frac{\partial T_{po}}{\partial r}\right) + \frac{\partial}{\partial z}\left(\lambda_{po\_eff}\frac{\partial T_{po}}{\partial z}\right) - \frac{6(1-\varepsilon_{b\_po})\alpha_{g\text{-}po}}{d_{p\_po}}(T_{po} - T_g)\end{aligned} \tag{4.23}$$

The energy conservation equations of gas in both zeolite bed and polyamide ball bed can be expressed by **Eq. (4.24)**.

$$\frac{\partial}{\partial t}\left(\varepsilon_{\mathrm{b\_(zeo,po)}}\rho_{\mathrm{g}}c_{p\mathrm{g}}T_{\mathrm{g}}\right)+\frac{\partial}{\partial z}\left(\rho_{\mathrm{g}}u_{\mathrm{g}}c_{p\mathrm{g}}T_{\mathrm{g}}\right)$$
$$=\frac{1}{r}\frac{\partial}{\partial r}\left(\lambda_{\mathrm{gr\_eff\_(zeo,po)}}\frac{\partial T_{\mathrm{g}}}{\partial r}\right)+\frac{\partial}{\partial z}\left(\lambda_{\mathrm{gax\_eff\_(zeo,po)}}\frac{\partial T_{\mathrm{g}}}{\partial z}\right)-\frac{6(1-\varepsilon_{\mathrm{b\_(zeo,po)}})\alpha_{\mathrm{g\text{-}(zeo,po)}}}{d_{\mathrm{p\_(zeo,po)}}}(T_{\mathrm{g}}-T_{\mathrm{(zeo,po)}}) \tag{4.24}$$

The specific heat capacity of dried zeolite was obtained by adiabatic calorimetry in the range of 0 to 300 °C. The result of specific heat capacity of dried zeolite was shown in **Fig. 4.15**. The specific heat capacity of dried zeolite was approximated by a quartic equation as a function of temperature as shown in **Table 4.6**. The specific heat capacity of zeolite with adsorbed water can be calculated by **Eq. (4.25)**. In this equation, the specific heat capacity of adsorbed water is treated as that of liquid water at the temperature of zeolite.

$$c_{p\mathrm{zeo}}=\frac{c_{p\mathrm{zeo0}}+qc_{p\mathrm{w\_ad}}}{1+q} \tag{4.25}$$

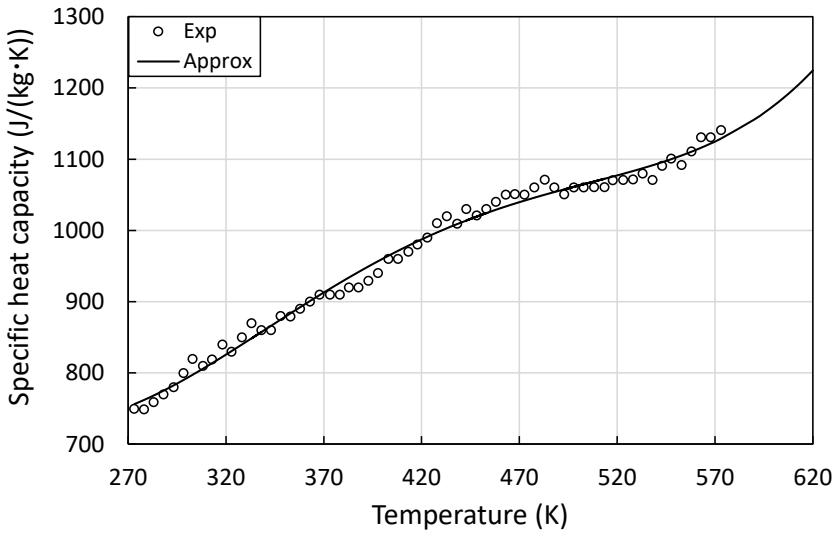

Fig. 4.15. Result of specific mass heat capacity of dried zeolite.

Axial and radial effective thermal conductivity of the solid phase in the zeolite bed were considered as the stagnant effective thermal conductivity of zeolite bed which was obtained by the hotwire method at 20, 150, 300 °C and was approximated in quadratic function of temperature. The effective thermal conductivity of polyamide ball bed was calculated simply as the following equation [9] using the inherent particle thermal conductivity of 0.25 W/(m·K).

$$\lambda_{po\_eff} = \lambda_g \varepsilon_{b\_po} + \lambda_{po}(1-\varepsilon_{b\_po}) \tag{4.26}$$

Axial and radial effective thermal conductivity of gas phase can be calculated by **Eqs. (4.27)** and **(4.28)**, respectively [10].

$$\frac{1}{Pe_{ax}} = \frac{1}{\frac{\rho_g u_g c_{pg} d_p}{\lambda_{gax\_eff}}} = \frac{0.73\varepsilon_{b\_(zeo,po)}}{Re_{p\_(zeo,po)}Pr} + \frac{0.5}{1+\frac{9.7\varepsilon_{b\_(zeo,po)}}{Re_{p\_(zeo,po)}Pr}} \tag{4.27}$$

$$\frac{1}{Pe_r} = \frac{1}{\frac{\rho_g u_g c_{pg} d_p}{\lambda_{gr\_eff}}} = \frac{1}{10} + \frac{2/3\,\varepsilon_{b\_(zeo,po)}}{Re_{p\_(zeo,po)}Pr} \tag{4.28}$$

The heat transfer coefficients between particle, gas and wall can be calculated by **Eqs. (4.29)** and **(4.30)**, respectively [10].

$$\alpha_{(zeo,po)\text{-wall}} = \frac{2.12\lambda_{eff\_(zeo,po)}}{d_{p\_(zeo,po)}} \tag{4.29}$$

$$Nu_{g\text{-wall}} = 0.6Re_{(zeo,po)}^{1/2}Pr^{1/3} \tag{4.30}$$

The heat transfer coefficient between particle and gas can be calculated by **Eq. (4.31)** [11].

$$Nu_{(zeo,po)\text{-g}} = 2.0 + 1.1Re_{(zeo,po)}^{0.6}Pr^{1/3} \tag{4.31}$$

Other thermophysical properties which were used in the calculation are shown in **Table 4.6**. The boundary conditions were shown in **Fig. 4.16**.

4.5.3 Experimental and numerical analysis result of heat transfer test

The experimental and numerical analysis result of radial temperature distribution under the steady state are shown in **Fig. 4.17**. The temperature distribution in lower Reynolds number condition is more uniform than that in higher Reynolds number condition because of less heat transport from the

above section. The numerical simulation has a good agreement with experimental result in all Reynolds numbers, and the heat transfer model was validated in the range of Reynolds number of Zeolite Boiler operation.

The history of temperature distribution at each measurement point under unsteady state test is shown in **Fig. 4.18**. At only Ch4 at r =24 mm, unexpected behavior was observed, but all the points except Ch4 indicate the same behavior. The experimental (Ch1, 6, 7 and 8) and numerical analysis result of the temperature distribution history are shown in **Fig. 4.19**. The peak of temperature rise of numerical simulation is relatively faster than experimental result, which is probably due to not considering the heat capacity of the stainless wall of the reactor in the numerical analysis. However, the numerical result can simulate the temperature history of each point. From this result, the combined model of adsorption kinetics and heat transfer were validated.

Table 4.6. Thermophysical properties.

Heat capacity (J/(kg·K))
$c_{ps} = 13604 - 90.4304 \times T_g + 0.2774 \times T_g^{\,2} - 4.2126 \times 10^{-4} \times T_g^{\,3} + 3.1837 \times 10^{-7} \times T_g^{\,4} - 9.5615 \times 10^{-11} \times T_g^{\,5}$
$c_{pa} = 1047 - 0.3726 \times T_g + 9.4530 \times 10^{-4} \times T_g^{\,2} - 6.0241 \times 10^{-7} \times T_g^{\,3} + 1.2859 \times 10^{-10} \times T_g^{\,4}$
$c_{pw} = 12010 - 80.4073 \times T_w + 0.3099 \times T_w^{\,2} - 5.3819 \times 10^{-4} \times T_w^{\,3} + 3.6254 \times 10^{-7} \times T_w^{\,4}$
$c_{pzeo0} = 3290.40 - 29.482 \times T_{zeo} + 0.1184 \times T_{zeo}^{\,2} - 1.9412 \times 10^{-4} \times T_{zeo}^{\,3} + 1.1472 \times 10^{-7} \times T_{zeo}^{\,4}$
Thermal conductivity (W/(m·K))
$\lambda_s = 1.3173 \times 10^{-4} + 5.1497 \times 10^{-5} \times T_g + 3.8965 \times 10^{-8} \times T_g^{\,2} - 1.3681 \times 10^{-11} \times T_g^{\,3}$
$\lambda_a = -0.002276 + 1.1548 \times 10^{-4} \times T_g - 7.9025 \times 10^{-8} \times T_g^{\,2} + 4.1170 \times 10^{-11} \times T_g^{\,3} - 7.4386 \times 10^{-15} \times T_g^{\,4}$
Viscosity (Pa·s)
$\mu_s = -1.4202 \times 10^{-6} + 3.8346 \times 10^{-8} \times T_g - 3.8522 \times 10^{-12} \times T_g^{\,2} + 2.1020 \times 10^{-15} \times T_g^{\,3}$
$\mu_a = -8.3828 \times 10^{-7} + 8.3572 \times 10^{-8} \times T_g - 7.6943 \times 10^{-11} \times T_g^{\,2} + 4.6437 \times 10^{-14} \times T_g^{\,3} - 1.0659 \times 10^{-17} \times T_g^{\,4}$

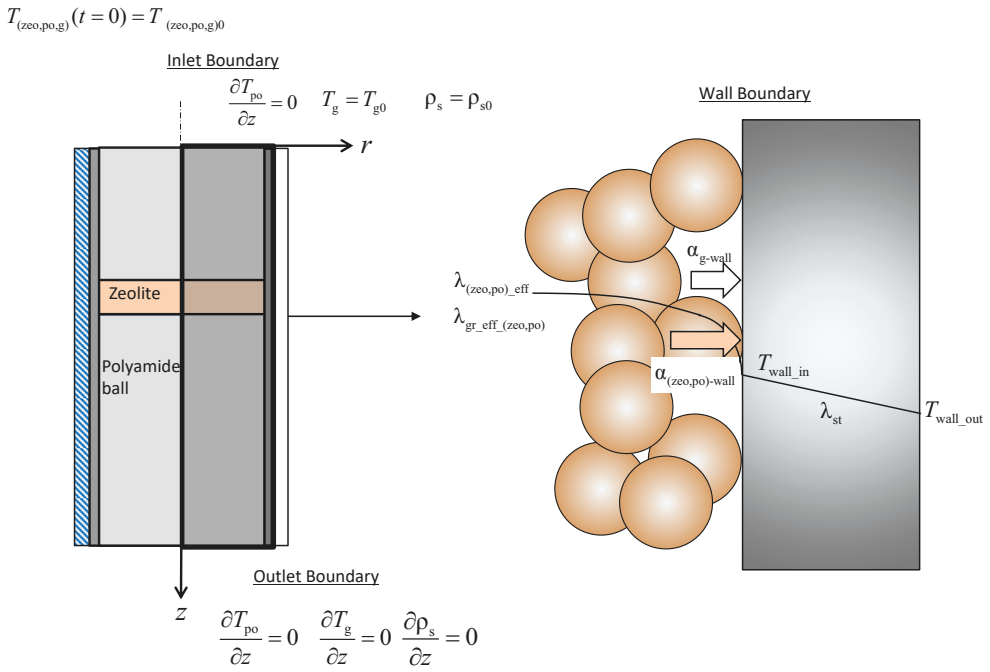

Fig. 4.16. Boundary conditions of heat transfer test.

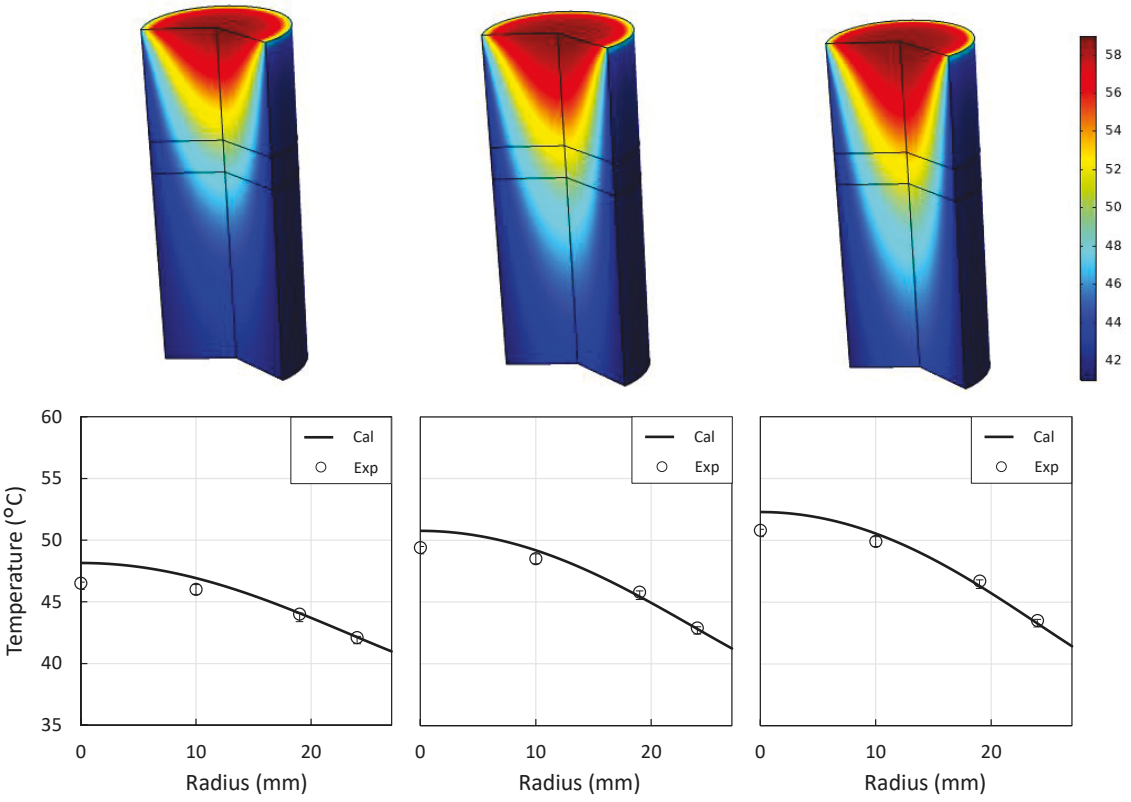

(a) Test 1 (Re_{p_zeo} = 3.79) (b) Test 2 (Re_{p_zeo} = 4.92) (c) Test 3 (Re_{p_zeo} = 5.69)

Fig. 4.17. Experimental and numerical analysis result of heat transfer test under steady state.

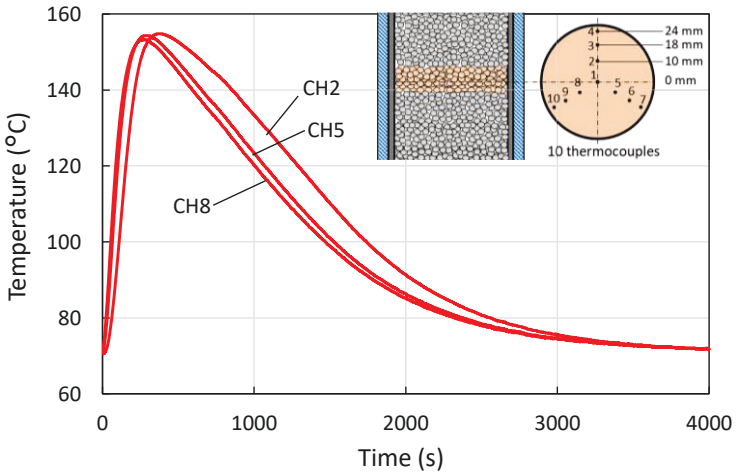

(a) r = 10 mm

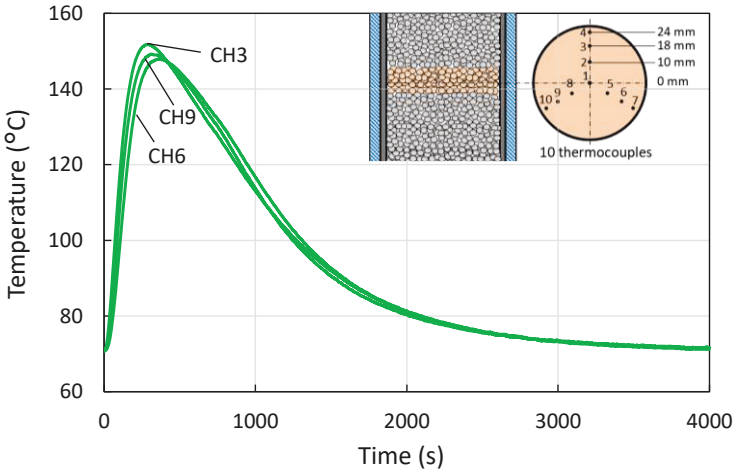

(b) r =18 mm

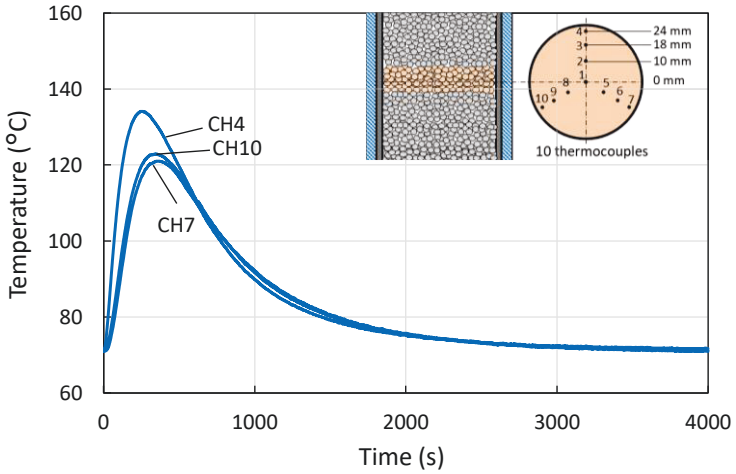

(c) r = 24 mm

Fig. 4.18. Result of temperature history at each point.

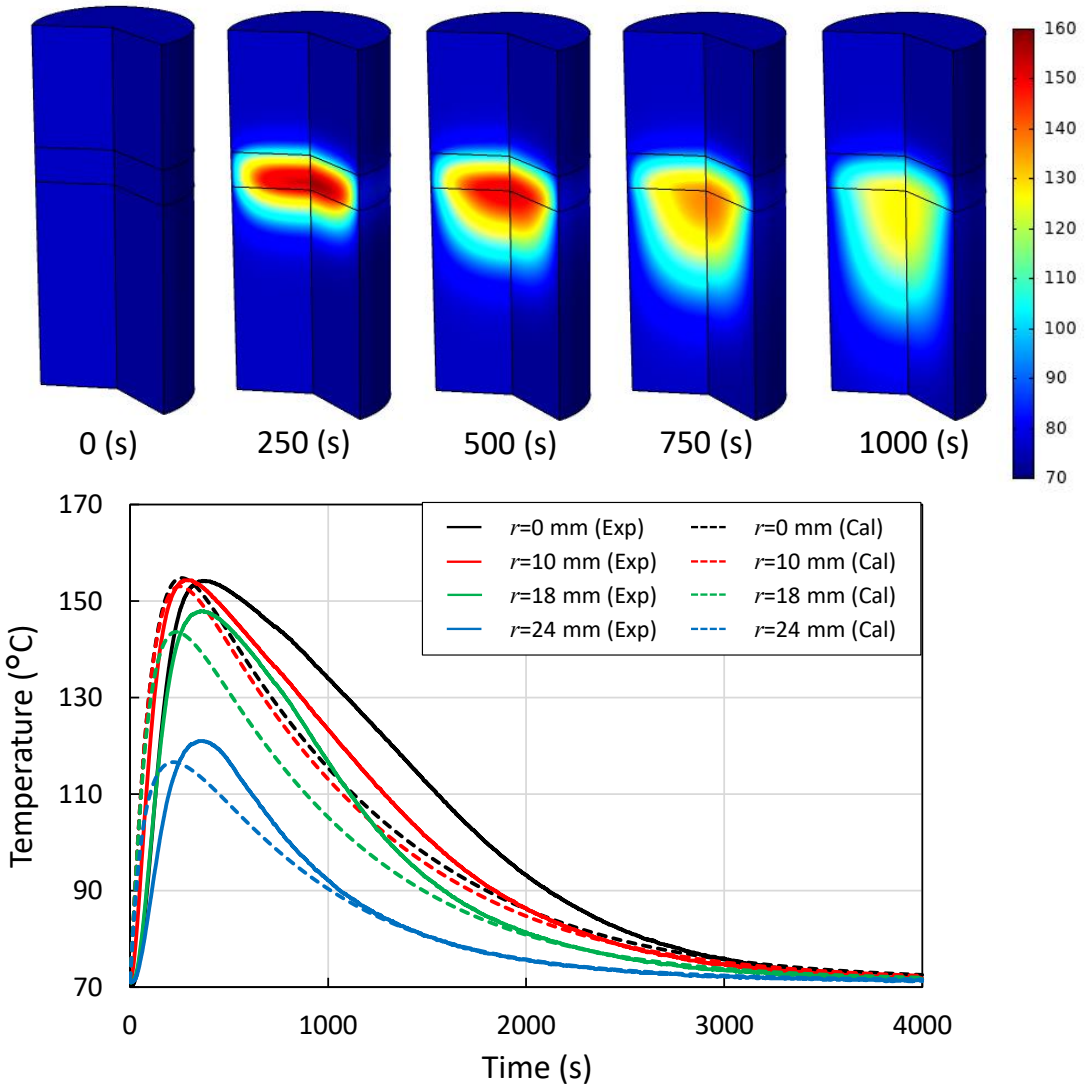

Fig. 4.19. Experimental and numerical result of temperature history during adsorption.

Assuming that the heat exchanging tubes are distributed uniformly across the cross-section area of Zeolite Boiler and surrounded by complete adiabatic vessel wall, 1D simulation models solving temperature and vapor pressure change with heat transfer and adsorption is applicable to modeling of Zeolite Boiler. Applicability of the 1D heat transfer model considering radial effective thermal conductivity of zeolite bed was investigated by comparing the cylindrical symmetric 2D model and 1D model of heat transfer test. The radial effective thermal conductivity of zeolite bed, which is dominant factor in heat transfer of the Zeolite Boiler, strongly affects the performance of Zeolite Boiler. The effect of radial effective thermal conductivity on the overall wall heat transfer coefficient of cylindrical reactor in 1D model was reported by Wasch and Froment as shown in the following equation [12].

$$\frac{1}{\alpha_{\text{eff}}}=\frac{1}{\alpha}+\frac{r_{\text{c}}}{4\lambda_{\text{eff}}} \tag{4.32}$$

where r_{c} is the radius of the cylindrical reactor. To evaluate the applicability of this model to the zeolite bed, a 1D unsteady simulation model was built for the heat transfer test. The mass conservation equations of solid (**Eq. (4.33)**) and gas phase (**Eqs. (4.34)** and **(4.35)**), the steam conservation equations (**Eqs. (4.36)** and **(4.37)**) and the energy conservation equations (**Eqs. (4.38)**, **(4.39)** and **(4.40)**) are expressed as following equations.

(Mass balance of zeolite)

$$\frac{\partial \rho_{\text{zeo}}}{\partial t}=\rho_{\text{zeo0}} r_{\text{ad}} \tag{4.33}$$

(Mass balance of gas in zeolite bed)

$$\frac{\partial}{\partial t}\left(\varepsilon_{\text{b\_zeo}}\rho_{\text{g}}\right)+\frac{\partial}{\partial z}\left(\rho_{\text{g}} u_{\text{g}}\right)=-\rho_{\text{zeo0}} r_{\text{ad}} \tag{4.34}$$

(Mass balance of gas in polyamide ball bed)

$$\frac{\partial}{\partial t}\left(\varepsilon_{\text{b\_po}}\rho_{\text{g}}\right)+\frac{\partial}{\partial z}\left(\rho_{\text{g}} u_{\text{g}}\right)=0 \tag{4.35}$$

(Steam conservation in zeolite bed)

$$\frac{\partial}{\partial t}\left(\varepsilon_{\text{b\_zeo}}\rho_{\text{s}}\right)+\frac{\partial}{\partial z}\left(\rho_{\text{s}} u_{\text{g}}\right)=\frac{\partial}{\partial z}\left(D_{\text{ax\_zeo}}\frac{\partial \rho_{\text{s}}}{\partial z}\right)-\rho_{\text{zeo0}} r_{\text{ad}} \tag{4.36}$$

(Steam conservation in polyamide ball bed)

$$\frac{\partial}{\partial t}\left(\varepsilon_{\text{b\_po}}\rho_{\text{s}}\right)+\frac{\partial}{\partial z}\left(\rho_{\text{s}} u_{\text{g}}\right)=\frac{\partial}{\partial z}\left(D_{\text{ax\_po}}\frac{\partial \rho_{\text{s}}}{\partial z}\right) \tag{4.37}$$

(Energy conservation of zeolite bed)

$$\begin{aligned}&\frac{\partial}{\partial t}\left(\rho_{\text{zeo}} c_{p\text{zeo}} T_{\text{zeo}}\right)\\&=\frac{\partial}{\partial z}\left(\lambda_{\text{zeo\_eff}}\frac{\partial T_{\text{zeo}}}{\partial z}\right)-\frac{6(1-\varepsilon_{\text{b\_zeo}})\alpha_{\text{g\_zeo}}}{d_{\text{p\_zeo}}}\left(T_{\text{zeo}}-T_{\text{g}}\right)-\frac{4\alpha_{\text{eff\_zeo}}}{d_{\text{c}}}\left(T_{\text{zeo}}-T_{\text{wall\_in}}\right)+\rho_{\text{zeo0}} r_{\text{ad}}\Delta H\end{aligned} \tag{4.38}$$

(Energy conservation of polyamide ball bed)

$$\begin{aligned}&\frac{\partial}{\partial t}\left(\rho_{\text{po}} c_{p\text{po}} T_{\text{po}}\right)\\&=\frac{\partial}{\partial z}\left(\lambda_{\text{po\_eff}}\frac{\partial T_{\text{po}}}{\partial z}\right)-\frac{6(1-\varepsilon_{\text{b\_po}})\alpha_{\text{g\_po}}}{d_{\text{p\_po}}}\left(T_{\text{po}}-T_{\text{g}}\right)-\frac{4\alpha_{\text{eff\_po}}}{d_{\text{c}}}\left(T_{\text{po}}-T_{\text{wall\_in}}\right)\end{aligned} \tag{4.39}$$

(Energy conservation of gas)

$$\frac{\partial}{\partial t}\left(\varepsilon_{b\_(zeo,po)}\rho_g c_{pg} T_g\right)+\frac{\partial}{\partial z}\left(\rho_g u_g c_{pg} T_g\right)$$
$$=\frac{\partial}{\partial z}\left(\lambda_{gax\_eff\_(zeo,po)}\frac{\partial T_g}{\partial z}\right)-\frac{6(1-\varepsilon_{b\_(zeo,po)})\alpha_{g\_(zeo,po)}}{d_{p\_(zeo,po)}}(T_g-T_{(zeo,po)})-\frac{4\alpha_{eff\_g}}{d_c}(T_g-T_{wall\_in}) \quad (4.40)$$

Heat transfer from solid phase to the wall considering the radial effective thermal conductivity of the bed can be calculated by **Eq. (4.41)**.

$$\frac{1}{\alpha_{eff\_(zeo,po,g)}}=\frac{1}{\alpha_{(zeo,po,g)\text{-}wall}}+\frac{r_c}{4\lambda_{(zeo,po,gr)\_eff}} \quad (4.41)$$

The numerical analysis result of axial temperature distribution calculated by both cylindrical symmetric 2D and 1D model under the steady state are shown in **Fig. 4.20**. The temperature history of the center of zeolite bed calculated by both models under unsteady state are shown in **Fig. 4.21**. In the 2D model calculations, temperatures were defined as cross-sectional area weighted temperatures and are drawn in the **Figs. 4.20** and **4.21**. In the steady state, there is few discrepancies between each case. In the unsteady model, the result of 1D model has higher peak temperature than that of 2D model. This means 1D model may underestimate heat transfer coefficient slightly. However, the difference between each model is up to 8 °C (equal to 2% of error) which has little impact on the performance. From this result, applicability of 1D heat transfer model considering the radial effective thermal conductivity of zeolite bed was confirmed.

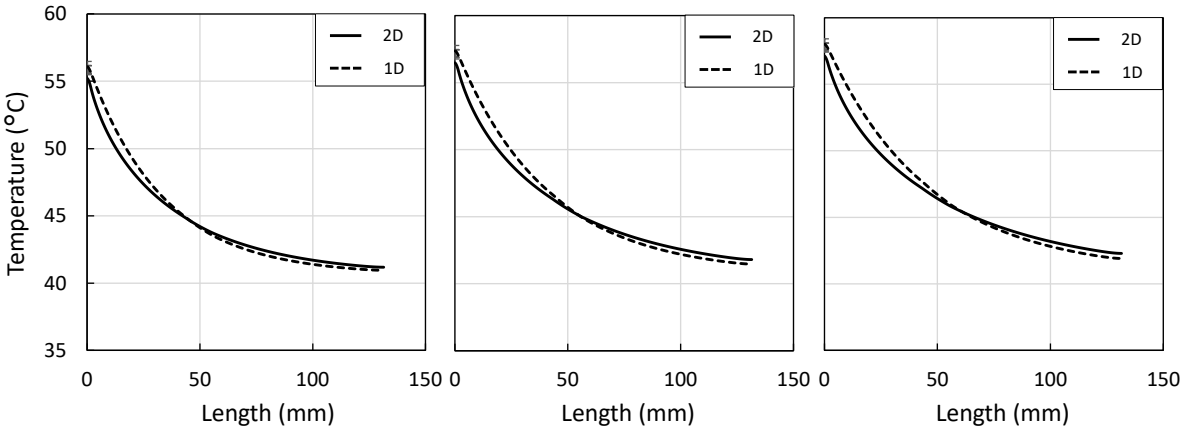

(a) Test 1 (Re_{p_zeo} = 3.79) (b) Test 2 (Re_{p_zeo} = 4.92) (c) Test 3 (Re_{p_zeo} = 5.69)

Fig. 4.20. Axial temperature change in 2D and 1D simulation of steady state.

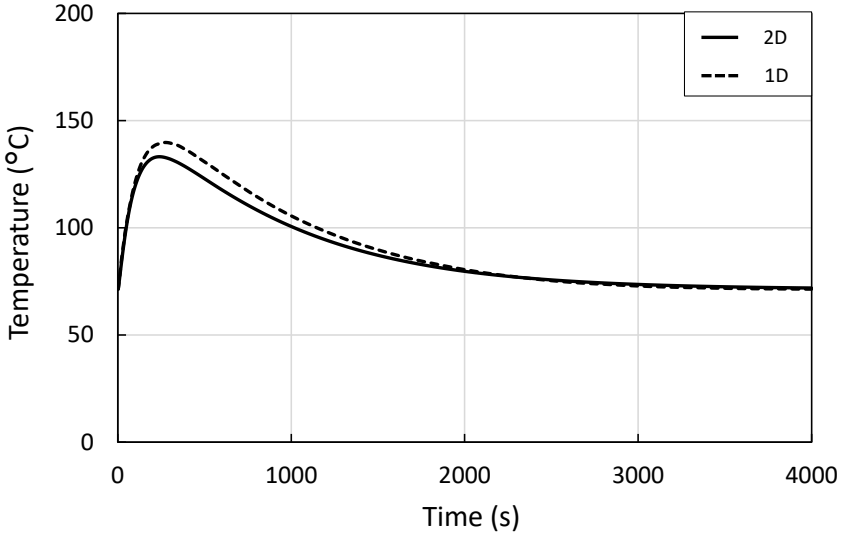

Fig. 4.21. Temperature history in 2D and 1D simulation during adsorption.

4.6 Zeolite Boiler test

This section summarized performance indices of Zeolite Boiler (**4.6.1**), and continuous generation of pressurized steam was demonstrated via Zeolite Boiler test (**4.6.2~4.6.4**). A 1D numerical simulation model of Zeolite Boiler was built (**4.6.5**) and analyzed the Zeolite Boiler test (**4.6.6**). The validated numerical simulation model was used to predict the performance of full-scale Zeolite Boiler in Tanegashima in following sections (**4.7** and **4.8**)

4.6.1 Fuel saving and heat recovery rate

The important performance indices of Zeolite Boiler are “fuel saving” and “heat recovery rate”. The fuel saving is the index how much enthalpy of generated steam H_{gen} can be increased from that of injection steam H_{inj}. In the experiment, the fuel saving was evaluated as the heat increasing rate η_{inc} which can be calculated by **Eq. (4.42)**.

$$\eta_{\mathrm{inc}} = \frac{H_{\mathrm{gen}} - H_{\mathrm{inj}}}{H_{\mathrm{inj}}} \tag{4.42}$$

The heat recovery rate η_{rec} is the ratio of the potential heat generation of zeolite $H_{\mathrm{potential}}$ to recovered heat (= H_{gen}) which can be calculated by **Eq. (4.43)**.

$$\eta_{\mathrm{rec}} = \frac{H_{\mathrm{gen}}}{H_{\mathrm{potential}}} \tag{4.43}$$

The density and specific heat capacity of zeolite increase due to adsorbed water by steam adsorption. Focusing on an adsorption process and heat recovery process of one particle of zeolite, temperature of zeolite T_{zeo} increases due to adsorption from the ambient temperature accompanying with increase in the density and the specific heat capacity of zeolite. Increase in T_{zeo} decreases the equilibrium water uptake q_{eq} on zeolite, and thereby the maximum T_{zeo} is determined consequently by the balance of current q and q_{eq}. After the zeolite reaches the maximum temperature, zeolite is cooled to the ambient temperature by sensible heat recovery. By cooling via the sensible heat recovery, the zeolite additionally adsorbs steam to the maximum water uptake $q_{\max}$ which is described below due to increase in q_{eq}. The $H_{\mathrm{potential}}$ is sum of the recovered sensible heat and the additional adsorption heat by cooling.

The $q_{\max}$ was determined considering the capillary effect. In the range of high relative humidity, the q increases due to the capillary effect as described in **4.4.3**. The adsorption isotherms calculated by both Dubinin-Astakhov model and Freundlich-Dubinin-Astakhov model at 15 °C which is the inlet T_{zeo} (See chapter 3) are shown in **Fig. 4.22**. The capillary effect might occur above the maximum water uptake capacity of Dubinin-Astakhov model ($W_{\max}$ = 237 mL/kg, 0.237 kg/kg at 15 °C). Adsorption in the capillary effect range does not contribute the fuel saving because only latent heat of adsorbed steam without additional adsorption heat is generated in this range. Therefore, the maximum mass flow rate of injection steam $m_{\mathrm{inj\_max}}$ should be limited, which can be calculated by **Eq. (4.44)**.

$$\begin{aligned} m_{\mathrm{inj\_max}} &= m_{\mathrm{zeo}}(q_{\max} - q_0) \\ q_{\max} &= 0.237\,\mathrm{kg/kg} \end{aligned} \tag{4.44}$$

The $H_{\mathrm{potential}}$ as a function of water uptake before adsorption (remaining water uptake after heat charging) is shown in **Fig. 4.23** in the case of $q_{\max}$ = 0.237 kg/kg.

4.6.2 Experimental setup

A 1/200$^{\mathrm{th}}$ scale Zeolite Boiler (called bench-scale Zeolite Boiler hereafter) was designed assuming that 0.4 t/h pressurized steam is continuously generated by the full-scale Zeolite Boiler applying an actual factory in Tanegashima. An overviewing picture and a piping and instrumentation diagram (P&ID) of the Zeolite Boiler test rig are shown in **Figs. 4.24** and **4.25**, respectively. A cylindrical stainless chamber with φ = 300 mm (t = 2 mm) × L = 500 mm was manufactured for the bench-scale Zeolite Boiler. The chamber was surrounded by a glass wool thermal insulation with 25 mm thickness. Two hoppers were attached to the top of chamber to supply the zeolite continuously.

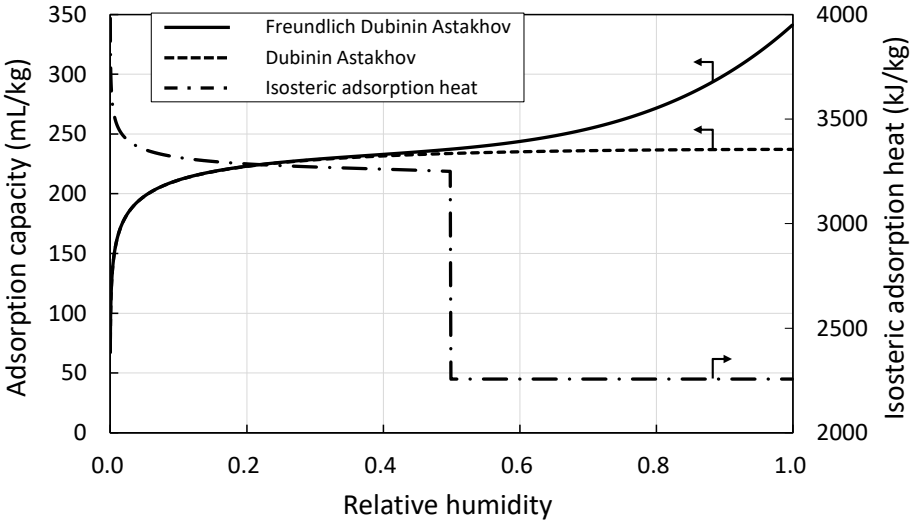

Fig. 4.22. Adsorption isotherms with/without capillary effect and isosteric adsorption heat.

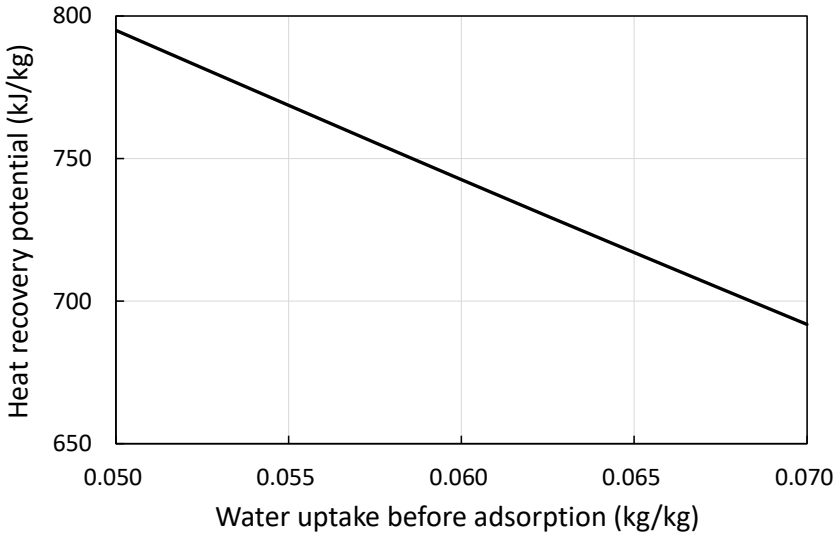

Fig. 4.23. Effect of inlet water uptake on heat recovery potential.

A one-through type stainless heat exchanger was settled into the chamber, while the multi-tubular heat exchanger was assumed to be installed in the full-scale Zeolite Boiler considering the heat leakage from the chamber wall. In the bench-scale Zeolite Boiler, the effect of heat leakage from the wall is larger than that of the full-scale Zeolite Boiler. The multi-tubular heat exchanger in the bench-scale Zeolite Boiler would have uneven heat flux on each tube due to the heat leakage from the wall, i.e. the heat exchanging tube near the wall has lower heat flux. To mitigate the expected discrepancy between experimental and analytical results, as shown in **Fig. 4.26**, 3/8-inch stainless tube (0.89 mm thickness) folded and distributed uniformly across the cross-section area was made and installed symmetrically in the chamber. Total heat transfer area of the heat exchanger was 0.95 m^2.

The steam injection port was mounted at x = 0 mm (= top of the heat exchanger) and superheated steam which was generated by the injection-steam-generator was injected from the port. The injection-steam-generator consisted of electrically heated two evaporators and a super heater. In the two evaporators, sheathed heaters were wrapped on the 1-inch stainless tubes in which alumina balls was packed to expand heat transfer area. Saturated steam evaporated by the two evaporators was introduced to the super heater made of 3/4-inch stainless tube with the same configuration with wrapping a sheathed heater and alumina ball packed bed. Demineralized water was pressurized by the pump and its flow rate was controlled by variable area flowmeters and needle valves, and concurrently supplied to the heat exchanger in the Zeolite Boiler and the injection-steam-generator.

The zeolite was discharged from the bottom by a particle discharger mounted under the bottom of chamber. As shown in **Fig. 4.27**, the particle discharger consisted of three disks of 10 mm in thickness. The first and third disk had diagonal two holes (φ =25 mm) and were fixed different phase positions by 90 degrees. The second (center) disk also has two holes and was rotated by a motor to discharge the zeolite in the holes. The volume of each hole is 4900 mm^3. The mass flow rate of zeolite could be controlled up to 20 kg/h by changing the rotation speed of second disk.

To measure the axial temperature distribution of zeolite bed, six K-type thermocouples were embedded along the center axis of the zeolite bed, of which junctions were placed at 0, 100, 200, 300, 400 and 500 mm from the top. The temperature of generated steam T_{w} and injection steam T_{inj} were measured by T-type thermocouples. The temperature of supplied water T_{w0} was measured by a K-type thermocouple. A logger recorded these temperatures every 10 seconds. Injection steam pressure and generated steam pressure were measured by pressure gage every 30 minutes. The water uptake on inlet q_0 and outlet q_{out} zeolite and the mass flow rate of zeolite were measured every 30 minutes.

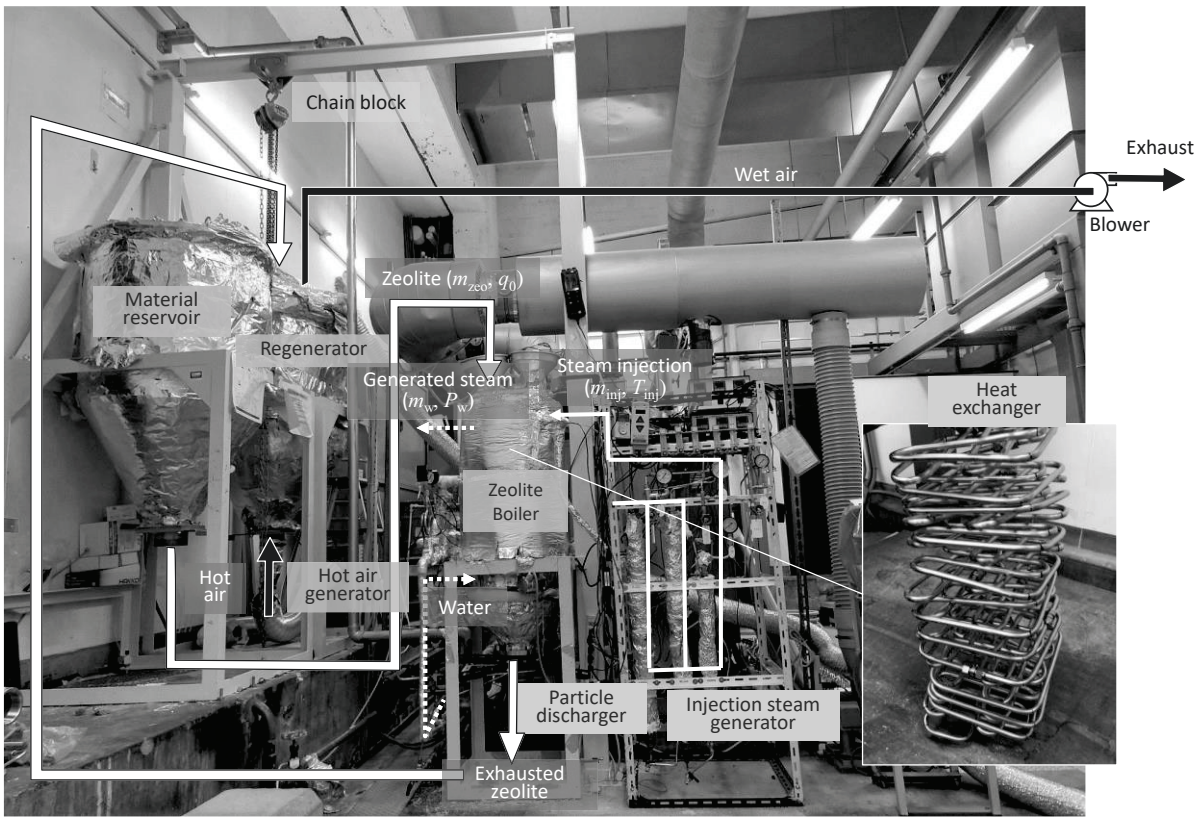

Fig. 4.24. Overview of experimental set up of bench-scale Zeolite Boiler.

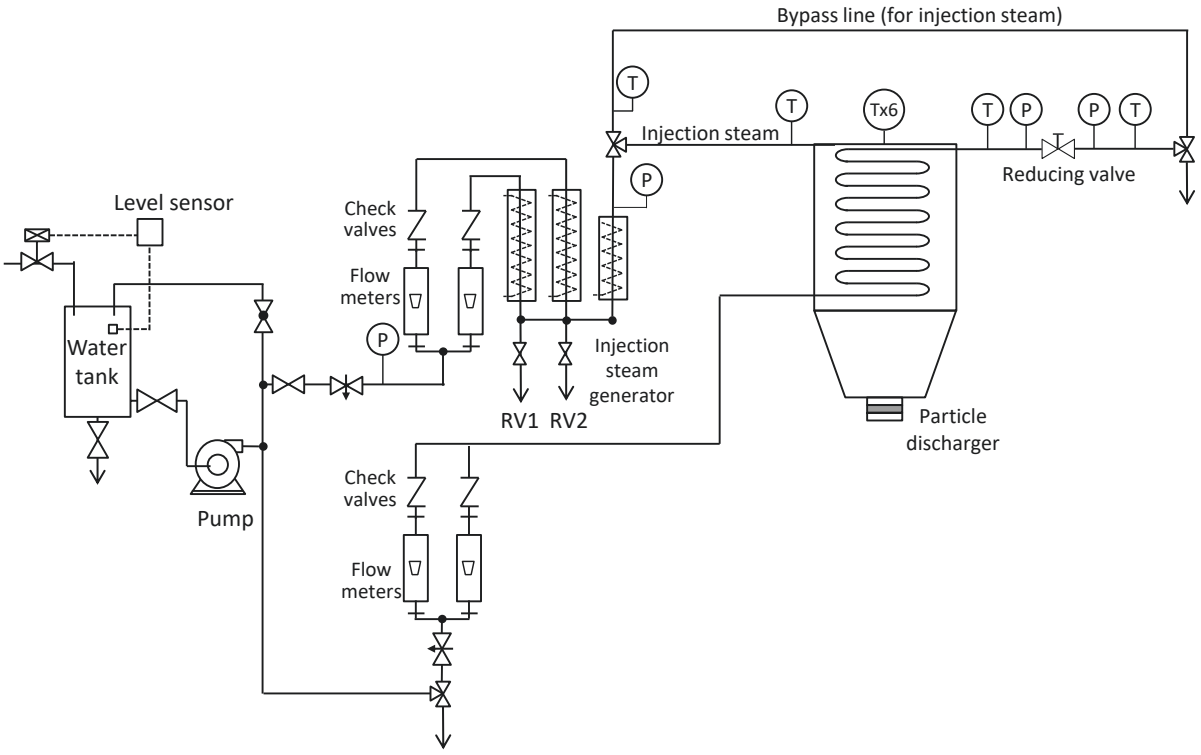

Fig. 4.25. Piping and instrumentation diagram (P&ID) of Zeolite Boiler test rig.

Fig. 4.26. Heat exchanger settled into the chamber of Zeolite Boiler.

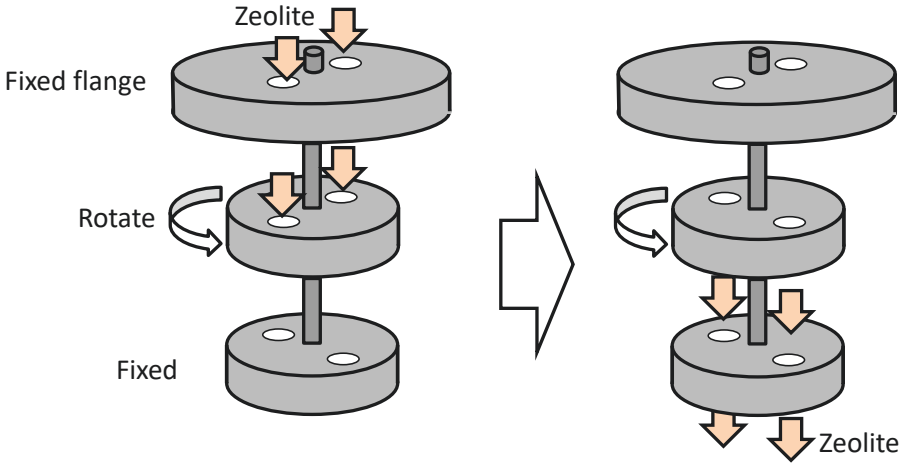

Fig. 4.27. Particle discharger attached to the bottom of chamber of Zeolite Boiler.

4.6.3 Experimental procedure

As a preliminary desorption treatment, water in zeolites was desorbed to the intended q_0. The stainless material reservoir with φ = 600 mm (t = 2 mm) × L = 800 mm was packed with zeolite, and hot air generated by a hot air generator was blown from the bottom of the vessel. By controlling the inlet temperature, the zeolite could be desorbed to the target water uptake.

Before starting the experimental procedure, the chamber of Zeolite Boiler was fully packed with zeolite. Demineralized water was pumped and introduced to the heat exchanger in the chamber and the injection-steam-generator. The water for the injection-steam-generator was depressurized to the ambient pressure and evaporated in the evaporators and the super heater. The generated steam was passed through the bypass line until the steam flow rate was stabilized at the outlet of the super-

heater. A back-pressure valve placed at the outlet of the heat exchanger was fully opened and water was circulated in the heat exchanger under the ambient pressure.

After the flow rate of injection steam in the bypass line became steady state, it was introduced into the Zeolite Boiler by quickly switching the valve. Concurrently, the particle discharger was started to discharge the zeolite, which means the experiment was commenced. The T_{zeo} increased from the top and hot zone gradually propagated to the bottom. When the outlet steam reached the superheated state under ambient pressure, the generated steam was started to be pressurized to 0.2 MPa by controlling the back-pressure valve for 2 ~ 3 hours. The Zeolite Boiler was operated for an hour under steady state after the all temperatures of each point were stabilized within ±5 °C for 30 minutes.

4.6.4 Experimental condition

The following parameters can be operable in the Zeolite Boiler test.

- Mass flow rate of zeolite m_{zeo}
- Initial water uptake on zeolite q_0
- Temperature of injection steam T_{inj}
- Mass flow rate of injection steam m_{inj}
- Pressure of generated steam p_{w}
- Mass flow rate of generated steam m_{w}

(1) Zeolite (Mass flow rate m_{zeo}, initial water uptake q_0)

The m_{zeo} was determined to 10 kg/h considering the maximum storable volume of material reservoir. In the full-scale Zeolite Boiler in Tanegashima, the q_0 depends on hot air conditions used for the heat charging process in the sugar mill. **Table 4.7** shows the maximum and minimum temperature of hot air for thermal energy storage (TES) and q_{eq} on zeolite under the ambient vapor pressure (=1.5 kPa) at each condition of heat charging station which are A)Current process of sugar mill, B)blow steam reduction, C)bagasse drying D)combined B) and C), and E)increase in power generation, which are described in Chapter 3. The minimum temperature approach between the flue gas and the hot air for TES was assumed to be 10 °C. The q_{eq} on zeolite of each process are approximately around 0.045 ~ 0.06 kg/kg. In the experiments, the q_0 was controlled in this range.

Table 4.7. Equilibrium water uptake on zeolite under the condition of heat charging station.

Heat charging process (See Chapter 3)	Flue gas temp (°C)		Temperature of hot air for TES (°C)		Equilibrium water uptake (kg/kg)	
	Max.	Min.	Max.	Min.	Min.	Max.
A) Current process of sugar mill	182		172		0.056	
B) Blow steam reduction	189	182	179	172	0.050	0.056
C) Bagasse drying	188	182	178	172	0.051	0.056
D) Combination of B) and C)	195	182	185	172	0.045	0.056
E) Increase in power generation	182	150	172	140	0.056	0.087

(2) Injection steam (Temperature T_{inj}, mass flow rate m_{inj})

In the full-scale Zeolite Boiler in Tanegashima, dried saturation steam of 0.6 MPa generated by the existing boiler is depressurized to the ambient pressure thorough isoenthalpic expansion and injected into the zeolite bed. The T_{inj} was set to approximately 140 to 150 °C.

The heat transfer area is limited to 0.95 m^2 in the bench-scale Zeolite Boiler due to the configuration of heat exchanger. Insufficient heat transfer area of heat exchanger increases exhaust T_{zeo} and decreases the q_{eq} at the bottom of heat exchanger in accordance with the equilibrium line. Excess steam injection increases slipped steam without adsorption, and unadsorbed steam would be condensed at the bottom of chamber due to heat leakage, which leads clogging problem at the bottom of chamber. To avoid condensation at the bottom of chamber, the m_{inj} was controlled to keep the q_{out} ≈ 0.18 kg/kg, while q_{max} = 0.237 kg/kg.

(3) Supplied water and generated steam (Pressure p_{w}, mass flow rate m_{w})

The p_{w} was controlled to 0.2 MPa which is the requirement of heat demand in Tanegashima. The m_{w} was set to keep the generated steam super-heated, which was predicted by the numerical simulation described in the following section.

4.6.5 Numerical model

To analyze the Zeolite Boiler test numerically, a 1D simulation model solving mass, steam, energy conservation equations of zeolite and gas phase in the void of bed, and momentum equation of gas phase was built on a commercial software COMSOL Multiphysics 5.3a®. As mentioned above, since the heat exchanger tube was distributed uniformly across the cross-section area of cylindrical chamber of the Zeolite Boiler, 1D modeling was applicable to solve axial distribution of T_{zeo} and q. The mass conservation equations for zeolite and gas can be expressed by **Eqs. (4.45)** and **(4.46)**, respectively.

$$\frac{\partial}{\partial x}(\rho_{zeo} u_{zeo}) = \rho_{zeo0} r_{ad} \tag{4.45}$$

$$\frac{\partial}{\partial x}(\rho_{g} u_{g}) = -\rho_{zeo0} r_{ad} \tag{4.46}$$

The steam conservation equation can be expressed by **Eq. (4.47)**.

$$\frac{\partial}{\partial x}\left(\rho_{s} u_{g}\right) = \frac{\partial}{\partial x}\left(D_{ax} \frac{\partial \rho_{s}}{\partial x} \right) - \rho_{zeo0} r_{ad} \tag{4.47}$$

The momentum equation for gas phase can be expressed by **Eq. (4.48)**.

$$\frac{\partial}{\partial x}\left(\frac{\rho_{s} {u_{g}}^{2}}{\varepsilon_{b}} \right) = -\varepsilon_{b} \frac{\partial p}{\partial x} - \frac{150(1-\varepsilon_{b})^{2} \mu_{g}}{{d_{p}}^{2} {\varepsilon_{b}}^{3}} u_{g} \varepsilon_{b} - \frac{1.75(1-\varepsilon_{b})}{d_{p} {\varepsilon_{b}}^{3}} \rho_{g} \left| u_{g} \right| u_{g} \varepsilon_{b} \tag{4.48}$$

The energy conservation equations for zeolite, gas and supplied water can be expressed by **Eqs. (4.49)**, **(4.50)** and **(4.51)**, respectively.

$$\begin{aligned} &\frac{\partial}{\partial x}\left(\rho_{zeo} u_{zeo} c_{pzeo} T_{zeo}\right) \\ &= \frac{\partial}{\partial x}\left(\lambda_{zeo\_eff} \frac{\partial T_{zeo}}{\partial x} \right) - \alpha_{g\text{-}zeo} \sigma_{g\text{-}zeo} (T_{zeo} - T_{g}) - \alpha_{zeo\text{-}w} \sigma_{zeo\text{-}w} (T_{zeo} - T_{w}) \\ &- \alpha_{zeo\text{-}amb} \sigma_{zeo\text{-}amb} (T_{zeo} - T_{amb}) + \rho_{zeo0} r_{ad} \Delta H \end{aligned} \tag{4.49}$$

$$\begin{aligned} &\frac{\partial}{\partial x}\left(\rho_{g} u_{g} c_{pg} T_{g}\right) \\ &= \frac{\partial}{\partial x}\left(\lambda_{gax\_eff} \frac{\partial T_{g}}{\partial x} \right) - \alpha_{g\text{-}zeo} \sigma_{g\text{-}zeo} (T_{g} - T_{zeo}) - \alpha_{g\text{-}w} \sigma_{g\text{-}w} (T_{g} - T_{w}) - \alpha_{g\text{-}amb} \sigma_{g\text{-}amb} (T_{g} - T_{amb}) \end{aligned} \tag{4.50}$$

$$-\frac{\partial}{\partial x}\left(\rho_{w} u_{w} h_{w}\right) = \alpha_{zeo\text{-}w} \sigma_{zeo\text{-}w} (T_{zeo} - T_{w}) + \alpha_{g\text{-}w} \sigma_{g\text{-}w} (T_{g} - T_{w}) \tag{4.51}$$

The specific heat transfer area between zeolite bed and wall of heat exchanger surface can be calculated by **Eq. (4.52)**.

$$\sigma_{(\text{zeo,g-w})} = \frac{A_{\text{trans}}}{V_{\text{c}}} \tag{4.52}$$

where V_{c} is the effective volume of zeolite in the chamber subtracting the volume of heat exchanger from the chamber volume. The specific heat transfer area between zeolite bed and wall of chamber can be calculated by **Eq. (4.53)**.

$$\sigma_{(\text{zeo,g-wall})} = \frac{d_{\text{c}}\pi}{A_{\text{c}}} \tag{4.53}$$

The heat transfer from the zeolite bed to the heat exchanger surface was calculated by the proposed model considering effective thermal conductivity of zeolite bed as described in **4.5**. The value of r_{c} in **Eq. (4.32)** can be determined as an equivalent radius explained as follows.

The flow passage of zeolite in heat exchanger shown in **Fig. 4.26** was modelled as a rectangular tube of which cross sectional area was 55 mm x 55 mm square, as shown in **Fig. 4.28**. For the heat transfer coefficient of 1D model, the rectangular tube was converted into a tube whose radius r_{c} = 20.3 mm was given in **Eq. (4.32)**, which was geometrically equivalent to the cross-sectional area surrounded by heat exchanging tube (hatched zone in **Fig. 4.28**). Concurrently, a 3D model true to the actual configuration of heat exchanger was built on COMSOL Multiphysics 5.3a® and its result was compared with the result of the 1D model. The symmetric boundary of the 3D model was set on the center line of tubes and a part of heat exchanger of this boundary was built as shown in **Fig. 4.28**. To compare temperature distributions simply without exothermic heat, adsorption process was ignored and only the energy conservation equation of zeolite was considered. The inlet T_{zeo} was set to 230 °C with m_{zeo} =10 kg/h. Temperature of supplied water in the heat exchanging tube was set to 120 °C constant, which is the saturation temperature of 0.2 MPa steam. The axial bending angle of tube in the 3D model was adjusted to equalize to the heat transfer area of the 1D model. By using the 3D and the 1D model, each temperature distribution in the length of 0.07 m from the top was computed, which was equal to 2 rounds of spiral tube.

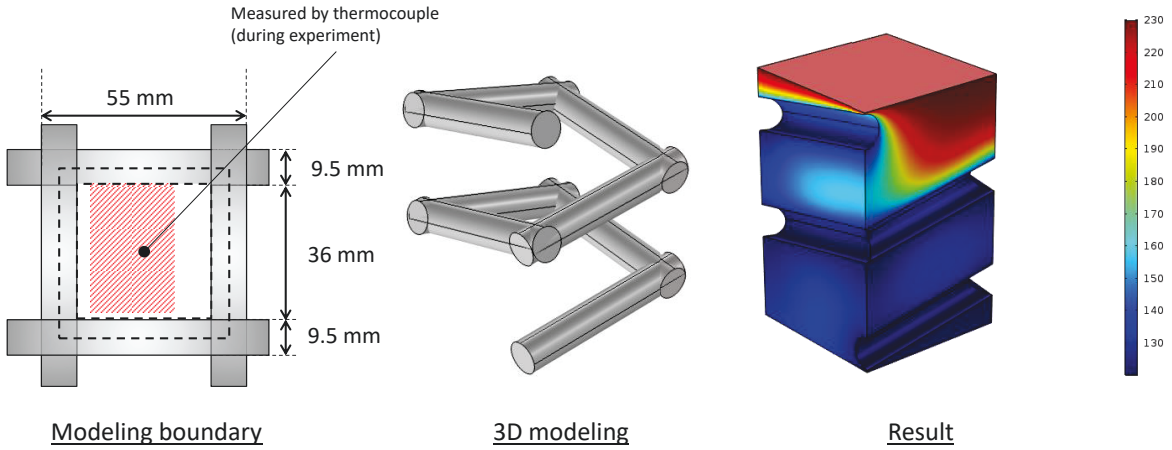

Fig. 4.28. Modeling boundary and numerical modeling on COMSOL of heat exchanger in bench-scale Zeolite Boiler.

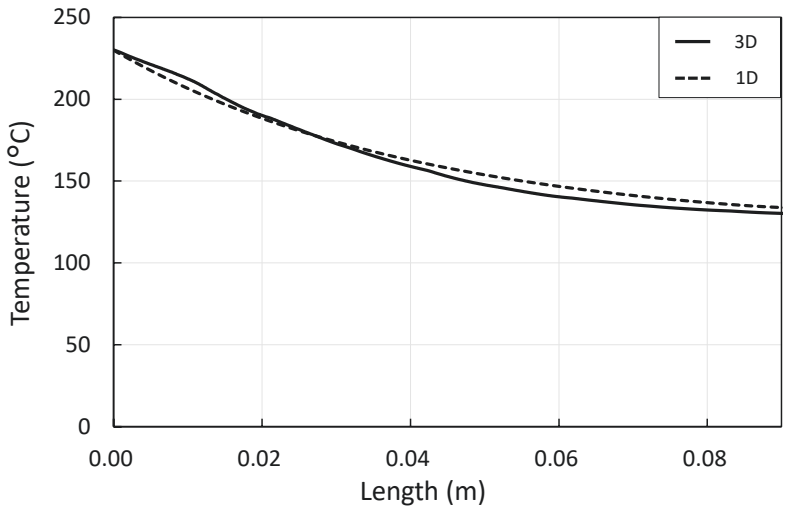

Fig. 4.29. Change in axial temperature distribution calculated by 3D and 1D model.

The axial temperature distribution calculated by both the 3D model and the 1D model are shown in **Fig. 4.29**. In-plane representative temperature of each cross-sectional area in 3D model T_{rep} was defined as the following equation.

$$T_{\mathrm{rep}} = \frac{1}{A\int \rho_{\mathrm{zeo}} c_{p\mathrm{zeo}} \Delta x dA} \int \rho_{\mathrm{zeo}} c_{p\mathrm{zeo}} T_{\mathrm{zeo}} \Delta x dA \qquad (4.54)$$

There are few discrepancies between each model. From this result, adequacy of applying r_c = 20.3 mm to the 1D model was confirmed.

The overall heat transfer coefficient from the zeolite bed to the supplied water consisted of heat transfer from the zeolite bed to the heat exchanger surface, thermal conduction through the tube wall and heat transfer from the inner tube wall to the supplied water. Assuming that the supplied water inside the heat exchanger was treated as well-developed tubular laminar flow, the Nusselt number of supplied water was set to 4.36. In the evaporating zone, the constant heat transfer coefficient of 2500 W/(m^2·K) was given as the boiling heat transfer. If the boiling heat transfer coefficient was changed, the overall heat transfer coefficient is little affected, because the heat resistance from zeolite bed to the heat exchanger surface is dominant factor to the overall heat resistance. In the energy conservation of supplied water, the thermal conduction in the water body was ignored because the Peclet number of supplied water was larger than 10.

The boundary conditions of numerical simulation of Zeolite Boiler are shown in **Fig. 4.30**. The zeolite is supplied continuously from the hoppers on the top. The zeolite from the hoppers prevents of the injection steam from moving up due to buoyancy. Nevertheless, the zeolite is pre-heated before reaching to the injection point due to axial heat conduction. The calculation model included additional 0.1 m zeolite bed above the injection point as the pre-heating zone. The boundary conditions around the tube wall and chamber wall are shown in **Fig. 4.31**.

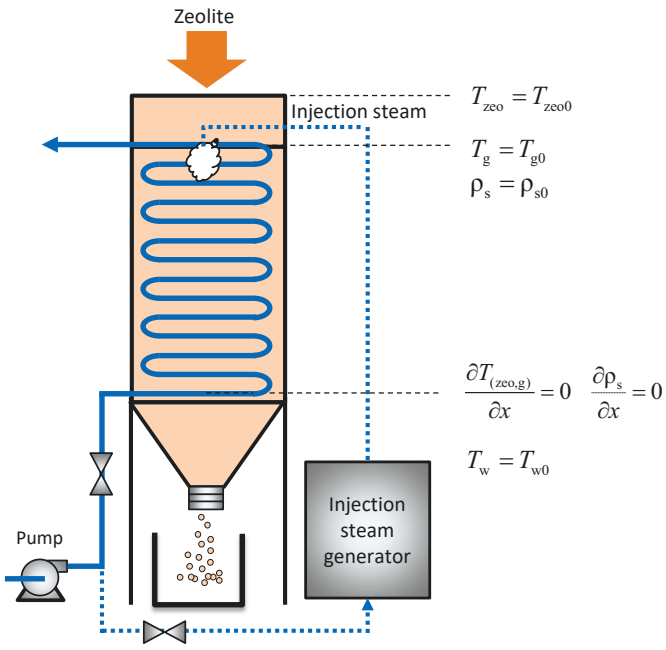

Fig. 4.30. Boundary conditions of numerical simulation of Zeolite Boiler.

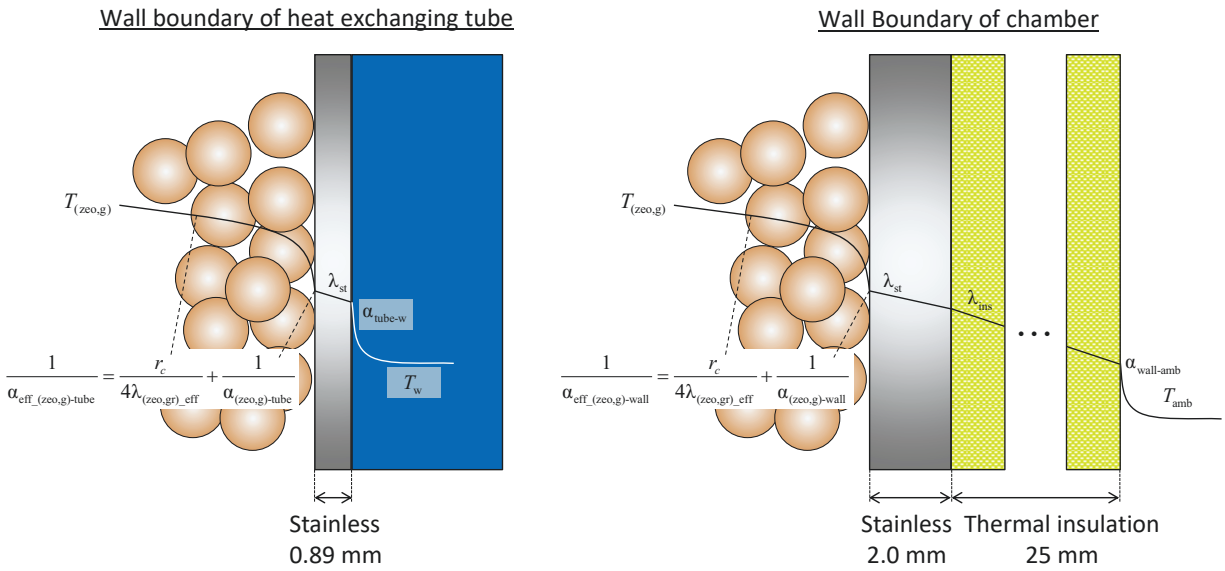

Fig. 4.31. Wall boundary conditions of heat exchanging tube and chamber.

4.6.6 Experimental and numerical analysis result of Zeolite Boiler test

The test was conducted under the conditions of m_{zeo}= 10 kg/h, m_{inj} = 1.26 kg/h, m_w = 1.38 kg/h and q_0 = 0.06 kg/kg. The mass balance of m_{zeo} and adsorbed water during the Zeolite Boiler test is shown in **Fig. 4.32**. The zeolite was stably discharged with 10 ± 0.2 kg/h during the test. Adsorbed water was gradually increased and reached steady state after 4.5 hours since the test started.

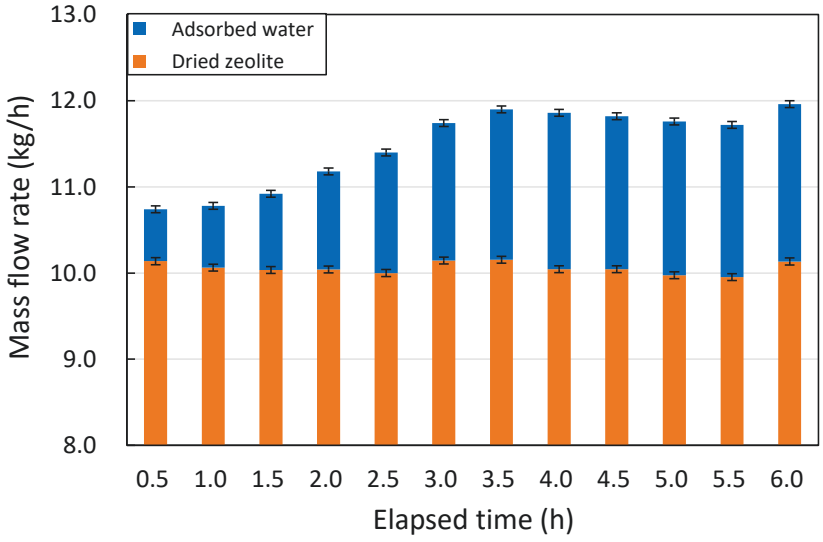

Fig. 4.32. Mass balance of Zeolite Boiler test.

The temperature history at each measuring point is shown in **Fig. 4.33**. Right after as the start of test, temperature at x = 0.0 m rapidly increased and stabilized at ≈210 °C. Temperatures of other

points increased from the top to the bottom. Pressurizing the supplied water was started after 2.5 hours and completed after 4.5 hours. All temperatures reached steady state after the pressurizing process.

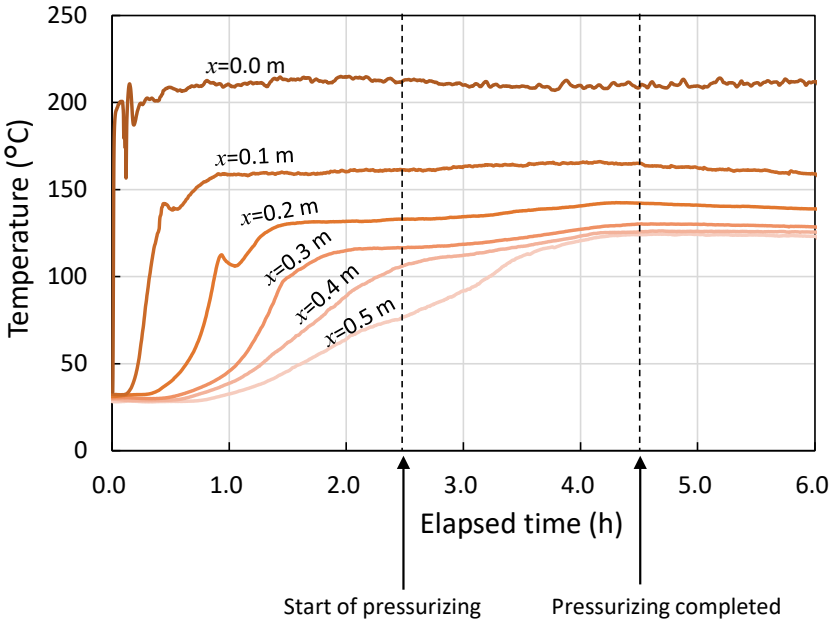

Fig. 4.33. Temperature histrory during Zeolite Boiler test.

The trend of steam temperature and saturated temperature by the steam table corresponding to the pressure for an hour (5.0 hours after the start) are shown in **Fig. 4.34**. Generated steam was kept in superheated state and continuous generation of pressurized superheated steam was accomplished.

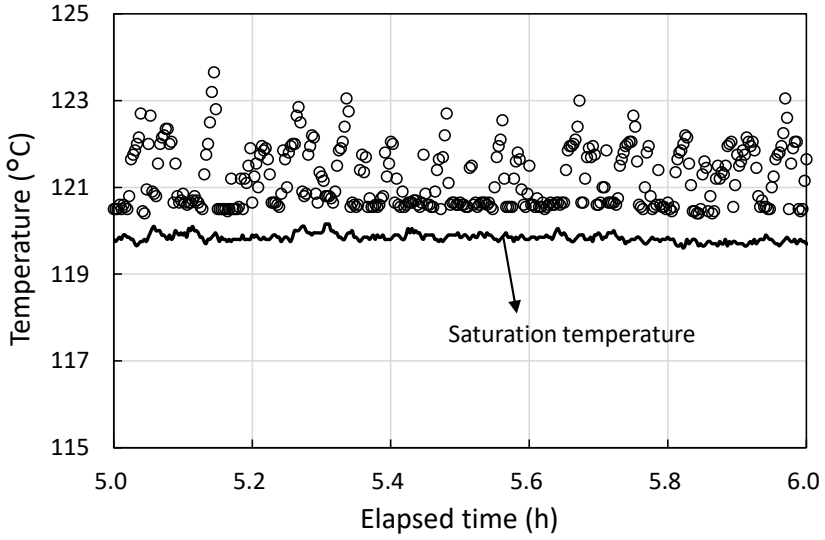

Fig. 4.34. Change in temperature of generated steam and saturation temperature with time.

The experimental result of axial T_{zeo} distribution is shown in **Fig. 4.35**. The numerical analysis result of axial T_{zeo} distribution of zeolite and supplied water are also shown in **Fig. 4.35**. The T_{zeo} rapidly increases around the steam injection point up to 215 °C and gradually decreases due to heat transfer to supplied water via the heat exchanger. The numerical analysis result can simulate the experimental data of temperature distribution. At the bottom of the bed, there is a temperature gap between experimental and numerical analysis. It is considered that the discrepancy is caused by due to the modeling dimension. During the test, the measuring points were on the central axis of square heat exchanger as shown in **Fig. 4.28**. Temperature difference between the T_{zeo} and the T_w at the bottom point is larger than those in above zone because cold water is introduced from the bottom. **Figure 4.36** shows the maximum and minimum T_{zeo} distribution in the range of x = 410 ~ 500 mm, which is calculated using the same 3D model as **Fig. 4.28**. As well as the calculation in **Fig. 4.28**, adsorption process was ignored and only the energy conservation equation of zeolite was considered. Temperature distribution of supplied water was given from the 1D calculation of the Zeolite Boiler in **Fig. 4.35**. At the bottom (x = 500 mm), temperature difference between maximum and minimum T_{zeo} reached around 55 °C. **Figure 4.36** also shows the T_{zeo} distribution calculated by 1D model and in-plane representative temperature of each cross-sectional area in 3D model T_{rep}. The discrepancies between each model is below 5 °C in spite of large temperature difference between T_{zeo} and T_w. Temperature difference between the maximum temperature calculated by 3D model and the result of 1D model is around 15 °C without considering adsorption process. This temperature difference is the reason of discrepancy of 1D model and experimental result at the bottom of the heat exchanger. Since the discrepancies between 1D model and 3D model is below 5 °C, adequacy of 1D model was confirmed. Nevertheless, noting that the 1D model may slightly overestimate the heat recovery.

The other test using a lower q_0 = 0.052 kg/kg zeolite was conducted. The test conditions were set to m_{zeo} = 10 kg/h, m_{inj} = 1.32 kg/h and m_w = 1.50 kg/h, respectively. **Table 4.8** summarizes experimental conditions and results. The experimental and numerical analysis results in different q_0 are shown in **Fig. 4.37**. The zeolite with lower q_0 generates more adsorption heat resulting higher temperature. The numerical analysis can capture this tendency as shown in **Fig. 4.37**. The results of the heat increasing rate and the heat recovery rate are summarized in **Table 4.8**. A lower heat recovery rate compared with the full-scale Zeolite Boiler in Tanegashima (described in the following section) is obtained due to the lack of heat transfer area in the bench-scale Zeolite Boiler, and less m_{inj} than m_{inj_max}. The heat increasing rate in the case of q_0 = 0.052 kg/kg is higher than that of q_0 = 0.060 kg/kg because more adsorption heat is generated by lower q_0.

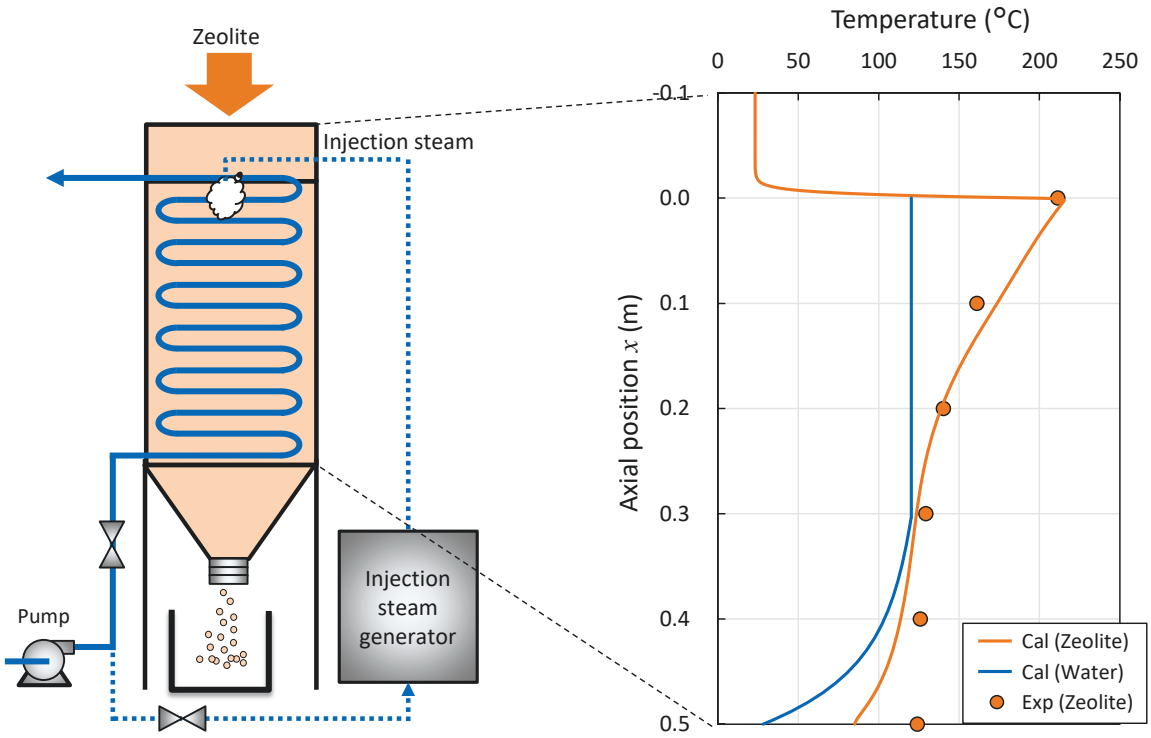

Fig. 4.35. Experimental and numerical analysis result of Zeolite Boiler test.

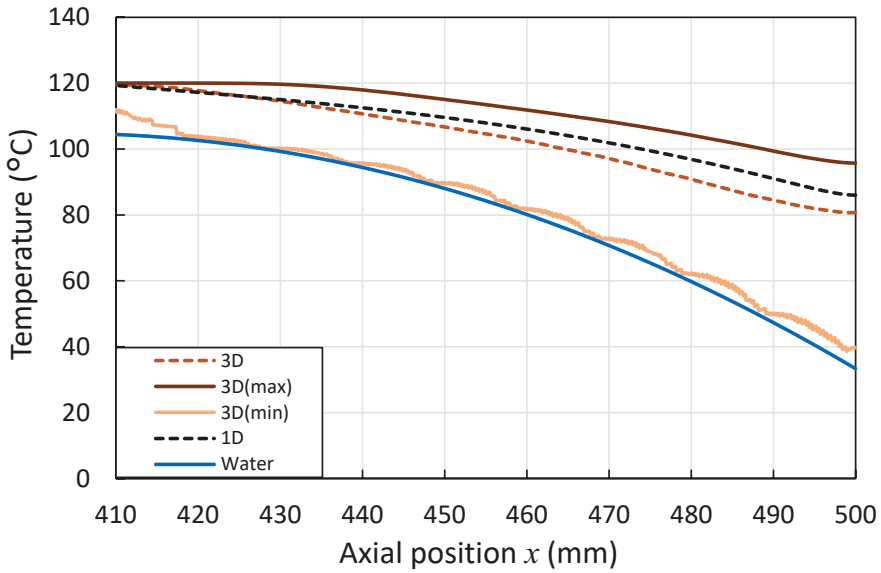

Fig. 4.36. Change in axial temperature distribution calculated by 3D and 1D model around the bottom.

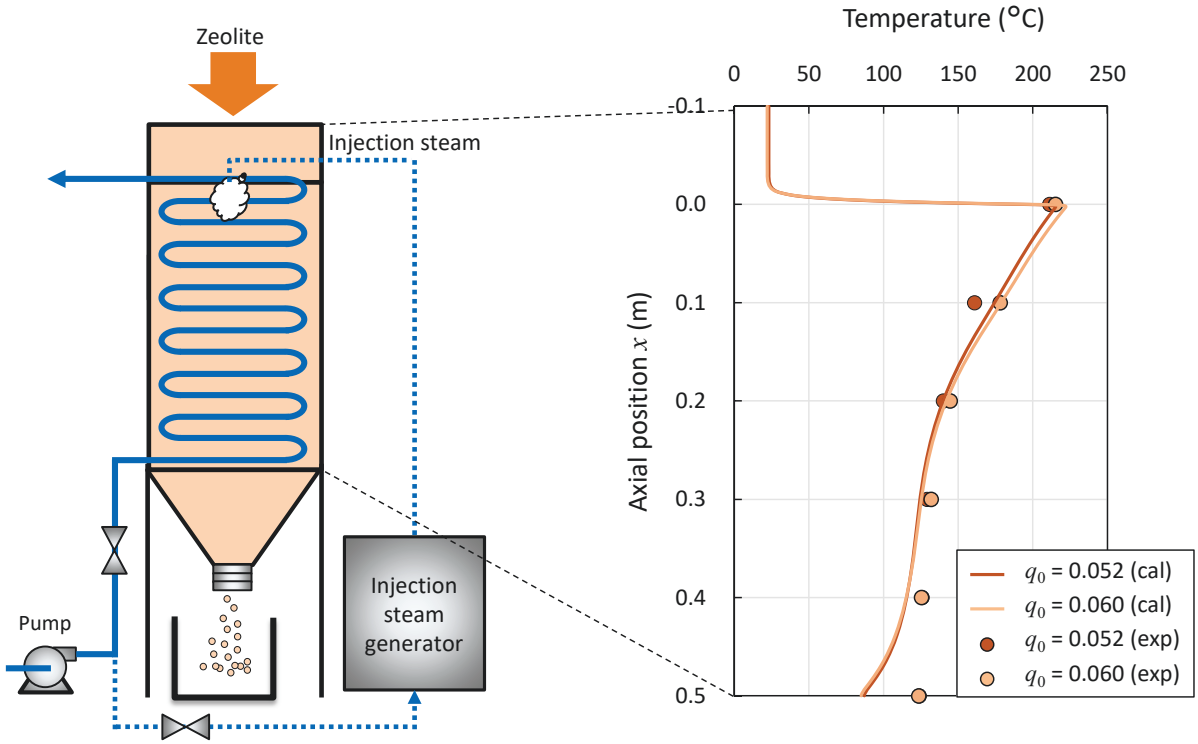

Fig. 4.37. Experimental and numerical analysis result of Zeolite Boiler test in different initial water uptake.

Table 4.8. Experimental conditions and results of Zeolite Boiler test.

Initial water uptake	(kg/kg)	0.060	0.052
Mass flow rate of zeolite	(kg/h)	9.95	10.08
Mass flow rate of injection steam	(kg/h)	1.26	1.32
Mass flow rate of supplied water	(kg/h)	1.38	1.50
Heat increasing rate	(%)	6.9	10.8
Heat recovery rate	(%)	50.3	49.8

4.7 Performance of full-scale Zeolite Boiler in Tanegashima

In this section, the 1D numerical simulation model validated in **4.6** was adapted to predict the performance of the full-scale Zeolite Boiler in Tanegashima (**4.7.1**). The relevant parameters of Zeolite Boiler were summarized (**4.7.2**) and the effect of each parameter on the performance was investigated (**4.7.3**). A comprehensive design method of Zeolite Boiler was proposed via the performance prediction of the full-scale Zeolite Boiler.

4.7.1 Heat transfer model

Before predicting the performance of the full-scale Zeolite Boiler in Tanegashima, an equivalent radius r_c in **Eq. (4.32)** of the heat transfer model in the 1D simulation model must be determined for the full-scale Zeolite Boiler. The stainless multi-tubular heat exchanger (φ_{tube} =15.9 mm, and t = 1.2 mm) of which header has 60 ° staggered tube array with 1.5φ_{tube} of pitch was assumed to be installed in the full-scale Zeolite Boiler. **Table 4.9** shows the relationship between the d_c and the maximum installable number of tubes n_{bt}.

For the heat transfer coefficient of 1D model, the equivalent radius r_c = 6.8 mm geometrically equivalent to the cross-section area surrounded by three tubes (hatched zone in **Fig. 4.38**) was given in **Eq. (4.32)**, and approximation of the 1D model was evaluated comparing to the 3D model. A heat exchanger with the length of 0.1 m was built on COMSOL Multiphysics 5.3a® and the analysis domain was set considering symmetry of the triangles shown in **Fig. 4.38**.

In the same manner as the calculation of bench-scale Zeolite Boiler, adsorption process was ignored and only the energy conservation of zeolite was computed. The inlet T_{zeo} was set to 230 °C with the mass flow rate of zeolite of 1500 kg/h. Temperature of supplied water into the heat exchanger was set to 120 °C. The configuration of 3D model and T_{zeo} distribution are shown in **Fig. 4.38**. The numerical analysis result of axial T_{zeo} distribution calculated by the 3D model and the 1D model are shown in **Fig. 4.39**. In-plane representative temperature of each cross-sectional area in 3D model T_{rep} was defined as **Eq. (4.54)**. There are few discrepancies between these models. From this result, adequacy of applying r_c = 6.8 mm to the 1D model was confirmed.

Table 4.9. Number of tubes of heat exchanger at each diameter.

Diameter of chamber d_c (m)	1.0	1.1	1.2	1.3	1.4	1.5
Number of tubes n_{bt}	1525	1819	2215	2581	3037	3463

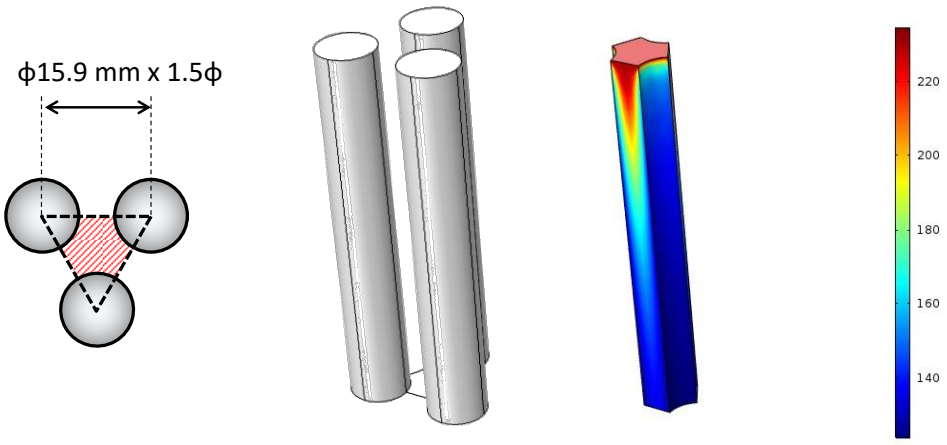

Fig. 4.38. 3D modeling of heat exchanger of full-scale Zeolite Boiler.

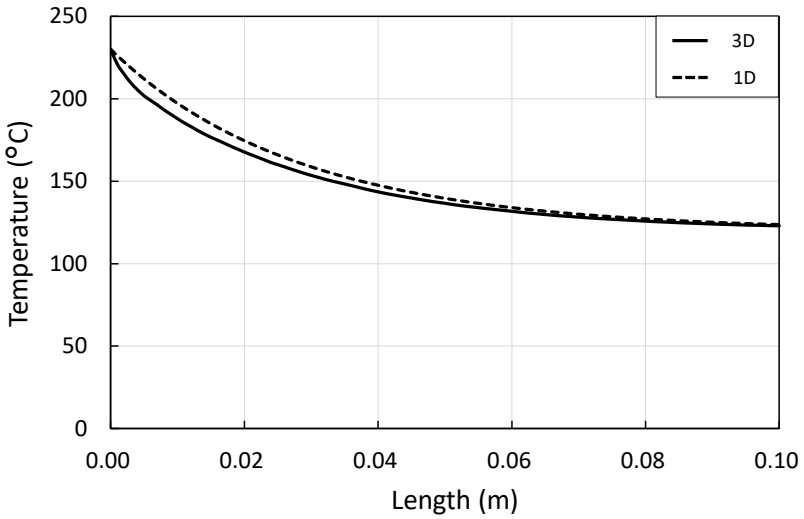

Fig. 4.39. Axial zeolite temperature distribution of 3D model and 1D model of full-scale Zeolite Boiler.

4.7.2 Design parameters of Zeolite Boiler

The design parameters of Zeolite Boiler are diameter of chamber d_c, length of heat exchanger L, mass flow rate of zeolite m_{zeo}, mass flow rate of injection steam m_{inj}, initial water uptake on zeolite q_0, pressure of generated steam p_w, and mass flow rate of supplied water (= generated steam) m_w. The linkage flow diagram of relationship among each parameter is shown in **Fig. 4.40**. The space velocity is calculated by the volumetric flow rate of zeolite and the effective volume of chamber packed with zeolite calculated by the d_c, L and n_{bt}. The total heat transfer area depends on only L and n_{bt}. The ultimate water uptake on exhaust zeolite q_{out} is determined by the m_{zeo}, m_{inj} and q_0. The difference between q_{out} and q_0 determines the total heat output by zeolite. The temperature difference between T_{zeo} and saturation temperature of generated steam T_{sat} under p_w determines the heat flux. The space velocity, heat transfer area and total heat output and flux determines heat recovery while zeolite passes through the heat exchanger. The m_w and the total heat recovery (= total transferred heat from zeolite to supplied water) determines the steam quality at the outlet of heat exchanger, and thereby the fuel saving can be calculated. The heat recovery rate was calculated by the total transferred heat and the potential heat recovery. These geometric and operation parameters were discussed in the following sections.

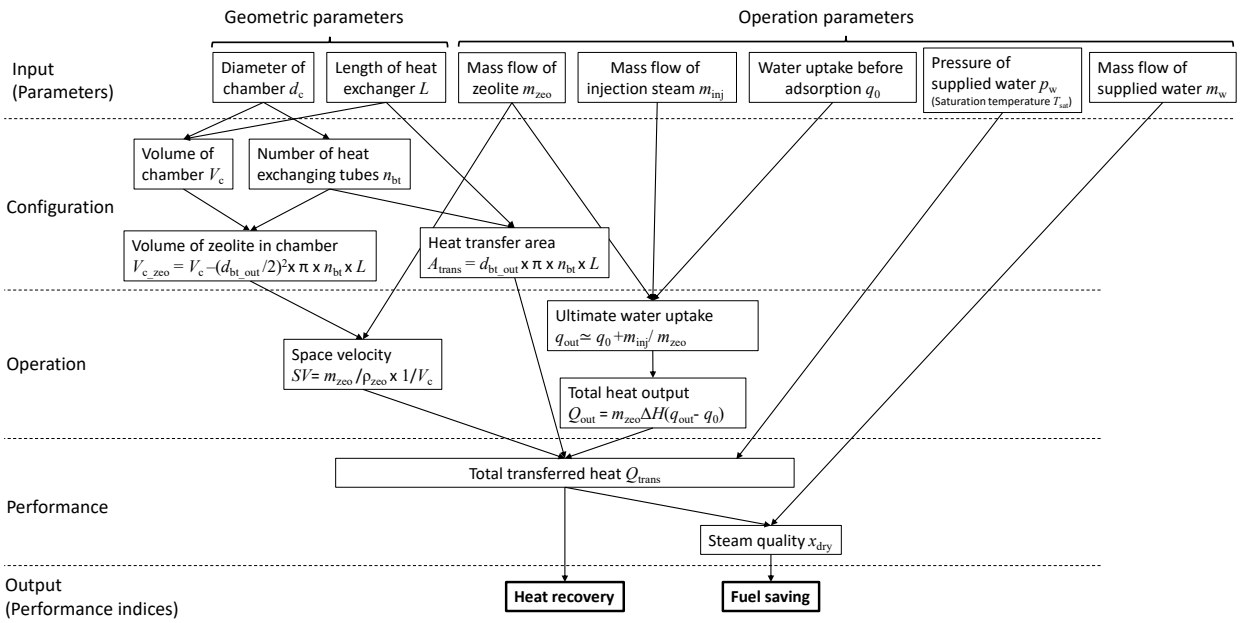

Fig. 4.40. Linkage flow diagram of relationship among each parameter of Zeolite Boiler.

4.7.3 Performance prediction of full-scale Zeolite Boiler

(1) Example model

The performance of the full-scale Zeolite Boiler in Tanegashima was predicted. In the experiment, superheated steam should be generated to evaluate the enthalpy of generated steam. In the full-scale Zeolite Boiler, a drain separator was assumed to be placed at the outlet of heat exchanger and separated water was back to before the pump as shown in **Fig. 4.41**. The mass flow rate of drain water m_w' can be calculated by **Eq. (4.55)**.

$$m_w' = m_w(1 - x_{dry}) \tag{4.55}$$

The inlet temperature of supplied water T_{w0} for the Zeolite Boiler can be calculated by **Eq. (4.56)**.

$$T_{w0} = \frac{m_w' T_{sat} + m_{w0} T_{amb}}{m_w} \tag{4.56}$$

The existing boiler generates excess exergy with high temperature/pressure steam (160 °C /0.6 MPa) than it is needed (120 °C/0.2 MPa). The Zeolite Boiler can reduce the steam consumption generated by the existing boiler, while generated steam by Zeolite Boiler has lower exergy with lower temperature/pressure (120 °C/0.2 MPa). The fuel saving of existing boiler can be calculated by **Eq.**

(4.57) considering the boiler efficiency η_{EB} of 0.9. In this study, change in boiler efficiency with change in load factor of the existing boiler was ignored.

$$FS = \frac{(m_w'' - m_{inj})h_w^{EB}}{\eta_{EB}} \cdot \frac{1}{HHV_{oil}} \tag{4.57}$$

where m_w" is the mass flow rate of dry saturation steam which is substantial output steam from the Zeolite Boiler. The heating value of heavy oil HHV_{oil} was 38.9 MJ/L.

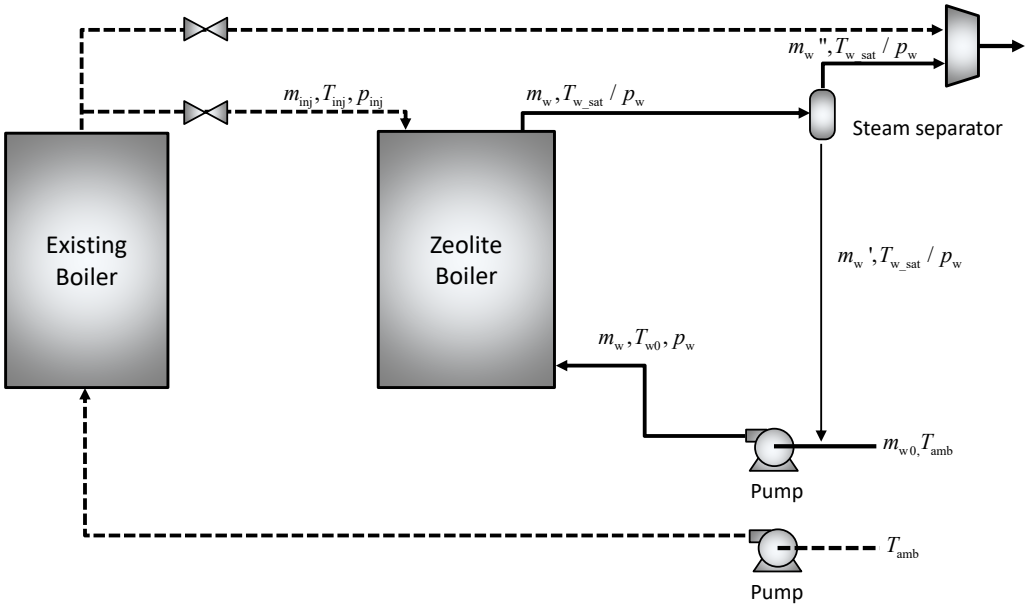

Fig. 4.41. Process flow diagram of Zeolite Boiler.

Distributions of T_{zeo}, T_w and q of example case are shown in **Fig. 4.42**. The conditions were temporally set to m_{zeo} = 1500 kg/h, m_w = 350 kg/h, d_c = 1.5 m, L = 1.5 m, q_0 = 0.06 kg/kg and m_{inj} = 266 kg/h calculated by **Eq. (4.44)**. The effect of the d_c, L, m_w, m_{inj}, q_0 and p_w on the performance were investigated in the following section.

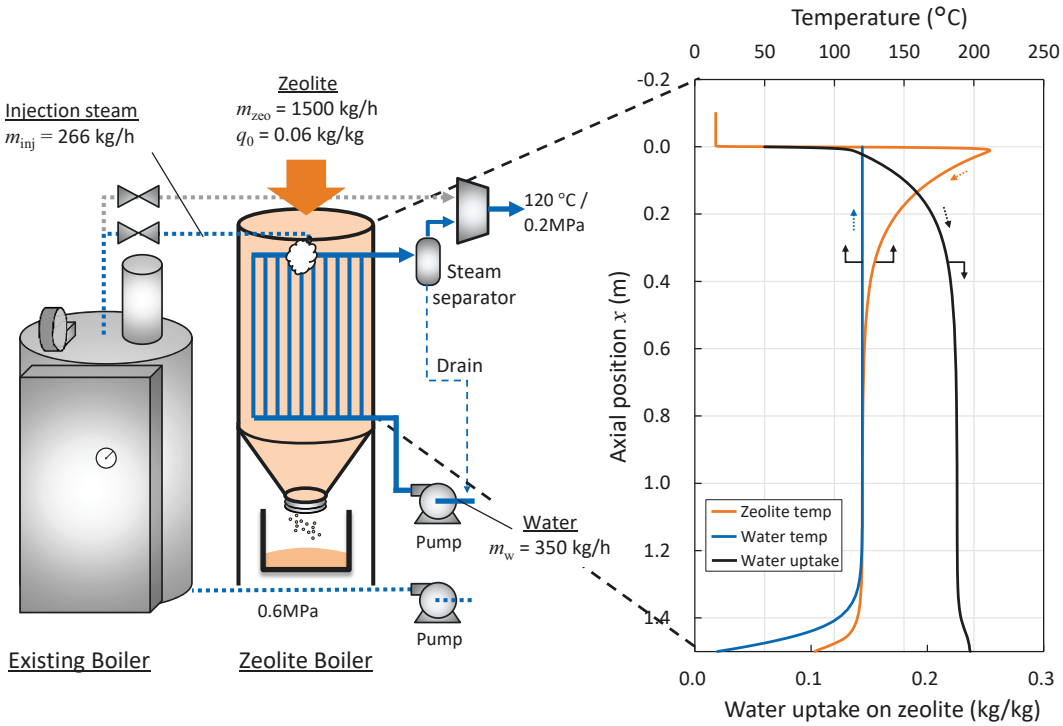

Fig. 4.42. Distributions of zeolite and water temperatures and water uptake in full-scale Zeolite Boiler.

(2) Effect of chamber diameter d_c

Smaller d_c requires longer L to keep the same heat transfer area as shown in **Fig. 4.43** because of reduction of n_{bt} as summarized in **Table 4.9**. Since the Zeolite Boiler co-operates with the existing boiler, it requires additional installation place. The d_c is limited to 1.5 m so that the footprint of Zeolite Boiler may be roughly equal to that of existing package boiler. The T_{zeo} distribution predicted by the numerical simulation in the case of d_c = 1.5 m is shown in **Fig. 4.44**. The heat transfer area is 259 m^2 corresponding to L = 1.5 m. The calculation conditions were set to m_{zeo} = 1500 kg/h, m_w = 350 kg/h, m_{inj} = 266 kg/h and q_0 = 0.06 kg/kg, respectively. The T_{zeo} decreases to the saturation temperature (= 120 °C) around x = 1.0 m where further heat recovery is not expected in the case of 259 m^2 of heat transfer area.

Figure 4.44 also shows various d_c of which L were calculated by the same heat transfer area of 259 m^2 and the installable number of heat exchanging tubes. The T_{zeo} distributions of various d_c in the normalized length are summarized in **Fig. 4.44**. As can be seen from **Fig. 4.44**, the d_c gives little impact on the performance. The d_c should keep large as along as install space is allowed because the total height of Zeolite Boiler can be reduced. In this study, the d_c was set to 1.5 m for all calculations.

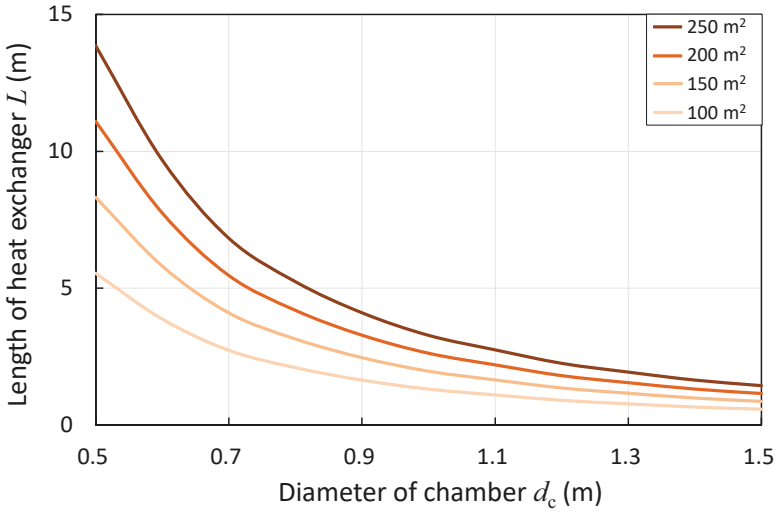

Fig. 4.43. Required length of heat exchanger as a function of diameter of chamber for the same heat transfer area.

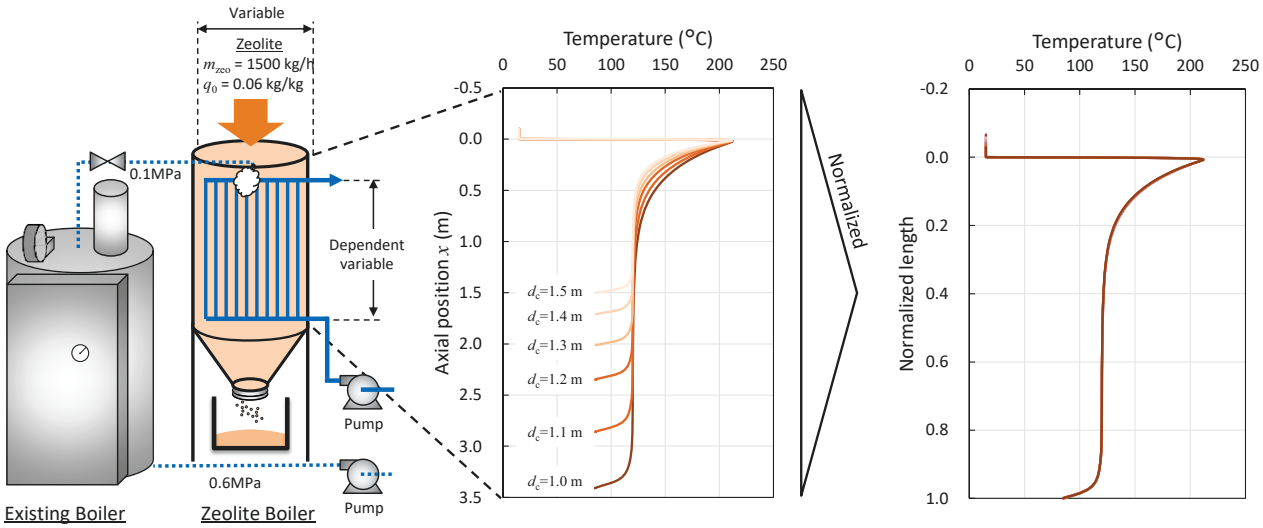

Fig. 4.44. Change in zeolite temperature with various diameter d_c.

(3) Effect of length of heat exchanger L

The change in the fuel saving and the exhaust T_{zeo} as a function of L are shown in **Fig. 4.45**. The calculation conditions were set to m_{zeo} = 1500 kg/h m_w = 350 kg/h and q_0 = 0.06 kg/kg, respectively. The m_{inj} was calculated by **Eq. (4.58)**.

$$m_{inj} = m_{zeo}(q_t - q_0) \tag{4.58}$$

where q_t is the target water uptake at the bottom of heat exchanger. The q_t was set to 0.223 kg/kg determined in the following section.

As can be seen from **Fig. 4.45**, the addition of L increases the fuel saving because of improving the heat recovery of sensible heat of zeolite at the bottom. However, the fuel saving reached maximum when the L = 1.5 m was given, which indicates the maximum heat recovery was achieved in this condition. Excess L (= chamber length) increases both installation cost and the heat leakage from the outer wall of chamber. In this study, the length at which 99% of maximum fuel saving can be achieved was selected i.e. the slope of increase in the fuel saving as compared to the increase in L is nearly zero.

In the example calculation in **Fig. 4.45**, the fuel saving reached 99% of the maximum fuel saving in the case of L > 1.0 m. The optimized L at each condition (m_{zeo}, m_{inj}, m_w and q_0) should be selected.

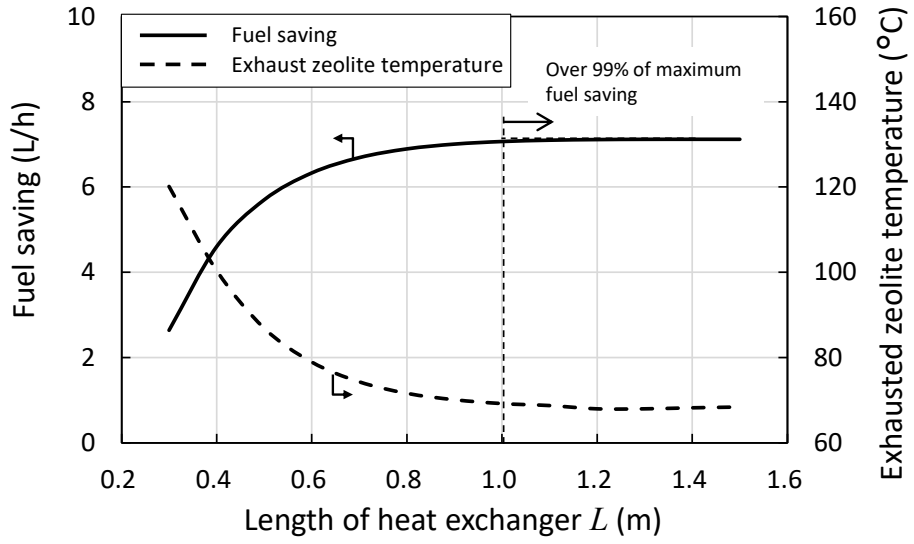

Fig. 4.45. Fuel saving and exhausted zeolite temperature for various heat exchanger length L.

(4) Effect of mass flow rate of supplied water m_w

The effect of the m_w on the fuel saving was evaluated. The calculation conditions were set to m_{zeo} = 1500 kg/h, m_{inj} = 245 kg/h (q_t in **Eq. (4.58)** is 0.223 kg/kg), q_0 = 0.06 kg/kg and L = 1.0 m, respectively. The effect of m_w on the fuel saving is shown in **Fig. 4.46**. Increase in the m_w decreases steam quality of generated steam under the same m_{inj} resulting decline in the fuel saving. However, the decrease in the fuel saving as compared to increase in the m_w is slight due to the heat recovery of separated drain. When the m_w decreases < 340 kg/h, generated steam becomes super-heated steam. However, the fuel saving declines due to decrease in heat flux from the zeolite bed to the super-heated steam because of decrease in the temperature difference (T_{zeo} - T_w) and heat transfer from the zeolite bed

to the super-heated steam. The m_w should be controlled to maximize the fuel saving, so is controlled to keep the quality of generated steam is close to 1.0 (in this case, m_w = 340~350 kg/h should be set).

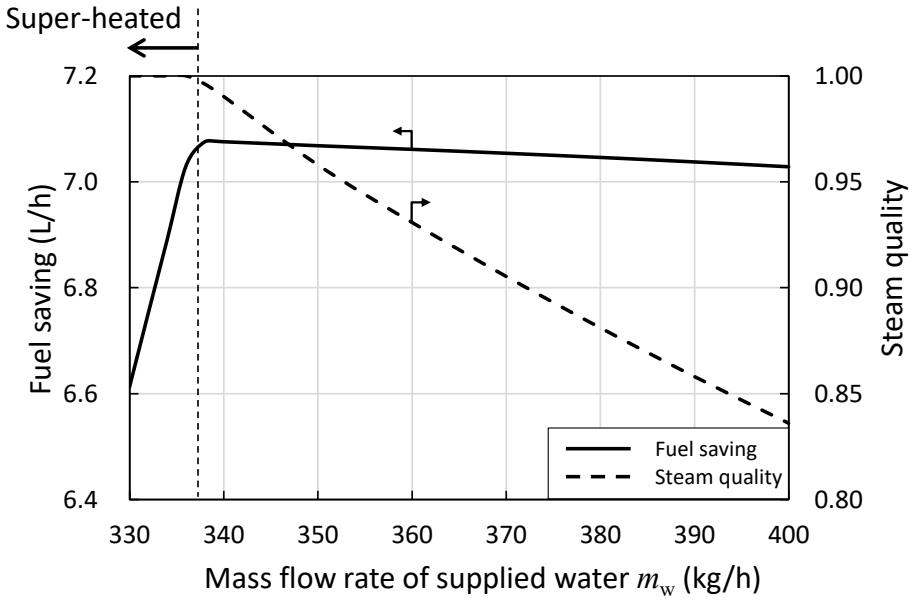

Fig. 4.46. Effect of mass flow of supplied water m_w on fuel saving and steam quality.

(5) Effect of mass flow rate of injection steam m_{inj}

The distribution of T_{zeo} and q when different m_{inj} is injected are shown in **Fig. 4.47** with the calculation conditions. Both the fuel saving and the heat recovery rate are improved with increase in the m_{inj} because of increase in total heat generation. Nevertheless, excess steam injection decreases fuel saving. As can be seen from **Fig. 4.47**, additional adsorption and accompanying heat generation occur around the bottom of the heat exchanger. However, heat transfer is too slow to recover the exothermic heat without slip and thereby outlet T_{zeo} increases. This means excess steam injection gives a negative effect on the fuel saving, while q_{out} and accompanying heat recovery rate are improved. This phenomenon gives a peak to the fuel saving. The effects of m_{inj} on the fuel saving and the heat recovery rate are shown in **Fig. 4.48**. The L was set to 1.0 m which is determined by the above section. As can be seen from **Fig. 4.48**, the fuel saving has a peak as a function of m_{inj}, while the heat recovery rate simply increases with increase in the m_{inj}. The fuel saving is maximized at m_{inj} = 245 kg/h (q_t = 0.223 kg/kg calculated by **Eq. (4.58)**). This discordant operating mode to maximize the fuel saving and the heat recovery rate is inconvenient for operators in heat discharging stations. This shortcoming is resolved in the following section (described in **4.8.1**) by introducing an additional heat exchanger.

The effect of m_{zeo} on the fuel saving vs. m_{inj} is shown in **Fig. 4.49**. At all conditions of the m_{zeo}, the case of q_t = 0.223 kg/kg gives the maximum fuel saving.

The best m_{inj} (and q_t) which gives the maximum fuel saving is determined by heat transfer from the zeolite bed to the water. **Figure 4.50** shows the effect of pitch of each tube in the heat exchanger as a function of m_{inj} under the same m_{zeo} = 1500 kg/h and q_0 = 0.06 kg/kg. Narrower pitch of each tube decreases r_c and increases the overall heat transfer coefficient. Hence, the best m_{inj} increases slightly as shown in **Fig. 4.50** because additional adsorption and accompanying exothermic heat around the bottom can be recovered. The narrow pitch < $5\varphi_{zeo}$ may disturb the flow of zeolite [13], so $1.5\varphi_{tube}$ of pitch (the distance between each tube $\simeq 5\varphi_{zeo}$) was selected.

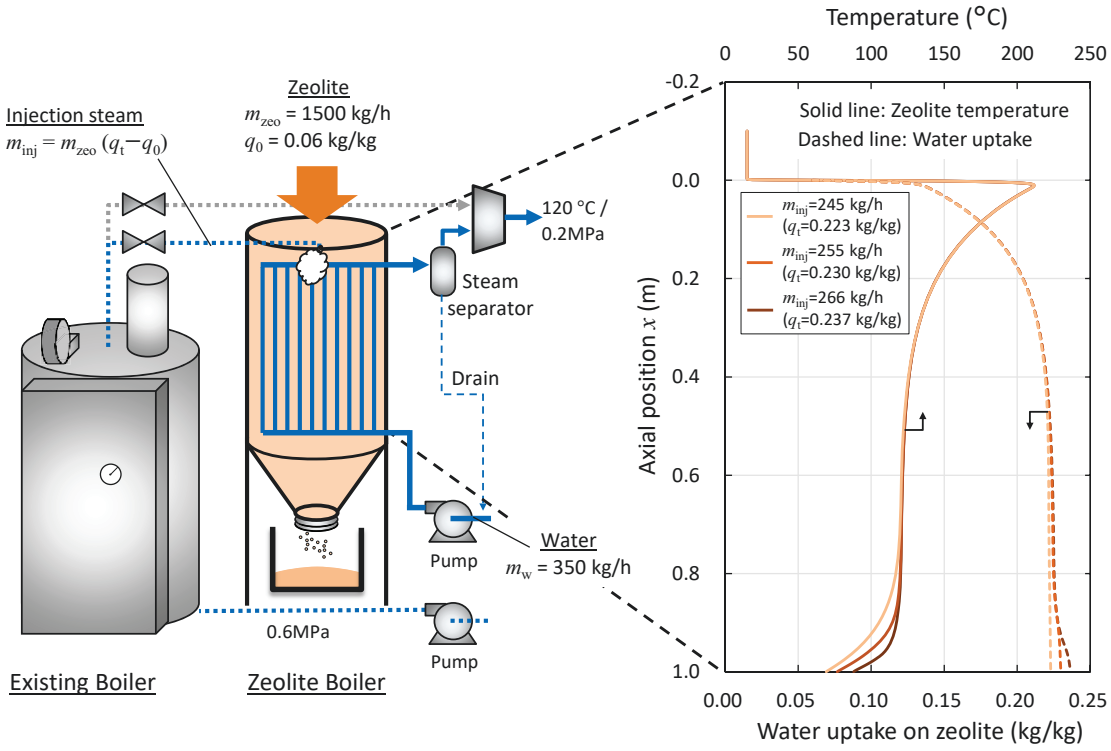

Fig. 4.47. Distribution of zeolite temperature and water uptake in different injection steam mass flow m_{inj}.

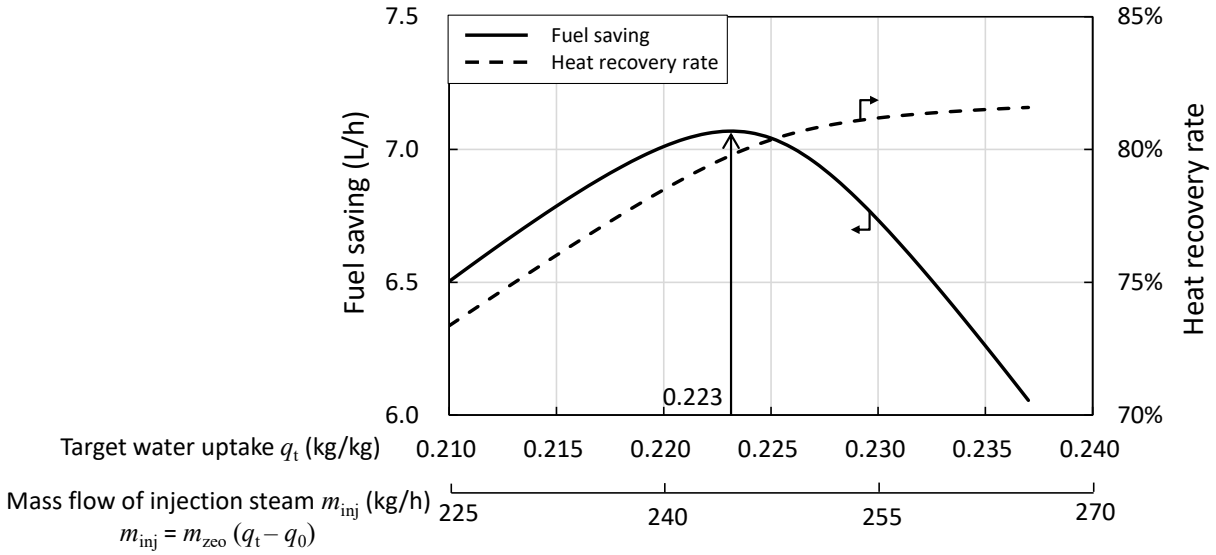

Fig. 4.48. Effects of mass flow rate of injection steam m_{inj} on fuel saving and heat recovery rate.

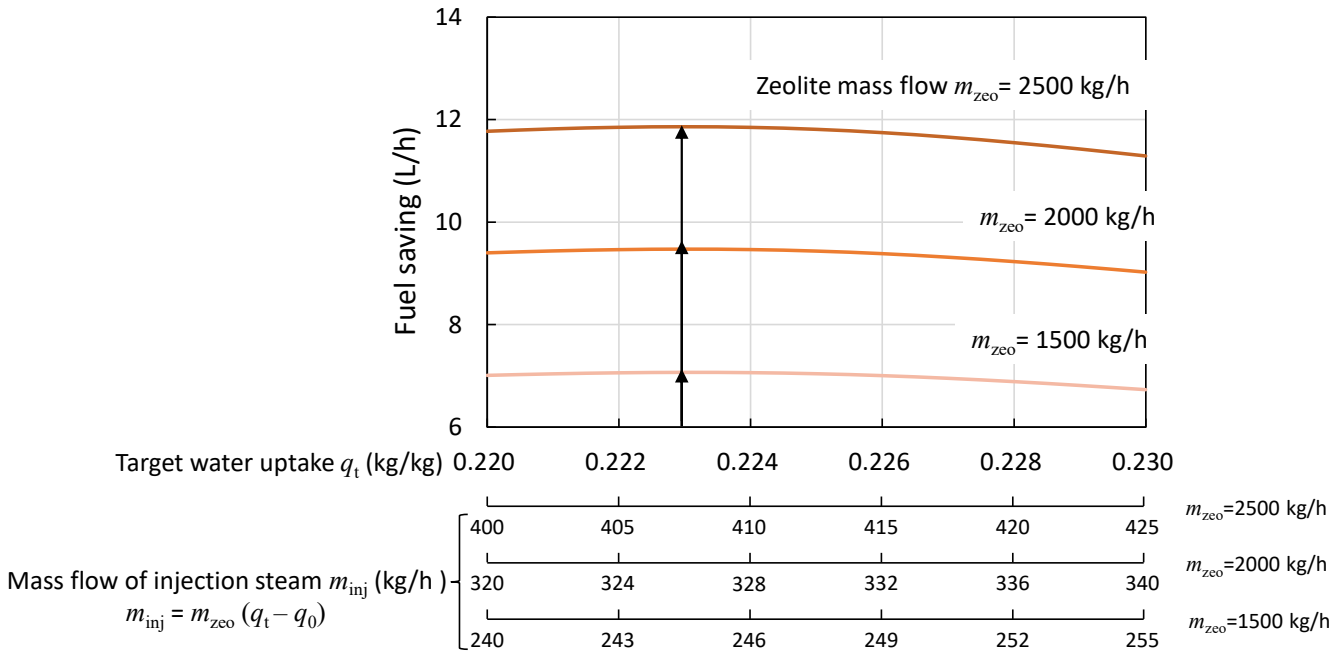

Fig. 4.49. Effect of mass flow rate of zeolite m_{zeo} on fuel saving vs. mass flow rate of injection steam m_{inj}.

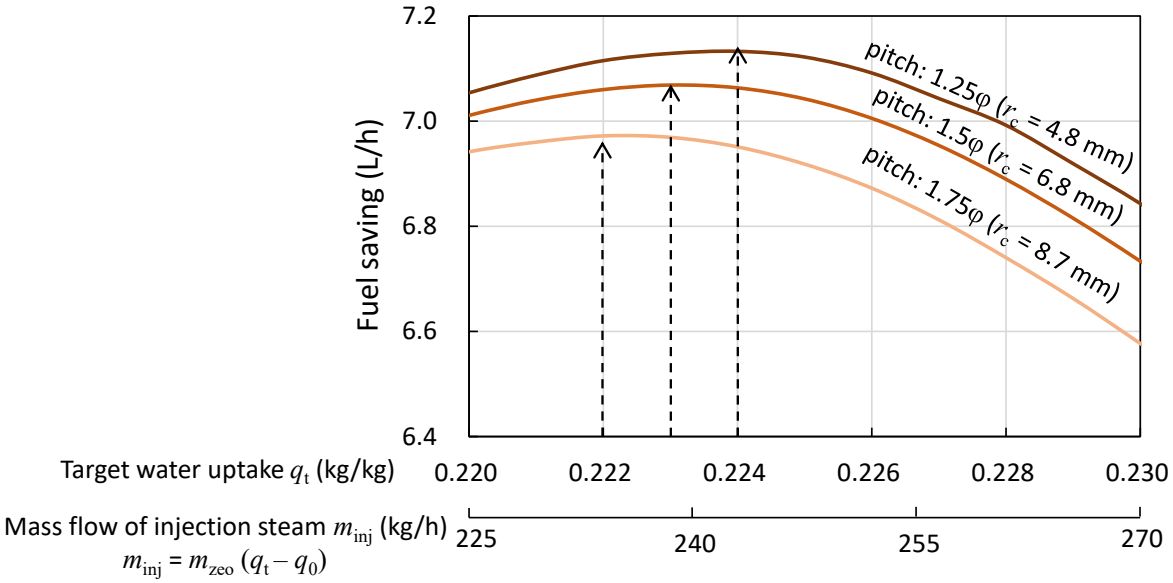

Fig. 4.50. Effects of mass flow rate of injection steam m_{inj} and pitch of tubes on fuel saving.

(6) Effect of initial water uptake on zeolite q_0

The effect of q_0 (0.06 ~ 0.13 kg/kg) on the fuel saving is shown in **Fig. 4.51**. The calculation conditions were set to m_{zeo} = 1500 kg/h, m_w = 350 kg/h and L = 1.0 m, respectively. Basically, larger q_0 decreases adsorption heat and thereby decreases the fuel saving. The Zeolite Boiler cannot reduce the fuel consumption of existing boiler in the case of q_0 > 0.12 kg/kg.

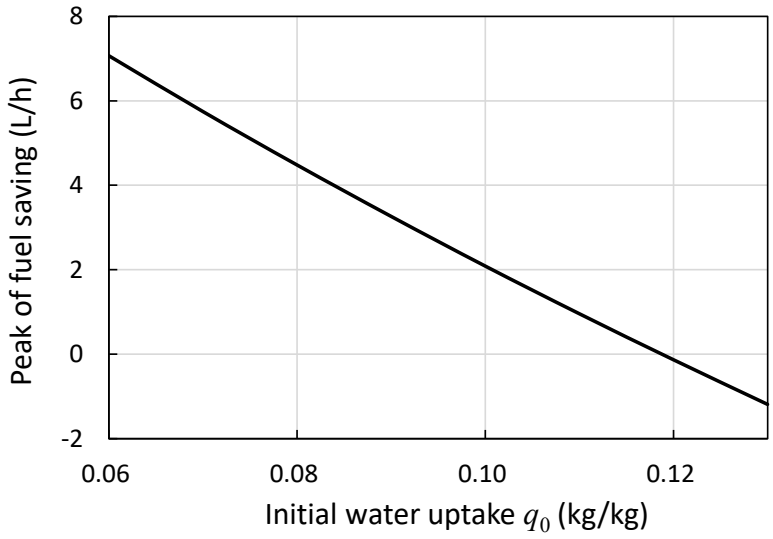

Fig. 4.51. Effect of inlet water uptake q_0 on fuel saving.

(7) Pressure of generated steam p_w

The distribution of T_{zeo} and T_w in the case of different p_w (= saturation temperature T_{sat}) are shown in **Fig. 4.52** with the calculation conditions. The m_w was controlled to keep the quality of generated steam is close to 1.0. When the p_w of saturated steam is increased, T_{sat} increases following steam table and heat flux which is determined by (T_{zeo} - T_w) decreases. In addition, zeolite is exhausted from the bottom with higher temperature when p_w and T_{sat} are set to higher value. From above reasons, the mass flow rate of generated steam and accompanying the fuel saving decrease.

The effect of p_w (or T_{sat}) on the fuel saving is shown in **Fig. 4.53**. The fuel saving decreases with increase in p_w and T_{sat}. The Zeolite Boiler cannot conserve the fuel consumption of the existing boiler in the case of p_w > 0.62 MPa (T_{sat} =160 °C). Since the heat demand in Tanegashima requires up to 0.2 MPa steam for their food processing process, the p_w was set to 0.2 MPa in the techno-economic and environmental analyses in Chapter 6.

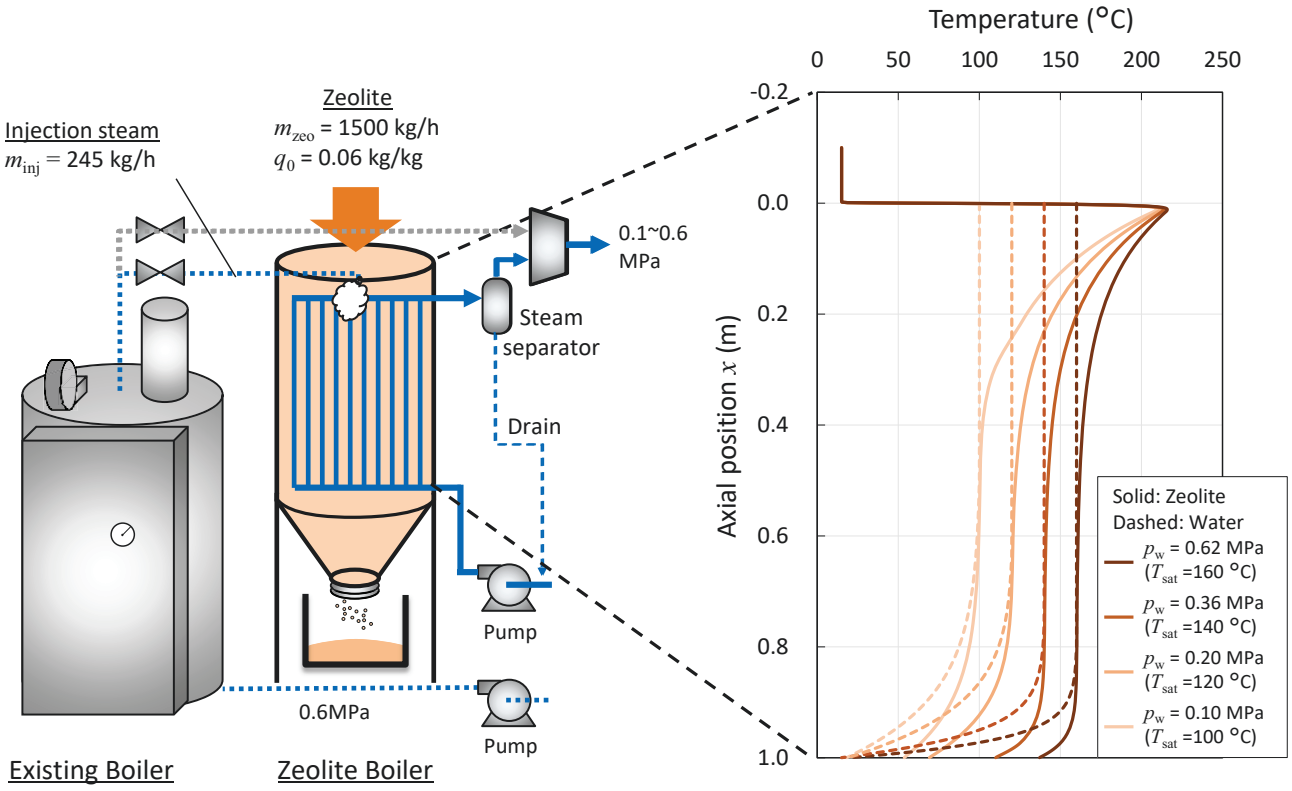

Fig. 4.52. Distribution of zeolite and water temperature in different pressure of generated steam p_w.

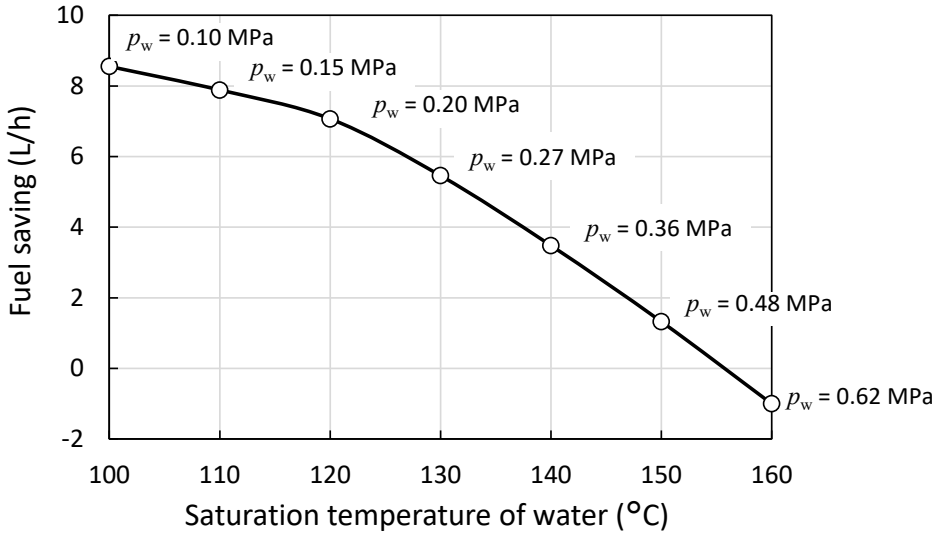

Fig. 4.53. Effect of pressure (saturation temperature) of generated steam p_w on fuel saving.

(8) Design method of Zeolite Boiler

The comprehensive design method of Zeolite Boiler is proposed as follows.

- Determine the d_c considering the space for installation. (d_c = 1.5 m in this study)
- Determine the L achieving 99% of maximum fuel saving at each condition.
- Set the m_{inj} giving the maximum fuel saving ($m_{inj} = m_{zeo}(q_t - q_0)$, q_t = 0.223 kg/kg).
- Control the m_w to keep the quality of generated steam ≈ 1.0.
- Control the p_w < 0.62 MPa.

The distribution of T_{zeo}, T_w and q designed by this method were shown in **Fig. 4.54**.

The relationship between the fuel saving and the heat recovery rate is shown in **Fig. 4.55**. The maximum fuel saving of 7.1 L/h is obtained at the heat recovery rate of 80% in the case of m_{zeo} = 1500 kg/h, which gives the best performance with operating condition of m_{inj} = 245 kg/h (q_t = 0.223 kg/kg). The following section discussed the alternative processes to improve the performance toward upper right side of **Fig. 4.55**.

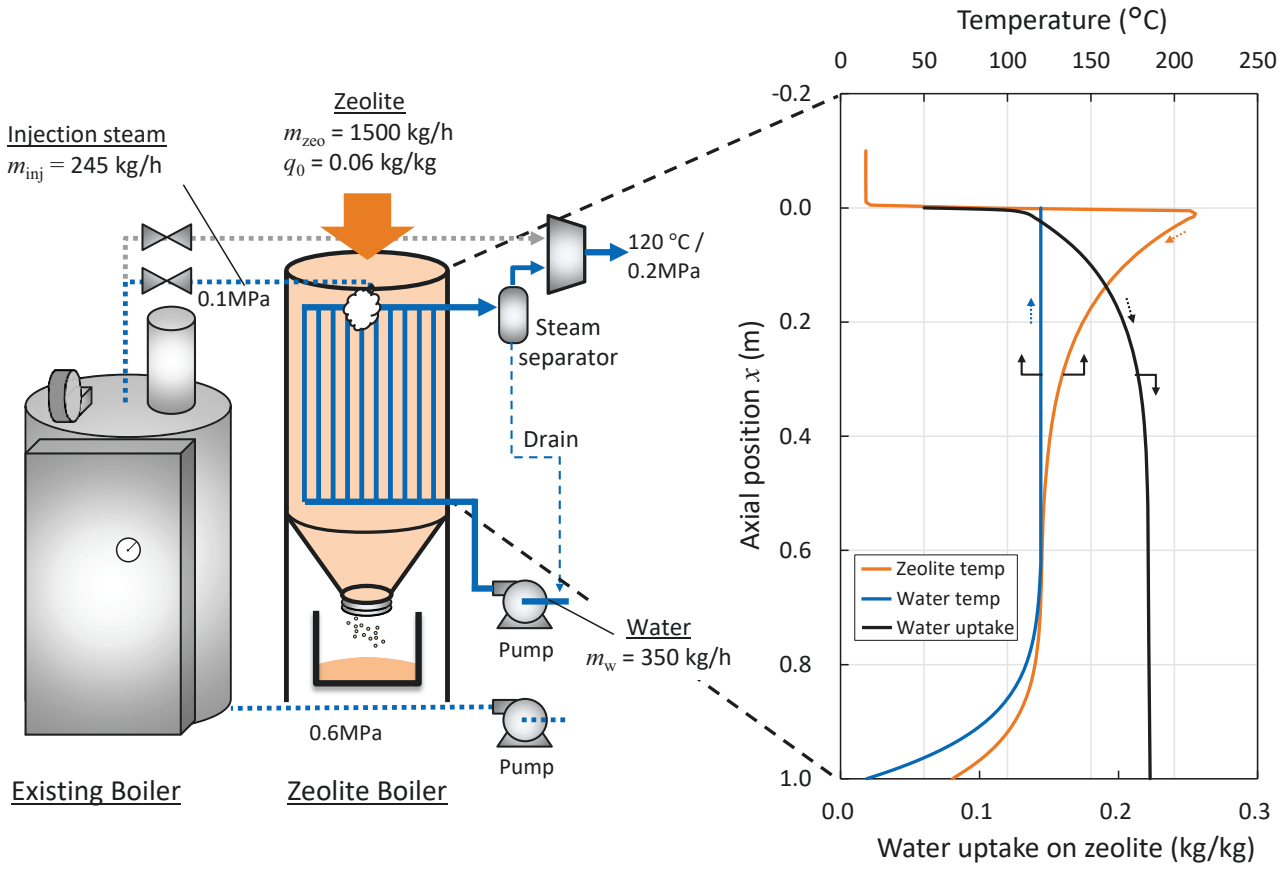

Fig. 4.54. Change in zeolite, water temperature and water uptake in optimized full-scale Zeolite Boiler.

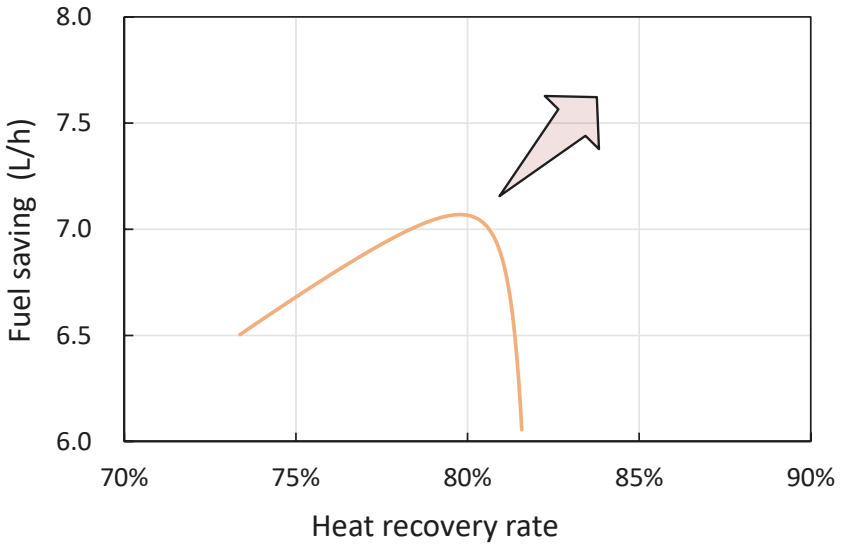

Fig. 4.55. Relationship between fuel saving and heat recovery rate.

4.8 Improving fuel saving and heat recovery

4.8.1 Addition of secondary heat exchanger

As shown in **Fig. 4.54**, the outlet T_{zeo} from the Zeolite Boiler is 60 ~ 80 °C, which means a certain amount of unrecovered heat remains in the zeolite. Recovery of this remaining sensible heat via a secondary heat exchanger increases the fuel saving, which gives similar function to economizers in commercial boiler system. The schematic design of Zeolite Boiler with the secondary heat exchanger is shown in **Fig. 4.56**. The secondary heat exchanger is settled below the primary heat exchanger and transfers the sensible heat of zeolite from the Zeolite Boiler to supplied water for the existing boiler.

The energy conservation equations of zeolite, gas and supplied water in the secondary heat exchanger part can be expressed by **Eqs. (4.59)**, **(4.60)** and **(4.61)**, respectively.

$$\begin{aligned}&\frac{\partial}{\partial x}\left(\rho_{\mathrm{zeo}} u_{\mathrm{zeo}} c_{p\mathrm{zeo}} T_{\mathrm{zeo}}\right)\\&=\frac{\partial}{\partial x}\left(\lambda_{\mathrm{zeo\_eff}}\frac{\partial T_{\mathrm{zeo}}}{\partial x}\right)-\alpha_{\mathrm{g\text{-}zeo}}\sigma_{\mathrm{g\text{-}zeo}}(T_{\mathrm{zeo}}-T_{\mathrm{g}})\\&-\alpha_{\mathrm{zeo\text{-}w2}}\sigma_{\mathrm{zeo\text{-}w2}}(T_{\mathrm{zeo}}-T_{\mathrm{w2}})-\alpha_{\mathrm{zeo\text{-}amb}}\sigma_{\mathrm{zeo\text{-}amb}}(T_{\mathrm{zeo}}-T_{\mathrm{amb}})+\rho_{\mathrm{zeo0}} r_{\mathrm{ad}}\Delta H\end{aligned} \tag{4.59}$$

$$\begin{aligned}&\frac{\partial}{\partial x}\left(\rho_{\mathrm{g}} u_{\mathrm{g}} c_{p\mathrm{g}} T_{\mathrm{g}}\right)\\&=\frac{\partial}{\partial x}\left(\lambda_{\mathrm{gax\_eff}}\frac{\partial T_{\mathrm{g}}}{\partial x}\right)-\alpha_{\mathrm{g\text{-}zeo}}\sigma_{\mathrm{g\text{-}zeo}}(T_{\mathrm{g}}-T_{\mathrm{zeo}})-\alpha_{\mathrm{g\_w2}}\sigma_{\mathrm{g\text{-}w2}}(T_{\mathrm{g}}-T_{\mathrm{w2}})-\alpha_{\mathrm{g\text{-}amb}}\sigma_{\mathrm{g\text{-}amb}}(T_{\mathrm{g}}-T_{\mathrm{amb}})\end{aligned} \tag{4.60}$$

$$-\frac{\partial}{\partial x}\left(\rho_{\mathrm{w2}} u_{\mathrm{w2}} c_{p\mathrm{w2}} T_{\mathrm{w2}}\right)=\alpha_{\mathrm{zeo\text{-}w2}}\sigma_{\mathrm{zeo\text{-}w2}}(T_{\mathrm{zeo}}-T_{\mathrm{w2}})+\alpha_{\mathrm{g\text{-}w2}}\sigma_{\mathrm{g\text{-}w2}}(T_{\mathrm{g}}-T_{\mathrm{w2}}) \tag{4.61}$$

The diameter, thickness, pitch and number of tubes of secondary heat exchanger were set to the same as those of primary heat exchanger. The Nusselt number of inner tubes in the secondary heat exchanger was given as 4.36 with the same assumption of the Zeolite Boiler without secondary heat exchanger (described in **4.6.5**). Thermal conduction of water in axial direction was negligible because the Peclet number of water flow was over 10. The inlet temperature of supplied water to the secondary heat exchanger is 15 °C.

The process flow diagram of Zeolite Boiler is shown in **Fig. 4.57**. The mass flow rate of supplied water to the secondary heat exchanger m_{w2} can be calculated by **Eq. (4.62)**.

$$m_{\mathrm{w2}}=m_{\mathrm{w\_EB}}-(m''_{\mathrm{w\_ZB}}-m_{\mathrm{inj}}) \tag{4.62}$$

where m_{w_EB} is the steam consumption in the heat demand. Since the Zeolite Boiler can generate m''_{w_ZB} = 340 kg/h with m_{zeo} = 1500 kg/h, the m_{w2} is equal to the m_{inj} ($m_{w2} = m_{inj}$) in the case of m_{w_EB} = 340 kg/h. As a representative case studies, **Fig. 4.58** shows the result of T_{zeo}, T_w, T_{w2} and q distribution in the Zeolite Boiler with the secondary heat exchanger in the cases of m_{w_EB} = 340, 750 and 1800 kg/h. The lengths of the primary L and secondary heat exchanger L_2 were set to 1.0 and 0.5 m, respectively.

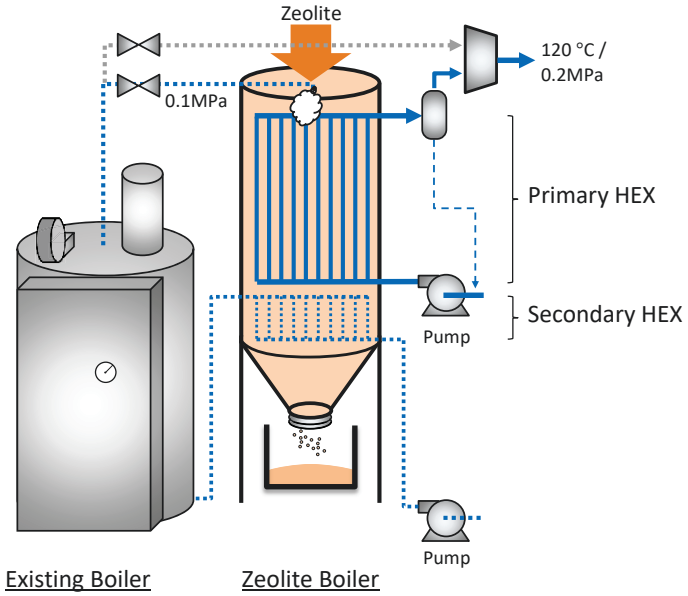

Fig. 4.56. Schematic design of Zeolite Boiler with the secondary heat exchanger.

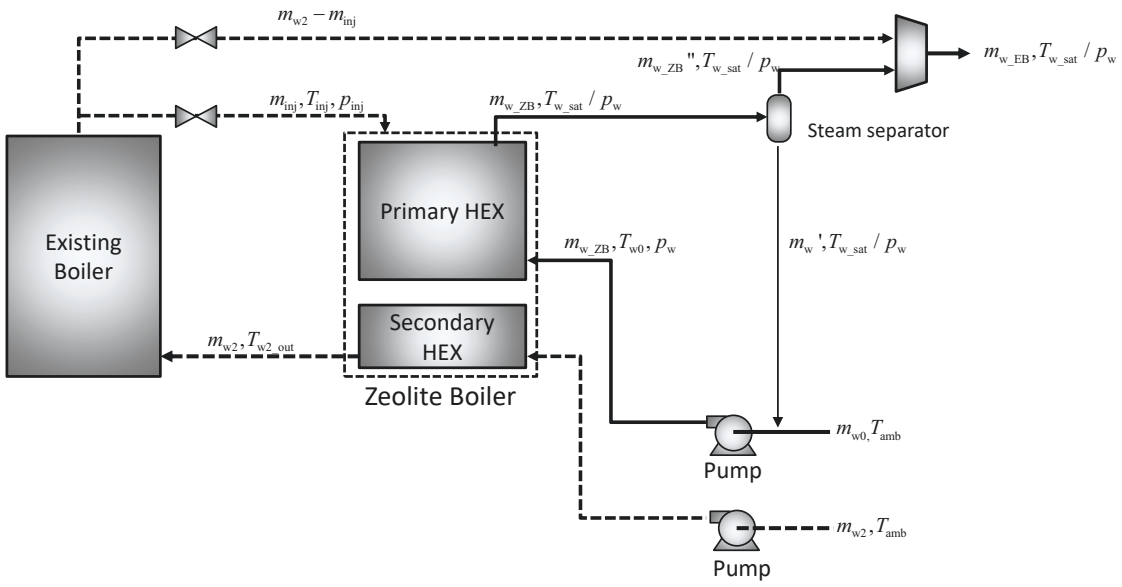

Fig. 4.57. Process flow diagram and schematic of Zeolite Boiler with the secondary heat exchanger.

The effect of m_{inj} (calculated by **Eq. (4.58)** using q_{t}) on the fuel saving is shown in **Fig. 4.59**. The length of secondary heat exchanger L_2 is determined by the same methodology as the primary heat exchanger, which is described in **4.7.3**. The effect of L_2 on the fuel saving and the outlet water temperature of secondary heat exchanger with $m_{\mathrm{w\_EB}}$ = 1800 kg/h are shown in **Fig. 4.60**. Longer L_2 increases the outlet temperature of supplied water and accompanying the fuel saving. In this condition, L_2 = 0.5 m is reasonable length because the fuel saving reaches 99% of the maximum fuel saving at this condition as can be seen from **Fig. 4.60**.

In the case of lower $m_{\mathrm{w\_EB}}$ and accompanying m_{w2} calculated by **Eq. (4.62)**, the exhausted zeolite still has remaining sensible heat as shown in **Fig. 4.58 (a)** due to slow heat transfer from the zeolite bed to the water. Hence, the fuel saving still has a peak as a function of m_{inj} as shown in **Fig. 4.59**, while the heat recovery rate simply increases with increase in the m_{inj} as well as the Zeolite Boiler without secondary heat exchanger described in **4.7.3**. The best q_{t} increases to 0.226 kg/kg from 0.223 kg/kg in the case of Zeolite Boiler without secondary heat exchanger because additional adsorption heat can be recovered via the secondary heat exchanger.

On the other hand, in the case of larger $m_{\mathrm{w\_EB}}$ and accompanying m_{w2}, the T_{zeo} exhausted from the Zeolite Boiler is cooled down to almost the inlet water temperature of 15 °C, because of the massive heat capacity of water in the secondary heat exchanger as shown in **Fig. 4.58 (c)**. The heat recovery rate of this case increases up to 99%, which means almost adsorption heat can be recovered. Two values of m_{inj} to maximize the fuel saving or the heat recovery rate of Zeolite Boiler without secondary heat exchanger agrees, and the issue of discordant operating mode is resolved.

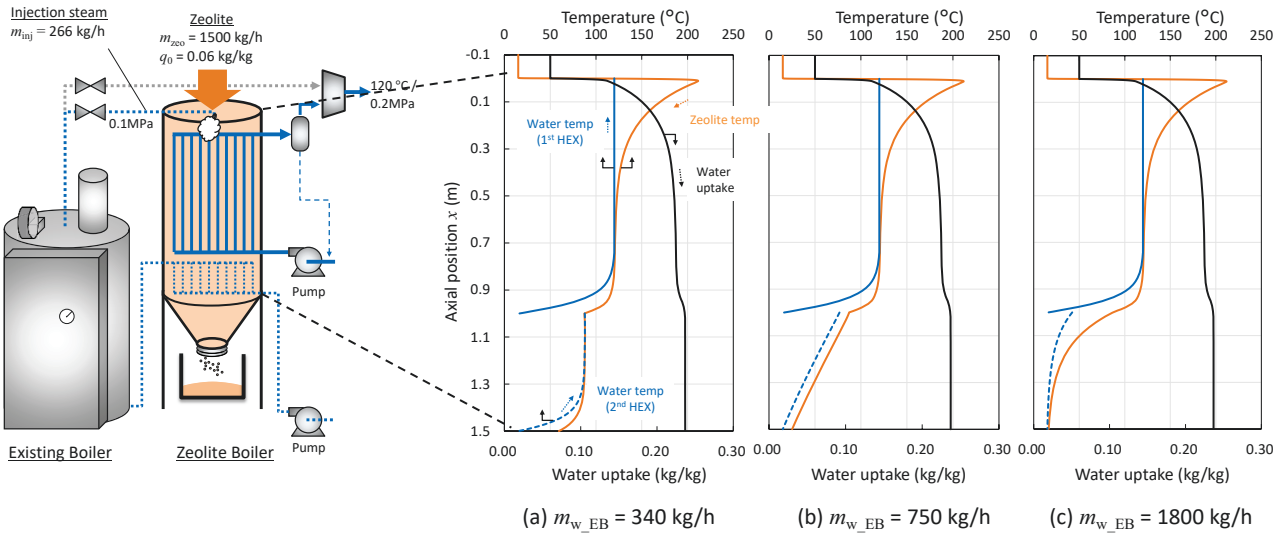

Fig. 4.58. Change in zeolite, water in primary heat exchanger, water in secondary heat exchanger and water uptake in Zeolite Boiler with the secondary heat exchanger.

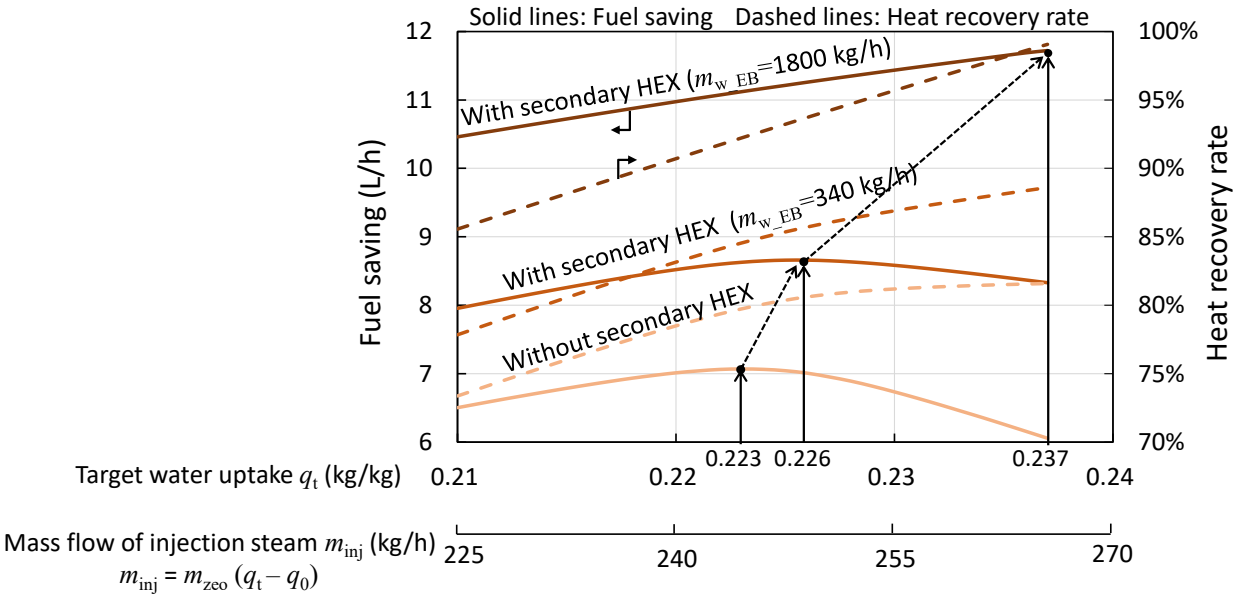

Fig. 4.59. Performance curve of Zeolite Boiler with the secondary heat exchanger.

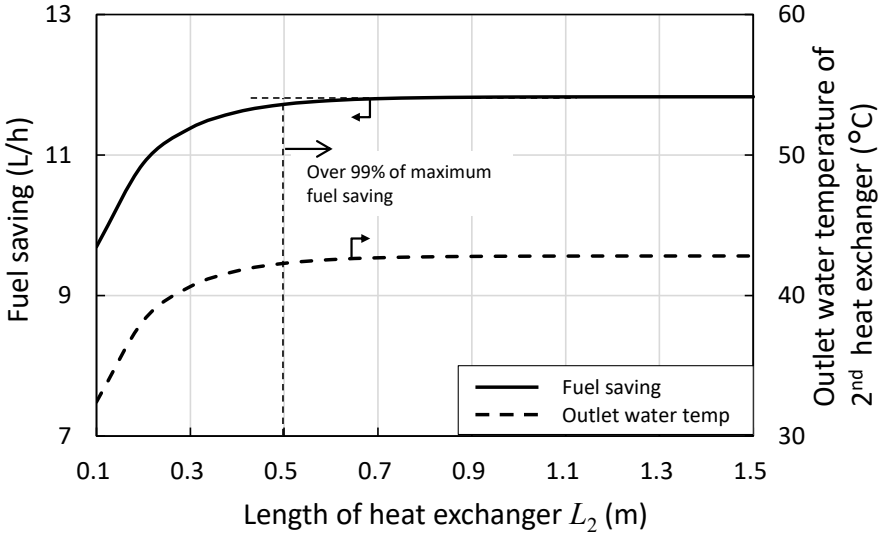

Fig. 4.60. Fuel saving and outlet water temperature vs. length of secondary heat exchanger L_2.

The effect of heat recovery via the secondary heat exchanger was determined by the balance between heat capacity of zeolite ($m_{zeo\_ad}\, c_{pzeo}$, m_{zeo_ad} : mass flow rate of zeolite with adsorbed water) and water in the secondary heat exchanger ($m_{w2}c_{pw2}$). In the case of m_{w_EB} = 750 kg/h, T_{zeo} and water temperature in the secondary heat exchanger T_{w2} decrease in parallel as shown in **Fig. 4.58 (b)**, which implies $m_{zeo\_ad}\, c_{pzeo} \simeq m_{w2}c_{pw2}$. The relationship between heat capacity of zeolite and water is shown in **Fig. 4.61**. The heat capacity of water in the secondary heat exchanger exceeds that of zeolite in the range of around m_{w_EB} > 750 kg/h. Thus, the m_{inj} can be set to the maximum (q_t = 0.237 kg/kg) in the

range of m_{w_EB} > 750 kg/h in the case of m_{zeo} = 1500 kg/h because the almost adsorption heat can be recovered when the appropriate L_2 is given due to larger heat capacity of water than that of zeolite. **Figure 4.62** shows the change in the fuel saving as a function of m_{w_EB}. The fuel saving reached maximum in the range of $m_{zeo\_ad}\ c_{pzeo} < m_{w2}c_{pw2}$ (m_{w_EB} > 750 kg/h). The length of secondary heat exchanger L_2 determined by the design method is also shown in **Fig. 4.62**. In the range of $m_{zeo\_ad}\ c_{pzeo} > m_{w2}c_{pw2}$ (m_{w_EB} < 750 kg/h), the L_2 increases with increase in m_{w_EB} to recover the sensible heat of zeolite. On the other hand, in the range of $m_{zeo\_ad}\ c_{pzeo} < m_{w2}c_{pw2}$ (m_{w_EB} > 750 kg/h), the L_2 can be reduced because massive heat capacity of water decreases the T_{zeo} quickly.

The relationship between the fuel saving and the heat recovery rate is shown in **Fig. 4.63**. By applying the secondary heat exchanger for the large existing boiler, two operating modes agree at the point of 11.7 L/h and 99%.

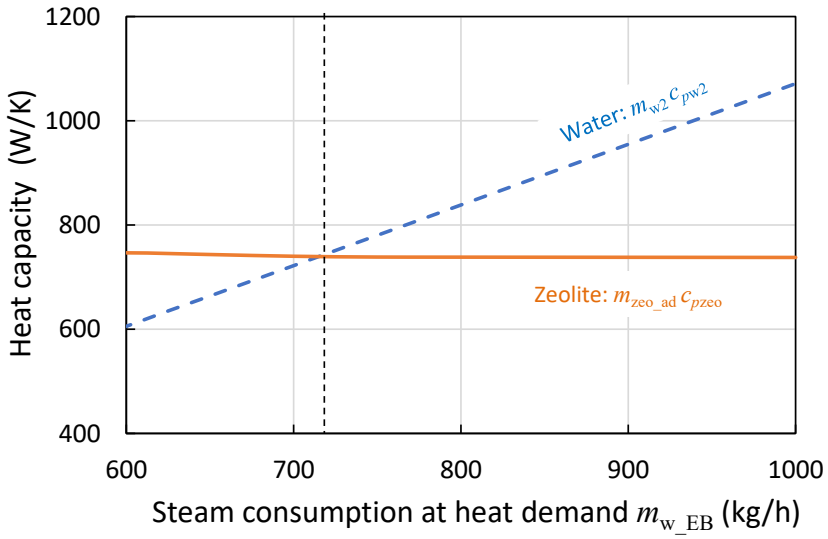

Fig. 4.61. Change in heat capacity of zeolite and water as a function of steam consumption at heat demand m_{w_EB}.

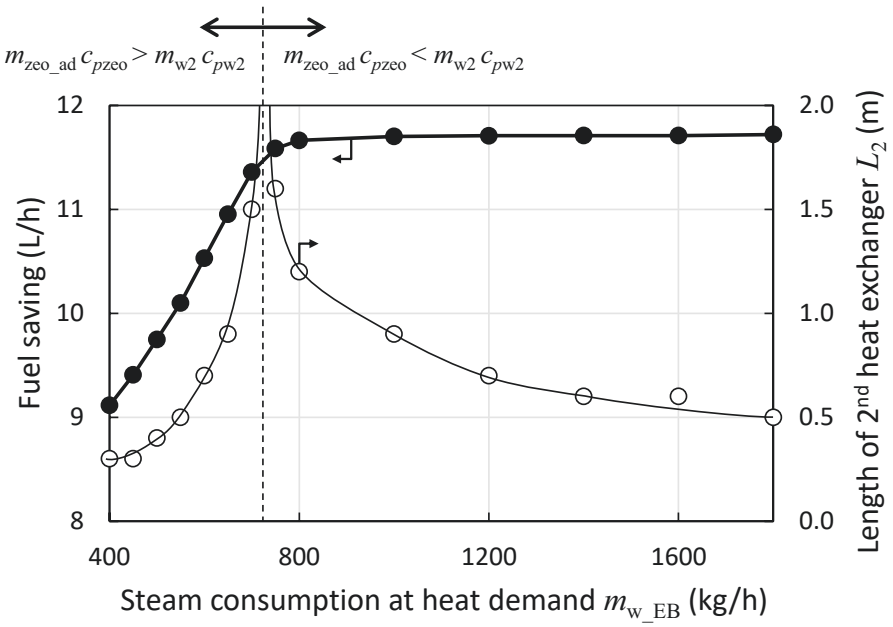

Fig. 4.62. Change in fuel saving and length of secondary heat exchanger L_2 as a function of steam consumption at heat demand m_{w_EB}.

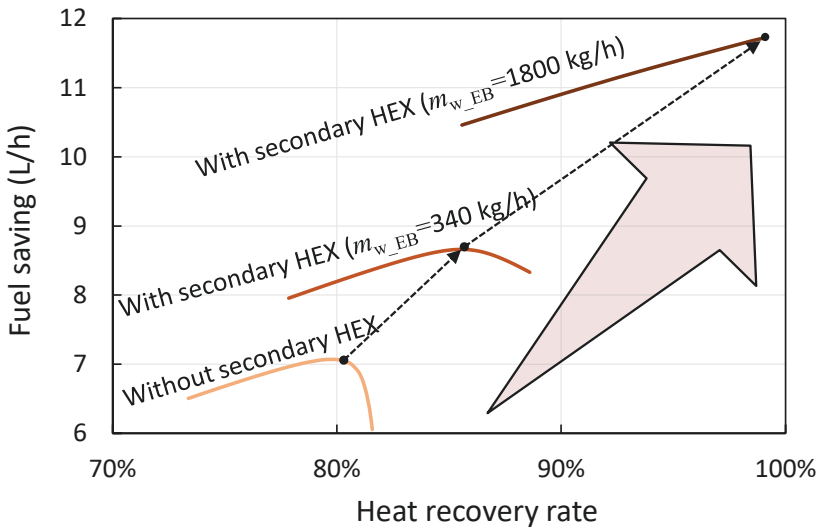

Fig. 4.63. Relationship between fuel saving and heat recovery rate of Zeolite Boiler with the secondary heat exchangers.

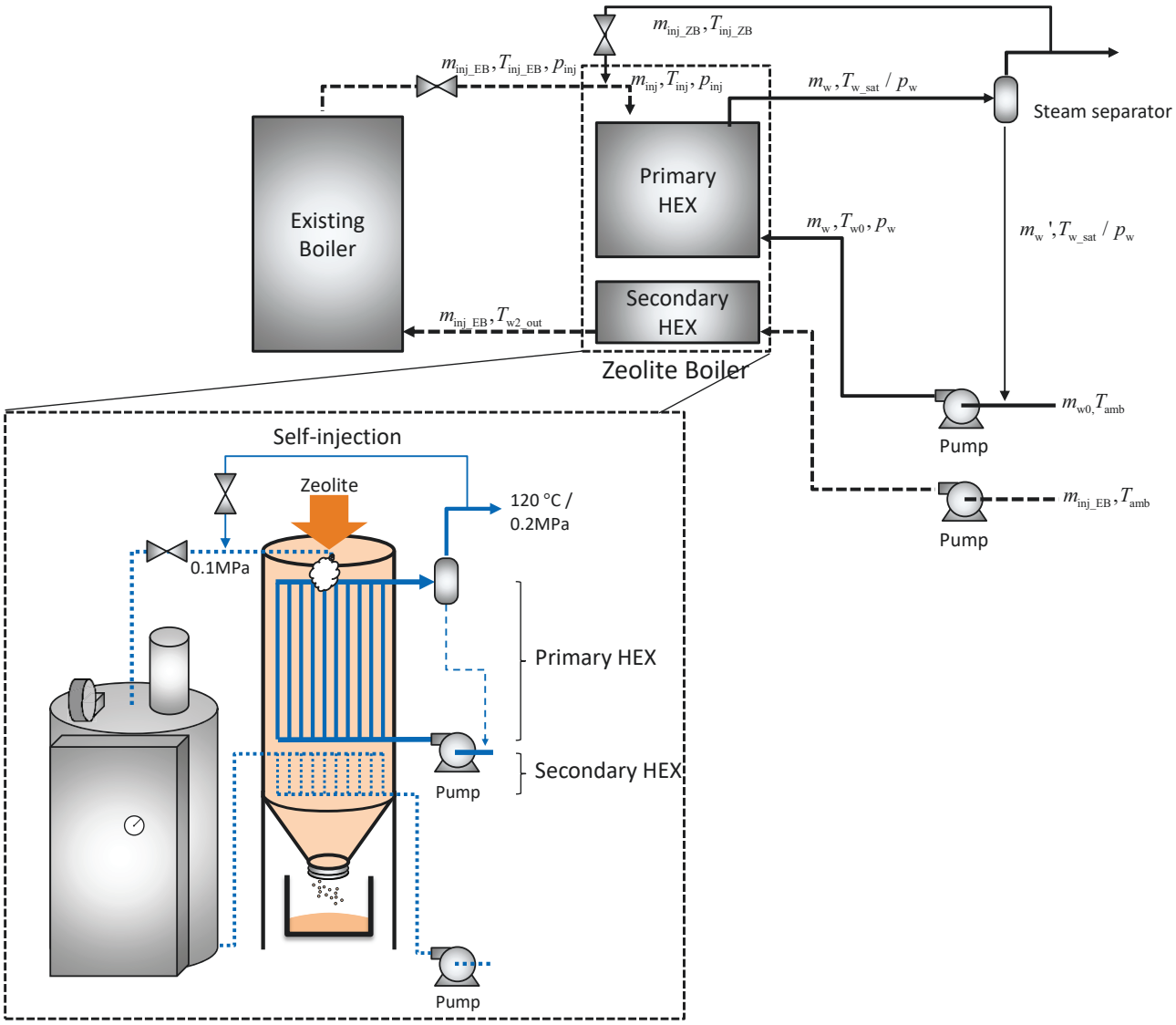

Fig. 4.64. Process flow diagram and schematic of Zeolite Boiler with self-injection process.

4.8.2 Self-injection process

In the range of $m_{zeo\_ad}\, c_{pzeo} > m_{w2} c_{pw2}$, the fuel saving is limited as shown in **Fig. 4.62**. A self-injection process was considered to overcome this limitation of the fuel saving in this range.

When the Zeolite Boiler generates more steam than demand, excess steam can be recycled into the Zeolite Boiler as a part of injection steam, and thereby the fuel saving can be improved. The schematic of the Zeolite Boiler with the self-injection process is shown in **Fig. 4.64**. The excess steam is mixed to the super-heated steam provided by the existing boiler, and thereafter the mixed steam is injected into the zeolite bed. The mass flow rate of injection steam m_{inj} can be calculated by **Eq. (4.63)**.

$$m_{inj} = m_{inj\_EB} (= m_{w2}) + m_{inj\_ZB} \tag{4.63}$$

where m_{inj_EB} and m_{inj_ZB} are the mass flow rate of injection steam generated by the existing boiler and the Zeolite Boiler, respectively. The water supplied to the existing boiler is pre-heated by the secondary heat exchanger of Zeolite Boiler ($m_{inj\_EB} = m_{w2}$). As a representative case study, the m_{w_EB} was assumed to be 340 kg/h in this case. The balance of excess (self-injection) steam and steam generated by existing boiler in the mixed steam is shown in **Fig. 4.65** by changing m_{zeo} =1500 ~ 2500 kg/h. The share of m_{inj_ZB} expands corresponding to increase in the m_{zeo}, and the m_{inj_EB} can be reduced. The fuel saving and the heat recovery rate are also shown in **Fig. 4.65**. The heat recovery rate decreases linearly with increase in m_{zeo}, while the fuel saving linearly increases because of reducing m_{inj_EB}. Since the m_{w2} decreases with the increase in m_{zeo} (see **Fig. 4.65**) , the heat capacity ratio of zeolite and water in the secondary heat exchanger ($m_{zeo\_ad}\, c_{pzeo}$ / $m_{w2} c_{pw2}$) increases as shown in **Fig. 4.66** ,which lead to higher exhaust T_{zeo} and accompanying less heat recovery rate.

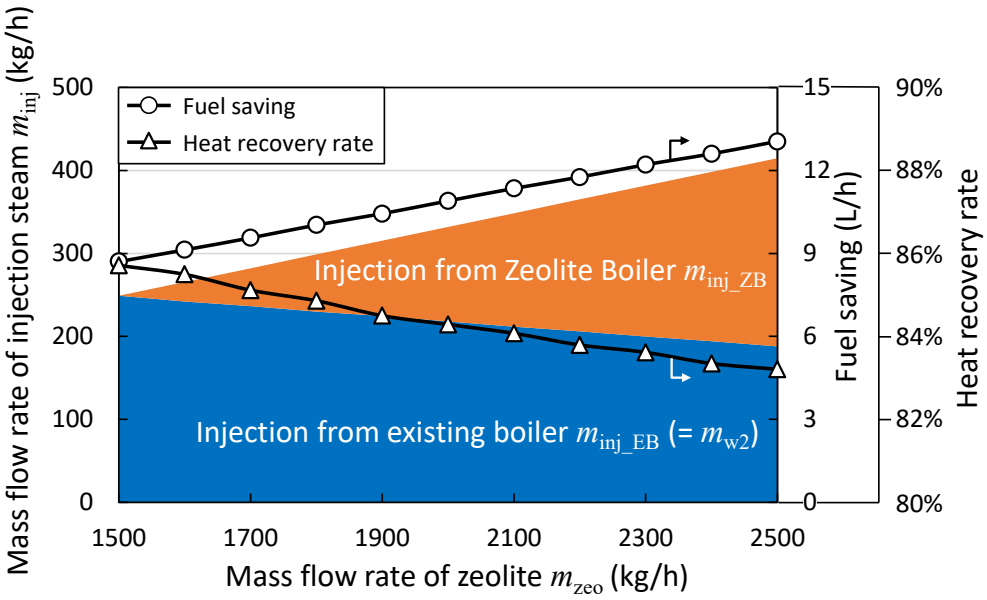

Fig. 4.65. Injection steam balance and fuel saving of Zeolite Boiler with self-injection process.

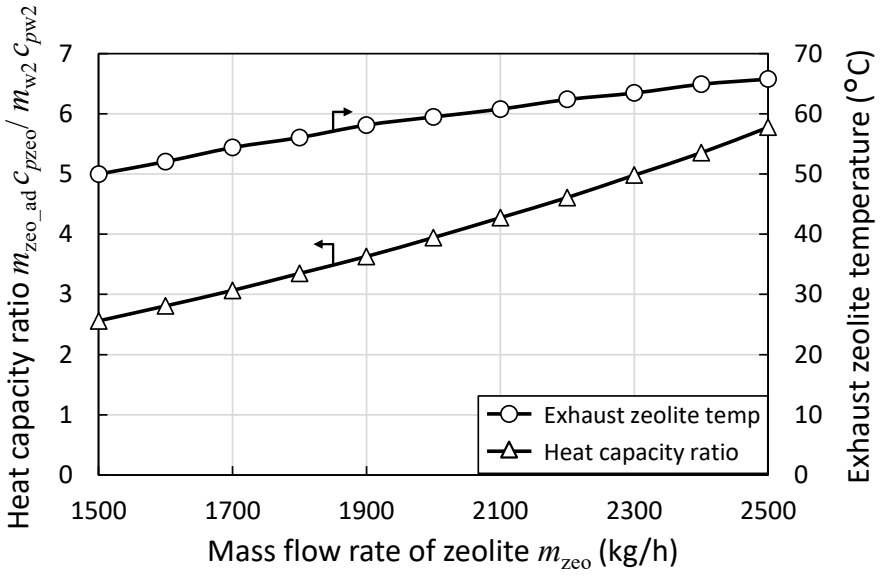

Fig. 4.66. Change in heat capacity rate and exhaust zeolite temperature as a function of m_{zeo}.

4.9 Chapter conclusion

In this chapter, a conceptual design of “Zeolite Boiler” employing a moving bed and an indirect heat exchanging process was introduced to generate pressurized steam continuously. A 1D numerical model of Zeolite Boiler including the empirical adsorption kinetics of zeolite and heat transfer characteristics was built and was experimentally validated by the bench-scale test. Performance characteristics of the full-scale Zeolite Boiler in Tanegashima was investigated numerically. Main achievements of this chapter were shown as follows;

- Equilibrium water uptake on zeolite was obtained by the diluted fixed bed test. Freundlich-Dubinin-Astakhov model can simulate the equilibrium line in the whole range of relative humidity.
- Adsorption rate was measured by the diluted fixed bed test and the 1D numerical model with Linear Driving Force model considering only macro pore diffusion can simulate the dynamic change of the outlet vapor pressure from the reactor.
- The heat transfer characteristics under steady and unsteady conditions were obtained experimentally by using fixed bed test. Applicability of the two-phase heat transfer models reported in literatures was confirmed by the 1D numerical model.
- The bench-scale Zeolite Boiler was built, and continuous generation of pressurized steam was successfully demonstrated. The developed 1D numerical model including the empirical adsorption and heat transfer model can simulate the performance well.
- The performance of the full-scale Zeolite Boiler was predicted using the validated numerical model. Effects of design parameters on the performance were investigated numerically by the model. The fuel saving has a peak as a function of mass flow rate of injection steam, while the heat recovery rate simply increases with increase in the mass flow rate of injection steam. The discordant operating modes to maximize the two common performance indices of heat recovery rate and fuel saving was indicated.
- The fuel saving and the heat recovery rate of the Zeolite Boiler can be improved by introducing a secondary heat exchanger to pre-heat supplied water to the existing boiler. By applying the secondary heat exchanger, two operating modes agree at the point that the mass flow rate of injection steam is set to maximize the ultimate water uptake on zeolite.
- The self-injection process, in which excess steam generated by Zeolite Boiler is recycled into the Zeolite Boiler as a part of injection steam, can increase the fuel saving even if the Zeolite Boiler is co-operated with the small existing boiler.

The result of outlet water uptake on zeolite from the Zeolite Boiler is used as the boundary condition of initial water uptake for the Heat Charger in Chapter 5. The design method of the full-scale Zeolite Boiler established in this chapter is used in the techno-economic and environmental analyses in Chapter 6.

Nomenclature

Symbols

A:	Area	m^2
A_{ad}:	Adsorption potential	kJ/kg -
c_p:	Specific heat capacity	J/(kg·K)
d:	Diameter	m
D:	Diffusivity	m^2/s
E:	Interaction energy	kJ/kg
FS:	Fuel saving	L/h
h:	Specific enthalpy	kJ/kg
H:	Enthalpy flow	kJ/h
HHV:	Higher heating value	kJ/kg
k:	Overall mass transfer coefficient	1/s
K:	Freundlich constant	-
L:	Length of heat exchanger	m
m:	Mass flow rate	kg/h
M:	Molecular weight	g/mol
n:	Heterogeneous parameter	-
n':	Freundlich constant	-
n_{bt}:	Number of boiler tubes	-
p:	Pressure	kPa
q:	Water uptake on zeolite	kg/kg
Q:	Heat flow	kJ/h
r:	Radius	m
R:	Gas constant	J/(mol·K)
r_{ad}:	Adsorption rate	1/s
SV:	Space velocity	1/h
t:	Time	s
T:	Temperature	K
u:	Velocity	m/s
V:	Volume	m^3
W:	Adsorption capacity	m^3/kg
x,y,z,r:	Dimension coordinate	m
x_{dry}:	Steam quality	-
α:	Heat transfer coefficient	$W/(m^2·K)$
ΔH:	Heat of adsorption	kJ/kg
ε:	Porosity	-
η:	Efficiency	-

λ:	Thermal conductivity	W/(m·K)
μ:	Viscosity	Pa·s
ρ:	Density	kg/m^3
σ:	Specific heat transfer area	m^2/m^3
τ:	Tortuosity	-
Ω:	Collision integral	-

Dimensionless parameters

Nu:	Nusselt number
Pe:	Peclet number
Pr:	Prandtl number
Re:	Reynolds number
Sc:	Schmidt number
Sh:	Sherwood number

Subscript

a:	Air
amb:	Ambient
ax:	Axial
ad:	Adsorption or Adsorbed
b:	Bed
bt:	Boiler tubes
c:	Chamber
co:	Collision
EB:	Existing boiler
eff:	Effective
eq:	Equilibrium
f:	Gas film
g:	Gas
gen:	Generated
heat:	Heat transfer
in:	Inner
inc:	Increasing
inj:	Injection
ins:	Insulation
kn:	Knudsen
LDF:	Linear driving force
m:	Molecular
max:	Maximum

oil:	Heavy oil
out:	Outer, outlet
p:	Particle
po:	Polyamide
pore:	Porous
potential:	Potential
r:	Radial
rec:	Recovery
rep:	Representative
s:	Steam
sat:	Saturation
st:	Stainless
t:	Target
trans:	Heat transfer
tube:	Heat exchanging tube
w:	Water
wall:	Wall
zeo:	Zeolite
ZB:	Zeolite Boiler
0:	Original or Initial
2:	Secondary

References

[1] Bering BP, Dubinin MM, Serpinsky V V. Theory of volume filling for vapor adsorption. J Colloid Interface Sci 1966;21:378–93. https://doi.org/10.1016/0095-8522(66)90004-3.

[2] Hauer A. Beurteilung fester adsorbentien in offenen sorptionssystemen für energetische anwendungen. Technischen Universität Berlin, 2002.

[3] Hauer A, Fischer F. Open adsorption system for an energy efficient dishwasher. Chemie Ing Tech 2011;83:61–6. https://doi.org/https://doi.org/10.1002/cite.201000197.

[4] Gorbach A, Stegmaier M, Eigenberger G. Measurement and modeling of water vapor adsorption on Zeolite 4A — equilibria and kinetics. Adsorption 2004;10:29–46. https://doi.org/http://dx.doi.org/10.1023/B:ADSO.0000039927.77359.40.

[5] Malek A, Farooq S. Kinetics of hydrocarbon adsorption on activated carbon and silica gel. AIChE J 1997;43:761–76. https://doi.org/10.1002/aic.690430321.

[6] Wakao N, Funazkri T. Effect of fluid dispersion coefficients on particle-to-fluid mass transfer coefficients in packed beds. Chem Eng Sci 1978;33:1375–84. https://doi.org/https://doi.org/10.1016/0009-2509(78)85120-3.

[7] Mette B, Kerskes H, Drück H, Müller-steinhagen H. Experimental and numerical investigations on the water vapor adsorption isotherms and kinetics of binderless zeolite 13X. Int J Heat Mass Transf 2014;71:555–61. https://doi.org/http://dx.doi.org/10.1016/j.ijheatmasstransfer.2013.12.061.

[8] Carniglia SC. Construction of the Tortuosity Factor from Porosimetry. J Catal 1986;102:401–18.

[9] Özgümüš T, Mobedi M, Özkol Ü, Nakayama A. Thermal dispersion in porous media - A review on the experimental studies for packed beds. Appl Mech Rev 2013;65:031001-1–19. https://doi.org/10.1115/1.4024351.

[10] Dixon AG, Cresswell DL. Theoretical prediction of effective heat transfer parameters in packed beds. AIChE J 1979;25:663–76. https://doi.org/https://doi.org/10.1002/aic.690250413.

[11] Wakao N, Kaguei S, Funazkri T. Effect of fluid dispersion coefficients on particle-to-fluid heat transfer coefficients in packed beds: Correlation of nusselt numbers. Chem Eng Sci 1979;34:325–36. https://doi.org/10.1016/0009-2509(79)85064-2.

[12] Wasch APDE, Froment GF. Heat transfer in packed beds. Chem Eng Sci 1972;27:567–76.

[13] Shinohara K, Takahashi H, Nakamura M. IDOUSOUKOUGAKU-JISAAI TO KISO (in Japanese). Hokkaido-daigaku-tosho-kankokai; 2000.

This page intentionally left blank.

Chapter 5 Heat Charger: Testing and design methodology

5.1 Objectives of this chapter

Figure 5.1 shows the structure of this dissertation and position of this chapter. This chapter focuses on the heat charging process in the thermochemical energy storage and transport system and develops a heat charging device namely “Heat Charger”. This chapter aims to establish a design method of the Heat Charger via demonstrating continuous heat charging. The design method is used in techno-economic and environmental analyses described in Chapter 6. To achieve the objective, the following research items are described in this chapter. The structure of this chapter consists of “Preparation of numerical simulation of Heat Charger”, “Bench-scale Heat Charger” and “Full-scale Heat Charger in Tanegashima” which is almost the same scheme of Zeolite Boiler.

Preparation of numerical simulation of Heat Charger

- Investigating desorption characteristics and formulation of equilibrium and kinetic model (described in **5.3**)

Bench-scale Heat Charger

- Developing a numerical model to simulate the Heat Charger (described in **5.4.3**).
- Designing a 1/400th scale (bench-scale) Heat Charger (described in **5.4.1**).
- Demonstrating continuous heat charging utilizing a bench-scale test rig of Heat Charger employing counter-flow Heat Charger (described in **5.4.4**).
- Validating the developed numerical model to predict the performance of full-scale Heat Charger employing counter-flow, co-current-flow and cross-flow Heat Charger (described in **5.4.4**).

Full-scale Heat Charger in Tanegashima

- Clarifying relationship among design parameters of Heat Charger via calculation of the performance characteristics (described in **5.5**).

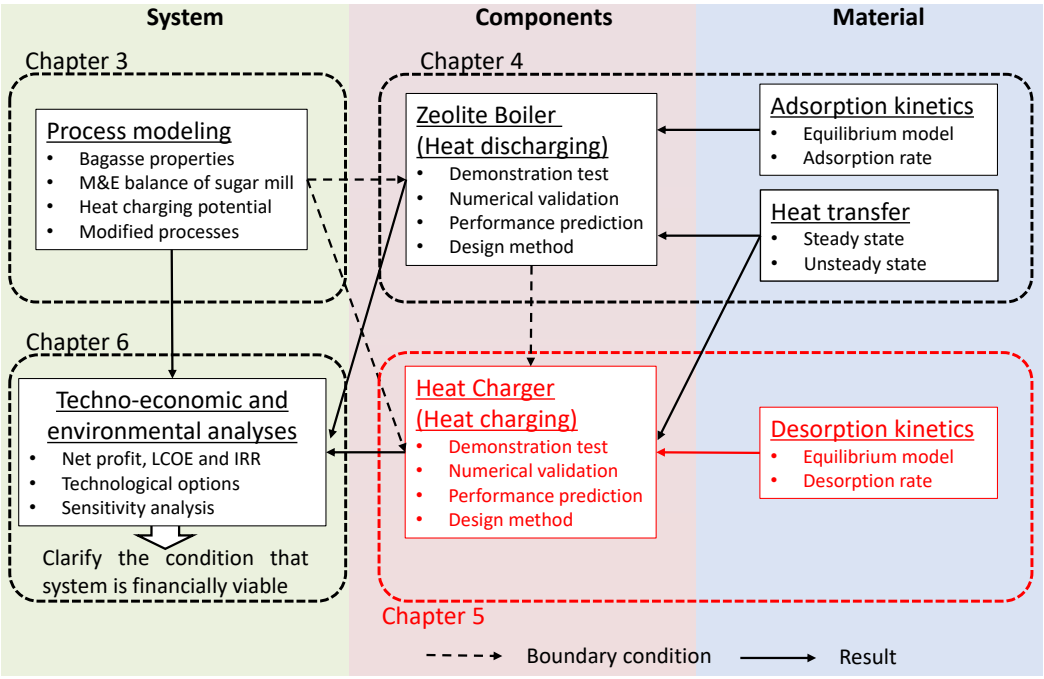

Fig. 5.1. Structure of dissertation and position of this chapter.

5.2 Conceptual design of "Heat Charger"

A heat exchanger is assumed to be installed between the electric precipitator and stack in the sugar mill to heat up the ambient air as shown in **Fig. 5.2**. The hot air for thermal energy storage (TES) heated by the flue gas via the heat exchanger is blown into the heat charging device namely "Heat Charger" to desorb the water in the zeolite. The reactor types of Heat Charger can be classified by employing fixed or moving bed of zeolite and direct or indirect heat exchanging process. The fixed bed reactor requires multiple chambers with large volume to charge the heat continuously and additional labor cost for replacement of the material. This study employed moving bed reactor as a conceptual design of Heat Charger for uninterrupted heat charging.

The direct heat exchanging process was employed in the Heat Charger because its specific heat transfer area between gas and particles is over 20 times larger than indirect heat exchanging process. The specific heat transfer area between zeolite particle and gas in the direct heat exchanging process is 2250 m^2/m^3 when the φ_p = 1.6 mm and bed porosity ε_b = 0.4, respectively. On the other hand, the specific heat transfer area in the indirect heat exchanging process is about 100 m^2/m^3 when the multiple heat exchanger is settled into the chamber. The configuration of heat exchanger is assumed to be the same as the Zeolite Boiler's (3463 number of heat exchanger tubes with φ_{tube} = 15.9 mm and 1.5φ_{tube} of pitch of each tubes) in Chapter 4.

The gas flow direction in the reactor with the moving bed and the direct heat exchanging process can be classified into counter-flow, co-current-flow and cross-flow as shown in **Fig. 5.3**. All processes were investigated in the following sections.

As well as the Zeolite Boiler, reduced dimension numerical models are preferable to reduce the computational time as long as the deteriorated result is allowable. The counter-flow Heat Charger was modelled by symmetric cylindrical 2D model and compared to the 1D model. The cross-flow Heat Charger was modelled by a 2D model.

Two important source terms (desorption and heat transfer characteristics) in energy conservation equations of Heat Charger determine the performance. Desorption characteristics were described in **5.3**. Equilibrium water uptake on zeolite in desorption process was obtained by diluted fixed bed test experimentally. A kinetic model was included in a 1D numerical model and was evaluated by comparing to the experimental data. Heat transfer characteristics were already evaluated in Chapter 4. The numerical model including empirical desorption and heat transfer characteristics were used for the simulation of the bench-scale and the full-scale Heat Charger in **5.4** and **5.5**.

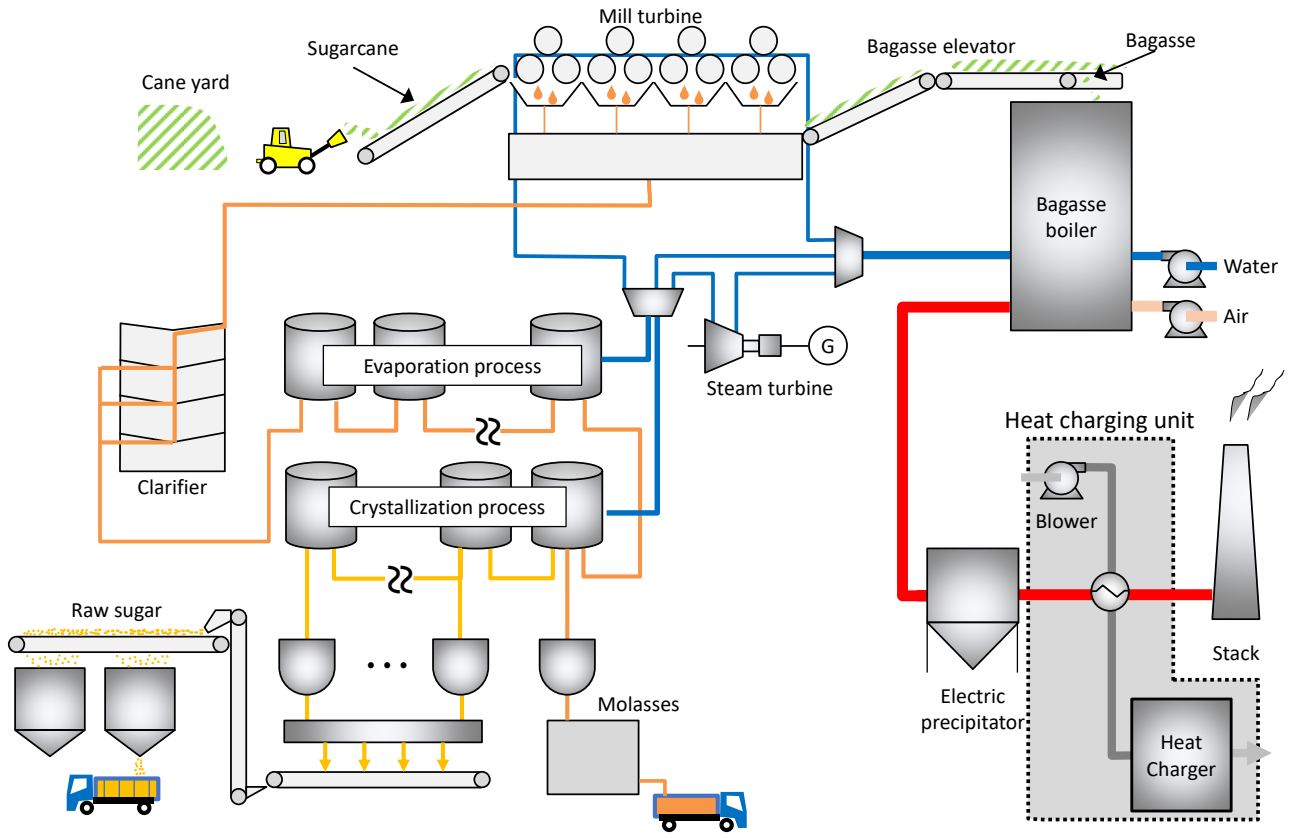

Fig. 5.2. Heat charging unit in sugar mill.

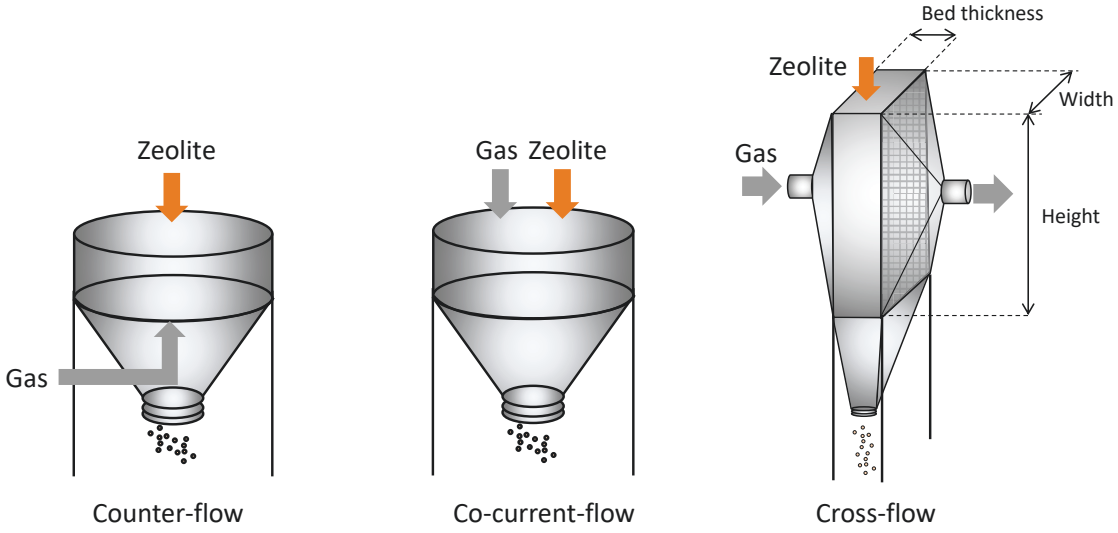

Fig. 5.3. Reactor types of moving bed reactor.

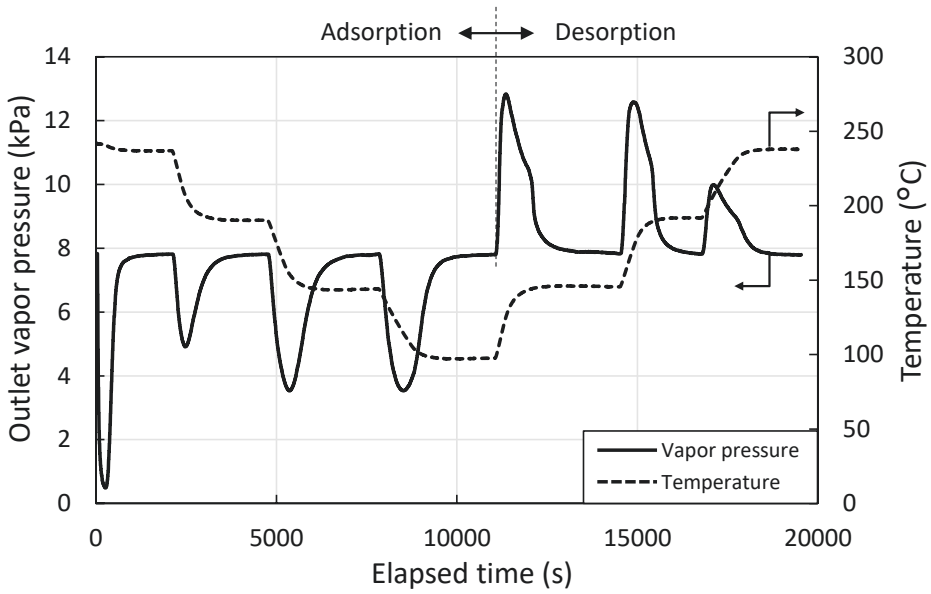

Fig. 5.4. Change in outlet vapor pressure and bed temperature during adsorption and desorption in diluted fixed bed test.

5.3 Desorption characteristics

5.3.1 Equilibrium model for desorption

Desorption kinetics relates to equilibrium water uptake and desorption rate. Some adsorbents have the hysteresis between equilibrium adsorption and desorption water uptake. To evaluate these values

under isothermal condition, a diluted fixed bed test was conducted. The experimental apparatus of diluted fixed bed test was described in Chapter 4.

Figure 5.4 shows the change in the bed temperature and outlet vapor pressure through a typical experimental run. After adsorption process completed, the bed and inlet gas temperature were simultaneously increased to the intended temperature. The equilibrium water uptake decreased with decrease in relative humidity. The zeolite desorbed water vapor according to the equilibrium desorption line, therefore the outlet vapor pressure was increased by desorption process. The equilibrium water uptake in desorption at intended relative humidity was calculated by subtracting the integrated water uptake in the first desorption step from the last adsorption process. By repeating this procedure with increasing the bed temperature stepwise, the equilibrium water uptake in desorption process at each relative humidity was obtained.

Table 5.1 summarizes the all experimental conditions and results of equilibrium water uptake. **Figure 5.5** shows the result of desorption isotherms with adsorption results. The same equilibrium model of adsorption process (Freundlich-Dubinin-Astakhov model, described in Chapter 4) can be applied to the desorption equilibrium model because there were little discrepancies between adsorption and desorption in the whole range of relative humidity as shown in **Fig. 5.5**.

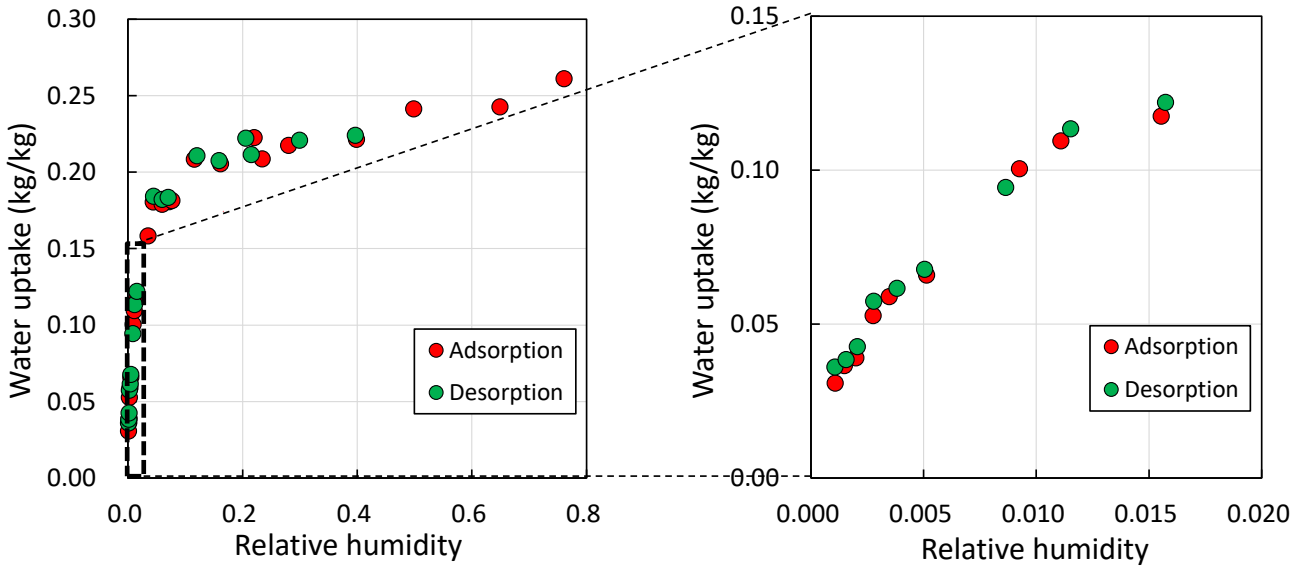

(a) Whole relative humidity range (b) Low relative humidity range

Fig. 5.5. Adsorption and desorption isotherms.

Table 5.1. Experimental conditions and results of diluted fixed bed test.

	Run	Step	Experimental conditions			Results
			Reactor temperature (°C)	Inlet vapor pressure (kPa)	Relative humidity (-)	Water uptake (kg/kg)
Higher temperature& Low relative humidity	Run 1	S1	246.9	7.74	0.0021	0.043
		S2	199.8	7.81	0.0050	0.068
		S3	151.3	7.76	0.0157	0.122
	Run 2	S1	246.9	5.88	0.0016	0.039
		S2	199.6	5.88	0.0038	0.062
		S3	152.4	5.86	0.0115	0.113
	Run 3	S1	250.7	4.27	0.0011	0.036
		S2	199.2	4.26	0.0028	0.057
		S3	151.2	4.25	0.0086	0.944
Lower temperature & High relative humidity	Run 4	S1	102.4	7.74	0.0702	0.183
		S2	73.5	7.79	0.2150	0.212
		S3	59.7	7.81	0.3969	0.224
	Run 5	S1	99.0	5.85	0.0598	0.182
		S2	73.9	5.86	0.1590	0.208
		S3	59.5	5.84	0.2995	0.221
	Run 6	S1	98.7	4.33	0.0448	0.184
		S2	73.4	4.34	0.1203	0.2107
		S3	61.2	4.33	0.2057	0.2223

5.3.2 Desorption kinetics

Overall mass transfer resistance consists of three resistances which are mass transfer through the gas film on zeolite particles, diffusion resistances into macro pore and micro pore as well as adsorption process. In the adsorption rate, only the diffusion resistance into macro pore was considered as the mass transfer resistance. The mass transfer resistance through the gas film in the desorption process is negligible because of a large Reynolds number caused by high flow rate of drying hot air in Heat Charger than Zeolite Boiler, which leads smaller resistance through the gas film. On the other hand, the diffusion resistances into micro pore resistance might affect on desorption rate [1]. The isothermal desorption test using the diluted fixed bed was conducted to evaluate the effect of diffusion resistance into micro pore under the isothermal condition.

The experimental apparatus for the isothermal desorption test was rebuilt using the diluted fixed bed test rig as shown in **Fig. 5.6**. Before the test, the humid air with 40 °Cdp of dew point controlled by the bubbler system was introduced to the reactor at intended temperatures (200, 150 and 100 °C) until the outlet vapor pressure resumed to the initial value as the pre-adsorption process. During this pre-adsorption process, humid air with 30 °Cdp of dew point was generated by the other bubbler system and was blown to the atmosphere (see **Fig. 5.7(a)**). After all the zeolite in the reactor adsorbed to equilibrium value, the valves 3, 4 and 5 were quickly switched. The humid air with 40 °Cdp of dew point was blown to the atmosphere after passing through the reactor to keep equilibrium state in the reactor. The dew point of humid air with 30 °Cdp was measured by a dew point sensor to check the stability of partial vapor pressure in the humid air (**Fig. 5.7(b)**). After that, the humid air with 30 °Cdp was introduced to the reactor by switching the valves 1, 2, 3 and 4 and desorption process commenced (**Fig. 5.7(c)**). **Table 5.2** shows the experimental conditions of isothermal desorption test. The initial water uptakes before each desorption process were predicted by Freundlich-Dubinin-Astakhov model under the pre-adsorption condition.

Figure 5.8 shows the experimental and numerical analysis result of change in outlet vapor pressure at each temperature condition. The governing equations of one-dimensional (1D) numerical simulation model for the diluted fixed bed test were the same as the adsorption process (see Chapter 4). The desorption rate in the numerical analysis was modeled by LDF (Linear Driving Force) model considering only the macro pore diffusion resistance neglecting other two terms. The numerical analysis can simulate the outlet vapor pressure at 200 °C and 150 °C as can be seen from **Fig. 5.8**. The outlet vapor pressure at 100 °C in the numerical analysis result decreases much faster than experimental result. Faster decrease in outlet vapor pressure in the numerical analysis indicates the desorption rate in the numerical model without the diffusion resistance into the micro pore is underestimated. Underestimation of desorption rate in the numerical model allows the diffusion resistance into micro pore, which makes desorption rate slower, is negligible in the desorption process as well as adsorption process. The applicability of the LDF model without diffusion resistance into micro pore to the prediction of desorption rate was confirmed by good agreement with experimental and numerical analysis result at higher temperature and no risk of overestimation of desorption rate at lower temperature.

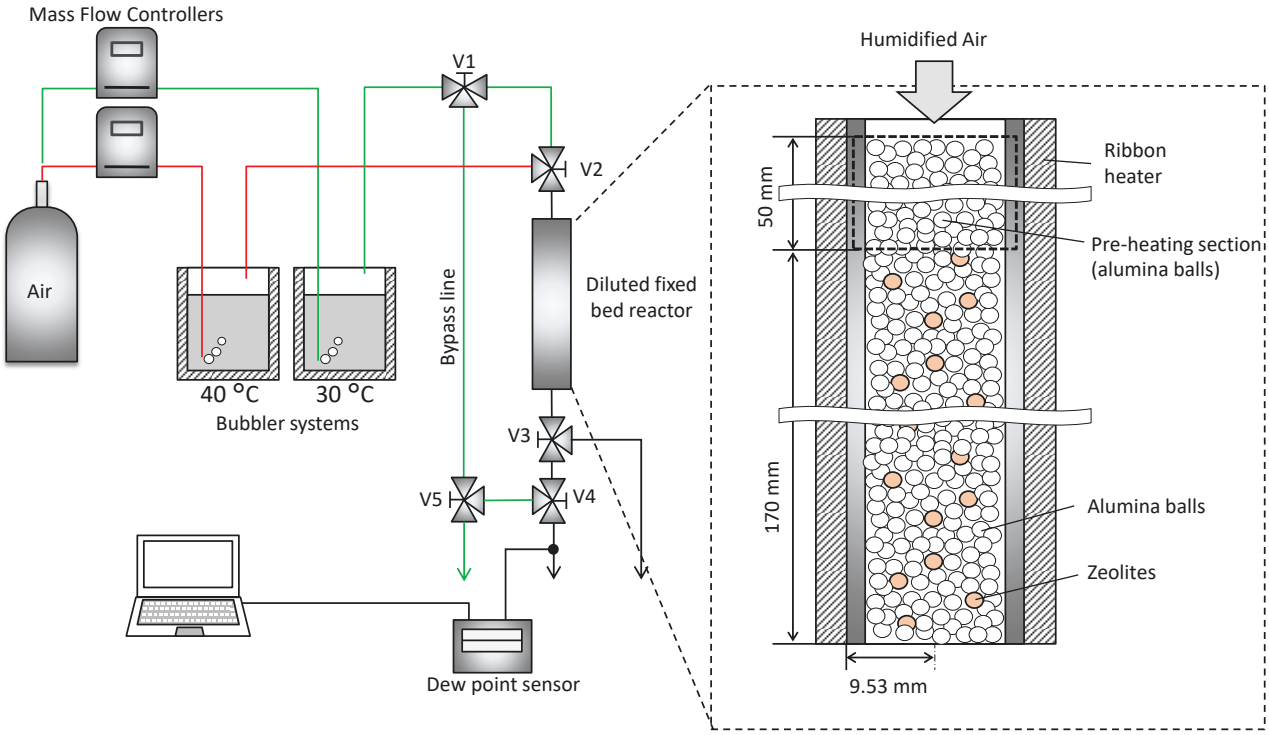

Fig. 5.6. Experimental apparatus of diluted fixed bed test for desorption kinetics.

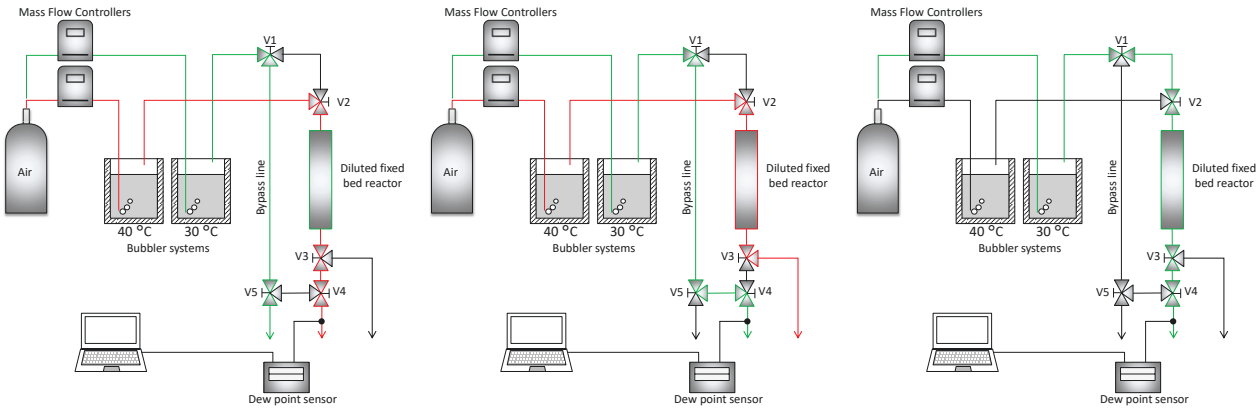

Fig. 5.7. Gas flow of diluted fixed bed test for desorption kinetics.

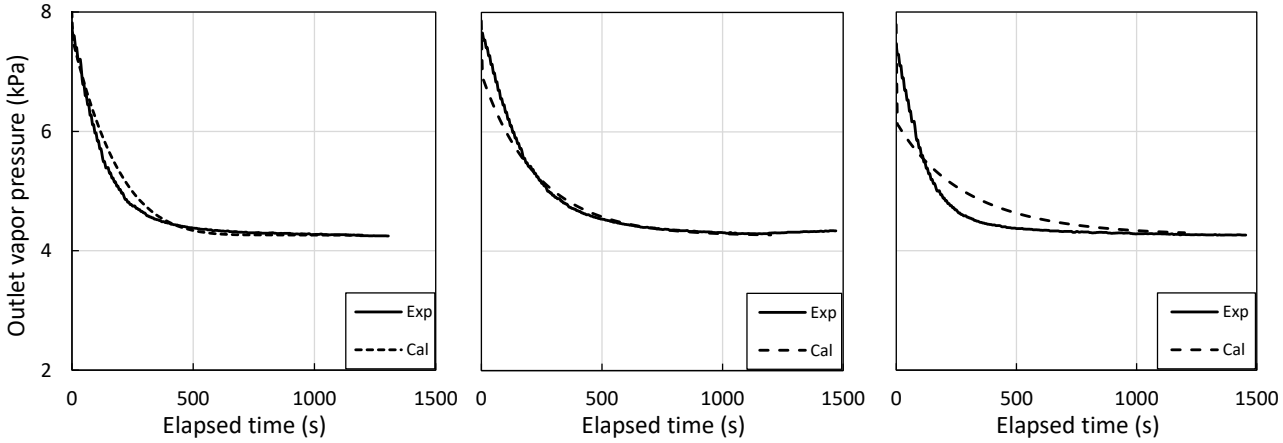

Fig. 5.8. Experimental and numerical analysis result of diluted fixed bed test during desorption process.

Table 5.2. Experimental conditions of isothermal desorption test.

		Test 1	Test 2	Test 3
Bed temperature	(°C)	197.2	151.0	100.9
Volumetric flow of air	(ccm)	1684	1519	1339
Vapor pressure during desorption process	(kPa)	4.26	4.26	4.26
Vapor pressure during pre-adsorption process	(kPa)	8.01	7.86	7.79
Water uptake before desorption	(kg/kg)	0.074	0.122	0.184

5.4 Heat Charger test

In this section, an experimental setup of the Hear Charger was made (**5.4.1** and **5.4.2**) and continuous heat charging was demonstrated via Heat Charger test (**5.4.4**). A symmetric cylindrical 2D numerical model was built (**5.4.3**) and analyzed results of the Heat Charger test (**5.4.4**). A 1D model was also developed (**5.4.3**) and was compared to 2D model (**5.4.4**). The validated 1D numerical simulation model was used to predict the performance of full-scale Heat Charger in Tanegashima employing a counter-flow, a co-current-flow and a cross-flow type in the following section (**5.5**)

5.4.1 Experimental setup

A 1/400th scale Heat Charger (called bench-scale Heat Charger hereafter) employing counter-flow was designed assuming that around 2000 kg/h of zeolite is regenerated in the full-scale Heat Charger applying the sugar mill in Tanegashima. **Figure 5.9** shows the schematic of experimental apparatus of the Heat Charger test rig. A cylindrical stainless chamber with φ = 300 mm (t = 2 mm) $\times$ L = 250 mm

was made for the bench-scale Heat Charger. The chamber was covered by a glass wool thermal insulation (t = 25 mm). Two hoppers were attached to the top of chamber to supply the zeolite continuously. In the chamber, zeolite was packed with 200 mm of height.

The gas was introduced from two branch pipes mounted at the bottom and exhausted from two holes from the top cover of chamber. The dew point and velocity of exhaust gas were measured by a dew point sensor (Testo, Robust digital humidity probe 06369753) and a pitot tube, respectively. To measure the axial temperature distribution of zeolite bed, four K-type thermocouples were embedded at z = 50, 100, 150 and 200 mm from the top along the center axis of the zeolite bed. The other K-type thermocouple measured the temperature of exhaust gas. The temperature of inlet gas was also measured by a K-type thermocouple. All temperatures measured by the thermocouples, the dynamic pressure of outlet gas and the dew point were logged every 10 seconds. The mass flow rate of zeolite m_{zeo} and the water uptake on exhaust zeolite q_{out} were measured every 30 minutes.

5.4.2 Experimental procedure

As a preliminary adsorption treatment, all the zeolite was packed in the material reservoir (the same equipment of the Zeolite Boiler test, described in Chapter 4) and ambient air was blown from the bottom of the vessel. The relative humidity of ambient air was over 0.01. The water uptake on zeolite q in the material reservoir reached around 0.2 kg/kg uniformly based on equilibrium line.

Before starting the experimental procedure, the chamber of Heat Charger was fully packed with zeolite adsorbing q = 0.2 kg/kg. The hot air generated by a hot air generator (Suiden, Hot Dryer SHD-7.5J) was blown into the bed from the bottom. Concurrently, the particle discharger (the same equipment of Zeolite Boiler test, described in Chapter 4) was started to discharge the zeolite. The temperature of zeolite T_{zeo} increased from the bottom and hot zone gradually propagated to the top.

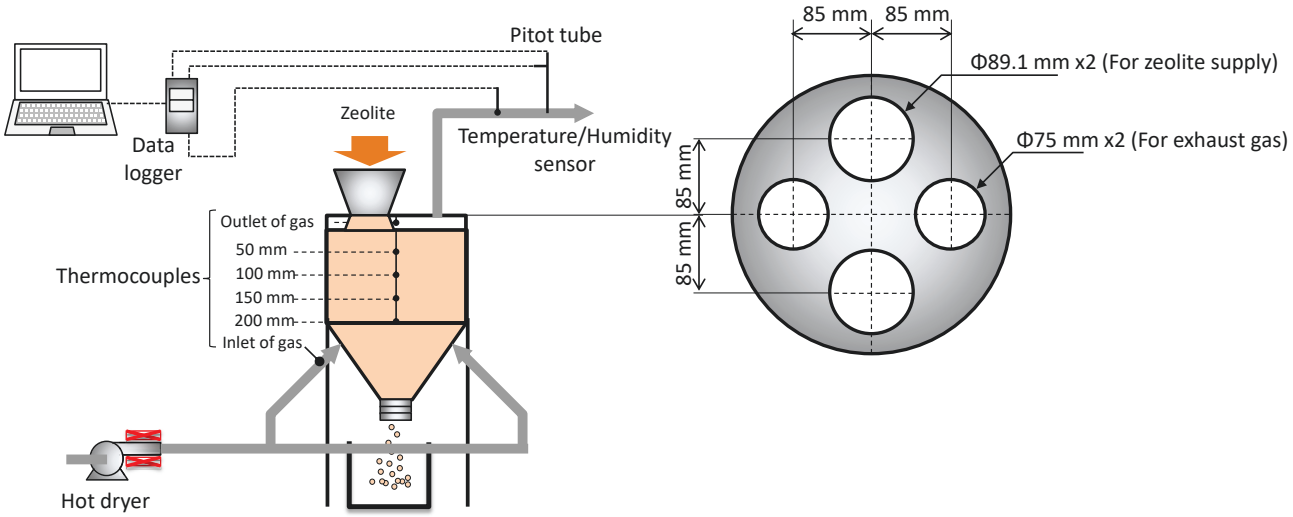

Fig. 5.9. Experimental apparatus of Heat Charger test.

5.4.3 Numerical model

To analyze the Heat Charger test numerically, a symmetric cylindrical 2D and 1D simulation models solving mass, steam, energy conservation equations of zeolite and gas phase in the void of bed, and momentum equation of gas phase were built on the COMSOL Multiphysics 5.3a®. The mass conservation equations of zeolite and gas in the 2D and 1D models can be expressed by **Eqs. (5.1)** and **(5.2)**, respectively. The radial velocity distribution of gas and zeolite were not considered, and gas flow was regarded as plug flow in this study.

$$\frac{\partial}{\partial z}(\rho_{zeo} u_{zeo}) = \rho_{zeo0} r_{des} \tag{5.1}$$

$$-\frac{\partial}{\partial z}(\rho_{g} u_{g}) = -\rho_{zeo0} r_{des} \tag{5.2}$$

The desorption rate can be calculated by **Eq. (5.3)**.

$$r_{des} = k_{LDF}(q_{eq} - q) \tag{5.3}$$

The steam conservation equation in the 2D and 1D models can be expressed by **Eqs. (5.4)** and **(5.5)**, respectively.

$$-\frac{\partial}{\partial z}(\rho_{s} u_{g}) = \frac{1}{r}\frac{\partial}{\partial r}\left(D_{m} \frac{\partial \rho_{s}}{\partial r} \right) + \frac{\partial}{\partial z}\left(D_{ax} \frac{\partial \rho_{s}}{\partial z} \right) - \rho_{zeo0} r_{des} \tag{5.4}$$

$$-\frac{\partial}{\partial z}(\rho_{s} u_{g}) = \frac{\partial}{\partial z}\left(D_{ax} \frac{\partial \rho_{s}}{\partial z} \right) - \rho_{zeo0} r_{des} \tag{5.5}$$

The momentum equation for gas phase can be expressed by **Eq. (5.6)**.

$$\frac{\partial}{\partial z}\left(\frac{\rho_{s} {u_{g}}^{2}}{\varepsilon_{b}} \right) = -\varepsilon_{b}\frac{\partial p}{\partial z} + \frac{150(1-\varepsilon_{b})^{2}\mu_{g}}{{d_{p}}^{2}{\varepsilon_{b}}^{3}} u_{g}\varepsilon_{b} + \frac{1.75(1-\varepsilon_{b})}{d_{p}{\varepsilon_{b}}^{3}} \rho_{g} \left| u_{g} \right| u_{g}\varepsilon_{b} \tag{5.6}$$

The energy conservation equations for zeolite in the 2D and 1D models can be expressed by **Eqs. (5.7)** and **(5.8)**, respectively.

$$\frac{\partial}{\partial z}\left(\rho_{zeo}u_{zeo}c_{pzeo}T_{zeo}\right) = \frac{1}{r}\frac{\partial}{\partial r}\left(\lambda_{zeo\_eff}\frac{\partial T_{zeo}}{\partial r}\right)+\frac{\partial}{\partial z}\left(\lambda_{zeo\_eff}\frac{\partial T_{zeo}}{\partial z}\right)-\frac{6(1-\varepsilon_b)\alpha_{g\text{-}zeo}}{d_p}(T_{zeo}-T_g)+\rho_{zeo0}r_{des}\Delta H \quad (5.7)$$

$$\frac{\partial}{\partial z}\left(\rho_{zeo}u_{zeo}c_{pzeo}T_{zeo}\right) = \frac{\partial}{\partial z}\left(\lambda_{zeo\_eff}\frac{\partial T_{zeo}}{\partial z}\right)-\frac{6(1-\varepsilon_b)\alpha_{g\text{-}zeo}}{d_p}(T_{zeo}-T_g)-\frac{4\alpha_{zeo\text{-}amb}}{d_c}(T_{zeo}-T_{amb})+\rho_{zeo0}r_{des}\Delta H \quad (5.8)$$

The energy conservation equations for gas phase in the 2D and 1D models can be expressed by **Eqs. (5.9)** and **(5.10)**, respectively.

$$-\frac{\partial}{\partial z}\left(\rho_g u_g c_{pg}T_g\right)=\frac{1}{r}\frac{\partial}{\partial r}\left(\lambda_{gr\_eff}\frac{\partial T_g}{\partial r}\right)+\frac{\partial}{\partial z}\left(\lambda_{gax\_eff}\frac{\partial T_g}{\partial z}\right)-\frac{6(1-\varepsilon_b)\alpha_{g\text{-}zeo}}{d_p}(T_g-T_{zeo}) \quad (5.9)$$

$$-\frac{\partial}{\partial z}\left(\rho_g u_g c_{pg}T_g\right)=\frac{\partial}{\partial z}\left(\lambda_{gax\_eff}\frac{\partial T_g}{\partial z}\right)-\frac{6(1-\varepsilon_b)\alpha_{g\text{-}zeo}}{d_p}(T_g-T_{zeo})-\frac{4\alpha_{g\text{-}amb}}{d_c}(T_g-T_{amb}) \quad (5.10)$$

The heat transfer coefficient was predicted by the two-phase model [2] as well as the simulation of Zeolite Boiler, which can be calculated as following equations.

Axial effective thermal conductivity of gas

$$\frac{1}{Pe_{ax}}=\frac{1}{\frac{\rho_g u_g c_{pg}d_p}{\lambda_{gax\_eff}}}=\frac{0.73\varepsilon_b}{Re_p Pr}+\frac{0.5}{1+\frac{9.7\varepsilon_b}{Re_p Pr}} \quad (5.11)$$

Radial effective thermal conductivity of gas

$$\frac{1}{Pe_r}=\frac{1}{\frac{\rho_g u_g c_{pg}d_p}{\lambda_{gr\_eff}}}=\frac{1}{10}+\frac{2/3\,\varepsilon_b}{Re_p Pr} \quad (5.12)$$

Heat transfer on the inner wall of chamber

(zeolite-wall)

$$\alpha_{\text{zeo-wall}} = \frac{2.12\lambda_{\text{zeo\_eff}}}{d_{\text{p}}} \tag{5.13}$$

(gas-wall)

$$Nu_{\text{g-wall}} = 0.6Re_{\text{p}}^{1/2}Pr^{1/3} \tag{5.14}$$

For the 1D model, the overall heat transfer coefficient $\alpha_{\text{eff\_(zeo,g)}}$ from the zeolite bed to the wall surface can be calculated by **Eq. (5.15)** considering the effect of radial effective thermal conductivity λ_{eff} [3] of zeolite bed , which was applicable for the Zeolite Boiler described in Chapter 4.

$$\frac{1}{\alpha_{\text{eff\_(zeo,g)}}} = \frac{1}{\alpha_{\text{(zeo,g)-wall}}} + \frac{r_{\text{c}}}{4\lambda_{\text{(zeo,g)\_eff}}} \tag{5.15}$$

The zeolite in the hopper attached to the top cover of chamber was pre-heated before reaching inside the hopper due to axial heat conduction. The calculation model included additional 0.03 m zeolite bed as the pre-heating zone as well as the simulation of Zeolite Boiler in Chapter 4. The boundary conditions are shown in **Fig. 5.10**.

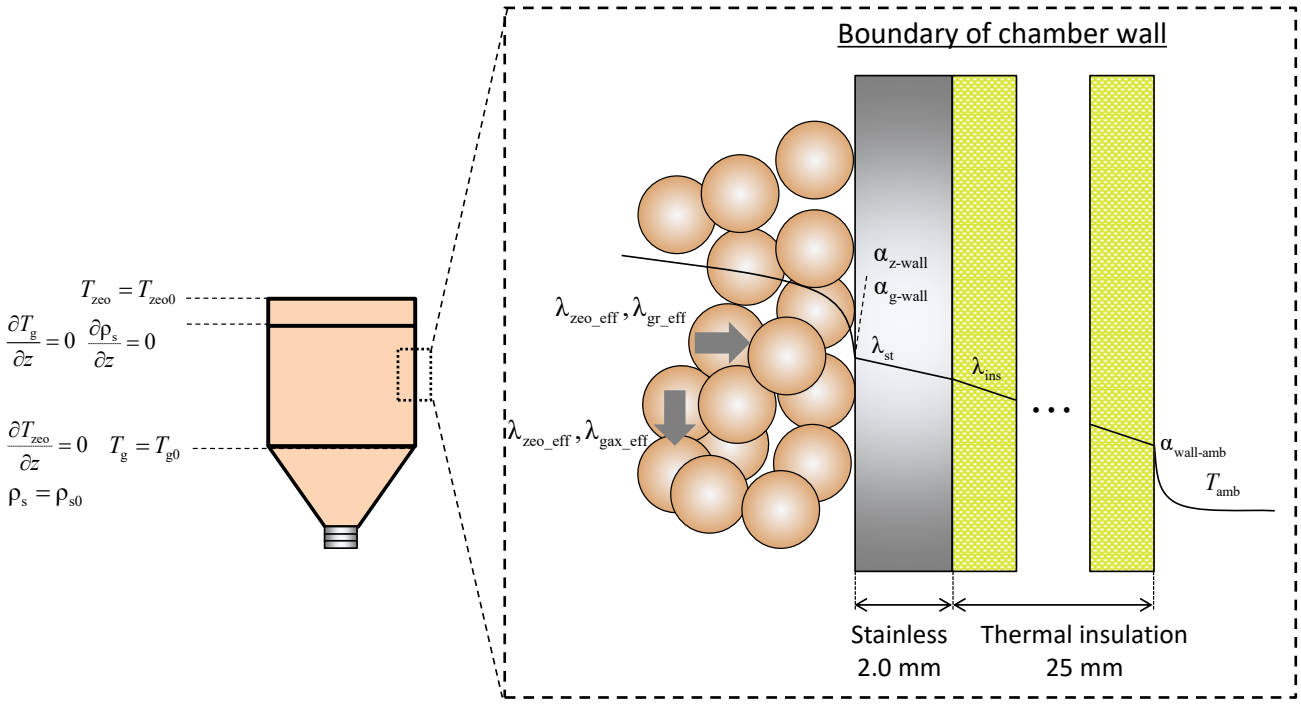

Fig. 5.10. Boundary conditions of numerical simulation of Heat Charger test.

5.4.4 Experimental and numerical analysis result of Heat Charger test

Table 5.3 summarizes the experimental conditions of the Heat Charger test. The mass balance of m_{zeo} and adsorbed water during the Heat Charger test is shown in **Fig. 5.11**. The zeolite was stably discharged at a constant rate of 4.7± 0.2 kg/h during the test. **Figure 5.12** shows the change in q_{out} with the elapsed time. After around 4.5 hours from the start, the q_{out} reached an equilibrium value under the test condition. **Figure 5.13** shows the temperature history at each measuring point during the Heat Charger test. Temperatures increased from the bottom where the gas was introduced to the top. After around 6 hours from the start, all bed temperatures reached steady state. The outlet gas temperature fluctuated even if the bed temperatures reached steady state due to heat leakage from the wall of chamber. **Figure 5.14** shows the experimental result of axial T_{zeo} distribution and q_{out} after 6.5 hours operation. **Figure 5.14** also shows the cylindrical symmetric 2D numerical analysis result of axial T_{zeo} and q distribution at the center ($r = 0$) and the wall ($r = r_{\mathrm{c}}$) positions. The 2D simulation model can simulate the experimental data of T_{zeo} distribution and the q_{out} from the Heat Charger.

Next, the 1D model was compared to the 2D model. In the 2D simulation, in-plane representative temperature of each cross-sectional area model was defined as the following equation and is drawn in the **Fig. 5.15**.

$$T_{\mathrm{rep}} = \frac{1}{A\int \rho_{\mathrm{zeo}} c_{p\mathrm{zeo}} \Delta z dA} \int \rho_{\mathrm{zeo}} c_{p\mathrm{zeo}} T_{\mathrm{zeo}} \Delta z dA \tag{5.16}$$

Figure 5.15 also shows the T_{zeo} and q distribution calculated by the 1D model. There are few discrepancies between each model. From this result, adequacy of the 1D model considering radial effective thermal conductivity was confirmed.

Table 5.3. Experimental conditions of Heat Charger test.

Zeolite	Mass flow rate (kg/h)	Inlet temperature (°C)	Inlet water uptake (kg/kg)
	4.7	24.2	0.194
Gas	Volumetric flow (m^3/min)	Inlet temperature (°C)	Vapor pressure (kPa)
	1.1	164.8	1.34

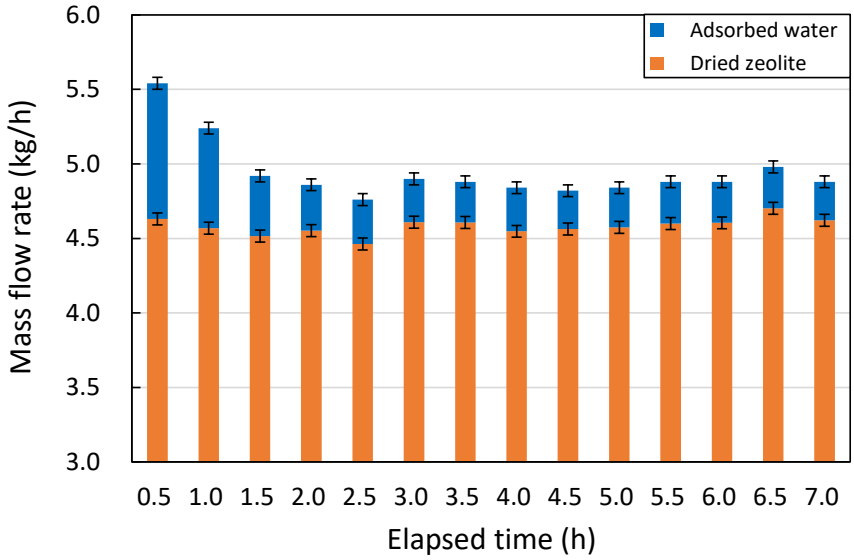

Fig. 5.11. Mass balance of Heat Charger test.

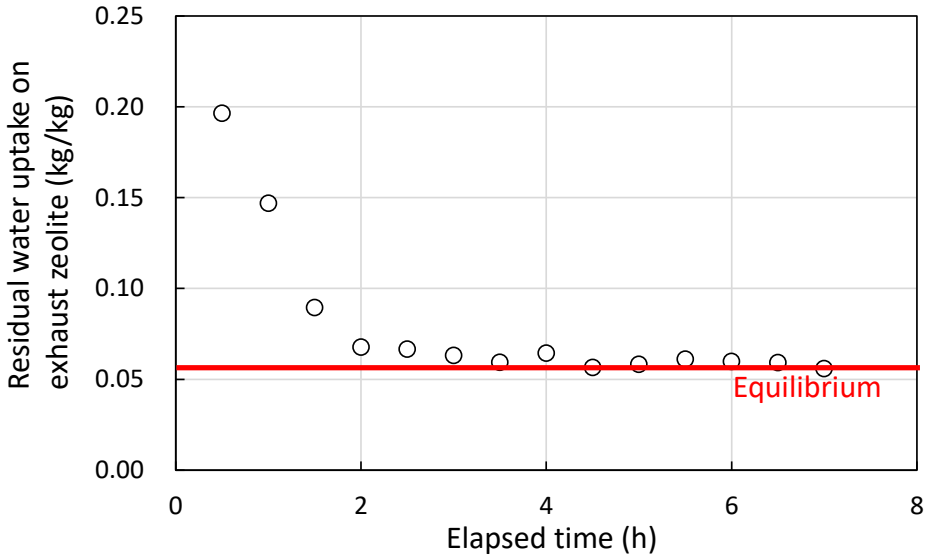

Fig. 5.12. Residual water uptake on exhaust zeolite during heat charging test.

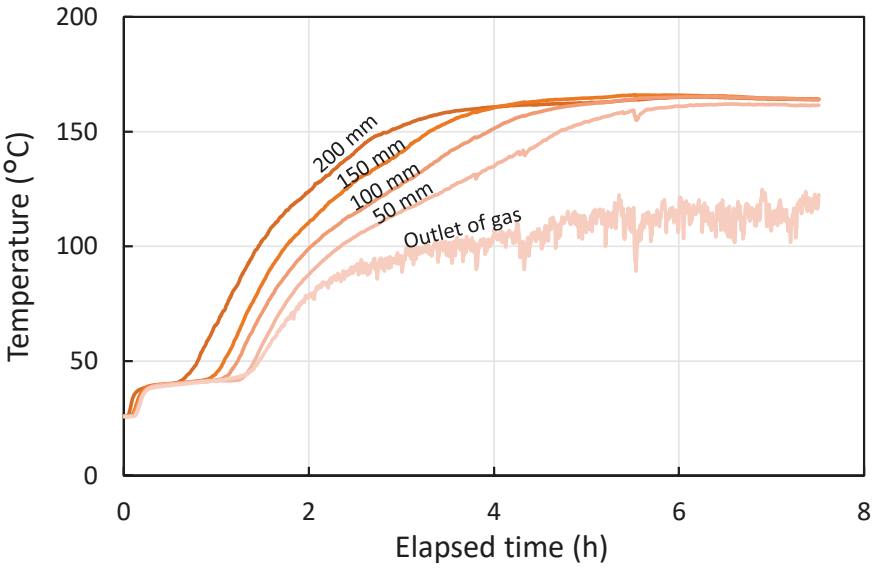

Fig. 5.13. Temperature history during Heat Charger test.

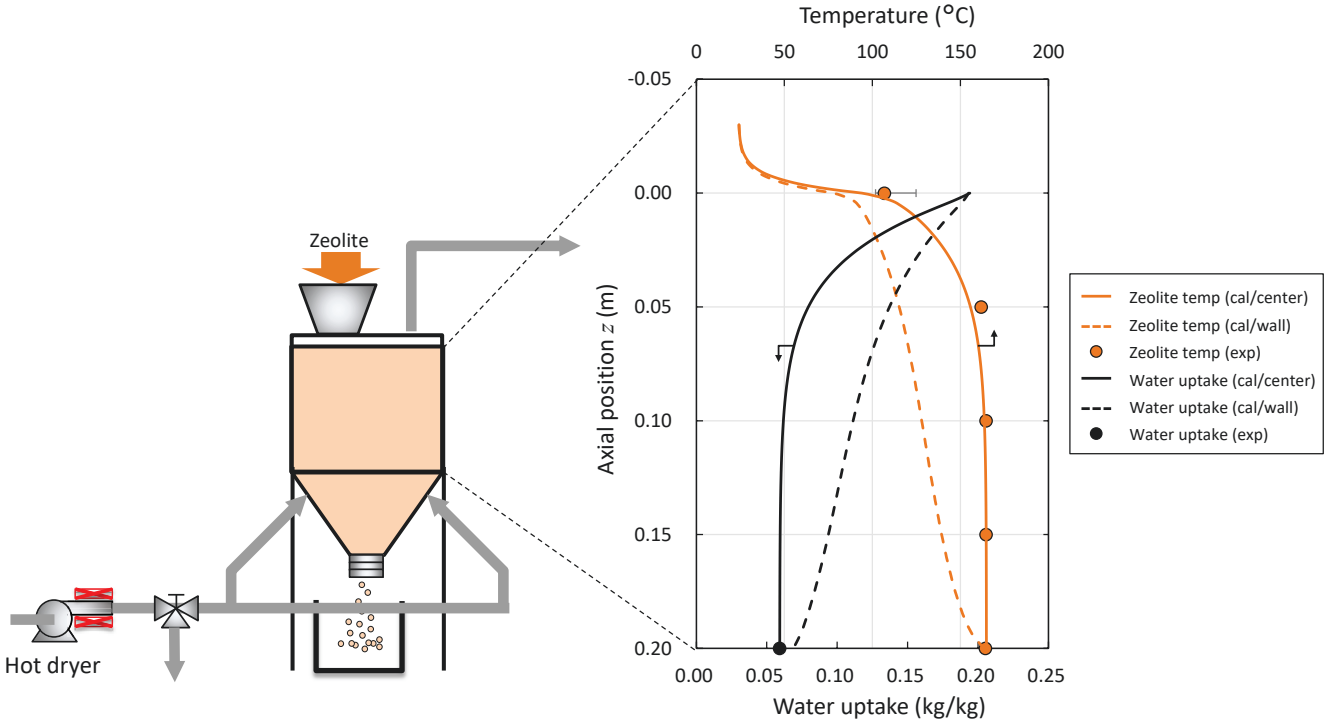

Fig. 5.14. Experimental and numerical analysis result of Heat Charger test.

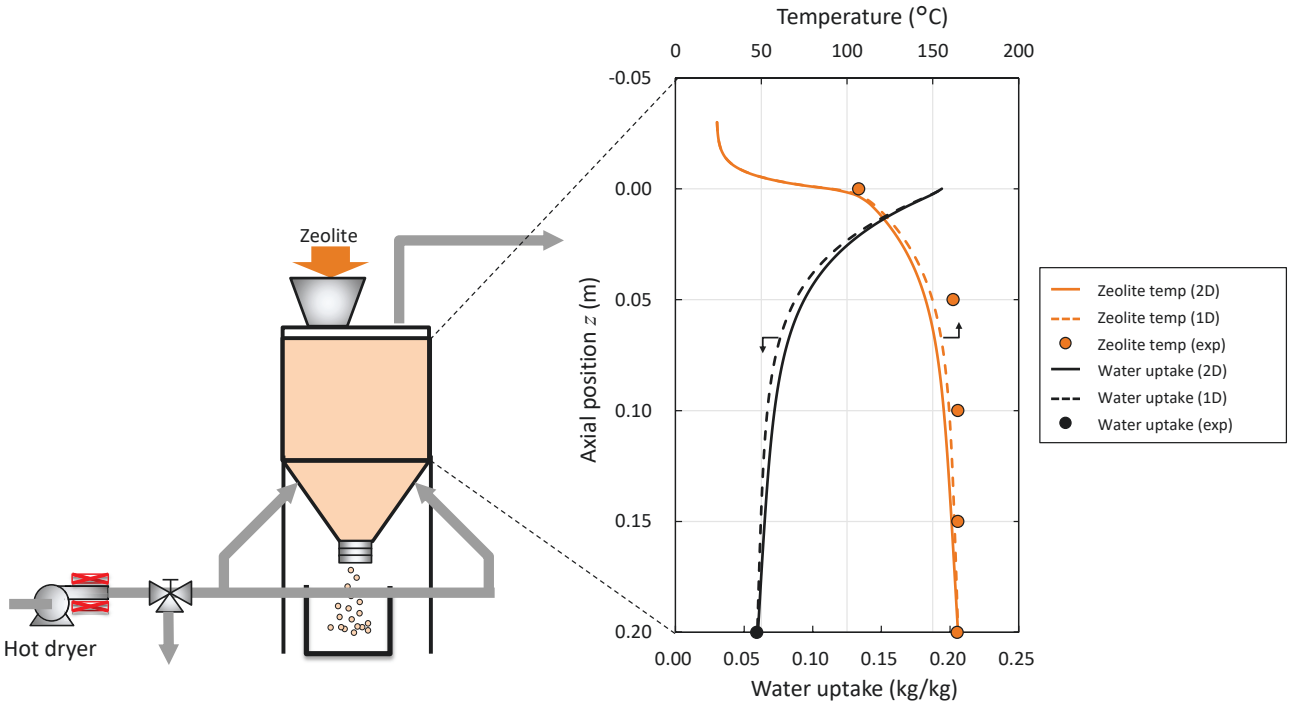

Fig. 5.15. Numerical analysis result of 2D and 1D simulations of Heat Charger test.

5.5 Performance of full-scale Heat Charger in Tanegashima

In this section, the 1D numerical simulation model validated in **5.4** predicted the performance of the full-scale Heat Charger in Tanegashima employing each gas flow direction (counter-flow in **5.5.3**, co-current-flow in **5.5.4** and cross-flow in **5.5.5**). The calculation condition of inlet gas temperature and available space for the Heat Charger were summarized (**5.5.1** and **5.5.2**), and then a comprehensive design method of Heat Charger was proposed via the performance prediction of the full-scale Heat Charger.

5.5.1 Inlet gas temperature

As described in Chapter 3, the ultimate exhaust temperature of flue gas of the bagasse boiler in the current process is 182.2 °C, which is available for the proposed TES. When the ambient air is heated up via a heat exchanger as much as possible (like 180 °C of hot air) to capture the unused heat of the flue gas, the heat charging amount increases but the heat exchanger with enormous heat transfer area costs a lot, and vice versa. This study employed 10 K as the minimum temperature approach since conventional gas to gas heat exchangers employed 4~8 °C temperature approach [4].

5.5.2 Available space for Heat Charger and material reservoirs

In the Tanegashima sugar mill site, an area of 3.0 m x 5.0 m near the stack is available to install Heat Charger. The power consumption of blower W_{blower} mainly caused by pressure drop of packed bed is the dominant factor of the operating cost of the thermochemical energy storage and transport system which is discussed in next Chapter 6. **Figure. 5.16** shows the top view of space for heat charging components. The diameter of co-current and counter-flow Heat Charger was maximized to 3.0 m in order to reduce the W_{blower}. Water-adsorbed zeolite was transported from the heat discharging station, and was assumed to be packed in the reservoir which is mounted above the Heat Charger. A 2.0 m x 3.0 m material reservoir for water-desorbed zeolite was assumed to be placed right beside of the Heat Charger.

The width of zeolite bed of a cross-flow Heat Charger was set to 3.0 m and the height was described in the following section (**5.5.5**). Two 2.0 m x 1.5 m material reservoirs for water-adsorbed and desorbed zeolite were assumed to be placed right beside of cross-flow Heat Charger. Since the available space of 3.0 m x 5.0 m was roughly measured and was not needed to keep strictly, the thickness of thermal insulation and the offset between each chamber are negligible.

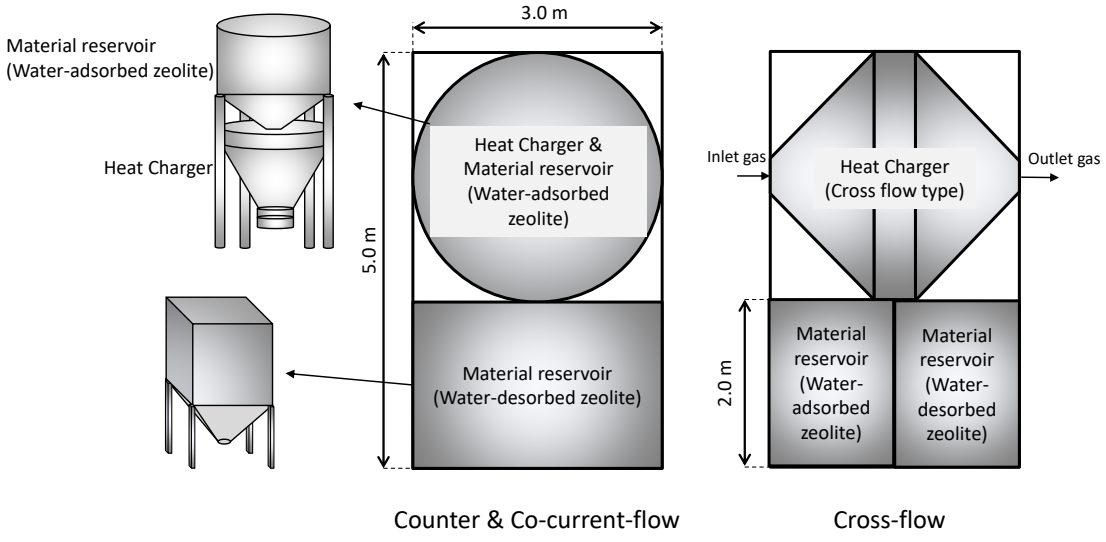

Fig. 5.16. Top view of space for heat charging components (Heat Charger and material reservoirs).

5.5.3 Counter-flow Heat Charger

As a representative case study, the mass flow rate of zeolite was set to m_{zeo} = 1000 kg/h. The 1D numerical simulation model of the full-scale counter-flow Heat Charger in the sugar mill was the same as that of bench-scale Heat Charger (see **5.4.3**). The mass flow rate of hot air for TES was set to the maximum flow rate in the heat charging station (m_{air} = 14.8 t/h) calculated by the material and heat flow analysis in Chapter 3. The diameter and bed height were φ = 3.0 m and H_{bed} = 0.5 m, respectively.

The initial water uptake on zeolite supplied to the Heat Charger was set to q_0 = 0.223 kg/kg, which is the water uptake on zeolite exhausted from the Zeolite Boiler without the secondary heat exchanger (see Chapter 4). **Figure 5.17** shows the axial distribution of T_{zeo}, equilibrium water uptake q_{eq} and q in the counter-flow Heat Charger with the boundary conditions. The q reaches q_{eq} around z = 0.2 m from the top. This result indicates the bed height H_{bed} can be reduced because the zeolite in z > 0.2 m does not exchange water vapor with the gas and just increases the heat leakage from the wall.

Figure 5.18 shows the linkage flow diagram of relationship among each parameter of the full-scale Heat Charger. Diameter of chamber φ was set to 3.0 m at a constant as described above. Initial water uptake on zeolite q_0 depends on the process of Zeolite Boiler. Bed height H_{bed}, m_{air} and m_{zeo} were variable parameters. The space velocity is calculated by the volumetric flow rate of zeolite and the volume of chamber packed with zeolite calculated by the d_c and H_{bed}. The balance of m_{air} and m_{zeo} determines the q_{out}. Power consumption can be calculated by H_{bed}, m_{air} and m_{zeo}. The design method to determine the H_{bed} and m_{air} at each m_{zeo} was explained below.

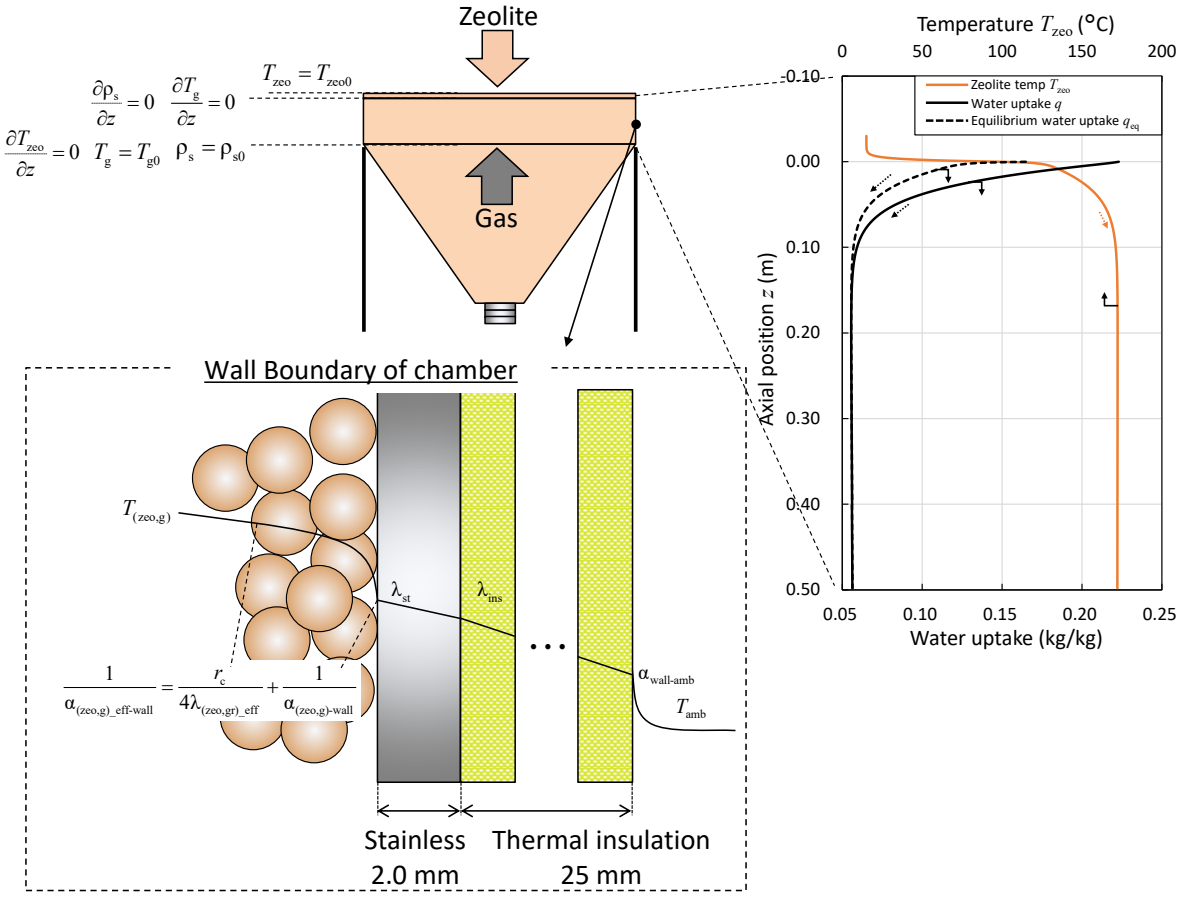

Fig. 5.17. Change in temperature, water uptake and equilibrium water uptake of counter-flow Heat Charger.

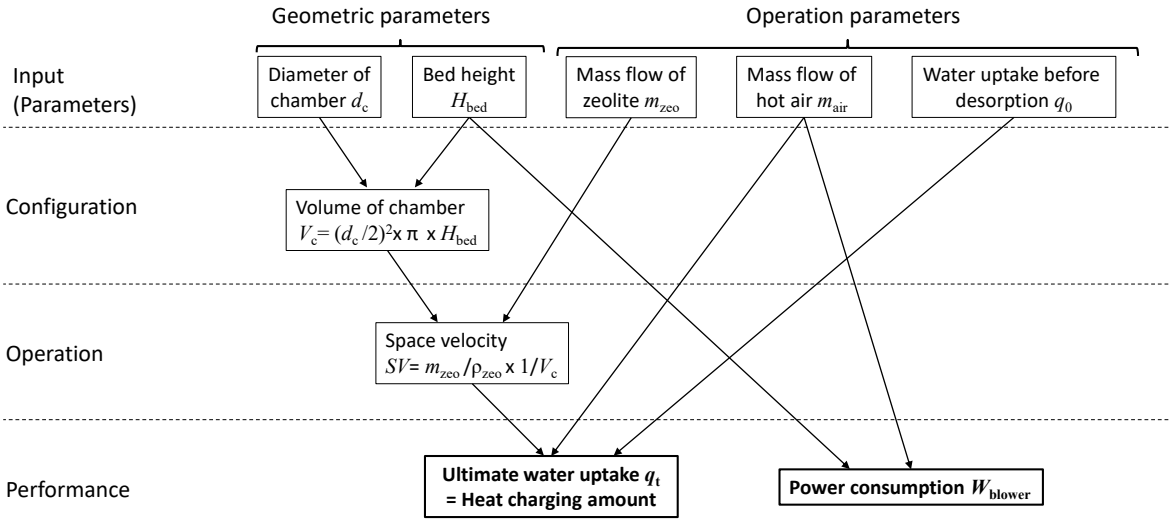

Fig. 5.18. Linkage flow diagram of relationship among each parameter of Heat Charger.

Figure 5.19 shows the q_{out} and the m_{air} as a function of the m_{zeo} in the case of H_{bed} = 0.1 m. The m_{air} was controlled to keep the q_{out} at target water uptakes q_t (0.06, 0.07 and 0.08 kg/kg). The maximum throughput of zeolite can be found from this diagram shown in **Fig. 5.19**. As a representative case, in the case of q_t = 0.06 kg/kg, the maximum m_{air} cannot desorb the zeolite to q_t = 0.06 kg/kg in the range of m_{zeo} > 1100 kg/h. In this case, m_{zeo} = 1100 kg/h is the maximum regenerable throughput of zeolite under this condition. The m_{air} and the maximum regenerable throughput of zeolite at each H_{bed} and q_t can be found by following this procedure.

The H_{bed} was selected to minimize the W_{blower} because the electricity cost derived from blower power dominates the operating cost of the system described in Chapter 6. **Figure 5.20** shows the required m_{air} to keep the q_{out} =q_t = 0.06 kg/kg and the pressure drop ΔP in the case of H_{bed} = 0.1 and 0.2 m as a function of m_{zeo}. The Heat Charger with H_{bed} = 0.1 m requires larger m_{air} than that with H_{bed} = 0.2 m to keep the q_{out} = q_t = 0.06 kg/kg because the residence time of zeolite in the chamber with H_{bed} = 0.1 m is half of that with H_{bed} = 0.2 m. **Figure 5.21** shows the W_{blower} as a function of the m_{zeo} in the case of H_{bed} = 0.1 and 0.2 m. Since the optimal blower was selected to match each volumetric flow of intake air, the constant blower efficiency (50% in this study) was given to calculate the power consumption. The Heat Charger with H_{bed} = 0.1 m requires more power consumption in the range of m_{zeo} > 900 kg/h than that with H_{bed} = 0.2 m due to larger m_{air}, in spite of smaller ΔP in the case of H_{bed} = 0.1 m. The H_{bed} = 0.2 m was selected in this case in the range of m_{zeo} > 900kg/h because of lower W_{blower}.

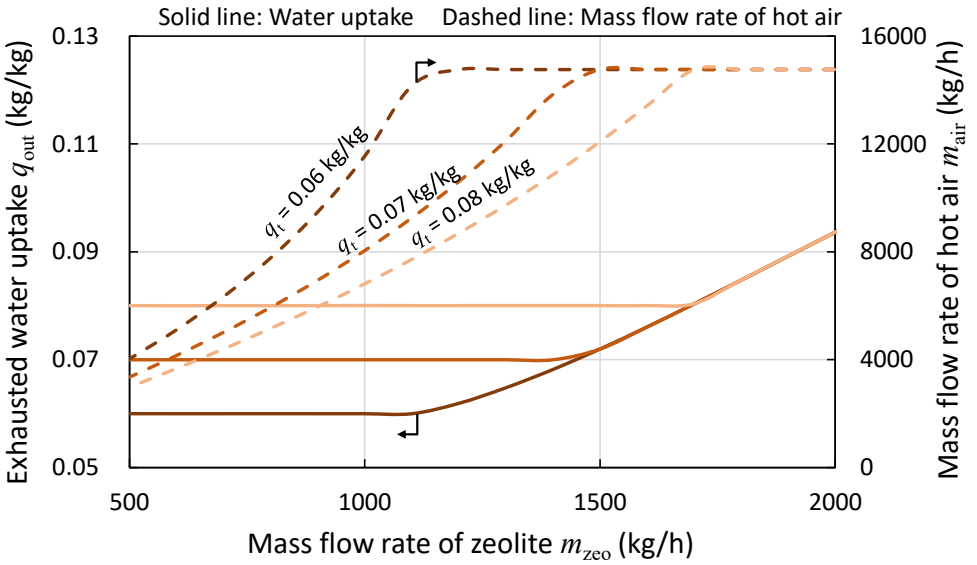

Fig. 5.19. Water uptake on exhausted zeolite and mass flow rate of hot air as a function of mass flow rate of zeolite (H_{bed} = 0.1 m).

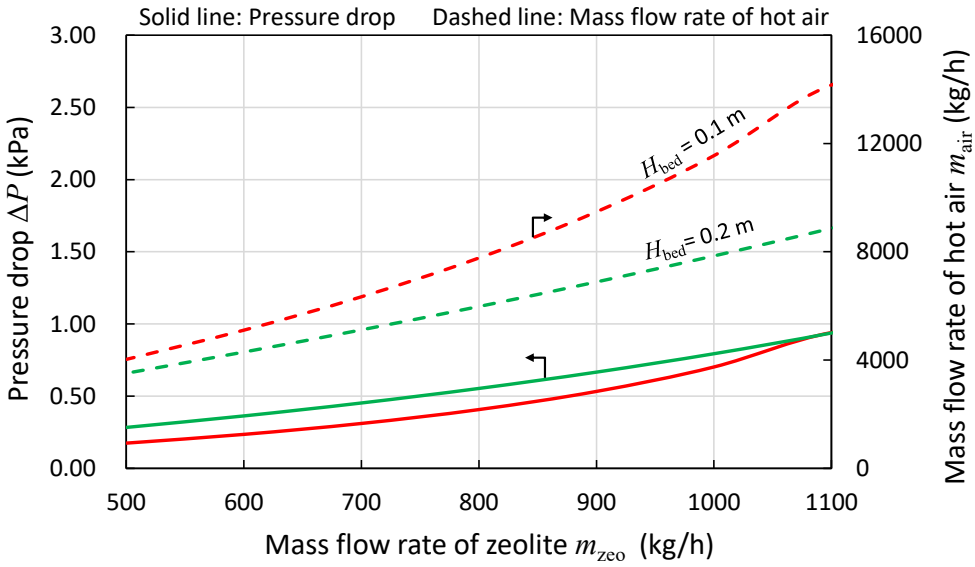

Fig. 5.20. Pressure drop and volumetric flow of gas as a function of mass flow rate of zeolite (q_t = 0.06 kg/kg).

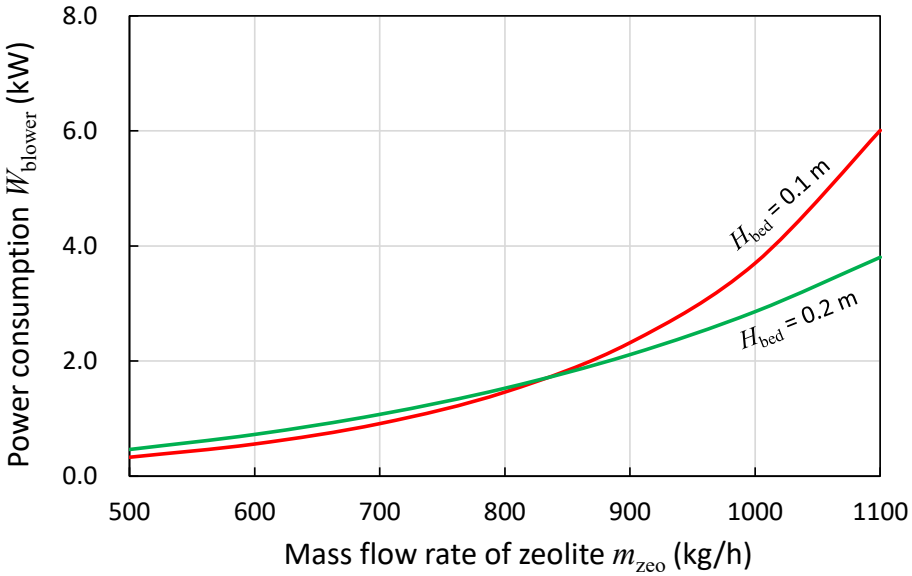

Fig. 5.21. Power consumption of blower as a function of mass flow rate of zeolite.

5.5.4 Co-current-flow Heat Charger

The governing equations for gas phase of the co-current-flow Heat Charger in the 1D numerical simulation exchanged the plus/minus sign of that of counter-flow Heat Charger (see **5.4.3**). **Figure 5.22** shows the axial T_{zeo}, q_{eq} and q distribution in the co-current-flow Heat Charger under the same condition of the representative case study of counter-flow Heat Charger (m_{zeo} = 1000 kg/h, m_{air} = 14.8 t/h, H_{bed} = 0.5 m and q_0 = 0.223 kg/kg). The partial vapor pressure in the gas and corresponding the q_{eq} increase accompanying with proceeding desorption, so the driving force of desorption (q_{eq} - q) decreases resulting the stable $q_{out} \simeq$ 0.10 kg/kg as shown in **Fig. 5.22**. The co-current-flow Heat Charger was eliminated from the candidates of reactor type of Heat Charger because the q_t (for example, 0.06, 0.07 and 0.08 kg/kg) was not able to be reached due to lower driving force of desorption.

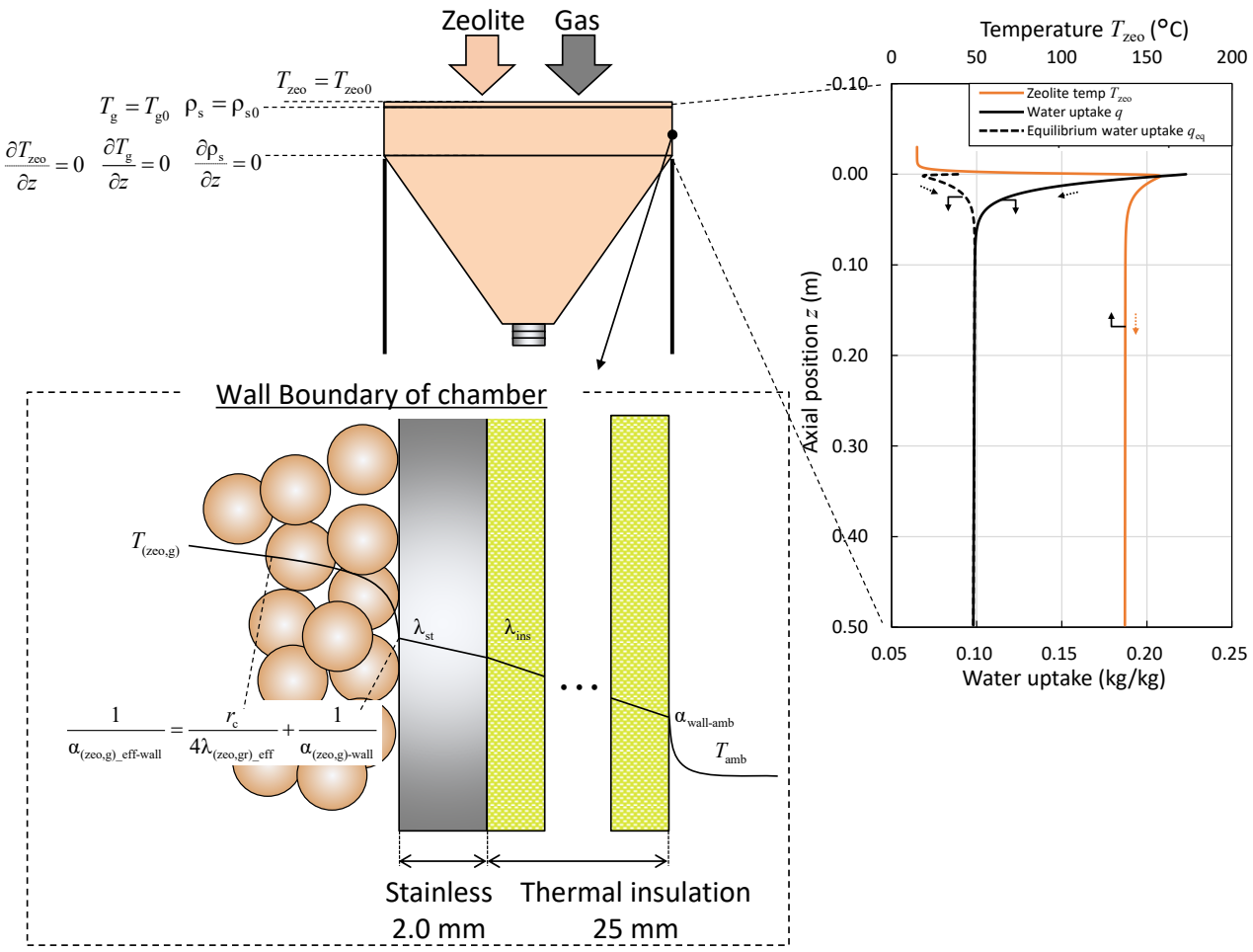

Fig. 5.22. Change in temperature, water uptake and equilibrium water uptake of co-current-flow Heat Charger.

5.5.5 Cross-flow Heat Charger

In the cross-flow Heat Charger, the hot air is introduced from the lateral direction into the zeolite bed. The mass and energy conservation equations of the cross-flow Heat Charger can be calculated as following equations. The orthogonal velocity distribution of gas and zeolite was not considered, and gas flow was regarded as plug flow. The dimension x and y mean gas and zeolite flow direction, respectively.

The mass conservation equations of zeolite and gas

$$\frac{\partial}{\partial y}(\rho_{zeo} u_{zeo}) = \rho_{zeo0} r_{des} \tag{5.17}$$

$$\frac{\partial}{\partial x}(\rho_g u_g) = -\rho_{zeo0} r_{des} \tag{5.18}$$

The steam conservation equation

$$\frac{\partial}{\partial x}(\rho_s u_g) = \frac{\partial}{\partial x}\left(D_{ax} \frac{\partial \rho_s}{\partial x} \right) + \frac{\partial}{\partial y}\left(D_m \frac{\partial \rho_s}{\partial y} \right) - \rho_{zeo0} r_{des} \tag{5.19}$$

The momentum equation

$$\frac{\partial}{\partial x}\left(\frac{\rho_s {u_g}^2}{\varepsilon_b} \right) = -\varepsilon_b \frac{\partial p}{\partial x} - \frac{150(1-\varepsilon_b)^2 \mu_g}{{d_p}^2 {\varepsilon_b}^3} u_g \varepsilon_b - \frac{1.75(1-\varepsilon_b)}{d_p {\varepsilon_b}^3} \rho_g |u_g| u_g \varepsilon_b \tag{5.20}$$

The energy conservation equations of zeolite and gas

$$\begin{aligned} &\frac{\partial}{\partial y}\left(\rho_{zeo} u_{zeo} c_{pzeo} T_{zeo} \right) \\ &= \frac{\partial}{\partial x}\left(\lambda_{zeo\_eff} \frac{\partial T_{zeo}}{\partial x} \right) + \frac{\partial}{\partial y}\left(\lambda_{zeo\_eff} \frac{\partial T_{zeo}}{\partial y} \right) \\ &- \frac{6(1-\varepsilon_b)\alpha_{g\text{-}zeo}}{d_p}(T_{zeo} - T_g) - \alpha_{zeo\text{-}amb}\sigma_{zeo\text{-}amb}(T_{zeo} - T_{amb}) + \rho_{zeo0} r_{des} \Delta H \end{aligned} \tag{5.21}$$

$$\begin{aligned} &\frac{\partial}{\partial x}\left(\rho_g u_g c_{pg} T_g \right) \\ &= \frac{\partial}{\partial x}\left(\lambda_{gx\_eff} \frac{\partial T_g}{\partial x} \right) + \frac{\partial}{\partial y}\left(\lambda_{gy\_eff} \frac{\partial T_g}{\partial y} \right) - \frac{6(1-\varepsilon_b)\alpha_{g\text{-}zeo}}{d_p}(T_g - T_{zeo}) - \alpha_{g\text{-}amb}\sigma_{g\text{-}amb}(T_g - T_{amb}) \end{aligned} \tag{5.22}$$

The axial and radial effective thermal conductivity models of gas phase in the cylindrical reactor [2] were applied to simulate the thermal dispersion in the x direction (Gas flow direction) and the y direction (Zeolite flow direction), respectively. The effective thermal conductivity of zeolite was regarded as stagnant thermal conductivity of zeolite bed as described in Chapter 4. The heat leakage from the wall was calculated by the specific heat transfer area and overall heat transfer coefficient. The specific heat transfer area σ was calculated by the chamber wall area and volume. The overall heat transfer coefficient consisted of heat transfer from the zeolite bed to the chamber wall surface, thermal conduction through the wall (t = 2 mm, stainless), thermal conduction through the thermal insulation (t = 25 mm, glass wool) and natural convection heat transfer from the outer wall of thermal insulation.

The calculation conditions were set to the same as the representative case study of the counter-flow Heat Charger (m_{zeo} = 1000 kg/h, m_{air} = 14.8 t/h and q_0 = 0.223 kg/kg). The height (y direction) and the width (z direction) of chamber were set to 4.5 m and 3.0 m, respectively. Two thickness of zeolite bed (x direction, 0.1 and 0.5 m) were investigated as representative case studies. **Figures 5.23** and **5.24** show the q and the T_{zeo} distribution, respectively. As can be seen from **Figs. 5.23** and **5.24**, the q and the T_{zeo} has similar trend among x and y direction, which means the desorption promptly proceeds when the temperature increases. The q_{out} exhausted from the cross-flow Heat Charger with 0.1 m thickness has a significant distribution along the x direction as shown in **Fig. 5.23** because of quick passage of zeolite though the chamber before temperature increases. However, all the zeolite exhausted from the cross-flow Heat Charger with 0.5 m thickness can be desorbed to equilibrium value uniformly, which indicates sufficient residence time of zeolite for desorption. This distribution in q_{out} makes the design of cross-flow Heat Charger more difficult as compared to the counter-flow Heat Charger from which q_{out} can be easily controlled by changing the temperature and the m_{air}.

Figure 5.25 shows the q distribution when the m_{air} was controlled to keep the in-plane representative water uptake on exhaust zeolite of each cross-sectional area which was defined as the following equation at q_{rep} = 0.06 kg/kg.

$$q_{rep} = \frac{1}{A\int \rho_{zeo0}\Delta y dA}\int \rho_{zeo0} q \Delta y dA \tag{5.23}$$

The q_{out} at the bottom left reached to 0.056 kg/kg (= equilibrium value) because the zeolite packed in the left side is continuously exposed to the inlet gas at the highest temperature. On the other hand, the q_{out} at the bottom right reached to 0.096 kg/kg due to lower temperature increase than the left side. Distribution in the q_{out} at the bottom affects on unstable performance of the Zeolite Boiler. To avoid this distribution in the q_{out}, the cross-flow Heat Charger was designed to desorb the zeolite to the equilibrium water uptake (= 0.056 kg/kg) uniformly.

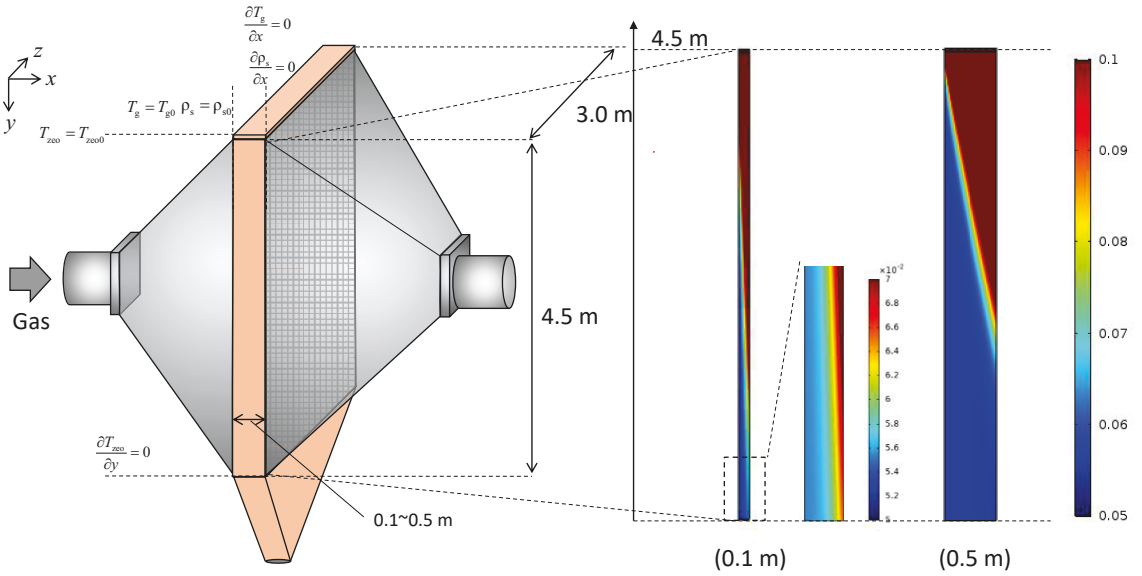

Fig. 5.23. Water uptake distribution in cross-flow Heat Charger.

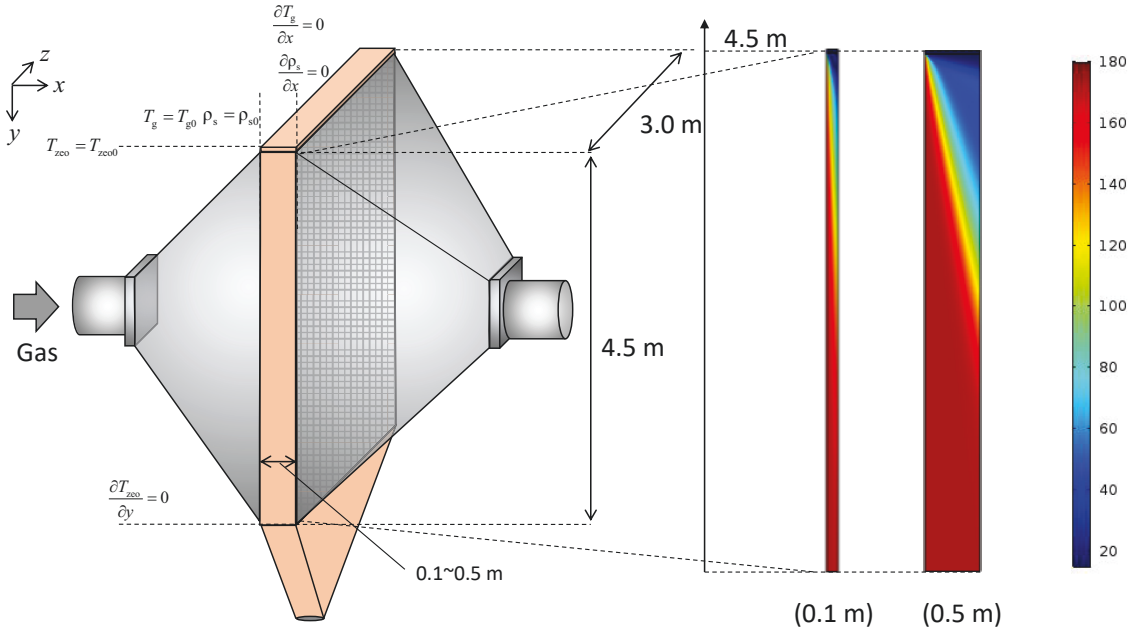

Fig. 5.24. Temperature distribution in cross-flow Heat Charger.

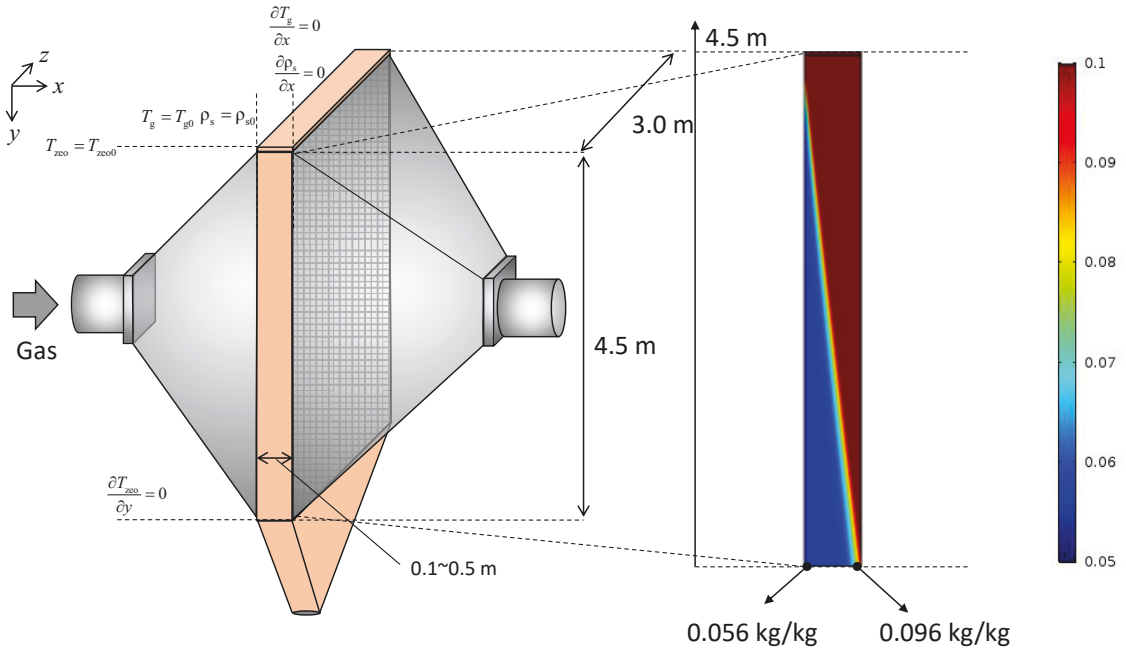

Fig. 5.25. Change in water uptake in cross-flow Heat Charger in the case of q_{rep} = 0.06 kg/kg.

The maximum height of chamber is limited to 5.0 m considering the diffuser installation in the available space shown in **Fig. 5.16**. Two diffusers with 120 ° diffusion angle were designed to connect to the duct with φ = 0.8 m to keep velocity of gas at around 10 m/s. The shorter height of Heat Charger allows thicker bed thicknesses under the same available space of 3 m x 3 m (see **Fig. 5.16**) because the footprint of diffusers become smaller. **Table 5.4** summarizes the allowable bed thickness at each bed height.

Table 5.4. Limitation of bed thickness at each height.

Height	(m)	5.00	4.75	4.50	4.25	4.00
Allowable bed thickness	(m)	0.25	0.35	0.50	0.60	0.75

Table 5.5. Configuration of cross-flow Heat Charger in the case of q_t = 0.056 kg/kg.

m_{zeo}	(kg/h)	500	600	700	800	900	1000	1100	1200
Width	(m)	3.0							
Bed thickness	(m)	0.15	0.15	0.15	0.20	0.25	0.35	0.45	0.60
Height	(m)	5.00	5.00	5.00	5.00	5.00	4.75	4.50	4.25

Table 5.6. Configuration of counter-flow Heat Charger in the case of q_t = 0.056 kg/kg.

m_{zeo}	(kg/h)	500	600	700	800	900	1000	1100	1200	1300
Height H_{bed}	(m)	0.14	0.16	0.18	0.22	0.24	0.28	0.30	0.34	0.44

The bed thickness and the height of chamber were determined to minimize the W_{blower} according to the same design method as the counter-flow Heat Charger described in **5.5.3**. **Table 5.5** shows the determined configuration of cross-flow Heat Charger at each m_{zeo} by the design method. **Figure 5.26** shows the m_{air}, the ΔP and the W_{blower} in both the counter-flow and the cross-flow Heat Chargers at each m_{zeo} determined by the design method when the q_{t} was set to equilibrium value (= 0.056 kg/kg). The pressure drop of flow path expansion and reduction of diffusers in the cross-flow Heat Charger were negligible due to much smaller value than the pressure drop of zeolite bed. The H_{bed} of counter-flow Heat Charger at each m_{zeo} are shown in **Table 5.6** determined by the design method. Cross-flow Heat Chargers have lower ΔP than counter-flow Heat Chargers in the range of m_{zeo}< 1100 kg/h due to its larger cross section area for gas flow direction. However, cross-flow Heat Chargers require a larger m_{air} to heat up the zeolite at the bottom-right point in the **Fig. 5.25**, which leads larger W_{blower} than counter-flow Heat Charger as shown in **Fig 5.26**.

The cross-flow Heat Charger was eliminated from the candidates of reactor type of Heat Charger because larger W_{blower} deteriorates the economic performance.

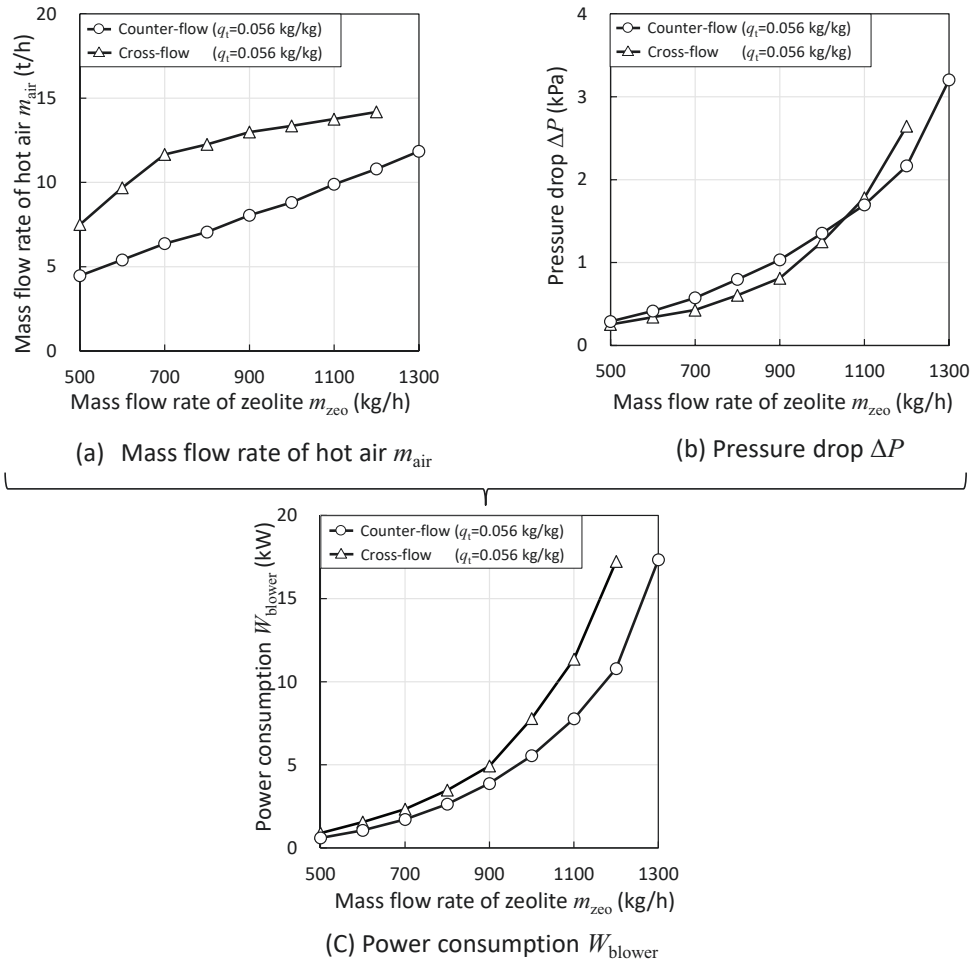

Fig. 5.26. Mass flow rate of hot air, pressure drop and power consumption of both counter-flow and cross-flow Heat Charger as a function of mass flow rate of zeolite.

5.6 Chapter conclusion

In this chapter, a conceptual design of “Heat Charger” employing a moving bed and a direct heat exchanging process was introduced to charge unused heat continuously. A 1D numerical simulation model of Heat Charger including empirical desorption kinetics of zeolite was built and was experimentally validated by the bench-scale test result. Performance characteristics of the full-scale Heat Charger with different gas flow direction (counter-flow, co-current-flow and cross-flow) in Tanegashima was evaluated numerically. Main achievements of this chapter were shown as follows;

- Few hysteresis of equilibrium water uptake between adsorption and desorption was experimentally confirmed by using the diluted fixed bed test.
- Desorption rate was measured by the diluted fixed bed test and 1D numerical model with the Linear Driving Force model considering only the macro pore diffusion can simulate the dynamic change of outlet vapor pressure from the reactor.
- The bench-scale Heat Charger with counter-flow was built and continuous heat charging was successfully demonstrated. The developed 1D numerical model including the empirical desorption and heat transfer model can simulate the performance well.
- The performance of the full-scale counter-flow Heat Charger was predicted using the validated numerical model. The bed height and the mass flow rate of hot air were determined to minimize the power consumption of blower.
- The co-current flow Heat Charger was eliminated from the process candidates of Heat Charger due to small driving force for desorption.
- The target water uptake on exhaust zeolite from the cross-flow Heat Charger should be set to equilibrium value to avoid the heterogeneous exhaust water uptake.
- The cross-flow Heat Charger was also eliminated from the process candidates of Heat Charger due to higher power consumption than the counter-flow Heat Charger.

The design method of the full-scale Heat Charger established in this chapter is used in the techno-economic and environmental analyses in Chapter 6.

Nomenclature

Symbols

A:	Area	m^2
c_p:	Specific heat capacity	J/(kg·K)
d:	Diameter	m
D:	Diffusivity	m^2/s
k:	Overall mass transfer coefficient	1/s
H_{bed}:	Height of bed	m
m:	Mass flow rate	kg/h
p:	Pressure	kPa
q:	Water uptake on zeolite	kg/kg
r:	Radius	m
r_{des}:	Desorption rate	1/s
SV:	Space velocity	1/h
T:	Temperature	K
u:	Velocity	m/s
V:	Volume	m^3
W_{blower}:	Blower power consumption	kW
x,y,z,r:	Dimension coordinate	m
α:	Heat transfer coefficient	$W/(m^2·K)$
ΔH:	Heat of desorption	kJ/kg
ΔP:	Pressure drop	kPa
ε:	Porosity	-
λ:	Thermal conductivity	W/(m·K)
μ:	Viscosity	Pa·s
ρ:	Density	kg/m^3
σ:	Specific heat transfer area	m^2/m^3

Dimensionless parameters

Nu:	Nusselt number
Pe:	Peclet number
Pr:	Prandtl number
Re:	Reynolds number

-

Subscript

air:	Air
amb:	Ambient
ax:	Axial

b: Bed
c: Chamber
eff: Effective
eq: Equilibrium
g: Gas
ins: Insulation
LDF: Linear driving force
m: Molecular
max: Maximum
p: Particle
r: Radial
rep: Representative
s: Steam
st: Stainless
wall: Wall
zeo: Zeolite
0: Original or Initial

References

[1] Simo M, Sivashanmugam S, Brown CJ, Hlavacek V. Adsorption / Desorption of Water and Ethanol on 3A Zeolite in Near-Adiabatic Fixed Bed. Ind Eng Chem Res 2009;48:9247–60. doi:https://doi.org/10.1021/ie900446v.

[2] Dixon AG, Cresswell DL. Theoretical prediction of effective heat transfer parameters in packed beds. AIChE J 1979;25:663–76. doi:https://doi.org/10.1002/aic.690250413.

[3] de Wasch AP, Froment GF. Heat transfer in packed beds. Chem Eng Sci 1972;27:567–76. doi:10.1016/0009-2509(72)87012-X.

[4] https://www.petroskills.com/blog/entry/00_totm/jun19-fac-impact-of-temperature-approach-of-the-heat-exchangers-on-the-capex (Accessed on Nov,2019) 2019.

This page intentionally left blank.

Chapter 6 Techno-economic and environmental analyses

6.1 Objectives of this chapter

Figure 6.1 shows the structure of this dissertation, and the position of this chapter. This chapter combines process modeling of the sugar mill with performance predictions for the Zeolite Boiler and Heat Charger to conduct techno-economic and environmental analyses. The design method of the Zeolite Boiler and Heat Charger established in Chapters 4 and 5, respectively, were used to determine the configurations and performance of each piece of equipment. In addition, the effects of technological options for the heat discharging station and the charging station on economic and environmental performance were investigated. The main objectives of this techno-economic analysis were to clarify the conditions under which the thermochemical energy storage and transport system would be financially viable, and to identify the dominant determinants of the net profit of the system at a proof-of-concept stage. In addition, the net CO_2 emissions of the system were evaluated.

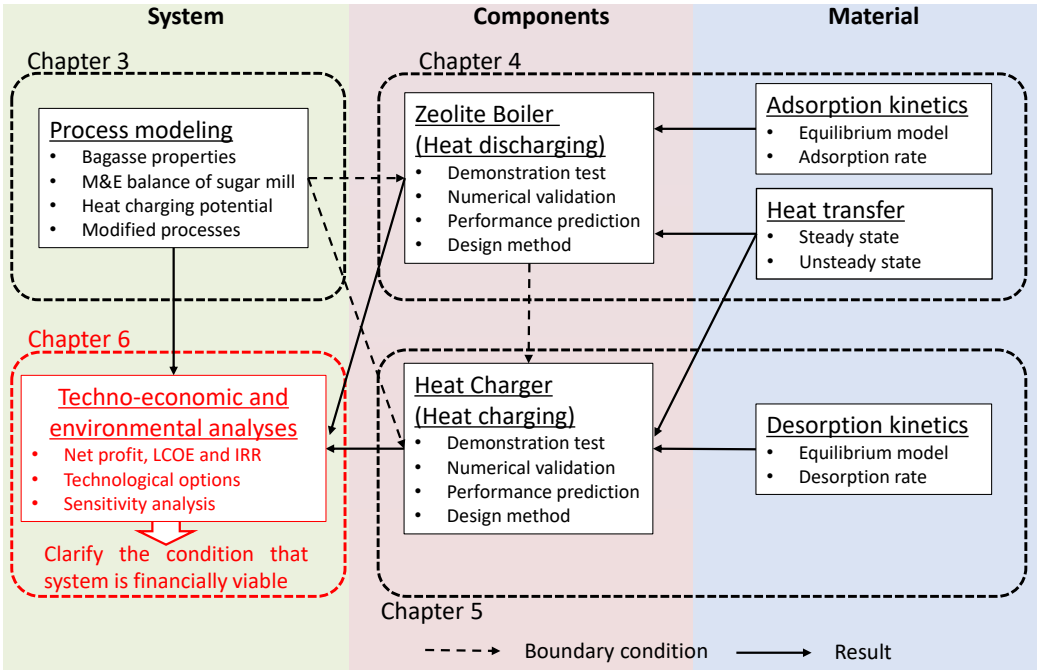

Fig. 6.1. Structure of dissertation and position of this chapter.

6.2 Preparation for techno-economic and environmental analyses

In this chapter, the ultimate water uptake on exhaust zeolite from the Heat Charger (i.e., the inlet water uptake on the zeolite supplied to the Zeolite Boiler) is defined as the “minimum water uptake in the system $q_{\min}$”, and the inlet water uptake on the zeolite supplied to the Heat Charger (i.e., the

ultimate water uptake on exhaust zeolite from the Zeolite Boiler) is defined as the "maximum water uptake in the system q_{max}". Zeolite exhausted from the Heat Charger and zeolite exhausted from the Zeolite Boiler are defined as "Water-desorbed zeolite" and "Water-adsorbed zeolite", respectively.

To evaluate the economic characteristics of the model, the following indices were introduced.

(1) Net profit

As described in **6.1**, the objectives of the techno-economic analysis in this study at the proof-of-concept stage were to clarify the conditions under which the system would be financially viable, and to identify the dominant determinants of the net profit of the system.

(2) Levelized cost of energy (LCOE)

The levelized cost of energy (LCOE) of the thermochemical energy storage and transport system was introduced to compare the economic aspects of different cases considering the effect of CAPEX (Capital expenditure). The LCOE of the thermochemical energy storage and transport system can be calculated by dividing the annual cost (annual CAPEX + OPEX, Operating expenses) by the effectively utilized energy amount in the heat discharging station (i.e., the saved energy by the Zeolite Boiler) which can be calculated by **Eq. (6.1)**.

$$\mathrm{LCOE} = \frac{\alpha \cdot \mathrm{CAPEX} + \mathrm{OPEX}}{\text{Effectively utilized energy}} \tag{6.1}$$

where α is the capital recovery factor and can be calculated by **Eq. (6.2)** using the interest rate i (2% in this study) and the lifetime of equipment N (15 years in this study).

$$\alpha = \frac{i(1+i)^N}{(1+i)^N - 1} \tag{6.2}$$

To clarify the required funding support of CAPEX, the LCOE, considering the subsidy rate β, can be calculated by **Eq. (6.3)**.

$$\mathrm{LCOE} = \frac{(1-\beta) \cdot (\alpha \cdot \mathrm{CAPEX}) + \mathrm{OPEX}}{\text{Effectively utilized energy}} \tag{6.3}$$

The LCOE in the case of β = 0% was calculated for comparison with conventional fuel (heavy oil; approximately 10 JPY/kWh). When the system was profitable (net profit > 0), the effect of β on LCOE was investigated to clarify the required subsidy rate to operate this system.

(3) Internal rate of return (IRR)

If the system is financially viable (net profit > 0), an investment can be returned when the appropriate CAPEX support is publicly provided. The internal rate of return (IRR) described in **Eq. (6.4)** was employed as a benchmark for the investment. The initial investment was determined in consideration of subsidy rate β.

$$0 = \sum_{n=1}^{N} \frac{C_n}{(1+\mathrm{IRR})^n} - (1-\beta)\cdot \mathrm{CAPEX}. \tag{6.4}$$

6.2.1 Zeolite Boiler in heat discharging station

A food processing factory was assumed as a heat consumer (heat discharging station) for the thermochemical energy storage and transport system in Tanegashima. The distance between the sugar mill and the food processing factory is 3 km. The food processing factory begins their operations from the beginning of December (approximately 10 days before the sugar mill commences the milling process), operates for 80 days, and ceases operations in the middle of February, as shown in **Fig. 6.2**. The sugar mill operates continuously from the middle of December to the middle of April with two downtime terms for washing vessels (typically at the year-end and new year holidays, and at the end of February; for details, see Chapter 3). The food processing factory is assumed to stop its operations during the year-end and new year holidays, and the thermochemical energy storage and transport system operates for the 70 days on which both the sugar mill and the food processing factory are in operation.

During the operating season, the existing oil-fired boiler operates for 42 hours and stops for 6 hours in 2 days and repeats this cycle (total operating time of heat discharging station: 1470 hours), while the sugar mill operates continuously (total operating time of charging station: 1680 hours). The mass flow rate of zeolite provided to the Zeolite Boiler (= $m_{\mathrm{zeo}}^{\mathrm{ZB}}$) in the heat discharging station was set to 1.14 (48 hours/42 hours) times greater than that in the heat charging station (= $m_{\mathrm{zeo}}^{\mathrm{HC}}$).

The food processing factory uses a 2000 kg/h-class commercial heavy oil-fired boiler. In this study, pressurized steam (0.2 MPa) of 1800 kg/h was assumed to be consumed for industrial processes. The boiler efficiency was assumed to be 90%. The revenue of this system was calculated by the reduction in the amount of heavy oil (heating value: 38.9 MJ/L) resulting from the application of the Zeolite Boiler, and its unit price (111 JPY/L).

The Zeolite Boiler was designed in accordance with the design method established in Chapter 4. The calculation range is $m_{\mathrm{zeo}}^{\mathrm{ZB}}$ = 500–2700 kg/h in 100 kg/h steps. The length at which 99% of the maximum fuel saving can be achieved was selected. **Figure 6.3** shows the fuel saving and length of the heat exchanger as a function of $m_{\mathrm{zeo}}^{\mathrm{ZB}}$. The fuel saving linearly increases with an increase in $m_{\mathrm{zeo}}^{\mathrm{ZB}}$

at any $q_{\min}$. The length of the heat exchanger increases stepwise by increasing ${m_{\text{zeo}}}^{\text{ZB}}$. This stepwise change in length is due to the calculation step of the length (0.1 m). The fuel saving and length of the heat exchanger were predicted by a linear approximation and a linear interpolation as a function of ${m_{\text{zeo}}}^{\text{ZB}}$, respectively.

The Zeolite Boiler starts its operations every 2 days. Thus, the time taken for a cold-start must be considered. The time taken for the Zeolite Boiler to reach steady state operation (cold-start time) roughly equals the residence time of zeolite in the chamber. The fuel saving was assumed to linearly increase during a cold-start in each condition. For example, in the case that Zeolite Boiler saves 10 L/h of heavy oil in steady operation because 1 hour is required for a cold-start, the fuel saving is 5 L/h in the first 1 hour, as shown in **Fig. 6.2**.

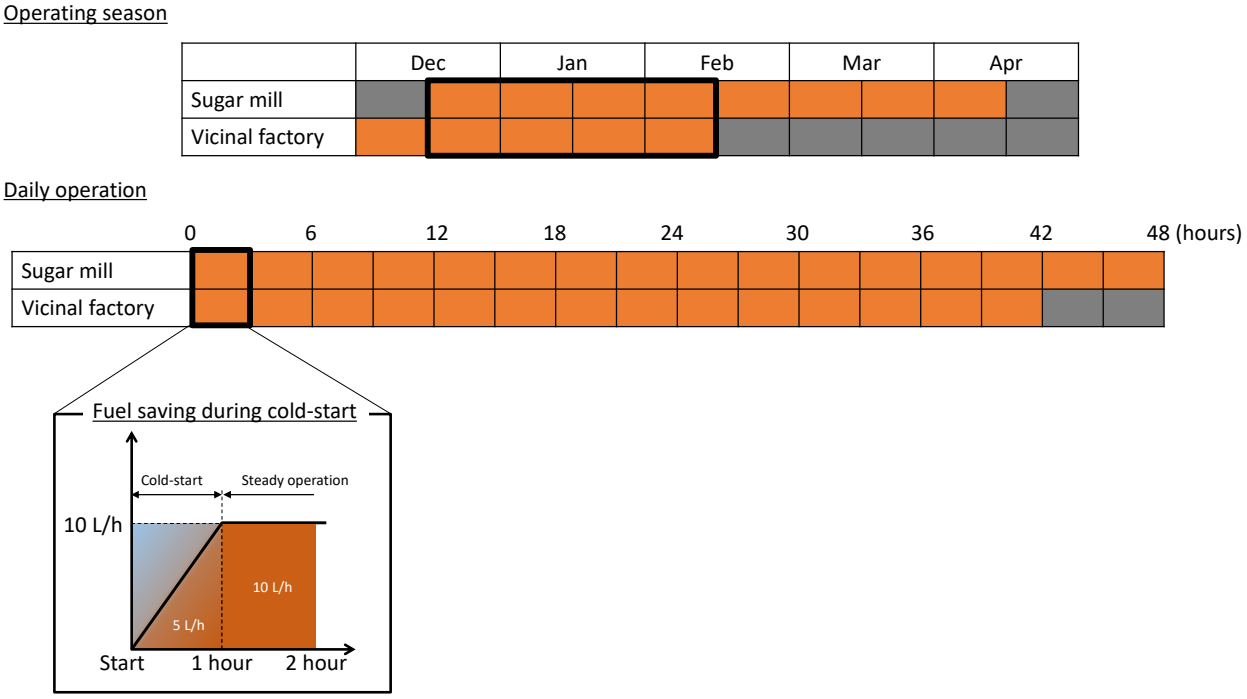

Fig. 6.2. Operation term of the sugar mill and heat consumer (food processing factory).

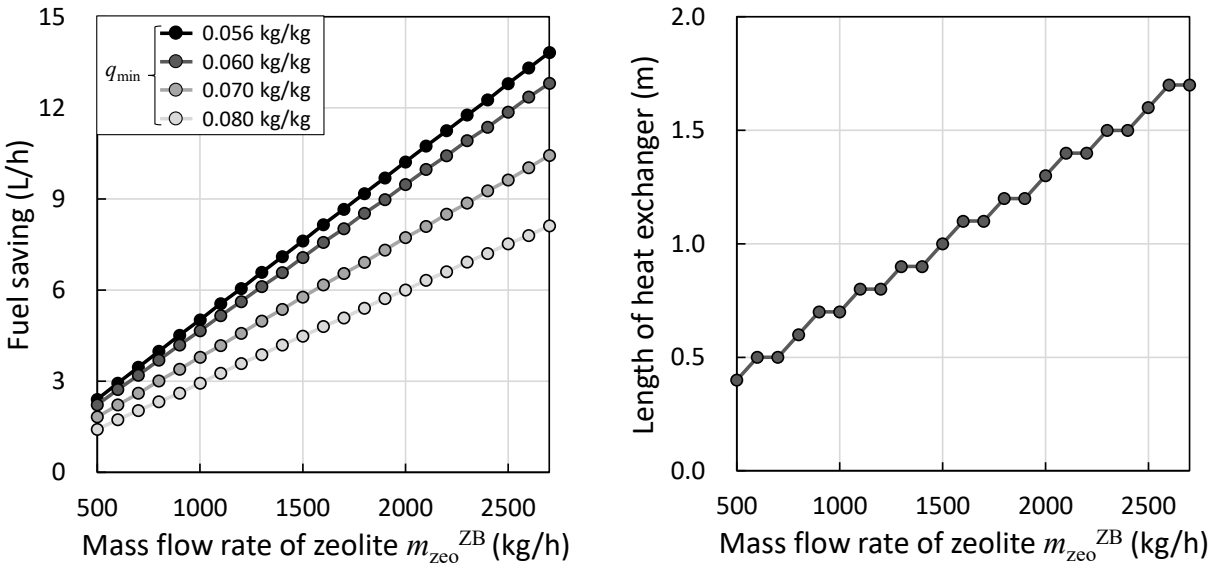

(a) Fuel saving (b) Length of heat exchanger

Fig. 6.3. Summary of fuel savings for the existing boiler and the length of the heat exchanger of the Zeolite Boiler.

6.2.2 Heat Charger in heat charging station

A counter-flow type reactor was employed as the conceptual design of the Heat Charger. As described in Chapter 5, the configuration and operating conditions of the Heat Charger (bed height H_{bed} and the mass flow rate of hot air m_{air}) were determined to minimize the power consumption of the blower W_{blower} which injects hot air into the zeolite bed.

As a representative case, a value of q_{min} = 0.060 kg/kg was considered. **Figure 6.4** shows the results of **(a)** the m_{air} and the H_{bed}, **(b)** the pressure drop ΔP, and **(c)** the W_{blower} as a function of m_{zeo}^{HC} which were determined in accordance with the design method of the Heat Charger. The m_{air} reached its maximum value at m_{zeo}^{HC} = 1800 kg/h. The m_{air} and the H_{bed} linearly increased with the increase in m_{zeo}^{HC} in the range of m_{zeo}^{HC} < 1800 kg/h. In the range of m_{zeo}^{HC} > 1800 kg/h, higher H_{bed} was required to extend the residence time of zeolite in the Heat Charger to desorb to the q_{min} = 0.060 kg/kg under the same maximum m_{air}. Therefore, the H_{bed}, ΔP and accompanying W_{blower} drastically increased in the range of m_{zeo}^{HC} = 1800–2100 kg/h. Zeolite is unable to be regenerated to the q_{min} = 0.060 kg/kg in the range of m_{zeo}^{HC} > 2100 kg/h even if the H_{bed} is increased.

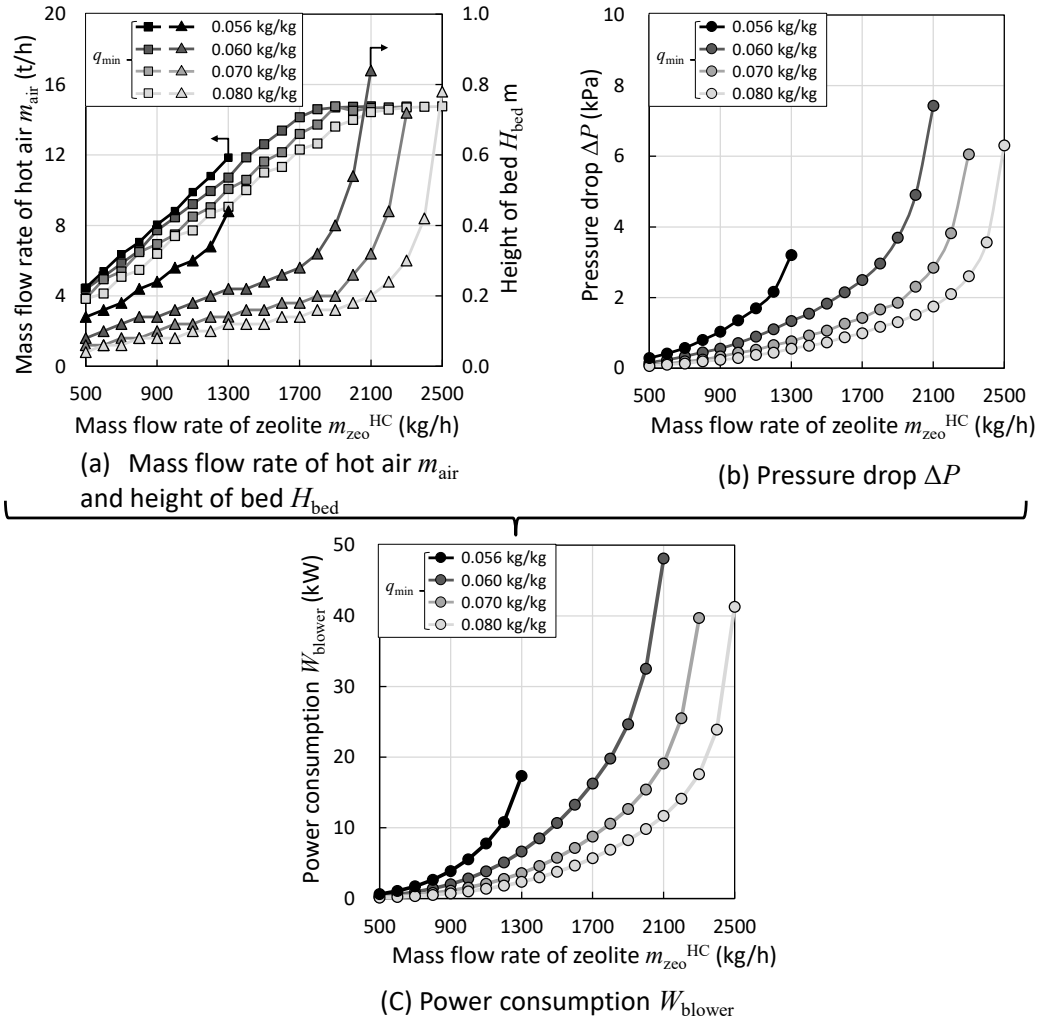

Fig. 6.4. Power consumption of the counter-flow Heat Charger W_{blower} calculated by the mass flow rate of hot air m_{air}, height of bed H_{bed} and pressure drop ΔP.

The above method for determining the configuration and operating conditions of the Heat Charger was conducted in cases of q_{min} = 0.056 (= equilibrium value q_{eq}), 0.070 and 0.080 kg/kg. **Figure 6.4** shows the results of m_{air}, H_{bed}, ΔP and W_{blower} at each q_{min}. Compared with the case of q_{min} = 0.056 and 0.060 kg/kg, greater m_{air} is needed to desorb to the q_{min} = 0.056 kg/kg (equilibrium value) because the driving force for desorption ($q_{\mathrm{eq}} - q$) is smaller than the case of q_{min} > 0.060 kg/kg. Therefore, the pressure drop and accompanying total pressure and partial vapor pressure of inlet air increase, leading to q_{eq} > 0.056 kg/kg in the range of $m_{\mathrm{zeo}}^{\mathrm{HC}}$ > 1300 kg/h. This causes the maximum throughput of zeolite in the case of q_{min} = 0.056 kg/kg to be limited to 60% of the case of q_{min} = 0.060 kg/kg.

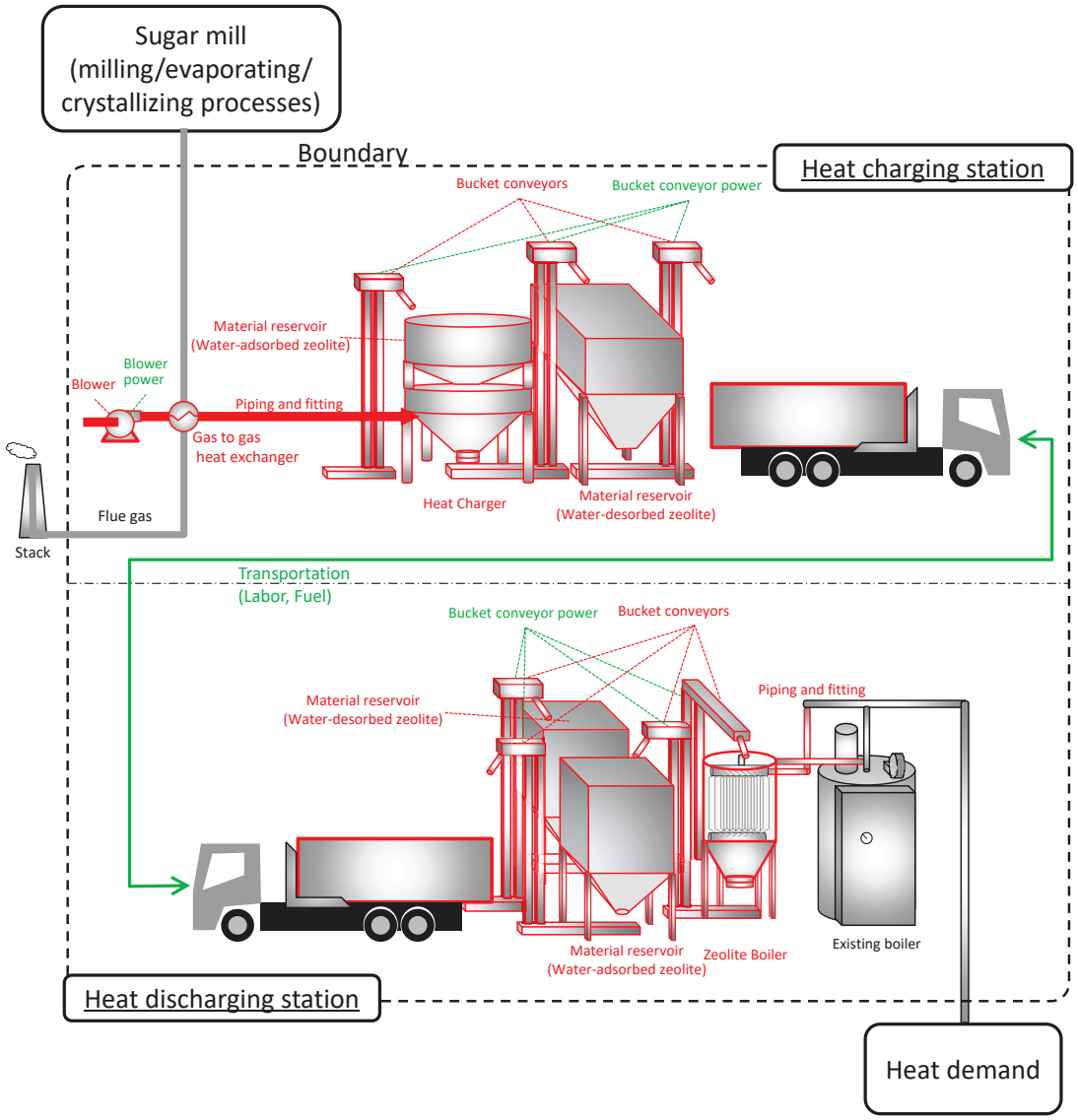

Fig. 6.5. Schematic of heat charging/discharging station and system boundary.

6.2.3 Boundary and cost estimation

Figures 6.5 shows the boundary of the techno-economic and environmental analyses and the schematic of the heat charging station and discharging station. The red and green items are related to the CAPEX and OPEX, respectively.

(1) Heat charging station

(Main chamber)

The diameter of the main chamber of the Heat Charger was assumed to be φ3.0 m (the maximum diameter for the allowable space), as described in Chapter 5. The H_{bed} was determined following the design method described above (described in **6.2.2**). The weight and volume of the chamber were

calculated, and the cost was estimated by the unit cost, including the installation cost per chamber weight in the cost handbook [1].

(Material reservoirs)

The counter-flow Heat Charger occupies 3 m × 3 m space in the allowable space of 3 m × 5 m (see Chapter 5). A material reservoir comprising a cylindrical hopper for water-adsorbed zeolite provided to the Heat Charger was assumed to be placed above the main chamber of the Heat Charger. The other material reservoir, comprising a rectangular hopper for water-desorbed zeolite, was assumed to be placed in the rest space (see Chapter 5). The transportation pattern of zeolite, which is described in the following section, determines the maximum storage amount of water-adsorbed and desorbed zeolite in the sugar mill. The volume of each hopper was determined by the maximum stock amount of zeolite and 10% of the chamber volume was added as a spatial margin. The cost of the hoppers was estimated using the cost handbook [1] as well as the main chamber of the Heat Charger.

(Gas to gas heat exchanger)

As described in Chapter 5, the minimum temperature approach between flue gas and hot air for TES was set to 10 °C. The overall heat transfer coefficient (UA value) was determined by the heat duty of the heat exchanger, and the heat transfer area was calculated with the assumption of 100 W/(m^2·K) of overall heat transfer coefficient. The cost of the heat exchanger was estimated by the unit cost per heat transfer area in the cost handbook [1]. As the installation cost, 40% of CAPEX of the heat exchanger was appropriated.

(Blower and its power consumption)

Because the optimal blower was selected to match each volumetric flow of intake air, the constant blower efficiency (50% in this study) was used to calculate the W_{blower} value, as described in Chapter 5. The cost of the blower was estimated by the unit cost per air flow rate using the cost handbook [1]. The CAPEX of the motor to drive the blower was calculated by the unit cost per output power using the cost handbook [1]. The OPEX was calculated by the W_{blower} multiplying the motor output and operating time of the heat discharging station. As the installation cost, 40% of the CAPEX of the blower and motor were appropriated.

(Particle discharger)

The particle discharger with three stainless disks described in Chapter 4 was assumed to be mounted under the bottom of the Heat Charger. The required power for rotating the disk of the discharger was negligible due to its small value. The CAPEX of the particle discharger was assumed to be roughly equal to the conventional rotary particle discharger.

(Bucket conveyors)

In the moving bed reactor, zeolite is provided from the top and moves down, driven by gravity. To realize the moving bed reactor, the potential energy has to be given to zeolite. Bucket conveyors were employed to transport the zeolite. The CAPEX of the bucket conveyors was estimated by referring to grain conveyors. As the installation cost, 40% of the CAPEX of bucket conveyors was appropriated.

(Piping and fitting)

As the piping and fitting cost, 5% of the CAPEX of the heat charging station was appropriated.

(Maintenance)

The yearly maintenance cost of 1% of the CAPEX of the heat charging station was appropriated to the OPEX.

(2) Heat discharging station

(Main chamber)

The diameter of main chamber of the Zeolite Boiler was set to φ1.5 m, as discussed in Chapter 4. The length of the heat exchanger was determined following the design method of the Zeolite Boiler described above (**6.2.1**). The cost was estimated by referring to the unit cost per chamber weight in the cost handbook [1].

(Heat exchanger)

The heat transfer area of multi-tubular heat exchanger was calculated by the length, pitch, and diameter of each tube, as described in Chapter 4. The CAPEX was estimated by referring to the unit cost per heat transfer area in the cost handbook [1]. As the installation cost, 40% of the CAPEX of the heat exchanger was appropriated.

(Material reservoirs)

Rectangular chambers with 2.5 m × 2.5 m cross-section area were employed as material reservoirs for both water-adsorbed and water-desorbed zeolite. The volume of each hopper was determined by the maximum stock amount of zeolite and 10% of the chamber volume was added as a spatial margin. The cost of hoppers was determined using the cost handbook [1].

(Particle discharger)

The particle discharger was same as for the heat charging station.

(Piping and fitting)

As well as the heat charging station, 5% of the CAPEX of the heat discharging station was appropriated as the piping and fitting cost.

(Bucket conveyor)

The bucket conveyor was same as for the heat charging station.

(Maintenance)

The maintenance was the same as for the heat charging station.

(3) Zeolite

The unit cost of zeolite was set to 50 JPY/kg based on the assumption of using Chinese manufactured zeolite.

(4) Transportation

(Transportation capacity)

As a transportation trailer, a detachable container trailer that enables easy loading and unloading of the container was employed and the CAPEX was estimated. In the European case study, a 20 ft or 40 ft container with heat storage material was assumed to be loaded onto a large trailer [2,3]. In Tanegashima, many mid-class trucks transport the sugarcane from the farm to the sugar mill (approximately 400 trucks during the sugar mill operation). In this study, a detachable container trailer with 8.6 t of maximum loading capacity (including container) was assumed to transport the zeolite because many drivers with licenses to drive semi-medium vehicles who usually transport sugarcane can also operate this type of mid-class trailer. Considering the container weight, 7 t of dried zeolite can be transported by a trailer. The maximum loading capacity of zeolite was determined by the maximum weight of water-adsorbed zeolite. When the Zeolite Boiler without a secondary heat exchanger was employed in the heat discharging station, the maximum loading capacity of zeolite was limited to 5.7 t, considering $q_{\max}$ = 0.223 kg/kg (see Chapter 4).

(Fuel and labor cost)

The fuel price (diesel oil) and fuel consumption rate of trailer were assumed to be 151 JPY/L and 3 km/L, respectively. During the sugar mill operating season in Tanegashima, a large number of cargo agents transport the sugarcane from sugarcane farms to the sugar mill. While the sugar mill is operated seasonally from winter to spring, almost all of the drivers belonging to cargo agent companies are employed as regular employees. These drivers work in other industries on the island

(such as the construction industry) in the other seasons. Therefore, the thermochemical energy storage and transport system does not require new drivers to be hired, and drivers with a license to drive medium or semi-medium vehicles were assumed to transport the zeolite. The labor cost was assumed to be 2500 JPY/h. The roundtrip transportation was assumed to take approximately 30 minutes for 3 km transportation including loading and unloading the container. The transportation cost per 1 t of dried zeolite in an hour, considering the labor cost and the fuel cost, was 440 JPY/ (t·h). A previous case study in Germany [4] assumed a cost of 45.5 €/h for transportation of 14 t of zeolite and a transportation cost per 1 t of zeolite in an hour of 3.25 €/(ton·h), which is roughly the same level of transportation cost in this study.

(Transportation trips)

Because the food processing factory repeats a pattern of 42 hours of operation every 48 hours, as shown in **Fig. 6.2**, the transportation pattern was designed in 48 hour cycles that were assumed to be repeated. The starting point of the trailer was set to be the heat charging station (the sugar mill). The transportation commences only when the containers hold the full payload. The number of roundtrip transportation trips was calculated by the $m_{\mathrm{zeo}}^{\mathrm{ZB}}$ and the maximum loading capacity of zeolite on the trailer. During the 6 hours of downtime of the food processing factory, additional transportation trips were made to initialize the balance of the amount of water-adsorbed and water-desorbed zeolite in the material reservoirs in each station. Because $m_{\mathrm{zeo}}^{\mathrm{HC}} < m_{\mathrm{zeo}}^{\mathrm{ZB}}$, the Zeolite Boiler may run out of water-desorbed zeolite during its 42 hours of operating time in each 2-day cycle unless the appropriate amount of water-desorbed zeolite is reserved in the heat discharging station before the activation of the Zeolite Boiler. The amount of zeolite required to avoid a shortage of water-desorbed zeolite in 42 hours of operation was packed in the material reservoir and 3 hours of reserve margin was additionally stored for unforeseen need in the heat discharging station. At the heat charging station, at least the amount of water-adsorbed zeolite which can be fully packed into the Heat Charger must be reserved at the starting time of each 48-hour cycle. The representative case of the transportation pattern is shown in **Fig. 6.6** in the case of $m_{\mathrm{zeo}}^{\mathrm{HC}}$ = 800 kg/h. The maximum reserved amount of water-adsorbed and desorbed zeolite in each station determines the volume of the material reservoirs.

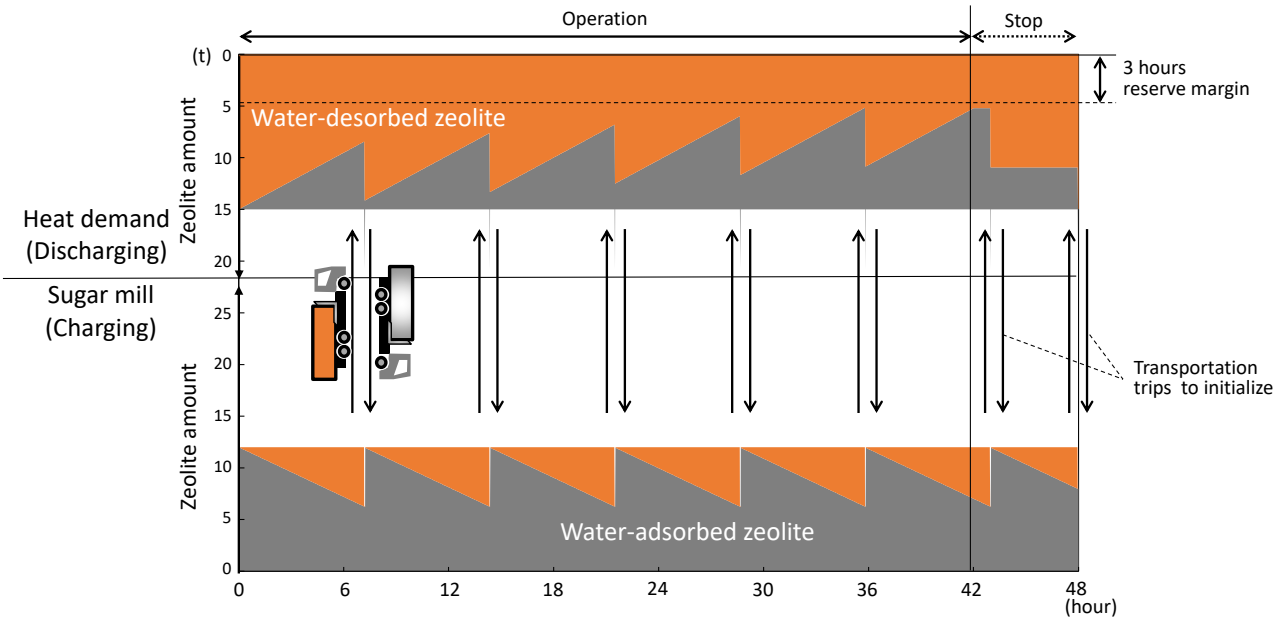

Fig. 6.6. Example transportation pattern.

(5) Energy cost

Relevant energy sources to the thermochemical energy storage and transport system were as follows:

- Heavy oil: Saved in the heat discharging station by applying the Zeolite Boiler
- Diesel oil: For transportation trailer
- Electricity: For the bucket conveyors in the heat charging and discharging stations and the blower introducing the air to the Heat Charger in the heat charging station.

Table 6.1 summarizes the fuel price. These values were calculated using the actual operation data of a specific food processing factory in Tanegashima.

(6) Chemical Engineering Plant Cost Index (CEPCI)

The cost handbook used to estimate the costs for most of the equipment was revised in 2000. The Chemical Engineering Plant Cost Index (CEPCI) was used to convert these costs based on the current price of equipment. The CEPCI was 394.1 in 2000 [5] and 603.1 in 2018 [6]. Therefore, the current cost was 1.53 times more expensive (603.1/394.1 = 1.53) than that in the cost handbook.

6.2.4 Net CO_2 emissions

The CO_2 emissions avoided by the proposed system were also calculated. The CO_2 emission factors for heavy oil, diesel oil and electricity were set to 2.71 t-CO_2/kL, 2.58 t-CO_2/kL, 0.000496 t-CO_2/kWh (base emission factor of Kyushu Electric Power) by referring to the database of the Ministry of

Environment of Japan [7]. The CO_2 emissions from the manufacturing process of zeolite and equipment were not considered in this study.

Table 6.1. Conditions of techno-economic and environmental analyses.

Charging station	
Operating time	70 days, 1680 hours (24 hours/day)
Inlet temperature	172 °C
Maximum mass flow rate of gas	14800 kg/h
Discharging station	
Operating time	70 days, 1470 hours (42 hours every 2 days)
Mass flow rate of steam of existing boiler without applying the Zeolite Boiler	1800 kg/h
Boiler efficiency	90%
Zeolite reserve margin	3 hours × mass flow rate of zeolite
Transportation	
Maximum loading capacity	7.0 t
Distance	3 km
Mean velocity	30 km
Fuel consumption rate	3 km/L
Transportation time, including handling time	0.53 hours/cycle
Cost information	
Fitting cost	5% of CAPEX
Maintenance cost	0.5% for zeolite 1.0% for others
Zeolite price	50 JPY/kg
Interest rate	2%
Period of consideration	15 years
Fuel price	
Heavy oil	111 JPY/L (38.9 MJ/L)
Diesel oil	151 JPY/L
Electricity	20 JPY/kWh
CO_2 emissions [7]	
Heavy oil	2.71 t-CO_2/kL
Diesel oil	2.58 t-CO_2/kL
Electricity	0.000496 t-CO_2/kWh

6.2.5 Summary of conditions of techno-economic and environmental analyses

Table 6.1 summarizes the calculation conditions of the techno-economic and environmental analyses.

6.3 Options and case setting

In the techno-economic and environmental analyses, a total of seven cases were evaluated, considering technological options for the Zeolite Boiler and the Heat Charger, and various operational options for seasonal storage.

6.3.1 Technological options in heat discharging station

The heat consumer can select whether or not a secondary heat exchanger is added to the Zeolite Boiler. The aim of adding the secondary heat exchanger to the Zeolite Boiler is to recover the waste sensible heat of the zeolite exhausted from the primary heat exchanger, as described in Chapter 4. The details of the calculation method are described in section **6.4.2**.

6.3.2 Technological options in heat charging station

The sugar mill has several options for operating the Heat Charger, as described below.

(1) Blow steam reduction

As described in Chapter 3, the sugar mill has the potential to reduce up to 400 kg/h of blow steam. Reduction of blow steam increases power generation and the temperature of flue gas. The effect of blow steam reduction on economic performance and CO_2 emissions of the system were investigated. The details of the calculation method are described in section **6.4.3**.

(2) Bagasse drying

As well as the blow steam reduction in the sugar mill, the bagasse drying process increases the heating value of bagasse, and would be expected to increase the flue gas temperature and amount of power generation. As described in Chapter 3, the moisture content of bagasse can be reduced by 2% in the bagasse conveyor belt. The effects of drying bagasse by 2% of moisture on economic performance and CO_2 emissions of the system were investigated. The details of the calculation method are described in section **6.4.4**.

(3) Increase in power generation

The effects of an increase in power generation under the current processes of the sugar mill on economic performance and CO_2 emissions of the system were investigated. The details of the calculation method are described in section **6.4.6**.

6.3.3 Operational options

The food processing factory assumed as a heat consumer starts its operation approximately 10 days before the sugar mill starts the milling process, as shown in **Fig. 6.2**. The effects of seasonal storage, which shifts the unused heat during the sugar milling season to the beginning of December on economic and environmental performance were investigated. The details of the calculation method are described in section **6.4.7**.

6.3.4 Case setting

Table 6.2 summarizes the cases for the techno-economic and environmental analyses. Cost breakdown trends were analyzed in Case 1, and the design parameters in Cases 2–7 (including $q_{\min}$, and the heat and power ratio in the sugar mill's processing) were determined based on the results of the cost analysis for Case 1.

Table 6.2. Case setting for the techno-economic and environmental analyses.

Options		Case number						
		1	2	3	4	5	6	7
Heat discharging (food processing factory)	Without secondary HEX	✓						
	With secondary HEX		✓	✓	✓	✓	✓	✓
Heat charging (sugar mill)	Current process	✓	✓					
	Blow steam reduction			✓		✓		✓
	Bagasse drying				✓	✓		
	Increase in power generation						✓	
Seasonal storage								✓

6.4 Results of techno-economic and environmental analyses

6.4.1 Case 1: Current process of sugar mill - Zeolite Boiler without secondary heat exchanger

(1) Economic performance

Figure 6.7 shows the results of the net profit and LCOE (subsidy rate β = 0%) as a function of $m_{\mathrm{zeo}}^{\mathrm{HC}}$. The cases of $q_{\min}$ = 0.056 (equilibrium value), 0.060, 0.070 and 0.080 kg/kg were investigated. All cases were in deficit, meaning that the system was financially infeasible. Overall, the case with lower $q_{\min}$ reduced the adverse balance due to a greater fuel saving effect (see **Fig. 6.3**) and lower transportation costs because of its higher energy density. However, the net profit of the case of $q_{\min}$ = 0.060 kg/kg improved compared with lower $q_{\min}$ = 0.056 kg/kg in the range of $m_{\mathrm{zeo}}^{\mathrm{HC}}$ > 900 kg/h, as seen in **Fig. 6.7 (a)**. This inversion of net profit was also exhibited in the range of $m_{\mathrm{zeo}}^{\mathrm{HC}}$ > 1800 kg/h (between $q_{\min}$ = 0.060 kg/kg and 0.070 kg/kg) and $m_{\mathrm{zeo}}^{\mathrm{HC}}$ > 2200 kg/h (between $q_{\min}$ = 0.070 kg/kg and 0.080 kg/kg), respectively.

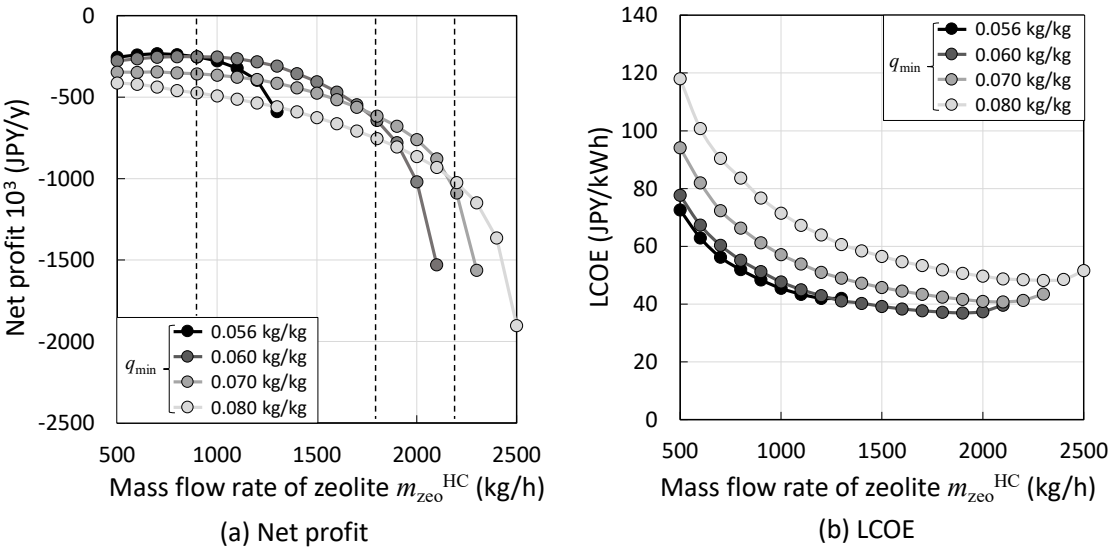

Fig. 6.7. Results of net profit and LCOE of the Case 1.

The reason for this inversion of net profit can be understood from the OPEX breakdown, which consists of the electricity cost derived from the blower in the heat charging station and the bucket conveyors in both stations, the fuel cost, the labor cost and the maintenance cost. **Figure 6.8** shows the OPEX breakdown at each q_{min} in the case of m_{zeo}^{HC} = 1300 kg/h which is the maximum throughput of zeolite in the case of q_{min} = 0.056 kg/kg. When the m_{zeo}^{HC} approaches the maximum throughput of m_{zeo}^{HC} = 1300 kg/h in the case of q_{min} = 0.056 kg/kg, greater m_{air} and a taller H_{bed} are required to desorb the zeolite (see **Fig. 6.4(a)**), causing the W_{blower} to drastically increase (see **Fig. 6.4(c)**). The increased electricity cost derived from the blower power becomes a large proportion of the OPEX, worsening the adverse balance compared with cases with q_{min} > 0.056 kg/kg, as shown in **Fig. 6.8**.

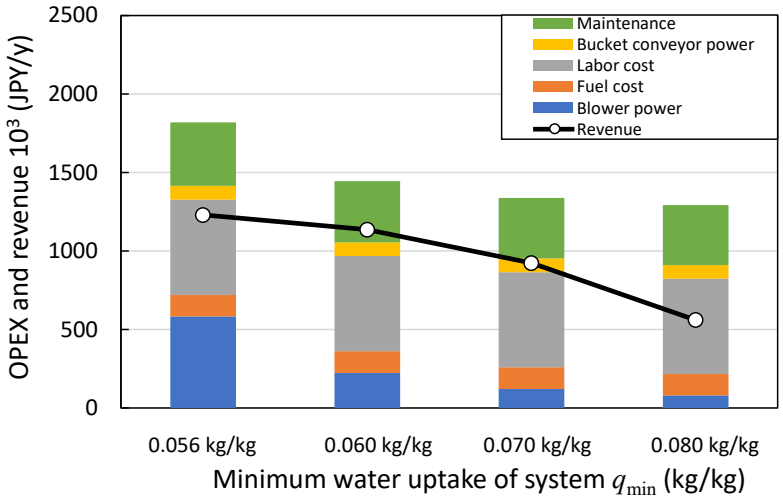

Fig. 6.8. Results of OPEX and revenue of each q_{min} in the case of m_{zeo}^{HC} = 1300 kg/h.

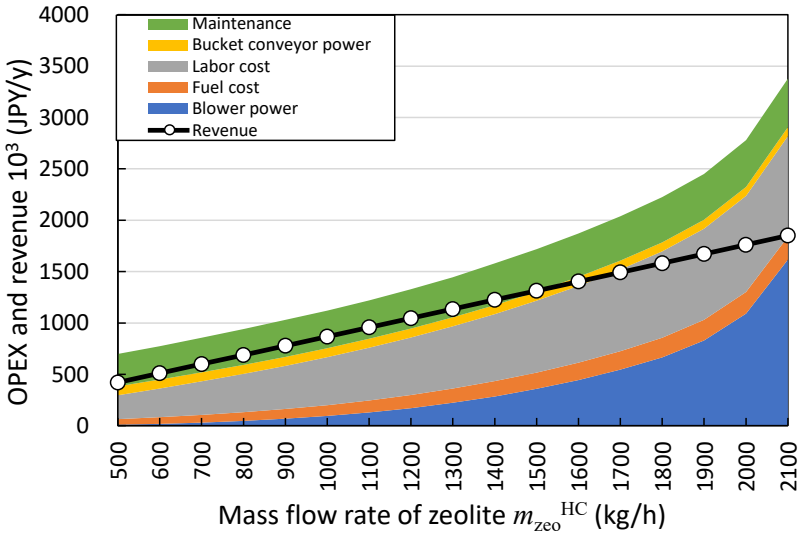

Fig. 6.9. OPEX breakdown as a function of the mass flow rate of zeolite at the charging station.

For the LCOE, the case of lower q_{min} has lower LCOE because the fuel saving and accompanying level of effectively utilized energy in **Eq. (6.3)** increase, and the transportation cost can be reduced by the higher energy storage density. However, compared with the best LCOE at each q_{min} case, q_{min} = 0.056 kg/kg has a higher LCOE at m_{zeo}^{HC} = 1300 kg/h than q_{min} = 0.060 kg/kg at m_{zeo}^{HC} = 1900 kg/h because the maximum throughput of zeolite and the accompanying total fuel saving in the case of q_{min} = 0.056 kg/kg is approximately 60% of that of q_{min} = 0.060 kg/kg, as described in **6.2.2**.

Figure 6.9 shows the results of the OPEX breakdown and revenue as a function of m_{zeo}^{HC} in the case of q_{min} = 0.060 kg/kg. The electricity cost derived from the blower power in the heat charging station and the labor cost for transportation constitute large components of the OPEX. The sensitivity of m_{zeo}^{HC} to the electricity cost derived from blower power is particularly high. Since the increasing ratio of the electricity cost derived from blower power against the increase in m_{zeo}^{HC} is greater than that of revenue, larger m_{zeo}^{HC} makes the adverse balance worse.

Figure 6.10 shows the CAPEX breakdown in the case of m_{zeo}^{HC} = 1900 kg/h which has the lowest LCOE in the case of q_{min} = 0.060 kg/kg. Approximately half of the CAPEX was related to the heat discharging station. In the heat discharging station, the two material reservoirs and the heat exchanger in the Zeolite Boiler constitute large proportions of the CAPEX. In the heat charging station, the two material reservoirs and the gas to gas heat exchanger (GGH) constitute large proportions of the CAPEX. **Figure 6.11** shows the balance of the annual cost, which consists of the annual CAPEX and OPEX as a function of the m_{zeo}^{HC}. Overall, the annual CAPEX is larger than the annual OPEX, whereas the OPEX increases in the higher range of the m_{zeo}^{HC}. **Figure 6.12** shows the breakdown of the annual cost. The electricity cost derived from the blower power and the labor cost for zeolite transportation in the OPEX constitute large proportions of the annual cost.

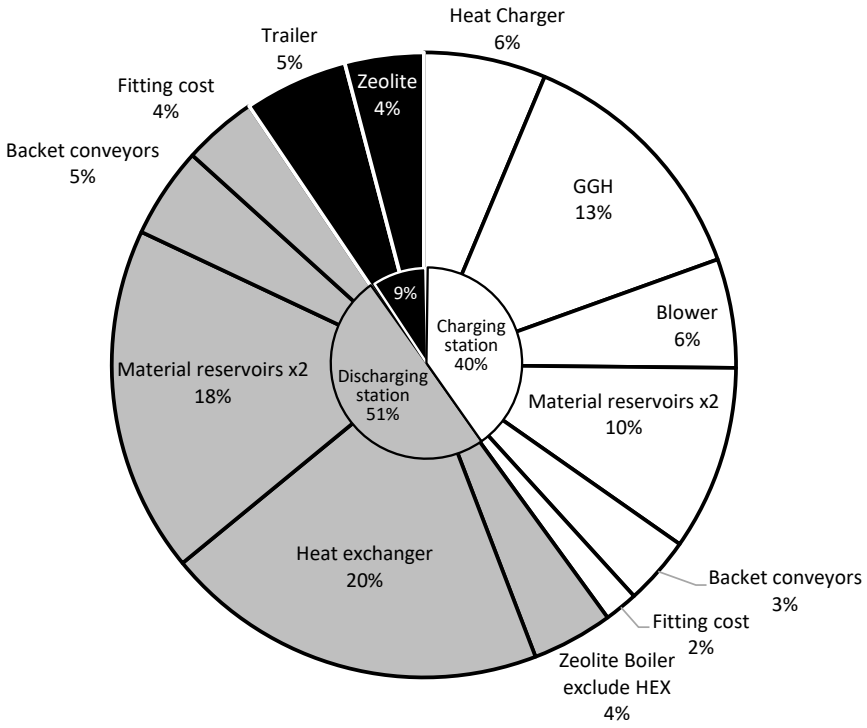

Fig. 6.10. CAPEX breakdown for Case 1 (zeolite mass flow rate: 1900 kg/h).

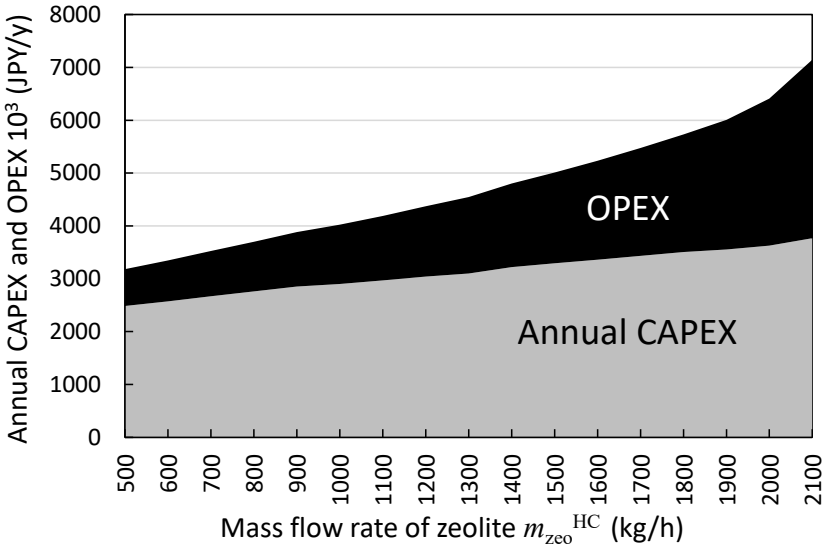

Fig. 6.11. CAPEX and OPEX balance as a function of the mass flow rate of zeolite at the heat charging station.

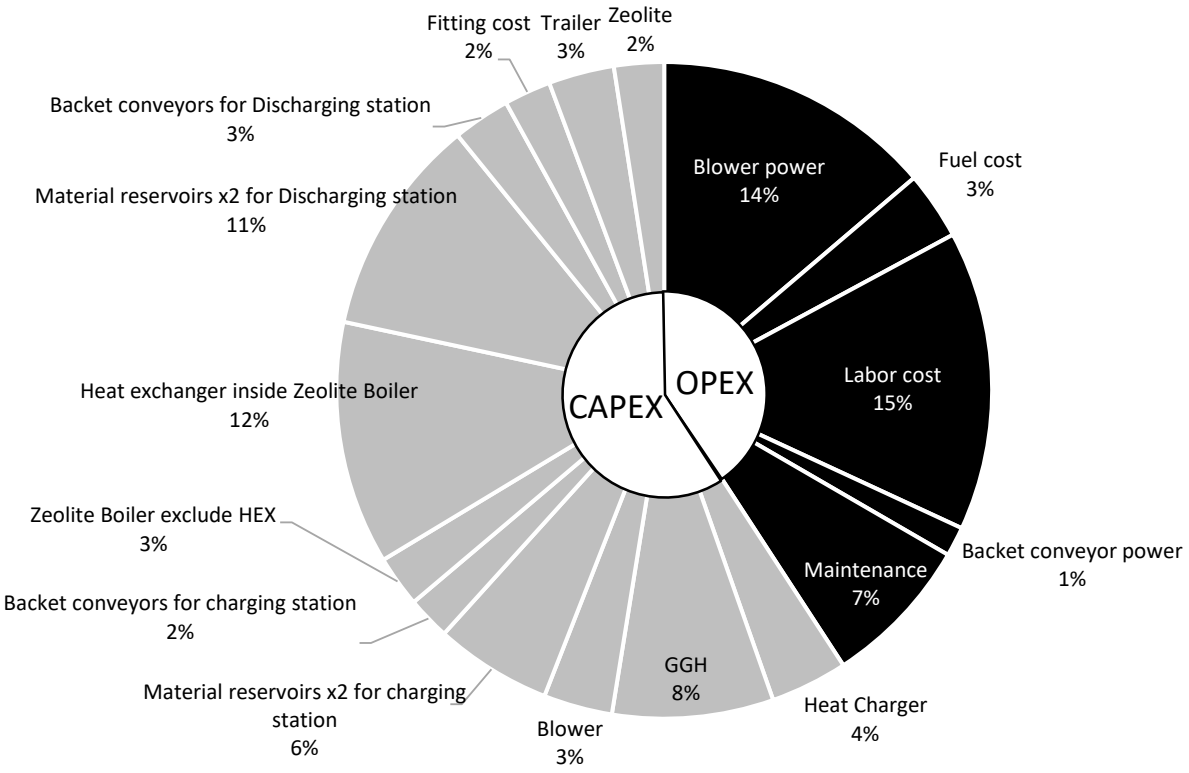

Fig. 6.12. Breakdown of the annual cost (zeolite mass flow rate: 1900 kg/h).

(2) Environmental performance

The CO_2 emission sources were the electricity consumed by the blower and bucket conveyors, which was purchased from the local power grid provided by the diesel power generation plant, and the diesel oil consumed by the transportation trailer. **Figure 6.13** shows the level of CO_2 emissions and the mitigation by fuel saving as a function of $m_{\mathrm{zeo}}^{\mathrm{HC}}$ in the case of $q_{\min}$ = 0.060 kg/kg. The level of CO_2 emission mitigation by the fuel saving linearly increased with increases in the $m_{\mathrm{zeo}}^{\mathrm{HC}}$. The case of $m_{\mathrm{zeo}}^{\mathrm{HC}}$ = 2100 kg/h avoided a small amount of CO_2 because the CO_2 emission derived by electricity consumption for the blower drastically increased in the higher range of $m_{\mathrm{zeo}}^{\mathrm{HC}}$. **Figure 6.14** shows the net CO_2 emissions from the system. In the case of $q_{\min}$ = 0.060 kg/kg, the net CO_2 emissions decreased in the range of $m_{\mathrm{zeo}}^{\mathrm{HC}}$ = 500–1500 kg/h due to the increase in fuel saving with increased $m_{\mathrm{zeo}}^{\mathrm{HC}}$. However, the level of net CO_2 emissions increased in the range of $m_{\mathrm{zeo}}^{\mathrm{HC}}$ > 1600 kg/h due to the increase in blower power and the number of transportation trips.

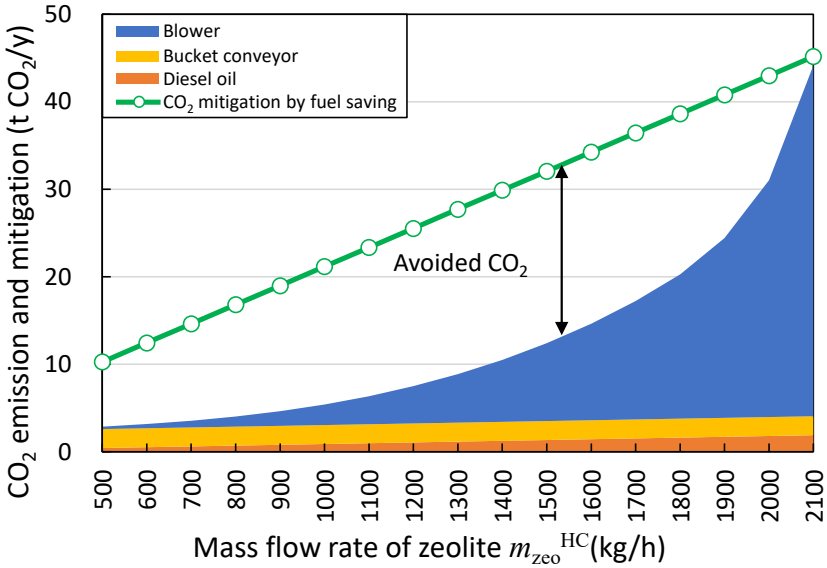

Fig. 6.13. Breakdown of CO_2 emissions and mitigation as a function of the mass flow rate of zeolite at the heat charging station.

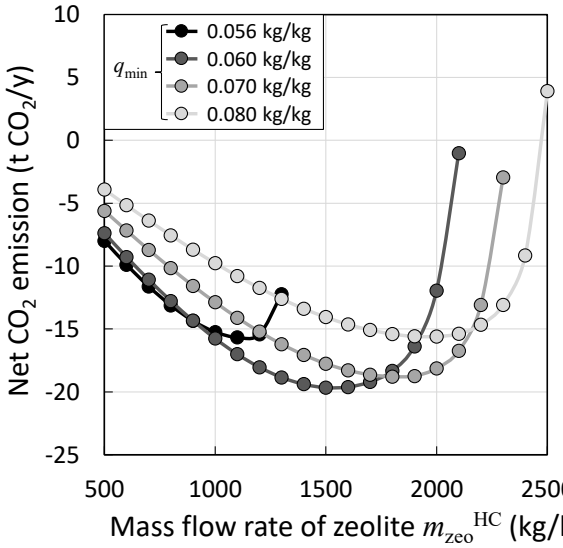

Fig. 6.14. Net CO_2 emissions in Case 1 as a function of the mass flow rate of zeolite at the heat charging station.

(3) Summary

As discussed above, the thermochemical energy storage and transport system in Case 1 is financially infeasible even if all of the CAPEX is publicly supplied (i.e., a subsidy rate β of 100%). The following sections outline several measures that could be undertaken to improve the revenue of the heat discharging station, and to reduce the electricity cost derived from the blower power in the heat charging station, which constituted a large proportion of the OPEX.

The case of $q_{\min}$ = 0.060 kg/kg, which achieved both greater energy density, lower transportation costs and lower blower power, is reasonable, and was used in Cases 2–7. As described in Chapter 3, blow steam reduction and a bagasse drying process in the sugar mill can both improve heat charging potential and power generation. To reduce the electricity cost of the blower, increasing the enthalpy of the flue gas of the bagasse boiler by applying blow steam reduction or bagasse drying is primarily used to increase additional power generation to provide electricity for the blower. Excess enthalpy is then used to increase the flue gas temperature.

6.4.2 Case 2: Current process of sugar mill - Zeolite Boiler with secondary heat exchanger

The effects of the addition of a secondary heat exchanger to the Zeolite Boiler on economic and environmental performance were considered. The length of the secondary heat exchanger at which 99% of maximum fuel saving can be achieved was selected at each $m_{\mathrm{zeo}}{}^{\mathrm{ZB}}$, in accord with the design method described in Chapter 4. **Figure 6.15 (a)** shows the fuel saving of the existing boiler by the Zeolite Boiler with and without the secondary heat exchanger as a function of $m_{\mathrm{zeo}}{}^{\mathrm{ZB}}$ in the case of $q_{\min}$ = 0.060 kg/kg. As well as the Zeolite Boiler without the secondary heat exchanger, the fuel saving by the Zeolite Boiler with the secondary heat exchanger increased linearly with increasing $m_{\mathrm{zeo}}{}^{\mathrm{ZB}}$. **Figure 6.15 (b)** shows the length of the secondary heat exchanger determined by the design method. The length increases stepwise with increase in the $m_{\mathrm{zeo}}{}^{\mathrm{ZB}}$. Therefore, the fuel saving and length of the secondary heat exchanger were predicted by linear approximation and linear interpolation as a function of the $m_{\mathrm{zeo}}{}^{\mathrm{ZB}}$, respectively.

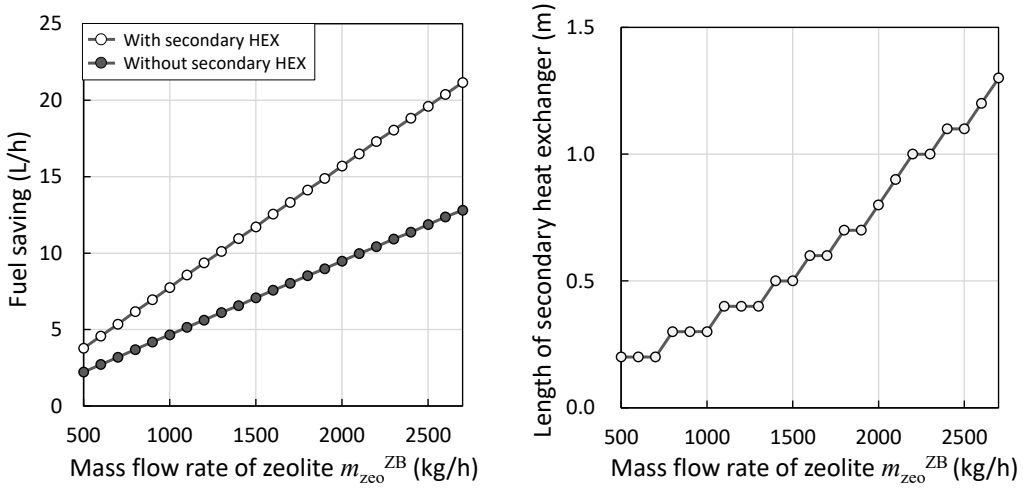

(a) Fuel saving (b) Length of secondary heat exchanger

Fig. 6.15. Summary of fuel saving of the existing boiler and the length of a secondary heat exchanger of the Zeolite Boiler.

A $q_{\max}$ value of 0.237 kg/kg was used to predict the performance of the Heat Charger because the Zeolite Boiler with the secondary heat exchanger applied to the 1800 kg/h class existing boiler

exhausts zeolite with 0.237 kg/kg, as discussed in Chapter 4. **Figure 6.16** shows the results of **(a)** net profit and **(b)** LCOE (subsidy rate β = 0%) of Case 2 in the case of q_{max} = 0.237 kg/kg and q_{min} = 0.060 kg/kg. **Figure 6.16** also shows the results of Case 1. The increase in fuel saving by the secondary heat exchanger makes the system profitable in the range of m_{zeo}^{HC} = 600–2000 kg/h. The LCOEs in Case 2 are approximately 65% of those in Case 1, due to the increased fuel saving in spite of the additional CAPEX of the secondary heat exchanger. **Figure 6.17** shows the effects of the subsidy rate on **(a)** LCOE and **(b)** IRR of the best net profit case (m_{zeo}^{HC} = 1400 kg/h) when a secondary heat exchanger is applied. The results indicated that the LCOE of the system becomes comparable to that of heavy oil and the IRR becomes positive when 90% of the CAPEX is publicly supported.

Figure 6.18 shows the net CO_2 emissions as a function of m_{zeo}^{HC}. The increased fuel saving by applying the secondary heat exchanger decreased net CO_2 emissions. However, the net CO_2 emissions in the range of m_{zeo}^{HC} > 1900 kg/h drastically increased because of the increase in electricity consumption by the blower, as in Case 1.

Since the addition of the secondary heat exchanger to the Zeolite Boiler improves both its economic and environmental performance, the techno-economic and environmental analyses in the following sections were employed with the Zeolite Boiler with a secondary heat exchanger.

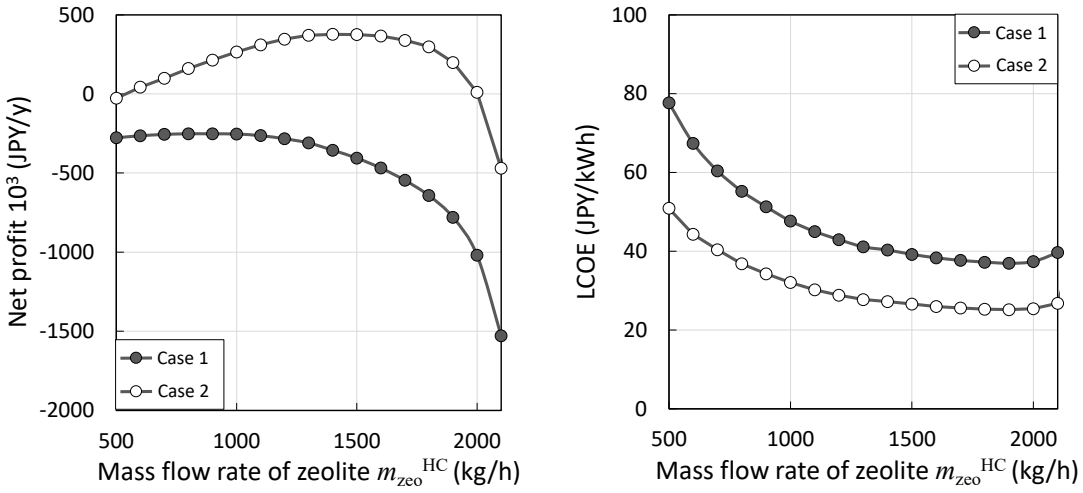

(a) Net profit (b) LCOE

Fig. 6.16. Net profit and LCOE with the addition of a secondary heat exchanger to the Zeolite Boiler.

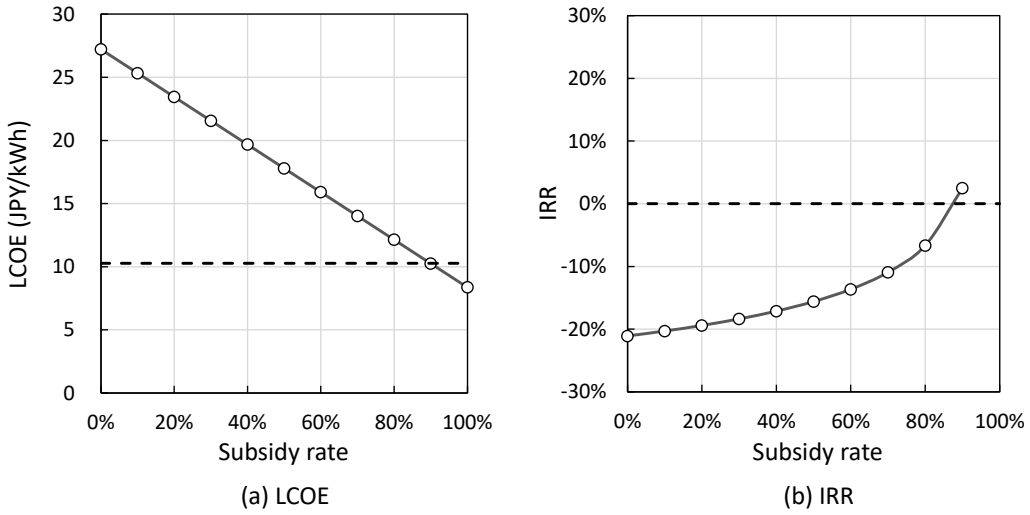

Fig. 6.17. Effects of subsidy rate on LCOE and IRR with the addition of a secondary heat exchanger to the Zeolite Boiler.

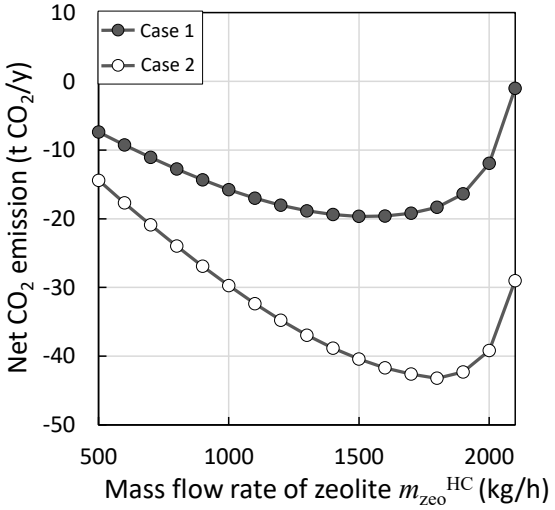

Fig. 6.18. Net CO_2 emissions with the addition of a secondary heat exchanger to the Zeolite Boiler.

6.4.3 Case 3: Blow steam reduction - Zeolite Boiler with secondary heat exchanger

The effects of blow steam reduction in the sugar mill on economic and environmental performance were investigated. As shown in **Fig. 6.19**, the T_{air0} and m_{air} linearly decrease with an increase in power generation when the flow rate of reduced blow steam was set to 400 kg/h (for details, see Chapter 3), and were predicted by a linear approximation as a function of the increase in power generation. The value of W_{blower} was calculated by the ΔP and the m_{air}; thereby, the T_{air0} and maximum m_{air} were updated following the linear approximation. **Figure 6.20** shows **(a)** the m_{air}, the maximum providable m_{air} and the H_{bed}, **(b)** the ΔP and the T_{air0}, and **(c)** the W_{blower} and the increment of power generation applying blow steam reduction as a function of the $m_{\mathrm{zeo}}^{\mathrm{HC}}$. The power generation increase caused by reducing the amount of blow steam is able to compensate for the blower power in the range of $m_{\mathrm{zeo}}^{\mathrm{HC}}$

< 2000 kg/h. However, the W_{blower} to regenerate $m_{\mathrm{zeo}}^{\mathrm{HC}}$ = 2100 kg/h exceeds the increment of power generation by blow steam reduction; therefore, 12 kW of additional electricity must still be purchased from the local power grid.

Figure 6.21 shows the results of **(a)** net profit and **(b)** LCOE (subsidy rate β = 0%) for Case 3. In the case of $m_{\mathrm{zeo}}^{\mathrm{HC}}$ < 2000 kg/h without any purchase of external electricity, the net profit linearly improves because W_{blower} can be provided by the increase in self-sufficient power when blow steam reduction is applied. When the system requires the purchase of additional electricity from the power grid in the case of $m_{\mathrm{zeo}}^{\mathrm{HC}}$ = 2100 kg/h, both the net profit and LCOE worsen. The case with $m_{\mathrm{zeo}}^{\mathrm{HC}}$ = 2000 kg/h resulted in the best LCOE of 21.4 JPY/kWh. **Figure 6.22** shows the effect of subsidy rate on **(a)** LCOE and **(b)** IRR of the best net profit case ($m_{\mathrm{zeo}}^{\mathrm{HC}}$ = 2000 kg/h) when blow steam reduction is applied. The LCOE of the system becomes comparable to that of heavy oil and IRR becomes positive when 70% of CAPEX is publicly supported.

Figure 6.23 shows the net CO_2 emissions as a function of $m_{\mathrm{zeo}}^{\mathrm{HC}}$ of Case 3. In the range of $m_{\mathrm{zeo}}^{\mathrm{HC}}$ < 2000 kg/h, net CO_2 emissions linearly decrease with increases in $m_{\mathrm{zeo}}^{\mathrm{HC}}$ because the fuel saving and accompanying CO_2 reduction by the Zeolite Boiler linearly increase with the increase in $m_{\mathrm{zeo}}^{\mathrm{ZB}}$. Since the 12 kW of electricity purchased via the local power grid is generated by a diesel engine power plant to regenerate $m_{\mathrm{zeo}}^{\mathrm{HC}}$ = 2100 kg/h, the net CO_2 emissions in this case are higher than when $m_{\mathrm{zeo}}^{\mathrm{HC}}$ = 2000 kg/h.

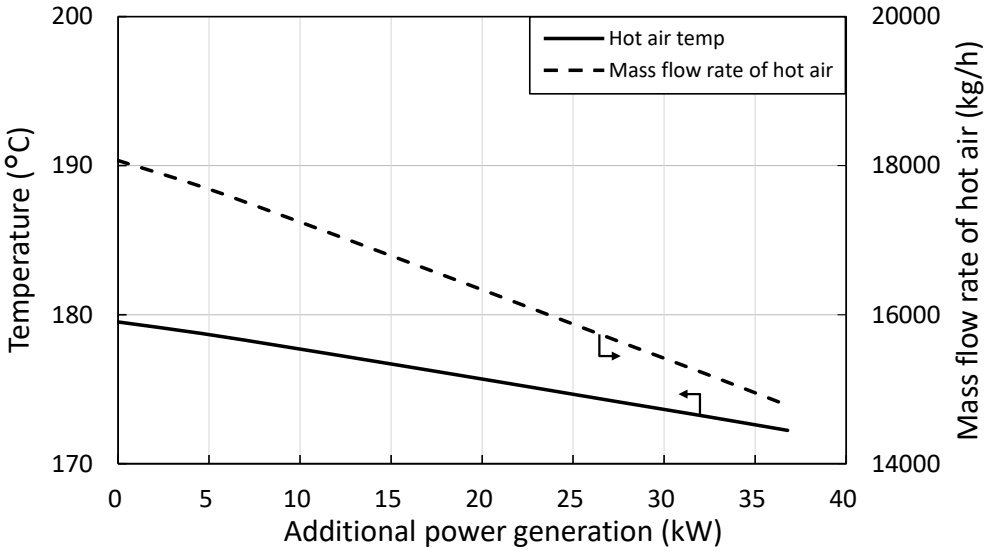

Fig. 6.19. Change in temperature and mass flow rate of hot air as a function of additional power applying blow steam reduction.

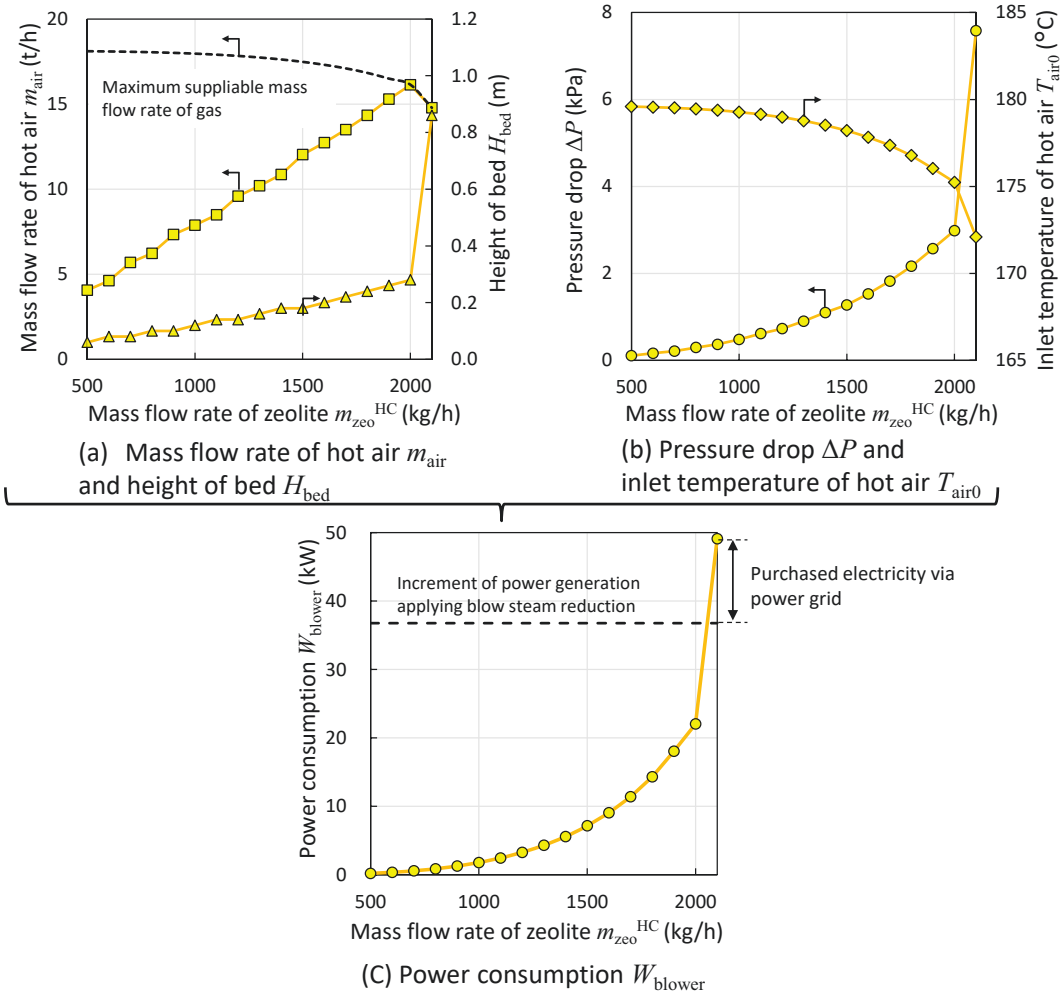

Fig. 6.20. Mass flow rate of air m_{air}, height of bed H_{bed}, pressure drop ΔP, inlet temperature of hot air T_{air0} and power consumption W_{blower} applying blow steam reduction.

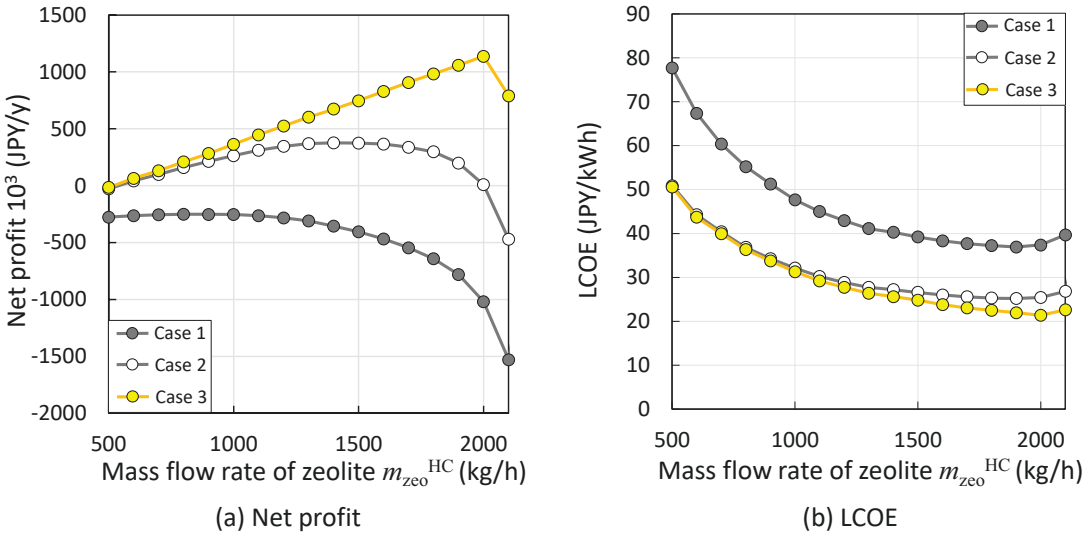

Fig. 6.21. Net profit and LCOE applying blow steam reduction.

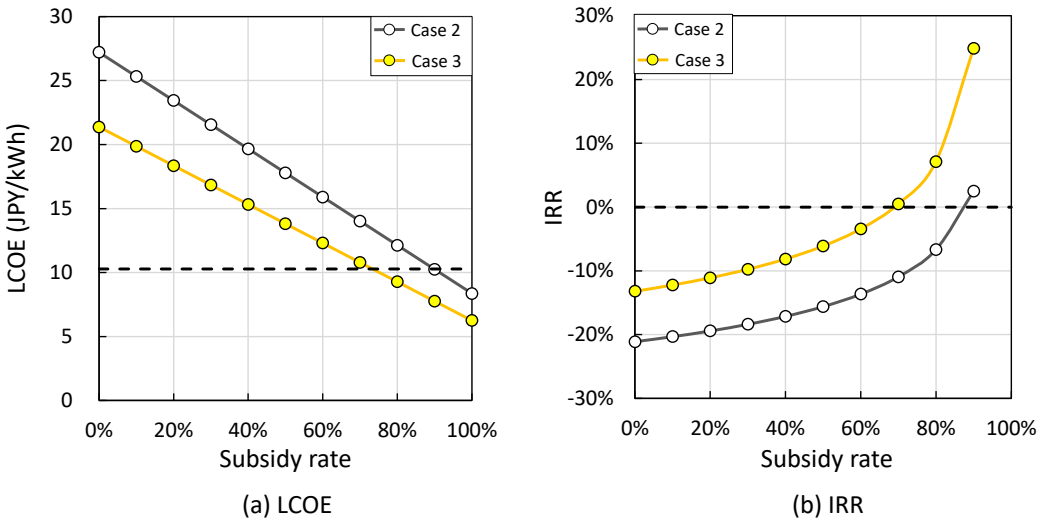

Fig. 6.22. Effect of subsidy rate on LCOE and IRR applying blow steam reduction.

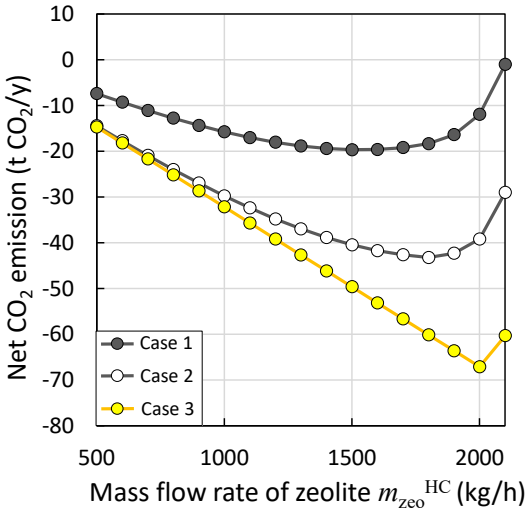

Fig. 6.23. Net CO_2 emissions applying blow steam reduction.

6.4.4 Case 4: Bagasse drying - Zeolite Boiler with secondary heat exchanger

The effects of drying bagasse on economic and environmental performance were considered. **Figure 6.24** shows T_{air0} and m_{air} as a function of the increase in power generation when the bagasse is dried to 42.4% of its moisture content.

The additional cost of the heat exchanger, blower, piping and fitting for the bagasse drying process must be considered. In the heat exchanger, air heated at 60 °C with 390 m^3/min can be obtained by 28 t/h of exhaust hot water at 70 °C from the sugar evaporating process (as described in Chapter 3). The heat transfer area of the heat exchanger was determined with an assumption of 100 W/(m^2·K) of heat transfer coefficient. The costs of the heat exchanger and blower were determined using the cost handbook [1]. As piping and fitting cost, 5% of blower and heat exchanger cost was appropriated.

The values of ΔP and the W_{blower} for the bagasse drying process were assumed to be 0.5 kPa and 5 kW, respectively.

Decreases in T_{air0} and m_{air} were predicted by linear approximation as a function of the increase in power generation. W_{blower} was calculated by ΔP and m_{air}. The additional power of 5 kW for drying bagasse was considered in the electricity consumption of the blower, and T_{air0} and the maximum providable m_{air} were updated by total power consumption following **Fig. 6.24**.

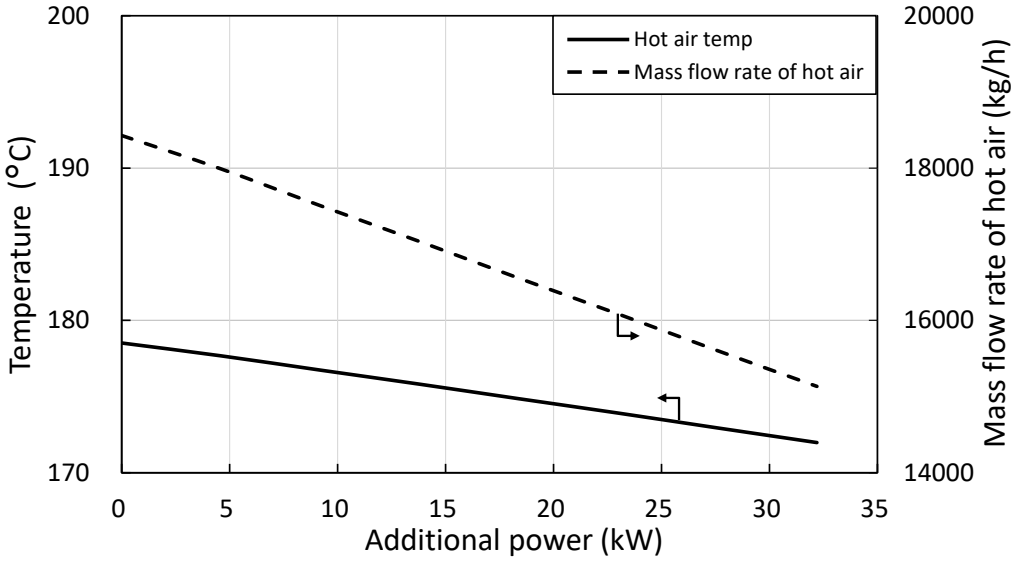

Fig. 6.24. Change in temperature and mass flow rate of hot air as a function of additional power generation applying bagasse drying.

Figure 6.25 shows **(a)** the m_{air} and the maximum providable m_{air}, and the H_{bed} , **(b)** the ΔP and the T_{air0}, and **(c)** the W_{blower} and increase in self-sufficient power by applying a bagasse drying process as a function of $m_{\mathrm{zeo}}^{\mathrm{HC}}$. The increase in power generation by drying bagasse can compensate for the blower power in the range of $m_{\mathrm{zeo}}^{\mathrm{HC}}$ < 1900 kg/h. However, since the blower power required to regenerate $m_{\mathrm{zeo}}^{\mathrm{HC}}$ = 2000 and 2100 kg/h exceeds the increase in self-sufficient power by drying bagasse, additional electricity must still be purchased from the local power grid.

Figure 6.26 shows the results of **(a)** net profit and **(b)** LCOE (subsidy rate β = 0%) of Case 4. The net profit increases linearly with increase in $m_{\mathrm{zeo}}^{\mathrm{HC}}$ in the range of $m_{\mathrm{zeo}}^{\mathrm{HC}}$ < 1900 kg/h. The net profit and LCOE deteriorated in the range of $m_{\mathrm{zeo}}^{\mathrm{HC}}$ > 2000 kg/h due to the purchased electricity from the local power grid. While power generation is expected to increase when bagasse drying is applied, the net profit of Case 4 is slightly less than that of Case 3 because of the additional maintenance and operating cost of bagasse drying. The case of $m_{\mathrm{zeo}}^{\mathrm{HC}}$ = 1900 kg/h resulted in the best LCOE of 24.7 JPY/kWh. **Figure 6.27** shows the effect of subsidy rate on **(a)** LCOE and **(b)** IRR of the best net profit

case (m_{zeo}^{HC} = 1900 kg/h) by applying bagasse drying. The LCOE of the system becomes comparable to that of heavy oil and IRR becomes positive when 80% of CAPEX is publicly supported.

Figure 6.28 shows the net CO_2 emissions as a function of m_{zeo}^{HC}. In the range of m_{zeo}^{HC} < 1900 kg/h, the net CO_2 emissions in Case 4 are the same as in Case 3. In the case of m_{zeo}^{HC} > 2000 kg/h, the net CO_2 emissions of the bagasse drying process are larger than those of the Case 3 due to purchasing the electricity from the local power grid.

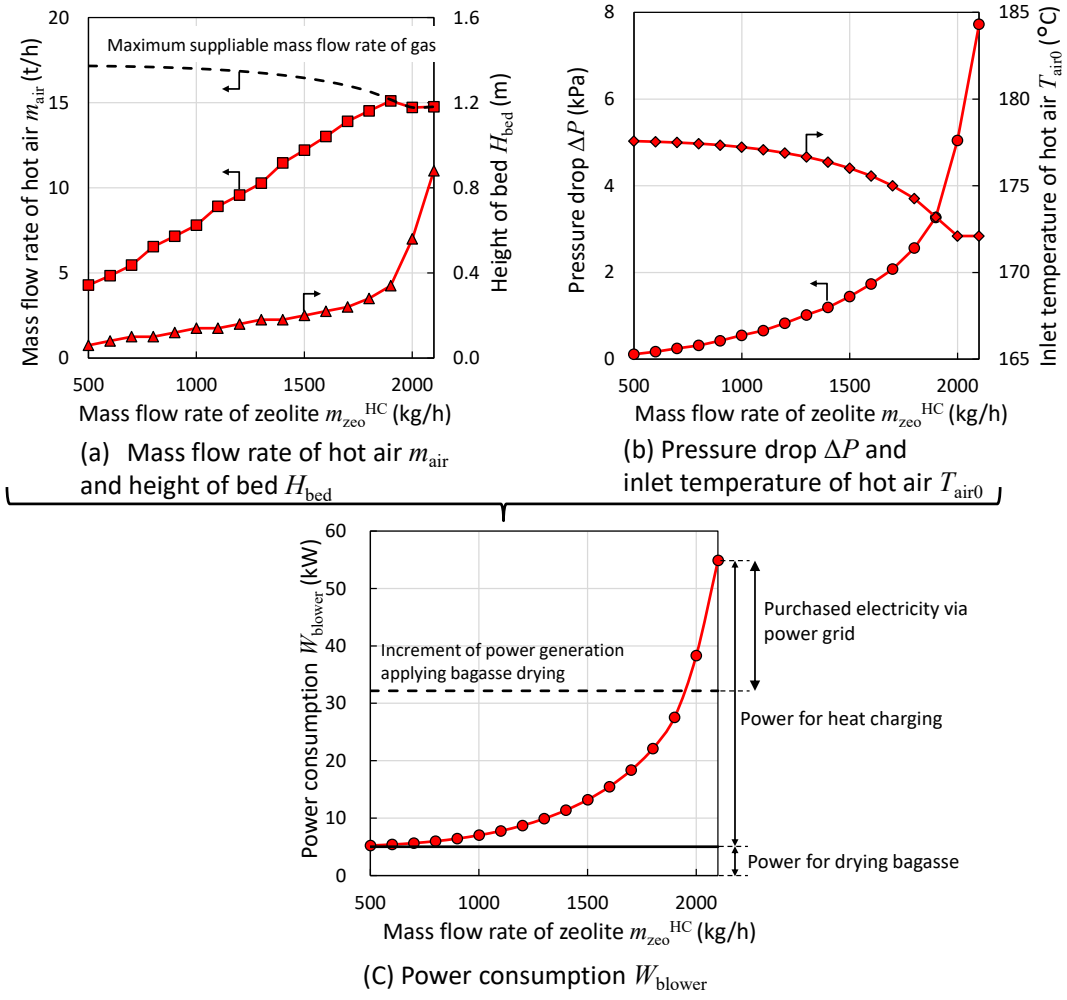

Fig. 6.25. Mass flow rate of air m_{air}, height of bed H_{bed}, pressure drop ΔP, inlet temperature of hot air T_{air0} and power consumption W_{blower} applying bagasse drying.

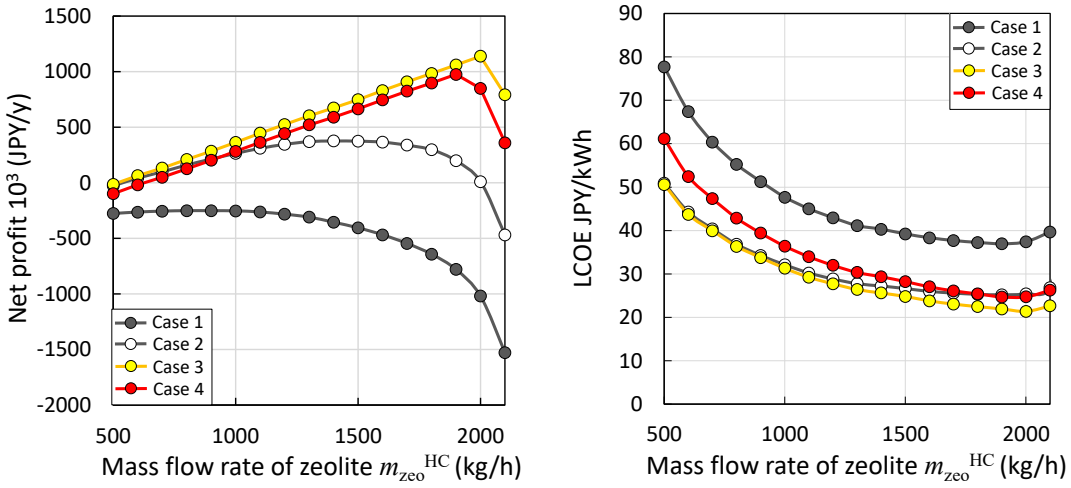

(a) Net profit (b) LCOE

Fig. 6.26. Change in net profit and LCOE by applying bagasse drying.

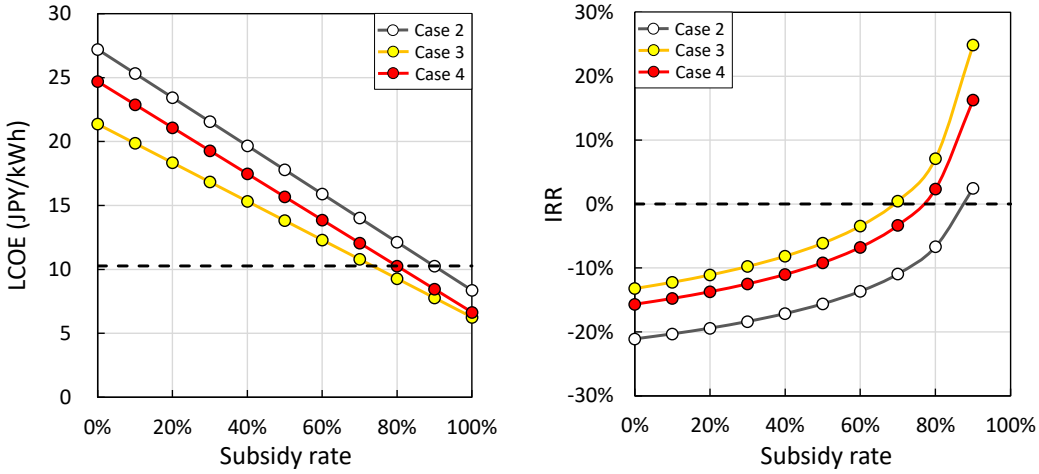

(a) LCOE (b) IRR

Fig. 6.27. Effect of subsidy rate on LCOE and IRR applying bagasse drying.

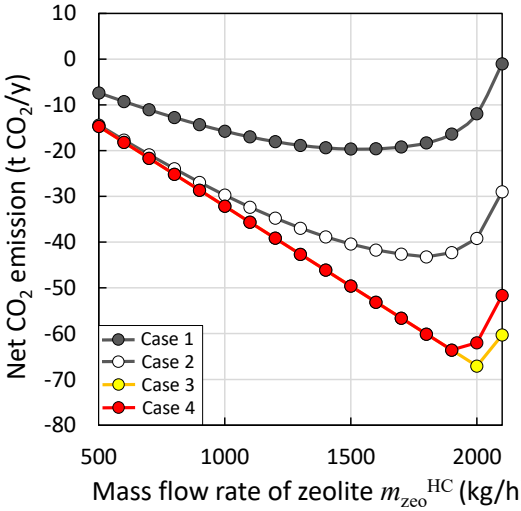

Fig. 6.28. Net CO_2 emissions applying bagasse drying.

6.4.5 Case 5: Blow steam reduction and bagasse drying - Zeolite Boiler with secondary heat exchanger

The effects of combining blow steam reduction and drying bagasse on economic and environmental performance were investigated. **Figure 6.29** shows the T_{air0} and the maximum providable m_{air} as a function of the increase in power generation when 400 kg/h of blow steam is reduced, and bagasse is dried to 42.4% of its moisture content. The decrease in T_{air0} and the maximum providable m_{air} were linearly approximated as a function of additional power generation. Additional power of 5 kW was considered as the auxiliary power to dry the bagasse.

Figure 6.30 shows **(a)** the m_{air}, the maximum providable m_{air} and the H_{bed}, **(b)** the ΔP and the T_{air0}, and **(c)** the W_{blower} and the increase in self-sufficient power by applying blow steam reduction and bagasse drying as a function of m_{zeo}^{HC}. The value of m_{air} reached the maximum limitation when m_{zeo}^{HC} = 2200 kg/h and m_{zeo}^{HC} = 2300 kg/h was the maximum throughput of zeolite. This combination of blow steam reduction and drying bagasse can generate up to 69 kW of additional power which can compensate for all of the required W_{blower}, as shown in **Fig. 6.30 (c)**.

Figure 6.31 shows the results of **(a)** net profit and **(b)** LCOE (subsidy rate β = 0%) of Case 5. In the range of m_{zeo}^{HC} < 1900 kg/h, the net profit in Case 5 was the same as that in Case 4. The net profit of Case 5 linearly improves with an increase in m_{zeo}^{HC} because all of the required W_{blower} can be provided by the sugar mill. The LCOE decreases with increases in m_{zeo}^{HC} until the maximum throughput of zeolite (m_{zeo}^{HC} = 2300 kg/h) is reached, and the minimum LCOE resulted in 22.4 JPY/kWh. The lowest LCOE of Case 5 is slightly higher than that of Case 3 because of the additional maintenance and operating cost of bagasse drying. **Figure 6.32** shows the effects of subsidy rate on **(a)** LCOE and **(b)** IRR of the best net profit case (m_{zeo}^{HC} = 2300 kg/h) of Case 5. The LCOE of the system becomes comparable to that of heavy oil and IRR becomes positive when 70% of CAPEX is publicly supported.

Figure 6.33 shows the net CO_2 emissions. Since Case 5 does not require the purchase of any electricity from the local power grid, the net CO_2 emissions decrease linearly, and can be reduced by up to 77 t/year.

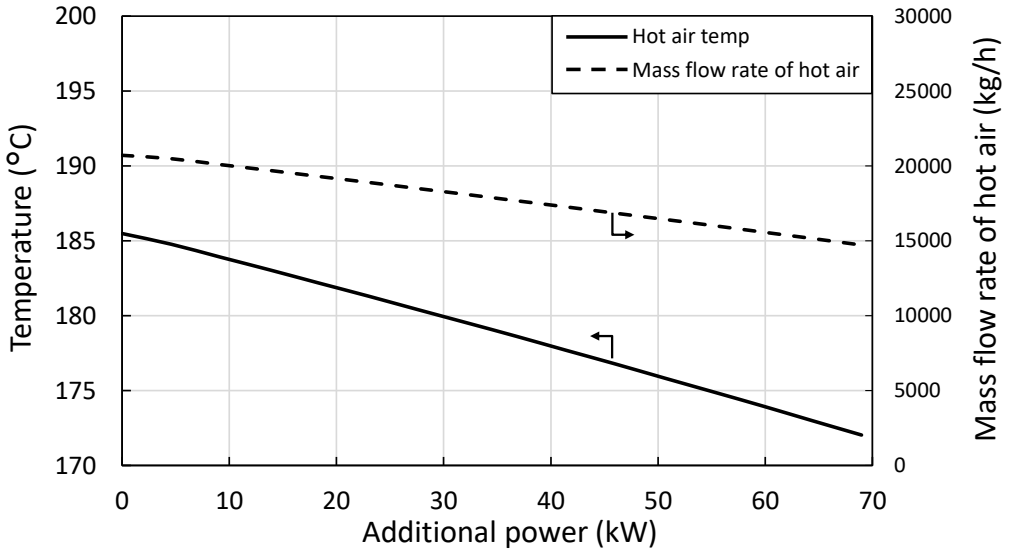

Fig. 6.29. Change in temperature and mass flow rate of air as a function of additional power applying both blow steam reduction and bagasse drying.

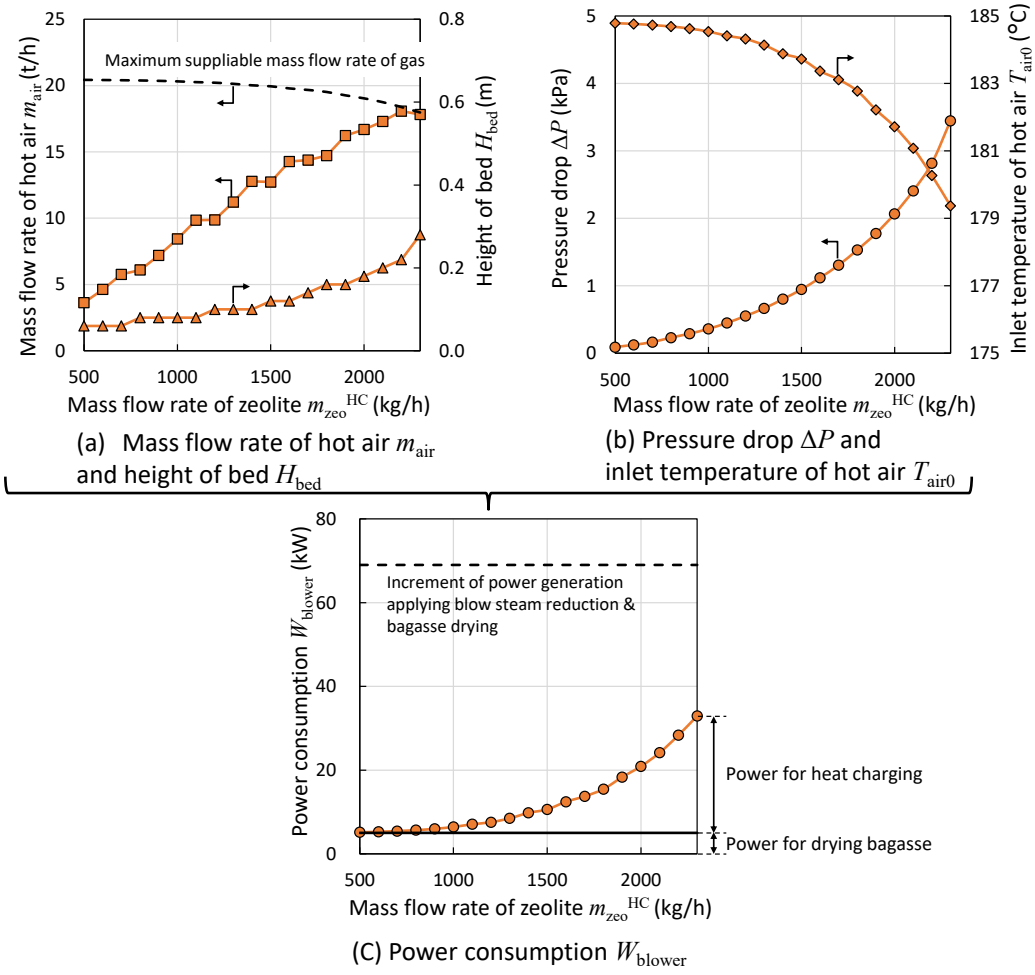

Fig. 6.30. Mass flow rate of air m_{air}, height of bed H_{bed}, pressure drop ΔP, inlet temperature of hot air T_{air0} and power consumption W_{blower} applying blow steam reduction and bagasse drying.

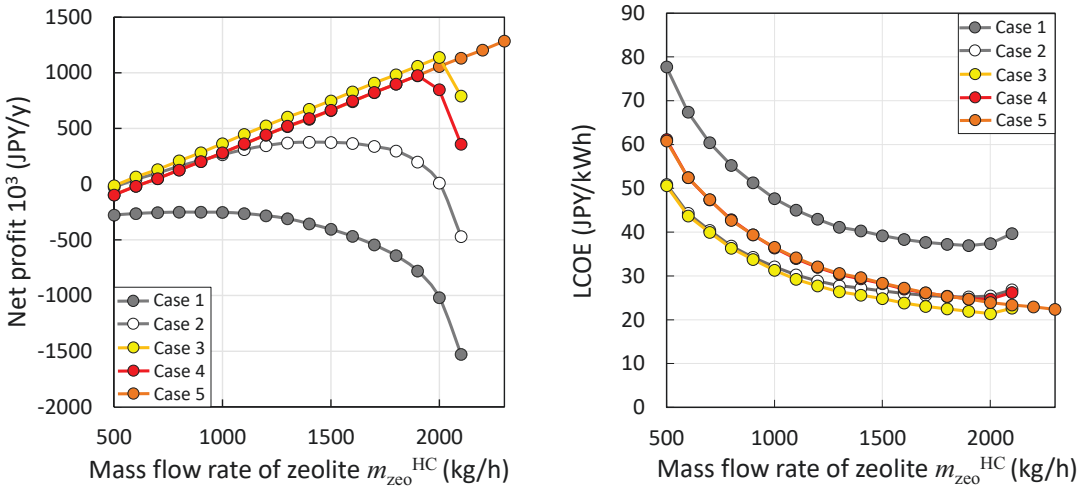

Fig. 6.31. Net profit and LCOE applying blow steam reduction and bagasse drying.

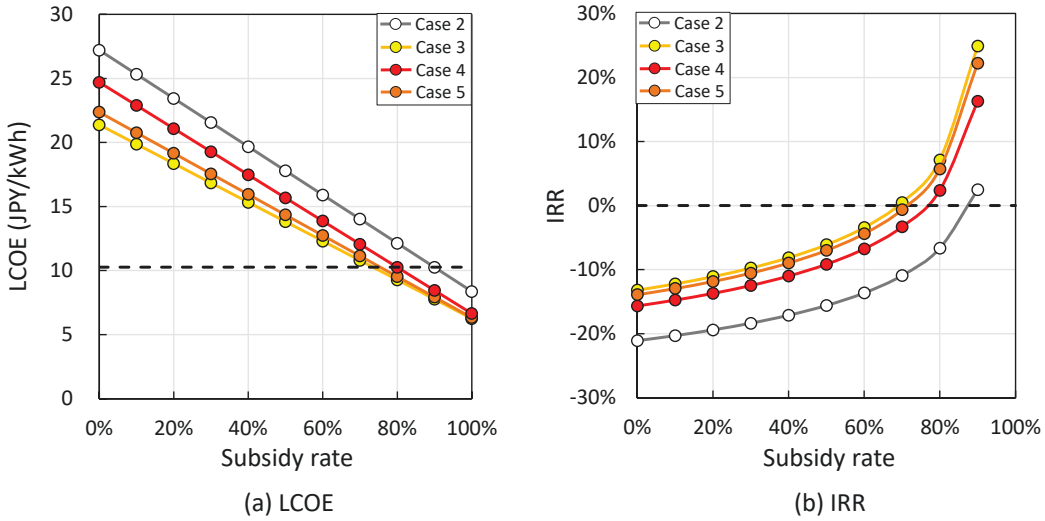

Fig. 6.32. Effect of subsidy rate on LCOE and IRR applying blow steam reduction and bagasse drying.

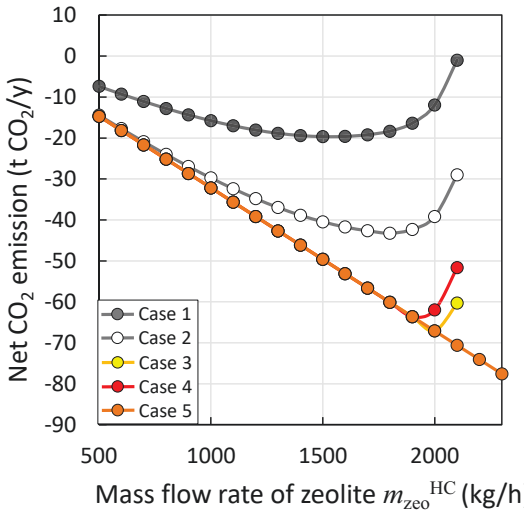

Fig. 6.33. Net CO_2 emissions applying blow steam reduction and bagasse drying.

6.4.6 Case 6: Increase in power generation - Zeolite Boiler with secondary heat exchanger

The effects of increase in power generation of the sugar mill on economic and environmental performance were considered. As shown in **Fig. 6.34**, the inlet gas temperature T_{air0} and maximum providable m_{air} linearly decreased with increased power generation (for details, see Chapter 3) and were predicted by a linear approximation as a function of the increase in power generation. The values of m_{air} and H_{bed} required to desorb the zeolite to the target of q_{min} were determined in accordance with the design method of the Heat Charger, enabling the values of ΔP and W_{blower} to be predicted. The maximum providable m_{air} and T_{air0} were updated by linear approximation using W_{blower}. **Figure 6.35(a)** shows the m_{air}, the maximum providable m_{air} and the H_{bed} as a function of ${m_{\mathrm{zeo}}}^{\mathrm{HC}}$. Since the required m_{air} in the case of ${m_{\mathrm{zeo}}}^{\mathrm{HC}}$ > 1600 kg/h exceeded the maximum providable m_{air}, the maximum throughput of zeolite in the Heat Charger was limited to 1500 kg/h. **Figure 6.35 (b)** shows the ΔP and the T_{air0} as a function of the ${m_{\mathrm{zeo}}}^{\mathrm{HC}}$. The value of T_{air0} decreases with increasing ${m_{\mathrm{zeo}}}^{\mathrm{HC}}$ and accompanying ΔP and W_{blower}, according to **Fig. 6.34**. **Figure 6.36** shows the results of **(a)** net profit and **(b)** LCOE (subsidy rate β = 0%). Since the W_{blower} can be provided from the sugar mill, both the net profit and LCOE of Case 6 improve compared with those of Case 2. However, since the maximum throughput of zeolite is limited to 1500 kg/h, the best net profit and LCOE of Case 6 were worse than those of Case 3. **Figure 6.37** shows the effects of subsidy rate on **(a)** LCOE and **(b)** IRR of the best net profit case (${m_{\mathrm{zeo}}}^{\mathrm{HC}}$ = 1500 kg/h) of Case 6. The LCOE of the system becomes comparable to that of heavy oil and IRR becomes positive when 80% of CAPEX is publicly supported.

Figure 6.38 shows the net CO_2 emissions as a function of the ${m_{\mathrm{zeo}}}^{\mathrm{HC}}$. By reducing the purchased electricity from the power grid on the island for W_{blower}, the net CO_2 emissions linearly decreased with increasing ${m_{\mathrm{zeo}}}^{\mathrm{HC}}$.

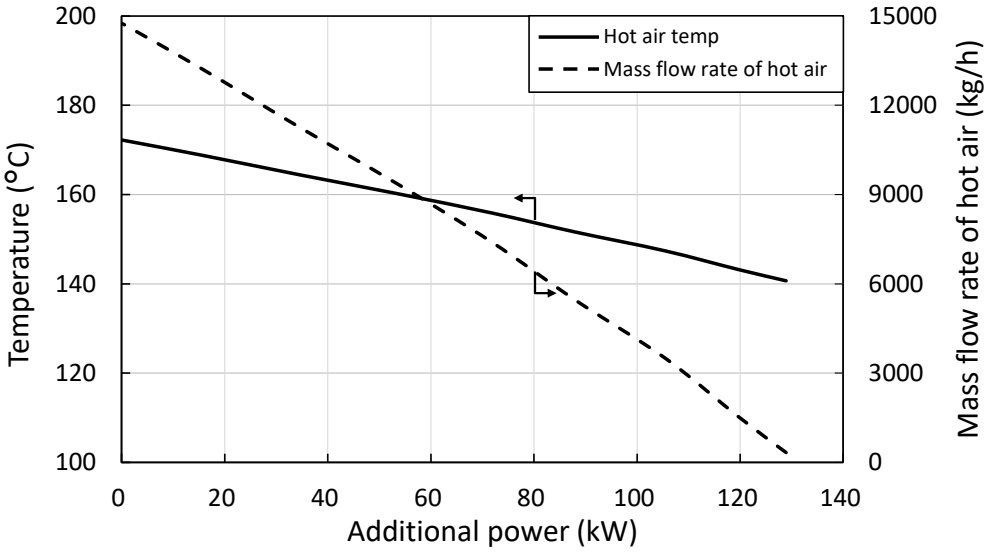

Fig. 6.34. Temperature and mass flow rate of hot air as a function of additional power applying increase in power generation.

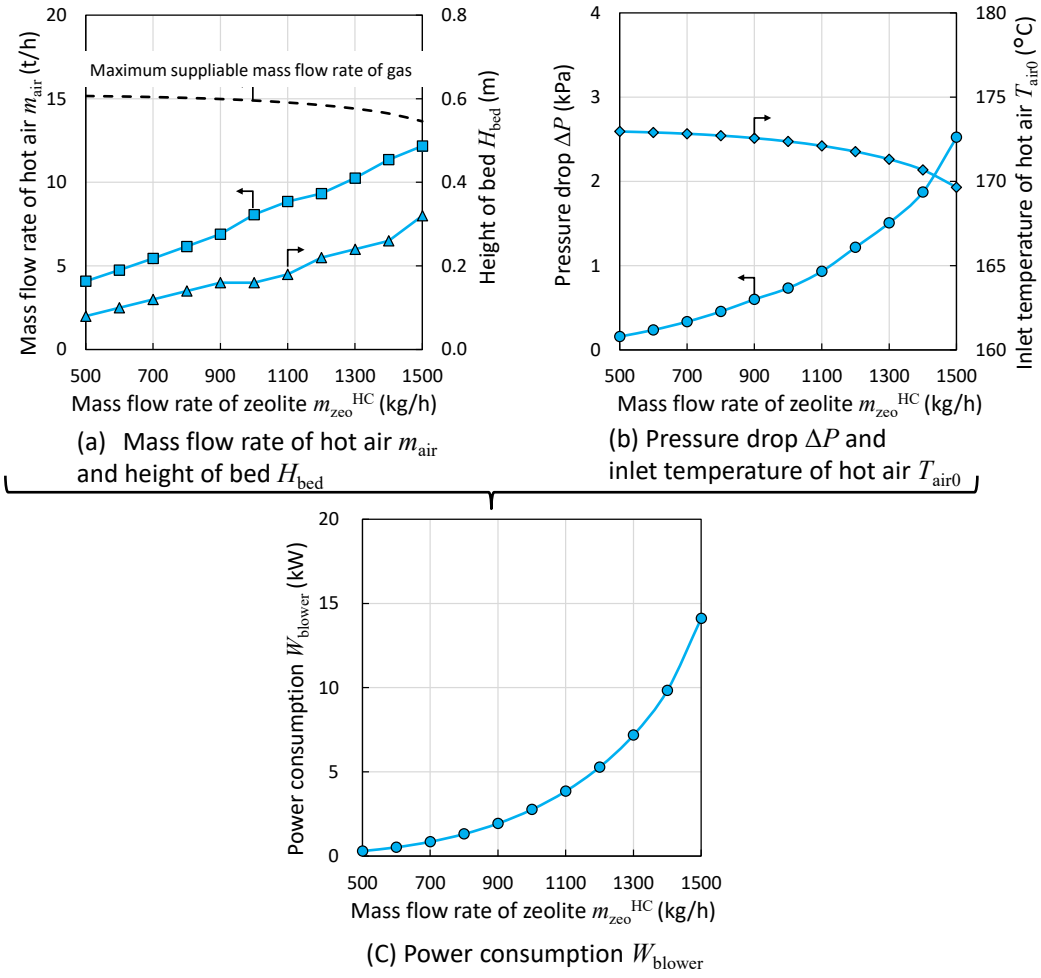

Fig. 6.35. Mass flow rate of air m_{air}, height of bed H_{bed}, pressure drop ΔP, inlet temperature of hot air T_{air0} and power consumption W_{blower} applying increase in power generation.

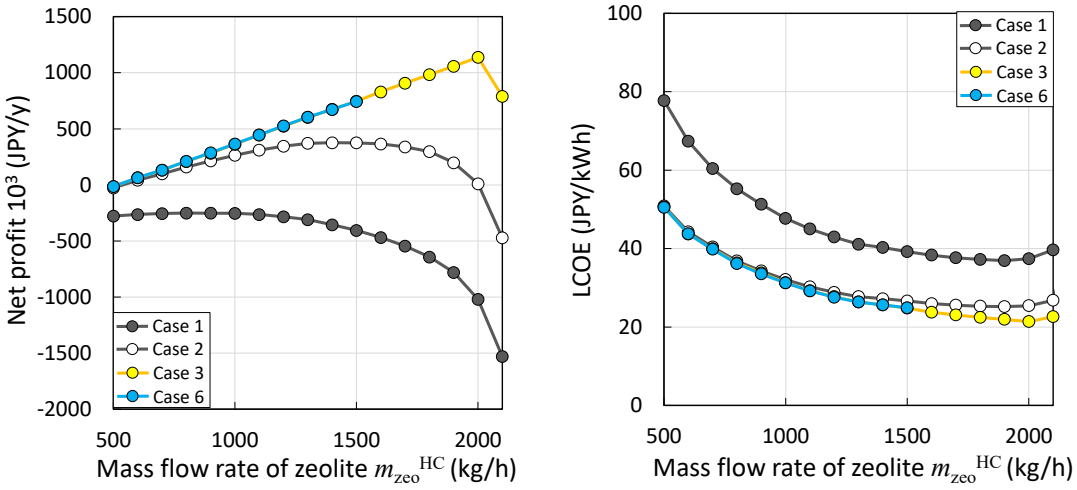

Fig. 6.36. Net profit and LCOE applying increase in power generation process.

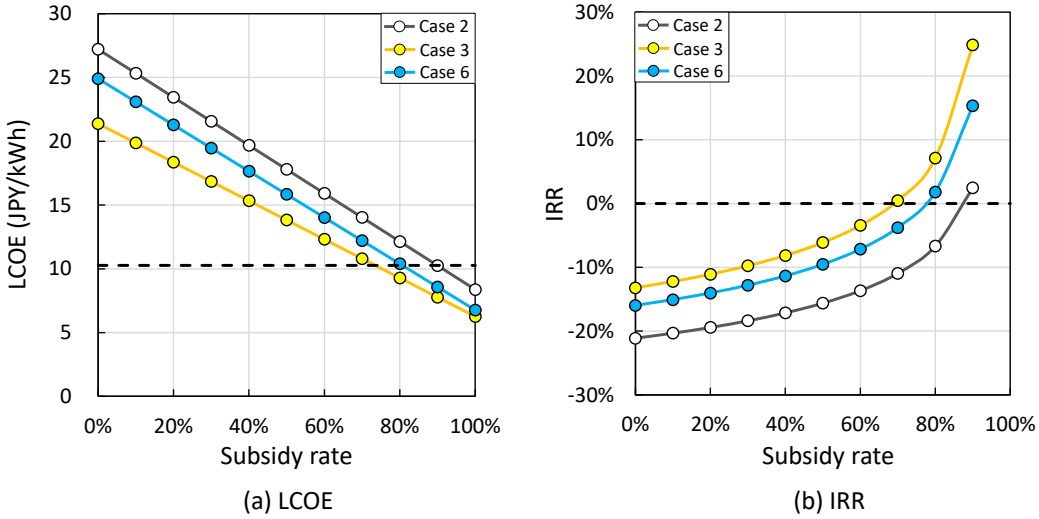

Fig. 6.37. Effects of subsidy rate on LCOE and IRR applying increase in power generation process.

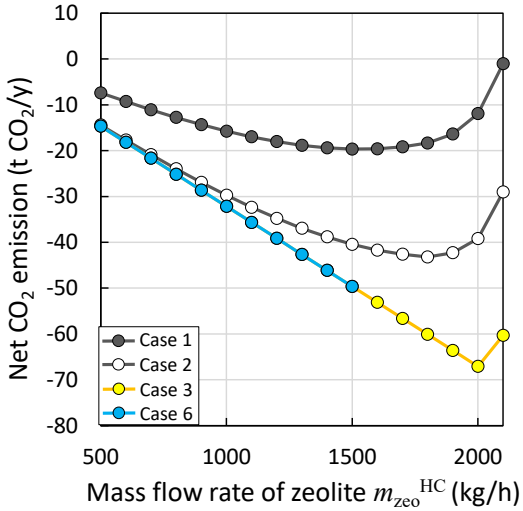

Fig. 6.38. Net CO_2 emissions applying increase in power generation process.

6.4.7 Case 7: Seasonal storage

The effects on economic and environmental performance of seasonal storage, in which unused heat is shifted to another season, were investigated. **Figure 6.39** shows the operation parameters of the Heat Charger and Zeolite Boiler when seasonal storage is applied. The food processing factory assumed to be a heat consumer begins its operations approximately 10 days before the sugar mill starts the milling process. Therefore, the Heat Charger in the sugar mill needs to operate for an additional period of up to 10 days after the food processing factory ceases its operations (i.e., the middle of February).

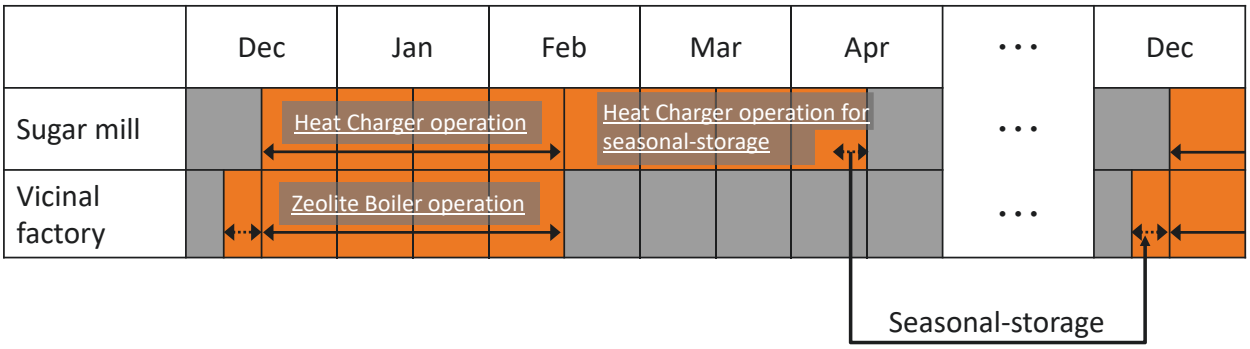

Fig. 6.39. Operating terms of the Heat Charger and Zeolite Boiler applying seasonal storage.

Water-desorbed (= heat charged) zeolite is assumed to be packed in containers. When the seasonal storage operates for 10 days (210 hours of operation in the heat discharging station), an additional 480 t of zeolite and 78 containers are needed. The required space for storage is 620 m^3 and 15 m × 15 m of space is required when the containers are assumed to be stacked in a double layer. Since the sugarcane yard in the sugar mill can be used for zeolite storage at the end of the sugar milling season because the yard becomes empty, the additional heat charging was assumed to be conducted in the middle of April, as shown in **Fig. 6.39**, and water-desorbed zeolite is stocked in the sugarcane yard. Stored zeolite is transported to the heat consumer in the beginning of December in the same year and provided to the Zeolite Boiler. This means the unused heat from the sugar mill in the middle of April is used for the food processing factory in the beginning of December.

Handling the container packed with water-desorbed zeolite is assumed to take 1 hour and the additional labor cost was estimated using the same unit labor cost described in **6.2.3**.

Figure 6.40 shows the net profit and LCOE (subsidy rate β = 0%) as a function of seasonal storage operation time in the case of m_{zeo}^{HC} = 2000 kg/h applying blow steam reduction. In the case of m_{zeo}^{HC} = 2000 kg/h, 40 t of zeolite is required to operate the system without seasonal storage. Since the system with up to 20 hours of seasonal storage consumes 40 t of zeolite, meaning there is no need to

purchase additional zeolite and containers, the net profit and LCOE improve compared with the case without seasonal storage. When there is more than 20 hours of seasonal storage operation time, the net profit decreases linearly with the increase in seasonal storage operation time because of the additional zeolite cost, as well as the additional container cost and labor cost for handling the containers. However, the system is still financially viable even if the total seasonal storage operation time reached the maximum level of 210 hours (10 days). The LCOE of seasonal storage of 210 hours resulted in a value of 25.5 JPY/kWh. **Figure 6.41** shows the effects of the subsidy rate on **(a)** LCOE and **(b)** IRR in the case of 210 hours seasonal storage. The LCOE of the system becomes comparable to that of heavy oil and IRR becomes positive when 85% of the CAPEX is publicly supported.

Figure 6.42 shows the results of the net CO_2 emissions as a function of seasonal storage operation time. The net CO_2 emissions linearly decreased with increased operating time because of the increased reduction in total heavy oil consumption at the heat discharging station.

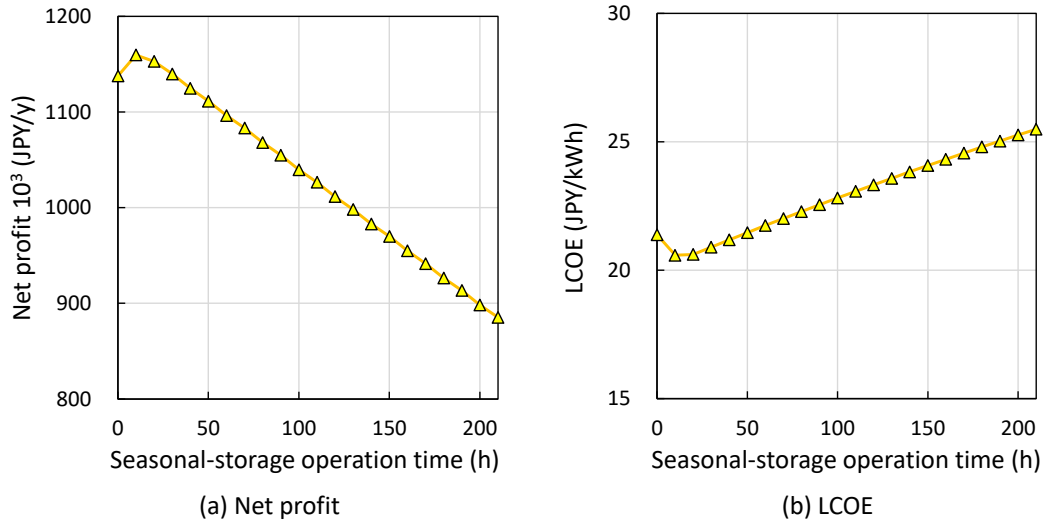

Fig. 6.40. Effects of seasonal storage on economic performance.

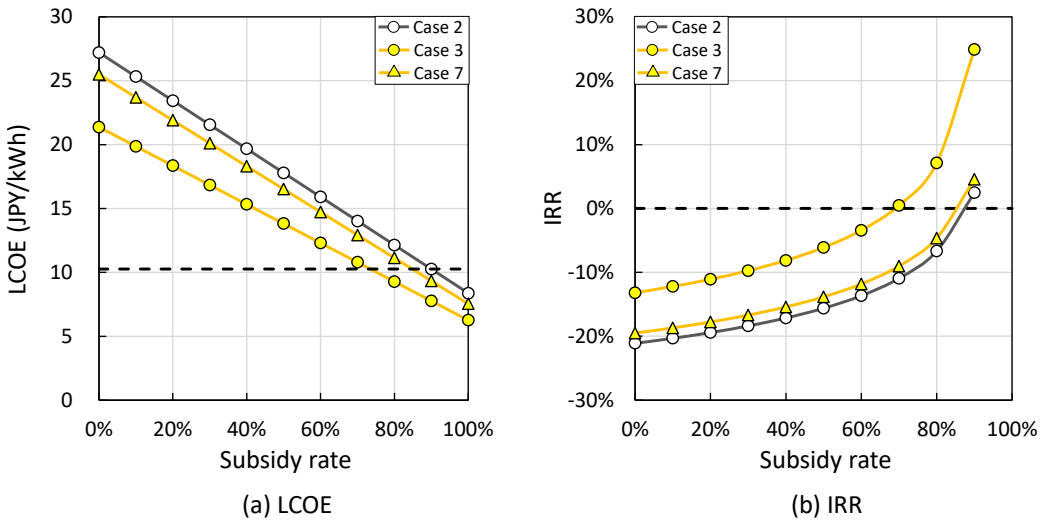

Fig. 6.41. Effects of subsidy rate on LCOE and IRR applying 210 hours of seasonal storage.

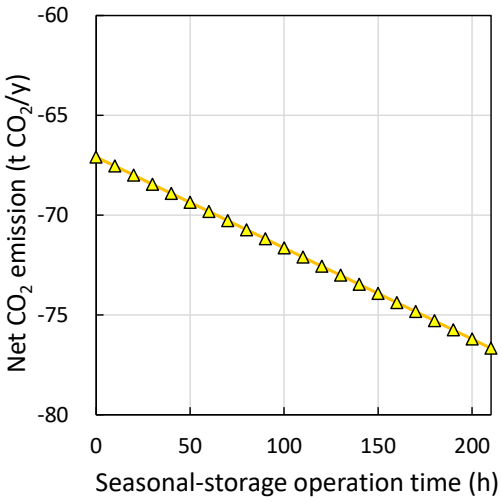

Fig. 6.42. Effects of seasonal storage on net CO_2 emissions.

6.4.8 Summary of techno-economic and environmental analyses

A secondary heat exchanger should be applied to the Zeolite Boiler because the effects of raising revenue by increasing fuel savings exceed the additional CAPEX and maintenance cost of the secondary heat exchanger (as described in **6.4.2**). Moreover, the relationships between blow steam reduction, bagasse drying, combined blow steam reduction and bagasse drying, and increase in power generation for the best net profit, LCOE and net CO_2 emissions, are summarized below.

- Net profit
  - Blow steam reduction and bagasse drying > blow steam reduction > bagasse drying > increase in power generation
- LCOE
  - Increase in power generation > bagasse drying > blow steam reduction and bagasse drying > blow steam reduction
- Net CO_2 emissions
  - Increase in power generation > bagasse drying > blow steam reduction > blow steam reduction and bagasse drying

In Case 1, the thermochemical energy storage and transport system is financially infeasible even with a subsidy rate of 100%. However, the profitability of system is remarkably improved by the addition of a secondary heat exchanger to the Zeolite Boiler. The system is financially viable when 70%–80% of the CAPEX is publicly supplied, and when blow steam reduction, a bagasse drying process and increase in power generation are employed at the sugar mill.

6.5 Sensitivity analysis

The sensitivity analysis was conducted for price and technological parameters. To evaluate the effect of uncertain price parameters, sensitivities of interest rate, maintenance factor, labor cost, zeolite price, total CAPEX and distance between heat charging and discharging stations (= related to transportation cost) on LCOE were investigated. For evaluating the effect of technological parameters, sensitivities of energy density, heat transfer coefficient of gas to gas heat exchanger and Zeolite Boiler (Zeolite bed to supplied water) on LCOE were investigated. The energy density of zeolite is related to the number of transportation trips. For the heat transfer coefficients, the overall UA values were fixed, which means heat transfer area of gas to gas heat exchanger and heat exchanger in the Zeolite Boiler were changed. The Zeolite Boiler with the secondary heat exchanger, the counter-flow Heat Charger and the blow steam reduction in the sugar mill were commonly applied. The m_{zeo}^{HC} = 2000 kg/h case was investigated because this case has the best LCOE.

Figures 6.43 and **6.44** show the result of sensitivity analysis on the LCOE (subsidy rate β = 70%) in which all variables are normalized based on the base scenario. In the price parameters, the CAPEX has the biggest sensitivity on LCOE, thus the system with lower CAPEX and carefully estimation of the insurance, the technical consultant fee and like that, which are not included in the techno-economic analysis at the proof-of-concept stage, are required for the implementation.

In the technological parameters, energy storage density gives a comparable impact on LCOE, which indicates materials with higher energy density should be developed and implemented.

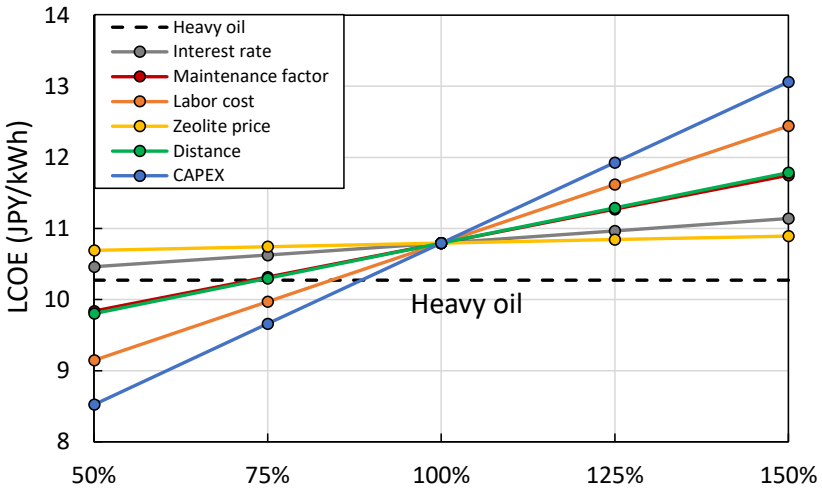

Fig. 6.43. Effect of price parameters on LCOE.

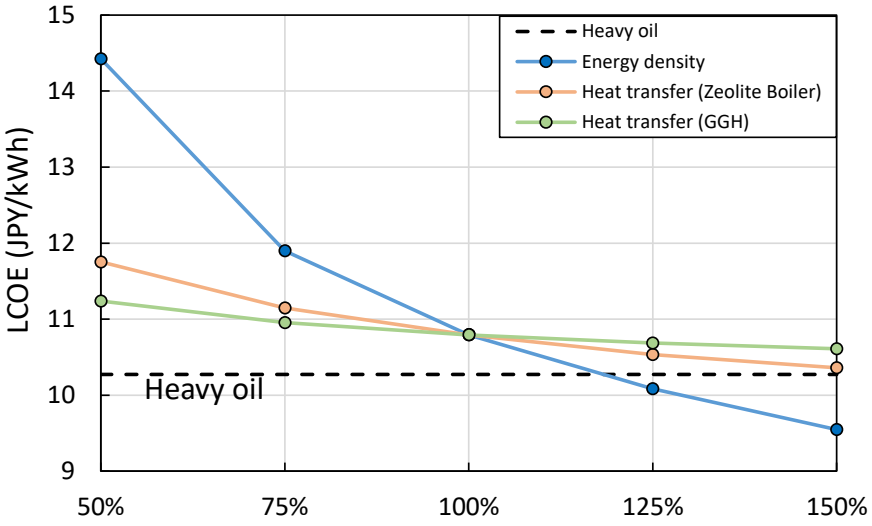

Fig. 6.44. Effect of technological parameters on LCOE.

The sensitivity of energy price on LCOE was also investigated. The relevant energy sources of the thermochemical energy storage and transport system are heavy oil, diesel oil and auxiliary electricity. **Figure 6.45** shows the results of LCOE (subsidy rate β = 0%) of the system when these energy prices are increased. The LCOE of the system linearly increases with increase in energy price. The LCOE of the system is comparable to that of heavy oil when the energy price is 2.2 times more expensive than current value in the case of $m_{\mathrm{zeo}}^{\mathrm{HC}}$ = 2000 kg/h.

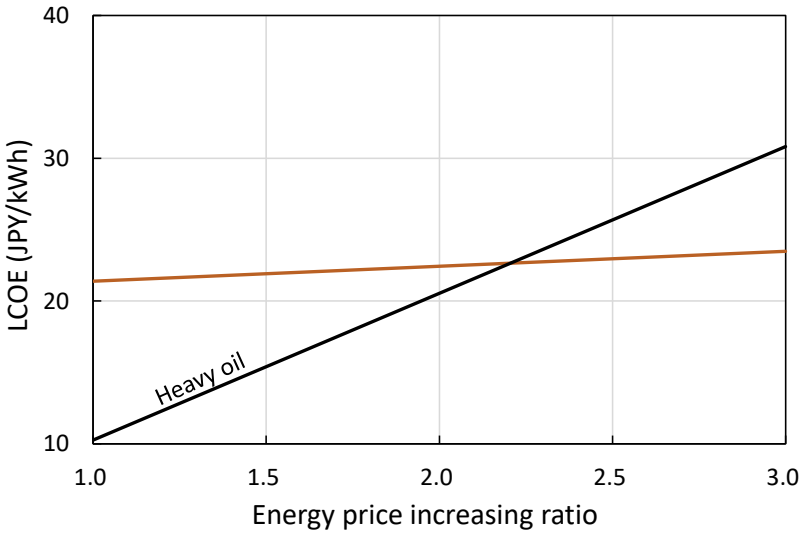

Fig. 6.45. Result of sensitivity analysis of energy price on LCOE.

6.6 Chapter conclusion

This chapter evaluated the economic and environmental performances of thermochemical energy storage and transport system. The Zeolite Boiler and the Heat Charger were designed by the methodologies which were established in Chapters 4 and 5, respectively. The net profit, the LCOE (Levelized Cost of Energy), the IRR (Internal Rate of Return) and the net CO_2 emission were quantified via the techno-economic and environmental analyses. The main achievements of this chapter are shown as follows.

- The Case 1 employing the Zeolite Boiler without the secondary heat exchanger and counter-flow Heat Charger is financially infeasible at any condition even if the 100% of CAPEX is publicly provided.
- The electricity cost derived from blower power and labor cost are the dominant determinants of the net profit of the system.
- The addition of the secondary heat exchanger to the Zeolite Boiler makes the system profitable because of increase in fuel saving.
- Increased power generation by blow steam reduction can compensate for the blower power for the Heat Charger, thereby making the system profitable.
- While power generation is expected to increase by introducing bagasse drying, the net profit is slightly less than the case of blow steam reduction because of additional maintenance and operating cost for bagasse drying.
- The combination of blow steam reduction and bagasse drying has potential to make the best net profit due to increase in throughput of zeolite at heat charging station. However, the LCOE is slightly less than the case of blow steam reduction because of the additional cost for bagasse drying.
- The case of increase in power generation limited the maximum throughput of zeolite due to decrease in the temperature and the mass flow rate of hot air for thermal energy storage.
- The system is financially viable when 70-80% of capital expenditure is publicly supplied and blow steam reduction or bagasse drying process are employed at the sugar mill.
- Seasonal storage up to 210 hours is financially viable when blow steam reduction is employed at the sugar mill.
- Larger energy storage density gives a comparable impact on the LCOE.

Nomenclature

C_n:	Net cash inflow	JPY/year
CAPEX:	Capital Expenditure	JPY
H_{bed}:	Bed height	m
i:	Interest rate	%
IRR:	Internal Rate of Return	%
LCOE:	Levelized Cost of Energy	JPY/kWh
m_{air}:	Mass flow rate of hot air	kg/h
m_{zeo}^{HC}:	Mass flow rate of zeolite of Heat Charger	kg/h
m_{zeo}^{ZB}:	Mass flow rate of zeolite of Zeolite Boiler	kg/h
N:	Life time of equipment	years
n:	The number of time period	years
OPEX:	Operating Expenses	JPY/year
q:	Water uptake	kg/kg
q_{eq}:	Equilibrium water uptake	kg/kg
q_{max}:	Maximum water uptake	kg/kg
q_{min}:	Minimum water uptake	kg/kg
T_{air0}:	Inlet temperature of hot air	°C
W_{blower}:	Power consumption	kW
α:	Capital recovery factor	%
β:	Subsidy rate	%
ΔP:	Pressure drop	kPa

References

[1] Saito Y. Cost estimation handbook for chemical engineers (in Japanese). Kogyo chosakai; 2000.

[2] Chiu JNW, Flores JC, Martin V, Lacarrière B. Industrial surplus heat transportation for use in district heating. Energy 2016;110:139–47. https://doi.org/http://dx.doi.org/10.1016/j.energy.2016.05.003.

[3] Storch G, Hauer A. Cost-effectiveness of a heat energy distribution system based on mobile storage units: two case studies. In: Ecostock, 10th internaional conference on thermal energy storage, New Jersey (USA): 2006.

[4] Krönauer A, Lävemann E, Brückner S, Hauer A. Mobile sorption heat storage in industrial waste heat recovery. Energy Procedia 2015;73:272–80. https://doi.org/http://dx.doi.org/10.1016/j.egypro.2015.07.688.

[5] Vatavuk WM. Updating the CE plant cost index. Chem Eng 2002:62–70.

[6] https://www.chemengonline.com/2019-cepci-updates-january-prelim-and-december-2018-final/ (accessed on Jul, 2019) 2019.

[7] https://ghg-santeikohyo.env.go.jp/files/calc/itiran2019.pdf (in Japanese, accessed on July, 2019) n.d.

This page intentionally left blank.

Chapter 7 Conclusions

7.1 Summary and novel contributions to the scientific community

In this study, a thermochemical energy storage and transport system utilizing zeolite ad/desorption cycle to resolve spatial and seasonal heat mismatch between unused heat from a sugar mill and industrial heat demands in Tanegashima was proposed, and the conditions that the system is financially viable were clarified via establishing design methods of heat charging and discharging devices. This doctoral dissertation consists of 7 chapters. Chapter 1 provides the context of the current situation of island areas in Japan, the quantity and quality of industrial unused heat and heat demand, and the current status of renewable heat.

Chapter 2 summarizes requirements of the system which are resolving the spatial and seasonal heat supply-demand mismatches and continuous generation of pressurized steam at the heat demands in Tanegashima. Thermal energy storage technology can be categorized into sensible, latent, and thermochemical types. Only thermochemical energy storage with any inherently reversible process can resolve spatial and seasonal heat supply-demand mismatches. Zeolite was employed as the heat storage material in this doctoral dissertation due to its safety, lack of degradation, and low cost. Main objectives of previous studies in mainly European countries are not to provide industrial process steam but to develop lower temperature applications for space heating, district heating systems and the like. Through the literature review of thermal energy storage technology from the perspective of material selection, component design, and system integration, a conceptual design of heat discharging device namely “Zeolite Boiler” co-operating with existing boilers in heat demands and employing moving bed and indirect heat exchanging process was developed to fulfill the requirement of industrial heat demand in Tanegashima of continuous generation of pressurized steam, while fixed bed reactors have been utilized widely for heat charging/discharging devices.

In Chapter 3, the heat charging potential and temperature of hot air for thermal energy storage were determined by material and heat flow analysis of the sugar mill in Tanegashima. The process flow diagram was built using a commercial process simulator based on empirically determined properties for sugarcane bagasse which is the residue of sugarcane after the milling process. The heat charging potential was calculated as the enthalpy of hot air. To improve the heat charging potential, blow steam reduction and bagasse drying were considered. In the bagasse drying process, the drying rate of bagasse is a key factor due to the limited heat source and time allotted for drying. The bagasse drying was designed based on a conveyor belt using heat derived from hot water exhausted from the sugar evaporation/crystallization process. The process was designed, and its performance was predicted numerically based on experimental data. The blow steam reduction and bagasse drying

process increase the heat charging potential and power generation by 52% and 70 kW of electricity, respectively.

Chapter 4 describes the design method of the heat discharging device namely “Zeolite Boiler”. The Zeolite Boiler can continuously generate pressurized steam by employing a moving bed of zeolite and an indirect heat exchanging process from zeolite bed to supplied water. This arrangement allows for the Zeolite Boiler to be cheaply manufactured as a non-pressurized chamber. Equilibrium water uptake on zeolite was obtained under isothermal condition and was modelled by Freundlich-Dubinin-Astakhov model. A one-dimensional numerical model solving mass and energy conservation equations including the empirical equilibrium water uptake model as source term predicted the performance of the Zeolite Boiler. A 1/200th scale Zeolite Boiler was designed when a full-scale Zeolite Boiler in Tanegashima is assumed to supply 0.4 t/h of steam. Continuous generation of pressurized steam of 0.2 MPa was demonstrated with a zeolite mass flow rate of 10 kg/h. Testing indicated discordant operating modes for two common performance indices: “heat recovery rate” and “fuel saving”. The heat recovery rate as compared to the exothermic potential of zeolite improves when the ultimate water uptake on zeolite increases. However, the fuel saving declines because the unrecovered adsorption heat at the outlet of the heat exchanger increases waste sensible heat of zeolite exhausted from the Zeolite Boiler. This inconvenient phenomenon was resolved by heat recovery of wasted sensible heat of the zeolite utilizing a secondary heat exchanger to pre-heat water supplied the existing boiler.

Chapter 5 focusses on the heat charging process. The heat charging device (Heat Charger) was designed following the same design methodology of Zeolite Boiler using numerical analysis as a moving bed in order to realize continuous heat charging. Based on the numerical results, a 1/400th -scale Heat Charger was manufactured, and continuous heat charging was demonstrated with a zeolite mass flow rate of 5 kg/h. Since the dominant factor of the operating cost of the thermochemical energy storage and transport system is power consumption of the blower as described in Chapter 6, the bed height and flow rate of air were designed to minimize the blower power.

Chapter 6 combines the results from Chapters 3-5 to conduct techno-economic and environmental analyses of the thermochemical energy storage and transport system and to clarify the conditions under which the system is financially viable. The electricity consumption of the blower for heat charging and the transportation cost of zeolite are the dominant determinants of the net profit of the system. The case, consisting of current sugar mill operation, a counter-flow Heat Charger, and a Zeolite Boiler without a secondary heat exchanger, results in economic loss under all conditions. However, the system becomes profitable by the addition of a secondary heat exchanger to the Zeolite Boiler. In terms of the sugar mill operation, power generation increased by blow steam reduction can compensate for the blower power for the Heat Charger, thereby making the system profitable. While power generation is expected to increase by introducing bagasse drying, the net profit is slightly less

than the case of blow steam reduction because of additional maintenance and operating cost for bagasse drying. Finally, this chapter shows that the system is financially viable when 70-80% of capital expenditure is publicly supplied and blow steam reduction or bagasse drying process are employed at the sugar mill.

7.2 Future research directions

Techno-economic and environmental analyses based on numerical simulation and validated by bench-scale testing were conducted in this dissertation. From these analyses, the conditions of financial viability for the system were clarified. The next stage of development involves demonstration of the system under real-world operations. In addition to gaining operating experience, the actions listed below would help improve implementation of the system in society.

(1) Material

In this dissertation, the well-studied Zeolite 13X was selected as the heat storage material. Other types of materials have different ad/desorption behaviors. **Figure 7.1** shows adsorption isotherms for different materials obtained by the diluted fixed bed test described in Chapter 4. Materials with different ad/desorption characteristics will cause performance “trade-offs” relative to Zeolite 13X that may lead to different system design decisions. For example, a material with a higher adsorption power (e.g., type LSX zeolite) has the potential to provide more adsorption heat to the consumer and thus, an increase in fuel saving at the heat discharging station. However, this material requires more heat usually at higher temperatures to desorb the water at the heat charging station, possibly reducing its range of applicability. To determine material preference based on the available equipment, heat sources, and heat demands, techno-economic and environmental analyses connecting the material level to the system level will be needed.

As described in Chapter 4, heat transfer in packed beds dominates the performance of Zeolite Boiler, which can be commonly observed in packed bed reactors. Enhancement of effective thermal conductivity by improving inherent thermal conductivity, bridging each particle, mixing with graphite and the like will improve the performance of heat charging and discharging devices, and reduce the initial cost of heat exchanger.

Chemical reaction materials such as MgO/H_2O, CaO/ H_2O and the like would be candidates of working pairs for thermochemical energy storage systems. Chemical reaction materials have higher energy storage density than adsorbents, which can reduce transportation cost and reactor volume. Flexible design of application for various temperature levels according to the reaction temperature would be allowed as long as the temperature level of heat source is higher than the reaction temperature, and the system has positive economic performance.

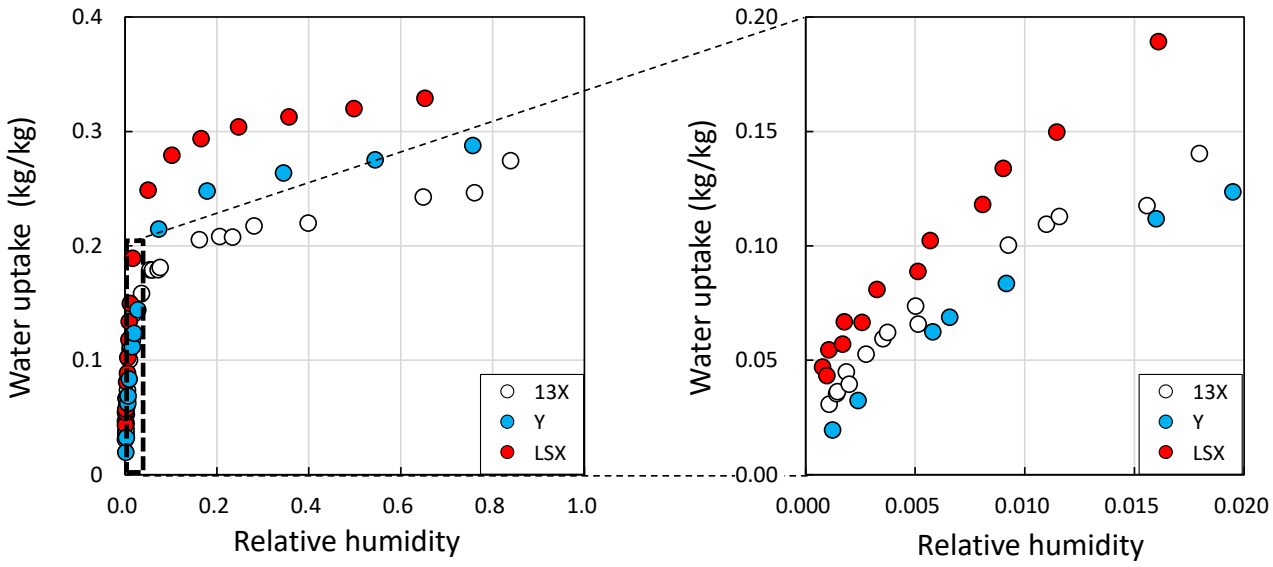

(a) Whole relative humidity range (b) Low relative humidity range

Fig. 7.1. Adsorption isotherms in different types of zeolite.

(2) Application

The thermochemical energy storage and transport system can be applied to other geographic areas and other fields with heat resources/demands. Domestic and overseas sugar mills can operate this technology utilizing their unused energy derived from sugarcane bagasse at much larger scales. The Zeolite Boiler can generate pressurized steam continuously, thus absorption chillers can be operated in tandem with the Zeolite Boiler as shown in **Fig. 7.2**. The major sugarcane producers are located around the tropical zone such as Brazil and Thailand where cold energy is required for air conditioning systems. Thus, the combined Zeolite Boiler-Absorption Chiller system is well-suited for the local resources and need for air conditioning.

An additional usage pathway for the Zeolite Boiler is to provide drying via indirect heating. In systems where process steam is used for drying, the humid exhaust exiting the dryer can be supplied to the Zeolite Boiler, thereby reducing the parasitic load on the existing boiler. **Figure 7.3** shows the schematic of humid air injection process. The indirect heating system dries material with the latent heat of steam and exhausts humid air with a high dew point. The humid air is mixed with steam from the existing boiler, reducing the mass flow rate of boiler steam and accompanying fuel consumption.

Coupling of industrial low-temperature waste heat and adjacent heat demands via the system described herein may help to reduce fossil fuel usage while maintaining profitability. Steam is also used extensively in a variety of industrial and chemical processes, as evidenced by the preponderance of boilers. Regardless of the application, adoption of the thermochemical energy storage and transport system to other fields should be conducted via techno-economic analysis.

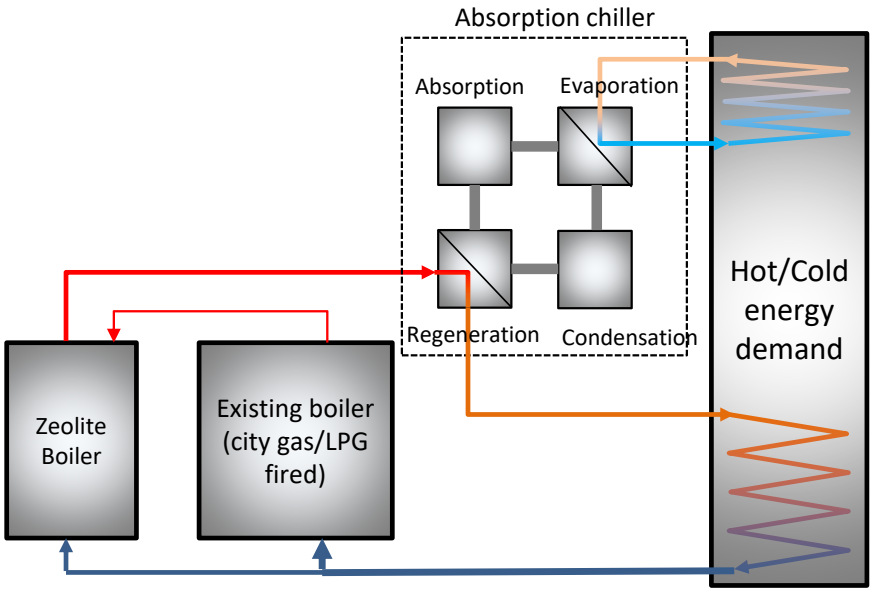

Fig. 7.2. Schematic of combined system with Zeolite Boiler and absorption chiller.

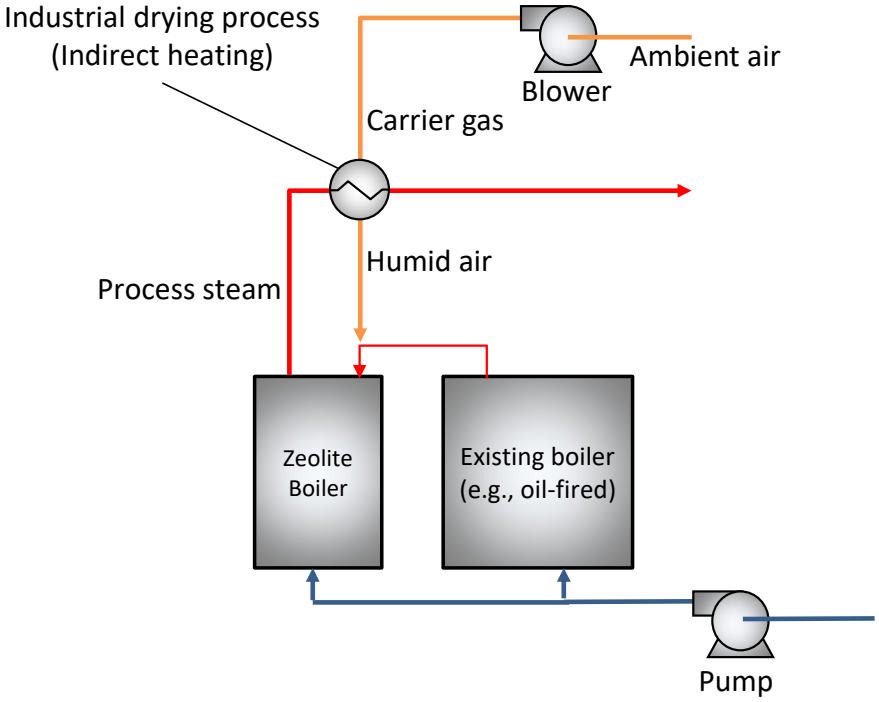

Fig. 7.3. Schematic of humid air injection process.

(3) System

The developed system in this study was discussed under mainly steady operation. System unsteadiness between heat charging and discharging stations (e.g., different operating hours) and unsteady characteristics of equipment (e.g., activation, load change and the like) need further

discussion. System unsteadiness can be resolved by controlling the balance of reserved heat storage material at each station. Since Zeolite Boilers have high thermal inertia which leads its low load-following capability, Zeolite Boilers should be operated to supply base-load heat demands, and load fluctuation should be followed by existing boilers co-operating with Zeolite Boilers. Even if existing boilers follow load fluctuations of heat demand, compact design of Zeolite Boiler with higher space velocity is preferable to enhance load-following capability and shorten the activation time. The time to achieve full load from cold-start might be reduced by employing fixed bed operation in activating the Zeolite Boiler until the device is sufficiently warmed, and then shifting to moving bed operation.

Energy issues effect the other areas of society such as the local economy, agricultural productivity, water availability, and the like. Solving individual problems in isolation may cause conflicts with other sub-systems (e.g., food vs fuel). Integrating relevant fields into a holistic approach (i.e., “Nexus Approach”), instead of focusing on individual issues, is required to realize sustainability goals without compromising other aspects of the environment or society. This dissertation established the design method of thermochemical energy storage and transport system from sugar mill utilizing a zeolite ad/desorption cycle and clarified the conditions that the system is financially viable. For the next stage, the effect of implementation of the thermochemical energy storage system on socio-economic factors, resource circulation, and the like should be evaluated via the *“*Nexus Approach*”*.

7.3 Conclusions

This dissertation designed the thermochemical energy storage and transport system of unused heat from sugar mill utilizing zeolite ad/desorption cycle. The design methodology of thermochemical energy storage system can be generalized as follows;

1. Selection of material and reactor types
   - Requirements and constraints of heat sources and heat consumers are firstly summarized.
   - Suitable material and reactor type which fulfill the requirements and constraints must be selected.
2. Process modeling
   - Heat charging potential is quantified by material and heat flow analysis of heat charging station.
   - Process modifications to improve the heat charging potential should be evaluated.
3. Design of heat charging and discharging devices
   - Governing equations (mass, chemical species, energy and momentum equations) must be coupled to simulate the performance of each device.
   - Kinetics and heat transfer characteristics which dominate the performance must be obtained experimentally and coupled into the governing equations to simulate the performance accurately.

- For the heat discharging device, since the fuel reduction of existing boiler determines the revenue of the system, sensitivities of design parameters on the fuel saving are required to be carefully investigated, and then the heat discharging device should be optimally designed to maximize the fuel reduction.
- For the heat charging device, direct heat transfer process between heat transfer fluid and material is commonly employed because of its large heat transfer area. Since the power consumption of blower to inject heat transfer fluid into the bed will deteriorate the economic performance, design parameters should be optimized to minimize the blower power consumption.

4. System evaluation via techno-economic and environmental analyses
   - The dominant determinants in economic performance should be identified by the techno-economic analysis, and 2. Process modeling and 3. Design of heat charging and discharging devices should be modified to eliminate the cost dominant determinants.
   - Increase in fuel saving, reducing auxiliary power consumption and reducing transportation trips improve the economic performance.

The thermochemical energy storage and transport system of unused heat from sugar mill utilizing zeolite ad/desorption cycle was considered and the system is financially viable when the appropriate CAPEX support is publicly provided. This research aimed to effectively utilize renewable energy from local agriculture wastes of island communities. The importance of the proposed system is not only that of fuel savings but also adding co-benefits to the extant agricultural system, revitalizing the regional economy, and increasing resource circulation. Thus, public funding of the system would induce multiple socio-economic benefits to the local area.

This dissertation clarified both the economic and environmental effects of technology implementation via multi-scale analyses (i.e., determination of material characteristics, bench-scale demonstration, simulation of a full-scale plant, and techno-economic and environmental analyses). Moreover, these methods were used to inform the direction for future research and development. By expanding the socio-economic analysis to include relevant stakeholders, the effect of technology implementation on macroeconomic indices and environmental burdens can be determined. The linked analysis from the technology level to the social level will enhance implementation by identifying synergies and avoiding impediments.

The Earth is now approaching a number of tipping points of potentially irreversible change. While Japan is the first developed country to exit year-on-year economic growth and reach a relatively stable output, a similar transition will occur elsewhere in the near future. If this transition can be used to concurrently achieve a sustainable society, it may be possible to prevent the planet from sliding into

irreversible environmental changes. I strongly expect that integration of research, development, and deployment of technology to the social system will be of paramount importance.

Research achievements

Journal articles

- Design of zeolite boiler in thermochemical energy storage and transport system utilizing unused heat from sugar mill, Applied Energy Vol. 238, pp. 561-571, March 2019, **Shoma Fujii**, Naoyuki Horie, Ko Nakaibayashi, Yuichiro Kanematsu, Yasunori Kikuchi, and Takao Nakagaki
- Improvement of heat recovery of Zeolite Boiler used for thermochemical energy storage and transport system utilizing unused heat from biomass (in Japanese), Journal of Japan Boiler Association Vol. 412, pp. 4-10, December 2018, Takao Nakagaki, and **Shoma Fujii**
- Techno economic analysis of thermochemical energy storage and transport system utilizing "Zeolite Boiler": case study in Sweden, Energy Procedia Vol. 149, pp. 102-111, September 2018, **Shoma Fujii**, Yuichiro Kanematsu, Yasunori Kikuchi, Takao Nakagaki, Justin NW Chiu, and Viktoria Martin
- Material and heat flow analysis in thermal energy storage and transport system utilizing unused heat from bagasse boiler, Mechanical Engineering Journal Vol. 3 No. 5 pp.16-00334, October 2016, **Shoma Fujii**, Yuichiro Kanematsu, Yasunori Kikuchi, and Takao Nakagaki

International conferences

- (Oral) Effect of ad/desorption characteristics on techno-economic aspects of thermochemical energy storage and transport system, The 5th International Symposium on Innovative Materials and Processes in Energy Systems IMPRES2019, Kanazawa Japan, October 2019, **Shoma Fujii**, Naoyuki Horie, Yuichiro Kanematsu, Yasunori Kikuchi, and Takao Nakagaki
- (Oral) Humidified air injection for zeolite boiler in thermochemical energy storage and transport system utilizing unused heat from sugar mill, International Sustainable Energy Conference 2018 ISEC, Graz Austria, October 2018, **Shoma Fujii**, Yuichiro Kanematsu, Yasunori Kikuchi, and Takao Nakagaki
- (Oral) Techno economic analysis of thermochemical energy storage and transport system utilizing "Zeolite Boiler": case study in Sweden, 16th International Symposium on District Heating and Cooling DHC 2018, Hamburg Germany, September 2018, **Shoma Fujii**, Yuichiro Kanematsu, Yasunori Kikuchi, Takao Nakagaki, Justin NW Chiu, and Viktoria Martin
- (Oral) Development of zeolite boiler in thermochemical energy storage and transport system utilizing unused heat from sugar mill, 14th International Conference on Energy Storage

EnerSTOCK 2018, Adana Turkey, April 2018, **Shoma Fujii**, Ko Nakaibayashi, Yuichiro Kanematsu, Yasunori Kikuchi, and Takao Nakagaki

- (Oral) Effect of multi injection process on “Zeolite Boiler” in thermochemical energy storage and transport system of unused heat from bagasse boiler, ASME 2017 Power and Energy Conference PowerEnergy & ICOPE 2017, Charlotte USA, June 2017, **Shoma Fujii**, Yuichiro Kanematsu, Yasunori Kikuchi, and Takao Nakagaki
- (Poster) Exploratory study of "Zeolite Boiler” in thermal energy storage and transport system of unused heat from bagasse boiler, The 4th International Symposium on Innovative Materials and Processes in Energy Systems IMPRES 2016, Sicily Italy, October 2016, **Shoma Fujii**, Kazuma Furutani, Yuichiro Kanematsu, Yasunori Kikuchi, and Takao Nakagaki
- (Oral) Transport system of unused heat from bagasse-boiler by using chemical heat storage in sugar milling and refinery process, International Conference on Power Engineering ICOPE-15, Yokohama Japan, November 2015, **Shoma Fujii**, Ryuichi Satoh, Yuichiro Kanematsu, Yasunori Kikuchi, and Takao Nakagaki

Domestic conferences

- (Oral) Performance prediction and experimental validation of heat charging device in thermochemical energy storage and transport system utilizing unused heat from sugar mill (in Japanese), The 24th National Symposium on Power and Energy Systems SPES2019, Tokyo, Japan, June 2019, Naoaki Arimoto, Yayoi Abe, **Shoma Fujii**, Yasunori Kikuchi, Yuichiro Kanematsu, and Takao Nakagaki
- (Oral) Continuous generation of pressurized superheated steam by Zeolite Boiler in thermochemical energy storage and transport system utilizing unused heat from sugar mill (in Japanese), The 24th National Symposium on Power and Energy Systems SPES2019, Tokyo, Japan, June 2019, Akihiro Higuchi, **Shoma Fujii**, Yasunori Kikuchi, Yuichiro Kanematsu, and Takao Nakagaki
- (Oral) Techno-economic analysis of thermochemical energy storage and transport system utilizing zeolite steam ad/desorption characteristics (in Japanese), The 56th National Heat Transfer Symposium, Tokushima Japan, May 2019, **Shoma Fujii**, Naoyuki Horie, Yuichiro Kanematsu, Yasunori Kikuchi, and Takao Nakagaki
- (Oral) Techno-economic design of heat charger in thermochemical energy storage and transport system utilizing unused heat from sugar mill (in Japanese), Mechanical Engineering Congress 2018, Osaka Japan, Yayoi Abe, Kazuma Furutani, Shoma Fujii, Yasunori Kikuchi, Yuichiro Kanematsu, Seichiro Kimura, and Takao Nakagaki

- (Oral) Effect of adsorption heat on heat transfer between zeolite packed bed and boiler tube wall (in Japanese), The 55th National Heat Transfer Symposium, Sapporo Japan, May 2018, Naoyuki Horie, **Shoma Fujii**, and Takao Nakagaki
- (Oral) Steam generation test of Zeolite Boiler in thermochemical energy storage and transport system using unused heat from sugar mill (in Japanese), The 22th National Symposium on Power and Energy Systems SPES2017, Toyohashi Japan, June 2017, Ko Nakaibayashi, **Shoma Fujii**, Yuichiro Kanematsu, Yasunori Kikuchi, and Takao Nakagaki
- (Oral) Scenario planning for sustainable utilization of plant-derived resources by integrated modeling of agricultural and industrial processes (in Japanese)，SCEJ 82nd annual meeting, Tokyo Japan, March 2017, Kotaro Ouchida, **Shoma Fujii**, Yuichiro Kanematsu, Yuko Oshita, Ryotaro Nakamura, I-ching Chen, Yasuhiro Fukushima, Takao Nakagaki, Tatsuya Okubo, and Yasunori Kikuchi
- (Oral) Increasing heat recovery of "Zeolite boiler" in thermal energy storage and transport system of unused heat from sugar mill (in Japanese)，SCEJ Regional Meeting in Fukushima 2016，Fukushima Japan, November 2016, **Shoma Fujii**, Yuichiro Kanematsu, Yasunori Kikuchi, and Takao Nakagaki
- (Oral) Preliminary design study on Zeolite Boiler in thermal energy storage and transport system using unused heat from sugar mill (in Japanese), Mechanical Engineering Congress 2016, Fukuoka Japan，September 2016, Kazuma Furutani，**Shoma Fujii**, Takao Nakagaki, Yasunori Kikuchi, Yuichiro Kanematsu, and Yousuke Hamada
- (Oral) Transport system of unused heat from bagasse-boiler by using zeolite (in Japanese), The 20th National Symposium on Power and Energy Systems SPES2015, Sendai Japan, June 2015，**Shoma Fujii**, Ryuichi Satoh, Yuichiro Kanematsu, Yasunori Kikuchi, and Takao Nakagaki

Awards

- Best Paper Award, The 14th International Conference on Energy Storage, Adana Turkey, April 2018
- Outstanding presentation award, JSME Power and Energy System division, The Japan Society of Mechanical Engineers, ICOPE-17, Charlotte USA, June 2017（日本機械学会動力エネルギーシステム部門　優秀講演賞）
- Azusa Ono Memorial Award, Waseda University, March 2017 （早稲田大学，小野梓記念学術賞）
- Miura Award, Japan Society of Mechanical Engineers, March 2017 （日本機械学会三浦賞）
- Student Award, The Society of Chemical Engineers, Japan Regional Meeting in Fukushima 2016, November 2016, （化学工学会学生賞（関東支部長賞）特別賞）

Funding

- JSPS Research Fellowship for Young Scientists (DC2) , April 2018（日本学術振興会特別研究員 DC2）
- JXTG エネルギー若手研究者奨励研究　採択　2017 年 7 月
- Graduate Program for Embodiment Informatics, Program for Leading Graduate Schools, Japan Society for the Promotion of Science, April 2015　（文部科学省博士課程教育リーディングプログラム，実体情報学博士プログラム）

Contribution of "*Embodiment Informatics*" to sustainable society

In 2015, I entered the *"Graduate Program for Embodiment Informatics"* as part of the "*Program for Leading Graduate Schools"* organized by the Ministry of Education, Culture, Sports, Science and Technology of Japan. The "*Program for Leading Graduate Schools"* aims to foster highly creative and interdisciplinary doctors who will play leading roles in the academic, industrial, and public sectors.

The *"Graduate Program for Embodiment Informatics"* managed by Waseda University aims to educate excellent doctoral students with "Imagination", "Foresight", and "Executive and Leadership ability", who will create new industries in the area of "*Embodiment Informatics*", which integrates many research fields such as mechanical engineering, information technologies and the like.

As described in Chapter 1 and 7, Planetary Boundaries and global societal issues are not independent, but rather are intertwined into a complex and adaptive system. To resolve these issues and enhance implementation of new technologies contributing to a sustainable society, collaborations with other fields is mandatory. I define *"Embodiment Informatics*" as "*the methodology to resolve issues in complicated systems and to enhance solution implementation by integration into existing frameworks and collaboration with many relevant parties including disparate research fields*". The methodology of *"Embodiment Informatics"* is essential to achieve a sustainable society, and project-based learning is critical to realize "*Embodiment Informatics*". Through project-based learning, I have come to appreciate differences in selection methodology and implementation method between disciplines. Attacking an issue from multiple angles through collaboration -as was done in collaborative projects for forest industries and education- improved outcomes and social acceptability.

"*Embodiment Informatics*" played a role in this research into the creation of a heat storage technology. Engineering design was a combination of mechanical, chemical, and systems engineering; however, the design was also influenced by on-the-ground discussions with the various stakeholders who would use and/or be effected by the realization of the thermochemical energy storage and transport system. Additionally, the designed system was examined at a larger societal level via techno-economic and environmental analyses.

During the overseas research term at the KTH Royal Institute of Technology in Sweden, I practiced project-based learning in collaboration with the KTH group. My contribution did not end in the laboratory, but rather extended to investigating real-world operational conditions, environmental effects, and techno-economic impacts of the heat transportation technology. Through this work, difference between Sweden and Japan came into focus and the Japan-specific system design became more realistic.

Based on my experiences, "*Embodiment Informatics*" is a crucial lever in solving the complex and adaptive issues facing society; extending the methodology will facilitate the transition to a sustainable society.

Main activities in *"Graduate Program for Embodiment Informatics"*

- Presentation at "Interdisciplinary Workshop for Leading Students (IW4LS)"
- Planning and organizing "Leading Camp 2015"
- Planning and organizing "Summer School with Tsukuba University"
- Attending exchange program at University of California, Davis
- Developing "forest road optimization system"
  - Patent: 路網ルート設計装置及びそのプログラム、並びに路網ルート生成表示システム，発明者：白井裕子，野澤直樹，藤井祥万，佐藤隆哉，加藤卓哉，出願番号：特願 2016-95747 号，2016 年 5 月
  - International Conference: Naoki Nozawa, Shoma Fujii, Ryuya Sato, Ryo Suzuki and Yuko Shirai, Forest roads design and 3D visualization for steep mountains, 125th IUFRO, International Union of Forest Research Organizations, IUFRO17-11155, Freiburg Germany, September 2017
- Poster presentation at "the third International Symposium on Embodiment Informatics"
- Participating in "the energy-related facilities exercise in Miyakojima" (organized by Leading Graduate Program in Science and Engineering, Waseda University).
- Presentation at "the 4th Waseda Vision 150 student competition" and received "Special Recognition Award"
- Planning and organizing "the 1st joint symposium between Leading Graduate Program in Science and Engineering and Graduate Program for Embodiment Informatics"
- Presentation at "the 1st joint symposium between Leading Graduate Program in Science and Engineering and Graduate Program for Embodiment Informatics"
- Chairing the invited talk by Project associate professor Yasunori Kikuchi, The university of Tokyo
- Planning "Leading Camp 2016"
- Research term (6 months) at KTH Royal Institute of Technology, Sweden
- Invited talk at "the 2nd joint symposium between Leading Graduate Program in Science and Engineering and Graduate Program for Embodiment Informatics"
- Presentation at "Leading Forum 2018"

Acknowledgements

To members of the “Graduate Program for Embodiment Informatics” in the “Program for Leading Graduate Schools” organized by Ministry of Education, Culture, Sports, Science and Technology,

I would like to acknowledge the support for my Masters and Doctoral course study at Waseda University.

To the Japan Society for the Promotion of Science,

I would like to acknowledge for understanding of the importance of my research via granting me the Research Fellowship for Young Scientist (Grand number: 18J11316).

To the people of the Shinko sugar mill in Tanegashima,

I would like to express my gratitude for your understanding, discussing, and funding my study.

To Professor Takao Nakagaki,

I would like to express my sincere appreciation for your spirit to lift me to a higher level. Your consistent guidance from my Bachelor to Doctoral thesis has made this work possible.

To my thesis reviewers, Professor Masafumi Katsuta and Professor Jin Kusaka of Waseda University, and Associate professor Yasunori Kikuchi of The University of Tokyo,

your earnest review and suggestions greatly improved this dissertation, thank you.

To Professor Viktoria Martin, Assistant professor Justin Chiu, Dr. Saman Gunasekara and members of the Energy Technology Department (EGI) at KTH, Royal Institute of Technology in Sweden,

thank you for welcoming me as a part of thermal energy storage group in KTH, and providing assistance to improve my study. I hope our collaboration can continue into the future.

To my laboratory members and members of the ESD (Exergy System Design) group,

I would like to recognize your constant support. Your hard work helped me greatly. I would like to give special appreciation to Dr. Corey Myers for the cooperation and competition. Let us continue our hard work for the Earth.

To people who of Tanegashima,

thank you for welcoming me, I love your home. I will keep working hard to achieve a sustainable society for you.

To Associate professor Yasunori Kikuchi of The University of Tokyo, Associate professor Yasuhiro Fukushima of Tohoku University, Project Assistant Professor Yuichiro Kanematsu of The University of Tokyo, and Dr. Yuko Oshita of The University of Tokyo,

our regular discussions and your consistent guidance have been invaluable, thank you.

To my family,

thank you for always understanding and encouraging me. My heartfelt appreciation goes to your love.

To the Earth,

thank you for being the driving force of my life, always motivating my work. Thank you in advance your great patience and resilience until I can save you.